Erratum & Addenda

p xxii line 2: Qualifying sentence: The valley dose is also a function of the array size.

p 15, line 4: Modify sentence to: A synchrotron produces very intense, quasi-parallel X-rays with a photon flux rate (number of photons per unit area, per unit time) several orders of magnitude greater than x-rays produced by conventional x-ray sources such as diagnostic x-ray units or linear accelerators for megavoltage radiotherapy.

p 21, para 2, lines 2 & 3: Modify sentence to: However, the interlaced method does not provide a good conformally-shaped distribution.

p 85, Table Legend: Table 2 instead of Table 1.

p 85, Table Legend: Add sentence: It should be stated that the array size is also a major parameter in determining the peak-to-valley dose ratios. Here, the beam size was 10.0 mm x 1.0 mm.

p 98, Figure 7 Legend: Add sentence: Given the quasi-parallel nature of the synchrotron X-ray beam, the wide scattering angles inside the collimator channels are exaggerated, for illustrative purposes.

pp 200 - 202, Legends for Figures 1, 2 & 3: Add sentence at the end of each legend:

Jeffrey C. Crosbie M.Sc.

Synchrotron Microbeam Radiation Therapy

PhD Thesis

Monash University

School of Physics

Contents

List of Figures

General Declaration

Monash University

Monash Research Graduate School

Declaration for thesis based or partially based on conjointly published or unpublished work

In accordance with Monash University Doctorate Regulation 17/ Doctor of Philosophy and Master of Philosophy (MPhil) regulations the following declarations are made:

I hereby declare that this thesis contains no material which has been accepted for the award of any other degree or diploma at any university or equivalent institution and that, to the best of my knowledge and belief, this thesis contains no material previously published or written by another person, except where due reference is made in the text of the thesis.

This thesis includes one original paper, presented as Chapter 4, published in a peer-reviewed journal and one submitted, but unpublished manuscript, presented as Chapter 6. The central theme of the thesis is synchrotron microbeam radiation therapy. The ideas, development and writing up of the papers in the thesis were the principal responsibility of myself, the candidate, working within the School of Physics under the supervision of Professor Robert A. Lewis and Dr. Imants Svalbe.

The inclusion of co-authors reflects the fact that the work came from active collaboration between researchers and acknowledges input into team-based research.

In the case of Chapters 4 and 6, my contribution to the work involved the following:

- Conception, planning and study design in order to refine the research question
- Execution of experimental research
- Analysis and interpretation of the data, including statistical analysis
- Drafting and revising the submitted manuscripts

For Chapter 6, Prof. Peter Rogers & Ms. Leonie Cann from the Centre for Women's Health Research, Monash Institute of Medical Research, provided significant assistance with executing the experimental research plan during our field trips to the SPring-8 synchrotron in Japan. Prof. Rogers and Ms. Cann performed the majority of the animal handling in preparation for irradiation, as well as the tissue harvesting and fixation. All laboratory histological and immunohistochemical staining presented in the thesis was performed by Ms. Leonie Cann, unless otherwise stated. However, all microscopy images and analysis were produced and performed by myself, the candidate.

Ms. Christina Restall from the Peter MacCallum Cancer Centre, Melbourne, inoculated the mice with the tumours prior to their transport to Japan and also measured the post-irradiation tumour growth characteristics. The conventional radiotherapy survival study, also described in Chapter 6, was performed by Ms. Christina Restall

and Dr. Jim Hagekriakou from the Peter MacCallum Cancer Centre. However, the analysis of the survival data presented in Chapter 6 was performed by myself, the candidate.

The thesis has been prepared using the LaTeX 2_ε document preparation system, with the exception of Chapters 4 and 6, which were prepared using Microsoft Word 2007. I have renumbered sections of submitted or published papers in order to generate a consistent presentation within the thesis.

Signed: Jeffrey C. Crosbie

Date: 11 December 2008

Copyright Notices

Acknowledgments

There are many individuals to thank who have helped me in various ways over the last few years to bring me to the stage of submitting a PhD thesis for examination. I apologise in advance if I have omitted anybody! The thesis is a multidisciplinary one with collaborations not only across different faculties within the University, but involving international collaborators as well.

Firstly, I thank Rob Lewis and Imants Svalbe from the Monash Centre for Synchrotron Science and the School of Physics, Monash University, for supervising the project and giving me their full support. Michael Morgan, the head of the School of Physics has also been very supportive of my research efforts. Thanks also go to the administrative and technical support staff within the School of Physics and the Monash Centre for Synchrotron Science who have helped me, in particular, Jean Pettigrew, Tracey Lawrence, Norma Hayes, James Gibbons, John MacDougall, Alan Holland, David Zuidema, Rod Mackie and Nino Benci, Peter Oliver, Darren Scott and Steve Morton. I thank current and past postgraduate students as well as postdoctoral fellows within the School for numerous, fruitful discussions and assistance, in particular; Ivan Williams, Marcus Kitchen, Sabeena Sidhu, John Gillam, Toby Beveridge, David Vine, Gary Ruben, Shekhar Chandra, John Daniels, Karen Siu, Stewart Midgley, Marian Cholewa and Chris Hall. I thank the School, the Monash Centre for Synchrotron Science and the Faculty of Science for financial support through the Faculty of Science's Dean's Postgraduate Scholarship.

I was fortunate to collaborate with Peter Rogers from the Centre for Women's

Health Research, within Monash University's department of Obstetrics & Gynaecology. When I started this project, there was no microbeam radiation therapy research performed at Monash University and Peter was instrumental in providing laboratory histology and immunohistochemistry facilities, to kick-start the radiobiological components. Peter also acted very much as an associate supervisor to me. His staff and students, past and present, were very helpful to me and I thank them, in particular, Leonie Cann, Penny Clay, Jane Girling, Caroline Gargett and Fiona Lederman. I am especially grateful to Peter and Leonie for their collaborative efforts with me at the SPring-8 synchrotron.

I acknowledge and thank our collaborators on the microbeam project in Melbourne and overseas; Robin Anderson and Tina Restall from Peter MacCallum Cancer Centre, Melbourne, Saleela Ruwanpura and Bryan Williams from the Monash Institute of Medical Research, Dr. Sarah Meachem from Prince Henry's Institute of Medical Research, Melbourne, Moshi Geso & Chris Wong from Royal Melbourne Institute of Technology, and Kai Rothkamm from the Health Protection Agency in the UK. I am very grateful to Naoto Yagi from the SPring-8 synchrotron in Japan for providing us with expert assistance and advice during our field trips to SPring-8. I also thank the beamline scientists, Kentaro Uesugi, Keiji Umetanti and Yashuiko Imai for their assistance.

During the course of my PhD, I worked one day a week as a medical physicist in the William Buckland Radiotherapy Centre at The Alfred Hospital in Melbourne. I am tremendously grateful to Malcolm Millar, Chief Physicist (retired) and his successor, Trevor Ackerly for offering me this lifeline, which is both financial and professional. I am very proud of my association with The Alfred Hospital.

I have been fortunate to have received grants by the Australasian College of Physical Scientists & Engineers in Medicine which has allowed me to travel to interstate and international conferences. I also acknowledge financial support for the microbeam project from the Australian Nuclear Science & Technology Organisation's Access to Major research Facilities Program, and the Cancer Council Victoria's Ven-

ture Grant Scheme.

Lastly and most importantly, I extend my heartfelt thanks to my family. My wife Maria has been a magnificent support to me during my PhD studies, it cannot have been easy looking after our children during my many overseas trips and during those stressful moments when I was there in person but not in spirit. In short, I could not have even attempted the PhD without Maria's love and encouragement, and words alone cannot suffice as thanks. I thank my two children, Nora and Eamonn, for reminding me of the truly important things in life. I also thank my parents, Anthony and Moya, in Dublin, Ireland, for their lifelong support and encouragement.

Dedication

I dedicate this thesis to the memory of my Grandmother; Mary (Nanny) Crosbie, who passed away on 19 October 2008.

Abstract

This thesis presents interdisciplinary, collaborative research in the field of synchrotron microbeam radiation therapy (MRT). Synchrotron MRT is an experimental radiotherapy technique under consideration for clinical use, following demonstration of efficacy in tumour-bearing rodent models with remarkable sparing of normal tissue. A high flux, X-ray beam from a synchrotron is segmented into micro-planar arrays of narrow beams, typically 25 μm wide and with peak-to-peak separations of 200 μm. The radiobiological effect of MRT and the underlying cellular mechanisms are poorly understood. The ratio between dose in the 'peaks'of the microbeams to the dose in the 'valleys', between the microbeams, has strong biological significance. However, there are difficulties in accurately measuring the dose distribution for MRT. The aim of this thesis is to address elements of both the dosimetric and radiobiological gaps that exist in the field of synchrotron MRT.

A method of film dosimetry and microdensitometry was adapted in order to measure the peak-to-valley dose ratios for synchrotron MRT. Two types of radiochromic film were irradiated in a phantom and also flush against a microbeam collimator on beamline BL28B2 at the SPring-8 synchrotron. The HD-810 and EBT varieties of radiochromic film were used to record peak dose and valley dose respectively. In other experiments, a dose build-up effect was investigated and the half value layer of the beam with and without the microbeam collimator was measured to investigate the effect of the collimator on the beam quality. The valley dose obtained for films placed flush against the collimator was approximately 0.25% of the peak dose. Within the

water phantom, the valley dose had increased to between 0.7–1.8% of the peak dose, depending on the depth in the phantom. We also demonstrated, experimentally and by Monte Carlo simulation, that the dose is not maximal on the surface and that there is a dose build-up effect. The microbeam collimator did not make an appreciable difference to the beam quality. The measured values of peak-to-valley dose ratio were higher than those predicted by previously published Monte Carlo simulation papers.

For the radiobiological studies, planar (560 Gy) or cross-planar (2 x 280 Gy or 2 x 560 Gy) irradiations were delivered to mice inoculated with mammary tumours in their leg, on beamline BL28B2 at the SPring-8 synchrotron. Immunohistochemical staining for DNA double strand breaks, proliferation and apoptosis was performed on irradiated tissue sections. The MRT response was compared to conventional radiotherapy at 11, 22 or 44 Gy. The results of the study provides the first evidence for a differential tissue response at a cellular level between normal and tumour tissues following synchrotron MRT. Within 24 hours of MRT to tumour, obvious cell migration had occurred into and out of irradiated zones. MRT-irradiated tumours showed significantly less proliferative capacity by 24 hours post-irradiation ($P = 0.002$). Median survival times for EMT-6.5 and 67NR tumour-bearing mice following MRT (2 x 560 Gy) and conventional radiotherapy (22 Gy) increased significantly compared to unirradiated controls ($P < 0.0005$). However, there was markedly less normal tissue damage from MRT than from conventional radiotherapy. MRT-treated normal skin mounts a more coordinated repair response than tumours. Cell-cell communication of death signals from directly irradiated, migrating cells, may explain why tumours are less resistant to high dose MRT than normal tissue.

CHAPTER 1

Introduction

1.1 Problem Statement

It is estimated that fifty per cent of all cancer patients receive radiation therapy as part of their treatment regimen (Bentzen, 2006). The goal of radiation therapy is to maximise the total radiation dose to the tumour and minimise the dose to the surrounding, normal, tissue. This goal can be difficult to achieve due to the shape of the tumour and/or nearby critical structures. A typical radiation therapy regimen might consist of a total dose of 70 Gy (J/kg), fractionated in time so that the patient receives 2 Gy per day over 35 days. The dose is fractionated primarily to allow irradiated normal tissue time to recover in between fractions. The side effects of radiation therapy range from serious to fatal, and modern radiotherapy techniques have evolved over the past few decades to conform the dose as tightly as possible to target the tumour tissue and spare the normal tissue. It is the tolerance of normal tissue to radiation which dictates the total dose that can be delivered to a tumour.

Synchrotron Microbeam Radiation Therapy (MRT) is an experimental form of radiation therapy in which synchrotron-generated X-rays (energy range 60 -150 keV) are spatially fractionated by a collimator, producing intense microbeams, tens of microns wide separated by hundreds of microns. Animal studies have shown that it is possible to deposit hundreds of Gray of peak, in-beam dose to normal and/or inocu-

lated tumour tissue in a fraction of a second. Remarkably, normal tissue appears to have an extraordinary tolerance to radiation when delivered in a spatially distributed, microplanar fashion. Further, normal tissue retains a high tolerance to spatially segmented dose distributions relative to the response from tumour tissue.

Despite the fascinating results obtained with MRT over the past decade, there are little or no data to explain this effect. The papers on synchrotron MRT have tended to report survival studies, with no mechanistic data to support or refute a hypothesis. Apart from some conventional histology, there are no immunohistochemistry data on the important cellular processes of proliferation, cell death and DNA repair, and how these processes behave over time, post-MRT. Nor is there comprehesnive data aimed at optimising the physical geometry of spatial dose distributions for a particular biological effect. There are several gaps (of strategic importance), in our understanding of the underlying radiobiology of MRT.

A confounding problem on top of this is the difficulty faced by physicists to accurately quantify the absorbed dose distributions that result from very high dose gradients across micron scale beam widths. There is no one dosimeter available that can simultaneously measure the high dose in the ‘peaks’of the microbeams, and the low dose in the ‘valley’ region between adjacent microbeams. Consequently, the majority of publications pertaining to MRT dosimetry have employed Monte Carlo methods to simulate the dose distributions. However, for MRT to gain acceptance by the radiation oncology community, it is important to have reliable and reproducible techniques of dosimetry. There is therefore another gap in the knowledge; MRT dosimetry, which must be filled in addition to pursuing more elaborate biological studies.

1.2 Thesis Aim & Objectives

The aim of the work reported in this thesis is to address elements of both the dosimetric and radiobiological gaps that exist in the field of synchrotron MRT. For the

MRT dosimetry study, the aim was to develop a technique that allows a simultaneous measurement of the peak and valley doses at micron spatial scales, as the microbeams propagate through air and into a tissue-equivalent phantom over short exposure times. Ideally, the accuracy of an MRT dosimetry method would be comparable to that achievable in conventional radiotherapy (typically $\pm$5%). For the radiobiology studies, the stated aim was to better understand the radiobiological mechanisms of MRT by quantifying stimulated changes in cellular processes such as proliferation, apoptosis and DNA repair, in the hours and days post-irradiation, in normal and tumour tissues.

1.3 Overview of the study

Chapter 2 provides an overview of the current state of the field of synchrotron MRT, surveying the most relevant literature on normal tissue and tumour tissue response to MRT.

Chapter 3 provides basic information on synchrotron design and the physical properties of synchrotron beams. The chapter also describes the physical properties of radiochromic films, which are used extensively in the research. Some remarks on Monte Carlo computer simulation are also made and an overview of radiation dosimetry, with an emphasis on topis of relevance to MRT is presented.

Chapter 4 reproduces in full a scientific paper, published in the journal *Physics in Medicine & Biology*. It describes a method to adapt film dosimetry and microdensitometry for synchrotron MRT in order to plug the dosimetry gap which exists in the MRT knowledge base. Using this technique, MRT peak-to-valley dose ratios were recorded at different depths in a water phantom for the first time.

Chapter 5 describes the search for immunohistochemical markers of MRT damage in skin tissue, and the novel application of the γ-H2AX immunohistochemical assay of DNA double strand breaks. This chapter is written in the style of a scientific paper and it is anticipated that portions of this chapter will be submitted for

publication in the near future.

Chapter 6 reproduces in full a scientific paper, submitted to the *Journal of the National Cancer Institute*. It describes the effects of MRT on normal skin and inoculated tumour over time in a mouse model and makes comparisons with a conventional radiotherapy study. Novel, radiobiological findings of cellular processes in these tissues post-MRT are described for the first time and possible mechanisms of effect are also discussed. These findings were facilitated by the γ-H2AX assay (an assay to detect DNA double strand breaks) described in Chapter 5.

Chapter 7 describes some novel experiments that are works in progress. These include investigations of γ-H2AX bio-dosimetry, more accurate Monte Carlo computer simulations, bi-directional MRT and treatment planning.

Chapter 8 serves as a 'Discussion & Conclusions 'chapter and brings together the dosimetry and radiobiology data in a cohesive manner.

A brief explanation of immunohistochemistry cell staining, to aid the reader not familiar with these techniques, is given as an appendix.

1.4 Field Trips to SPring-8, Japan

The data presented in this thesis are from a total of 6 overseas field work trips to the SPring-8 synchrotron facility in Japan. In all but one trip, experiments on live mice were performed. Figure 1 below tabulates these trips and the principal biological data collected for each trip.

Date	Beamtime allocation	Principal biological data obtained
Dec 2005	4 x 24 hrs, 12 shifts	Pilot data for histological studies on mouse skin
July 2006	4 x 24 hrs, 12 shifts	Immunohistochemical studies of cellular mechanisms in mouse skin (Chapter 5)
Dec 2006	3 x 24 hrs, 9 shifts	MRT survival studies in tumour-inoculated mice (Chapter 6)
July 2007	4 x 24 hrs, 12 shifts	Immunohistochemical studies of cellular mechanisms in mouse skin and inoculated tumour (Chapter 6)
Dec 2007	5 x 24 hrs, 15 shifts	Molecular biology tests on mouse skin & tumour
July 2008	4 x 24 hrs, 12 shifts	Dosimetry data; HVLs, films, gels (Chapter 4)

Figure 1.1: Field work trips to the SPring-8 synchrotron, Japan

Dosimetric data for collimated microbeams and broad beams in various materials (ion chamber, radiochromic films and gels) were also collected during each of these trips. The film dosimetry data presented in Chapter 4 were obtained during the July 2007, December 2007 and July 2008 trips.

CHAPTER 2

Background to MRT

2.1 Introduction to Radiation Therapy for the Treatment of Cancer

Radiotherapy with ionising radiation has been used for over 100 years to treat a wide variety of solid tumours (Bernier et al., 2004). Conceivably, every tumour could be successfully treated with a sufficiently high dose of radiation. However, the acute and late effects of radiation on surrounding, normal tissue act as dose-limiting factors. Radiotherapy is a balance therefore, between maximising tumour control and minimising normal tissue complications. There are several different techniques to optimise the distribution of dose in tissue, but the most commonly used are treatments involving electron linear accelerators producing electron and photon beams with energies between 4 MeV and 25 MeV (Greene and Williams, 1997). Modern radiotherapy has evolved to include sophisticated computerised treatment planning systems and numerous imaging modalities such as CT, MRI, ultrasound and PET to better visualise and localise malignant tissue.

The definition of a radiation field has also evolved, from basic collimation, to computerised, multi-leaf collimators. These multi-leaf collimators use narrow (3 mm–10 mm) leaves of lead or tungsten that permit exquisite conformal radiation therapy in three dimensions. Over the last 10–15 years, intensity modulated radi-

ation therapy has become more routine for the treatment of tumours located near sensitive structures such as the central nervous system. In this technique, the multi-leaf collimators 'slide 'across the radiation field, modulating the intensity and producing non-uniform fields. This has allowed oncologists to deliver curative doses of radiation to tumours where previously they may only have attempted to prescribe palliative doses (Clifford Chao et al., 2002).

2.1.1 How does radiotherapy work? The biological effects of radiation

This is not an easy question to answer. Nor is it possible to describe all aspects of radiation biology in a subsection of this thesis. For decades after Roentgen's discovery of X-rays, radiotherapy was largely an empirical discipline. Little was known about mechanistic effects. However, over the last 50 years, the field of radiobiology has matured and has developed ideas and frameworks to link energy deposition and cell survival.

For many years (until the mid-1990's), the prevailing wisdom or dogma of radiotherapy was that the DNA in a cell's nucleus was the sole target for radiation-induced cell death. This explained how cancer cells were killed and the early and late effects associated with normal tissue toxicity. Ionising radiation is effective at causing DNA double strand breaks and these have long been thought to be the most important effect for cell killing. Over the last two decades however, there has been a shift, away from a totally DNA-centric approach, to include other cellular effects and mechanisms which may contribute to the tissue response to ionising radiation at a cellular level, and to consider the consequences for the organ or organism as a whole (Prise et al., 2005). Further pressure on the DNA-centric model, or target cell hypothesis, has come from single cell microbeam studies. It was observed in these studies that cells in culture flasks in the vicinity of the irradiated cell could be killed without having been irradiated themselves (Bentzen, 2006). This is an example of the so-called 'bystander effect', which is discussed further in the next section.

In any tissue or organism, cells are not isolated from one another but are part of a 'community'or microenvironment of other cells that interact with each other and the various cellular products. The effects therefore of ionising radiation should not be considered from the perspective of isolated cells, but rather from the entire tissue (Barcellos-Hoff et al., 2005).

Soon after irradiation, DNA damage induces a stress response though the activation of proteins to facilitate DNA repair and prevent proliferation of damaged cells (Barcellos-Hoff et al., 2005; Bentzen, 2006). In addition, there are multicellular events that are initiated in response to damage from ionising radiation. Such events include the release of cytokines, chemokines and growth factors, proteins that signal between cells through secretion, and interaction with receptors on the cell's surface (Bentzen, 2006). These signals control vital processes such as proliferation, apoptosis, migration and differentiation. Certain cell types; fibroblasts, endothelial cells, pericytes, and the cells of the immune and inflammatory systems (collectively known as stromal cells), are involved in remodelling the extra-cellular matrix, the protein scaffold on which cells reside (Barcellos-Hoff et al., 2005).

In a review of the effects of radiation and the cellular micro-environment, Barcellos-Hoff et al. (2005) defined the micro-environment of a given target (i.e. tumour) cell, as the range of stromal cells (and their products), the extra-cellular matrix and signals (cytokines, chemokines and growth factors) that can act on the target cell. In short, ionising radiation alters the tissue micro-environment and such alterations can affect how tissues respond to radiation therapy and the effects of ionising radiation on the DNA in a target cell's nucleus should not be considered in isolation.

2.1.2 The bystander effect

In radiotherapy, bystander effects are loosely defined as the induction of biological effects in cells that are not directly traversed by ionising radiation, but are in close proximity to cells that are (Hall and Mitchell, 2003). This is illustrated schematically

in figure 2.1; a single cell receives ionising radiation and secretes molecular signals (proteins), which are capable of modifying the function of distant cells. Bystander effects have mostly been observed in *in vitro* assays. They are sometimes referred to as non-target effects or cell-cell communication. These effects were first reported in the 1950's, but interest in bystander effects have become more intense over the last 15 years. There have been a number of reviews of the bystander effect and its application to radiation therapy (Mothersill and Seymour, 2001; Mothersill et al., 2004; Mothersill and Seymour, 2004).

Data concerning bystander effects typically fall into two separate categories; First there are experiments involving the transfer of culture medium from irradiated cells to unirradiated cells, which results in a biological effect in the unirradiated cells. Second, the use of focussed, charged particle microbeams, which allow specific cells to be irradiated, and biological effects studied through the response from neighbouring cells (Hall and Mitchell, 2003).

Studies using radiation microbeams have made an important contribution to our understanding of cell death mechanisms. These sophisticated devices allow precise targeting of ionising radiation to individual cells and to precise regions within cells such as the mitochondria and cytoplasm. Most of the microbeams described in the literature are comprised of charged particles, collimated and focussed to dimensions of 1–2 μm. Soft X-rays are also employed for microbeam experiments and use zone plate diffraction lenses for focussing. These systems usually have computer-controlled stages coupled to advanced imaging systems which perform automatic cell detection and alignment (Folkard et al., 2001).

In a review of new insights on cell death from radiation exposure, Prise et al. (2005) list numerous bystander effect studies of cell killing which have been published since 1992. In all studies, unirradiated cells have ellicited a change in function when their neighbours were irradiated. The authors of this review described microbeam studies in which the irradiation of a single cell within a population was enough to induce bystander cell killing in fibroblast cells. In another microbeam

study cited by Prise et al. (2005), bystander responses were induced in radio-resistant glioma cells when only the cell cytoplasm was irradiated, showing that direct damage to cellular DNA by ionising radiation is not needed to trigger the effect.

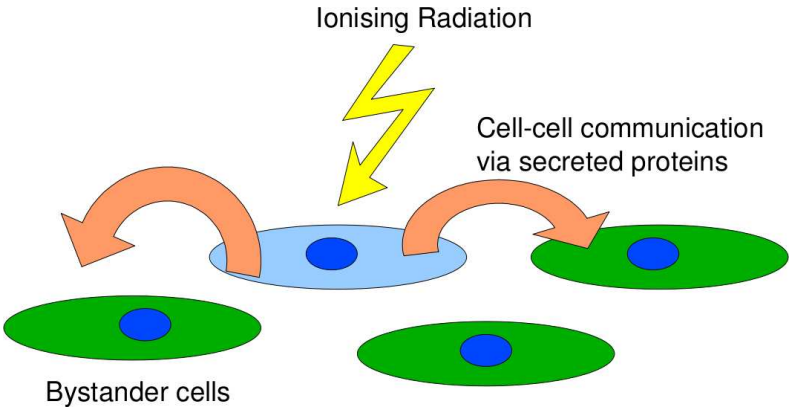

Figure 2.1: The bystander effect in radiation therapy, adapted from Prise et al. (2005). Molecular signalling can occur between irradiated and unirradiated cells which can result in cell death for the unirradiated cell as well as the irradiated cell.

In a review of the biological response to radiation therapy, Turesson et al. (2003) ponder the relevance of the bystander effect to human radiotherapy. Important questions arise including; what are the mechanisms involved? How dependent is the effect on cell-type and radiation quality? What uncertainties does the bystander effect introduce to the physical dosimetry (and *vice versa*), and should we consider a biological dose, not just the physical dose? To answer such questions, more *in vivo* human and animal studies are required which may better inform us of the role of the bystander effect in radiotherapy.

So-called abscopal effects, or 'distant' bystander effects, are also worth mentioning at this point. Abscopal effects are defined as radiation responses in tissue(s) distant from the site of local radiation (Kaminski et al., 2005). An example of an abscopal effect is radiation exposure in the abdomen of mice illiciting an inflammatory reaction in their lungs (Van der Meeren et al., 2005). The abscopal effect is controversial, with some reports supporting it and other reports refuting it (Kaminski et al., 2005). There is very little information on molecular mechanisms of abscopal ef-

fects, although they appear to be mediated by the cells of the immune system and the release of cytokines. Snyder (2004) and Kaminski et al. (2005) are useful reviews of radiation abscopal effects. Importantly, abscopal and bystander effects provide evidence that the target for the biological effects of ionising radiation includes the surrounding cells/tissue, not just directly irradiated cells.

2.1.3 The volume effect

In radiation therapy, the volume effect states that; as the volume of the irradiated, normal tissue decreases, the normal tissue's tolerance to radiation increases. The volume effect is complex and is not well defined. Tolerance is not clearly defined in many publications, sometimes referring to a patient's tolerance (or a clinician's impression) and sometimes to tissue tolerance (van der Kogel, 1993; Hopewell and Trott, 2000).

In a review of volume effects in radiobiology as applied to radiotherapy, Hopewell and Trott (2000) examined the evidence for volume effects by considering separately the anatomical or structural responses, and physiological or functional responses to small field irradiations. These authors observed that there was little or no volume effect for anatomical or structural damage to tissues, with cell migration of non-irradiated cells from the margins into the irradiated volume the more likely mechanism for the same effect (isoeffect) occuring at higher doses, in smaller volumes. The authors also state "For anatomical/structural damage, field size is an absolute concept, and is not applicable to a scaling factor that can be related to animal size". However, the authors also stated that there "were very pronounced volume effects reported in the literature for functional damage". For example, the spinal cord of rat serves as a useful experimental model of functional radiation damage (e.g. paralysis) and the volume effect (Hopewell et al., 1987; van der Kogel, 1993; Stewart and Van der Kogel, 2002). These spinal cord studies show little or no volume effect when cord lengths longer than 10 mm were irradiated, but a steep increase in tolerance doses for irradiated lengths of less than 10 mm. Studies of pig lungs irradi-

ated at different fractional volumes show lungs appear normal from a histological and radiological perspective and induction of structural lung damage to be independent of the volume irradiated. However, lung function showed dramatic improvements with the reduction of the treatment field (Herrmann et al., 1997). It seems the physiological function of the irradiated volume (or the physiological volume) is as important as the physically irradiated volume, when trying to understand the biologcal effects of ionising radiation. At the very least, it seems prudent to exercise caution when interpreting data pertaining to volume effects in biological tissue.

The volume effect and the bystander/abscopal effect may in fact be related phenomena, or at least, influence one another. When the dimensions of the incident radiation are comparable to, or smaller than, the dimensions of a single cell (10–20 μm approximately), the more likely it becomes for cell-cell communication between directly irradiated and unirradiated cells. MRT may amplify bystander effects by a high ratio of irradiated to un-irradiated cells. Cell migration of unirradiated (healthy) cells to sites of irradiated (damaged) cells may be in part, mediated through bystander effects. The same applies to cell death of bystander cells. One could speculate that increasing the dimension of the incident radiation beam may give rise to more distant (abscopal) bystander effects, such as inflammatory reactions in tissue distant from the local radiation site. Naturally, good quality experimental data are required to support or refute the ideas.

2.2 Introduction to Microbeam Radiation Therapy

2.2.1 A historical perspective

In the late 1950's, the first manned space flights were becoming a reality and scientists wanted to estimate the likely biological effect of cosmic radiation on astronauts. A megavoltage (22 MeV) deuteron microbeam, 25 μm in diameter was used to simulate the dose that high-energy, heavy-ion, cosmic particles might deposit in tissue. The team of Zeman, Curtis and Baker, working at the Brookhaven National Labo-

ratory in the USA, published a series of reports over a period of 8 years. In 1959, Zeman reported in the journal *Science*, "There is a striking relationship between the size of the impact area of the deuteron beam and the threshold dose for a radiogenic lesion in the mouse brain ". Zeman further reported "the threshold dose to produce a lesion in the mouse brain increased from 30,000 rad (300 Gy) for a 1 mm diameter beam to 1.1 x 10^6 rad (11,000 Gy) for a beam 25 μm in diameter ", (Zeman et al., 1959). A photograph from Zeman et al. (1961) is shown in figure 2.2.

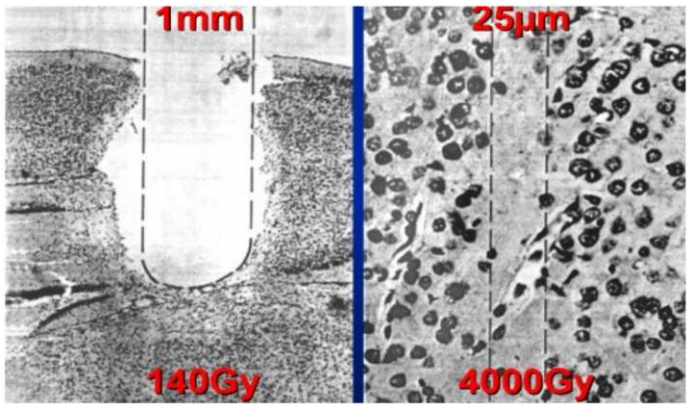

Figure 2.2: Photograph from the 1961 paper of Zeman et al. (1961) showing the relationship between the diameter of the beam and the dose to cause a lesion in mouse brain tissue. Copyright (1961) Radiation Research. Image used with permission.

In 1967, Howard Curtis reported that a dose of 400,000 rad (4000 Gy) delivered to the brain of rats using a 25 μm diameter beam of 22 MeV deuterons caused localised neuronal cell loss in the direct path of the microbeam, but did not cause a radiogenic lesion. Curtis hypothesised that the probable reason for the high tolerance to the microbeam was due to regeneration of radiation-damaged blood vessels by surviving endothelial cells located outside the microbeam (Curtis, 1967a,b).

2.2.2 Synchrotron microbeam radiation therapy - the first studies

Slatkin et al. (1992) published a paper describing how, in theory, synchrotron X-rays could be exploited to produce planar or cylindrical microbeams with energies in the

range of 50 keV to 150 keV. They published Monte Carlo simulations of dose deposition from different geometries and postulated on the practicalities of performing such a technique. A synchrotron produces very intense X-rays with a photon flux rate (number of photons per unit area, per unit time) several orders of magnitude greater than x-rays produced by conventional x-ray sources such as diagnostic x-ray units or linear accelerators for megavoltage radiotherapy. Importantly, the very high dose rates (10,000 Gy/s) achievable on a synchrotron mean that very high doses (hundreds of Gy) can be delivered in a very short period of time (msec), thus minimising blurring of the dose due to motion of the tissue (from cardiac pulses, for example). The physical properties of synchrotron X-rays and their suitability for MRT are discussed in more detail in Chapter 3.

Synchrotron microbeam radiation therapy permits an array of planar microbeams to be delivered, where the high peak dose (relative to the low dose in the 'valley 'region between the microbeams), can be maintained at depth in tissue with microscopically sharp absorbed dose gradients at the field edges (Laissue et al., 1999). Monte Carlo simulations have shown this depth can be as much as 16 cm in water (Stepanek et al., 2000). The energy of the synchrotron X-ray beam (approximately 100 keV) allows the peak and valley dose distribution to be maintained at depth. At 100 keV, the range of secondary photoelectrons in water is only some tens of microns, compared to millimetres in the megavoltage range. Increasing the X-ray beam energy would increase the valley dose (because the range of secondary electrons increase), thus reducing the peak-to-valley dose ratio in tissue (Siegbahn, 2007).

A piece of radiochromic film, which has been exposed to planar X-ray microbeams and a broad beam is shown in figure 2.3, illustrating the spatially fractionated nature of MRT. Whilst the width of a single microbeam may be of the order of 25 μm, the planar nature of the beam means a microbeam can extend over tens of mm.

Slatkin et al. (1995) published the first paper on synchrotron MRT using data from animal studies. The Brookhaven group had fashioned a single-slit, tantalum collimator to segment the x-ray broadbeam into a planar microbeam able to be varied

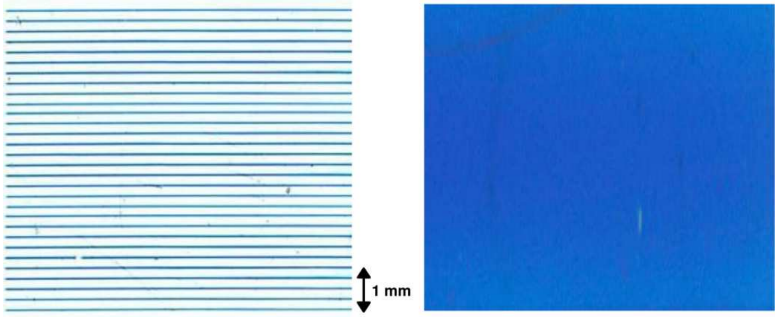

Figure 2.3: The spatially fractionated nature of MRT. Radiochromic film exposed to planar X-ray microbeams (left) and uniform, broad beam (right). The blue areas are maximally exposed and the clear areas are minimally exposed. The centre-to-centre spacing of the microbeams is 200 μm.

in width from 20 μm to 42 μm. The target was the cerebellum in the brain of rats. After a single exposure, the animal was moved on a precision goniometer a distance of 200 μm or 75 μm and further exposed to the microbeam. This process continued for a series of steps. The entrance dose was varied from 312 Gy to 10,000 Gy. Figure 2.4, from Prof. Jean Laissue, illustrates how the radiation was incident on the rat brain for this experiment.

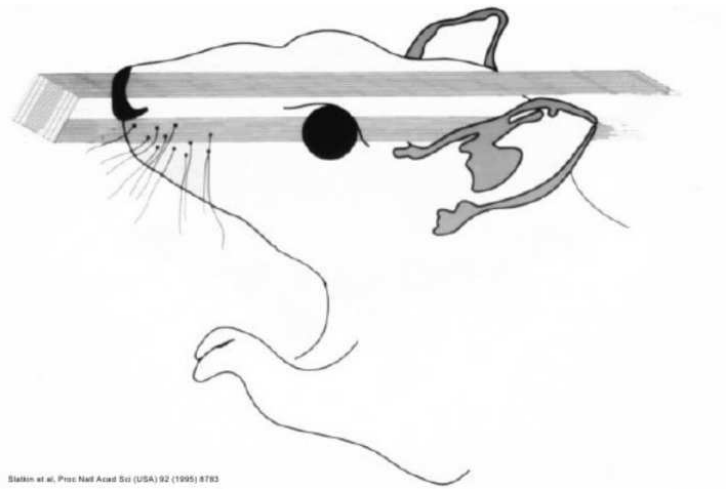

Figure 2.4: Schematic of irradiation setup in the first synchrotron MRT paper using animals by Slatkin et al. (1995). An array of microplanar radiation was incident on the rat's skull. From a sketch by Prof. Jean Laissue, University of Bern, Switzerland. Image used with permission

Slatkin et al. (1995) reported histological findings for rat brain tissue post-MRT. Under low magnification light microscopy, the authors noted a "loss of neuronal and astrocytic nuclei in the paths of the microbeams for doses in excess of 1250 Gy". They observed the tracks of the microbeam in the tissue sections as 'stripes' in regions of dense nuclei, but not in regions of sparse nuclei. Interestingly, brain tissue irradiated with 312 Gy or 625 Gy appeared histologically normal for up to one month post-irradiation. The authors attributed this exceptional resistance of subacute brain damage by ionising x-radiation to "hyperplasia and immigration of minimally irradiated endothelial cells (cells used to create blood vessels) and oligodendrocytes (used for myelination of nerve cells) between the slices of irradiated tissue" (i.e. minimally irradiated tissue). The authors concluded that MRT could be effective for certain brain tumours, for example, shallow, brain stem gliomas in small children.

Since Slatkin et al. (1995), there have been almost twenty articles published in international journals in which animals (rodents mostly) have been irradiated with synchrotron MRT. An intriguing aspect to synchrotron MRT is that all the published literature, researchers agree on findings that are quite novel and somewhat counter intuitive for radiobiology. These findings, and a review of a selection of MRT papers follows in the next section.

2.3 Synchrotron MRT: Normal Tissue Studies

Figure 2.5 tabulates a summary of the findings for a selection of normal tissue studies in MRT between 2000 and 2007 and shows at a glance the irradiated subjects, the geometry of the beams, the peak and valley doses and the principal observations. The paper by Laissue et al. (2001) was an important piece of work because, for the first time, it included data on behavioural and neurological tests performed on the animals post-irradiation. Between 12 and 15 months post-irradiation, the pig presentation and behaviour were normal as observed and tested by experienced farmers and veterinary scientists blinded to which piglets were irradiated or sham-irradiated. Their results

Author, Date	Subject	Beam geometry	Peak & *Valley* Dose(s)/Gy	Principal Findings
Schweizer *et al.,* 2000	*Drosopohila Melongaster* (fruitfly)	25 μm/100 μm,	75 – 3000 *Valley doses not stated*	High dose MRT only slightly disturbed morphogenetic process. Sharply delineated lesions seen in compund eye, wing and abdomen corresponding to irradiated microplanes
Laissue *et al.,* 2001	Weaning piglet cerebellum	25 μm/210 μm, 15 mm x 15 mm field size	150, 300, 425, 600, *7 - 28*	Irradiated piglets were developmentally, behaviouraly, neuroligically normal 15 months post-MRT. Tracks observed in cerebellum (fig. 2.5).
Zhong *et al.,* 2003	Rat skin	90 μm/300 μm, 1.5 mm x 35 mm field size	835 – 1335 *21 - 33*	Skin had extremely high tolerance to MRT, attributed to surving clonogenic cells between beams.
Blattmann *et al*., 2005	Chorio-allontic membrane (Chick egg)	27 μm/200 μm,	300 – 1200 *Valley doses not stated*	Massive damage observed in microvascular regions traversed by microbeams but not between beams, vascular 'bridges' seen post MRT across areas directly in path of microbeam (fig. 2.6).
Dilmanian *et al*., 2006	Expt. 1 – Rat spinal cord	270 – 680 μm wide, 4 mm spacing (fig. 2.7a)	400	In 680 μm group, 1/4 rats culled due to paralysis, remaining rats regained leg strength by 1 month. Weight differences c.f. control group, but rotorod performance returned to control levels by 1 month. Spinal cord tolerant of thick microbeams.
	Expt. 2 – Rat brain	680 μm wide, 1.36 mm spacing, 8 mm x 10.2 mm field size (2.7b)	110 – 170 *~12 – 19*	Radiation tolerated by rat brain up to 170 Gy with some hyperactivity which subsided by 5 h post-MRT. Rats gained weight normally, no signs of limb weakness
	Expt. 3 – Rat brain	2 x 680 μm wide interlaced beams, 1.36 mm spacing, 3.4 x 3.4 x 3.4 mm^3 cube (2.7c)	90 – 150 *~15 – 25 (non-interlaced region)*	No significant effects with 90 and 120 Gy but significant oedema and atrophy in 150 Gy group
Serduc *et al.,* 2006	Mouse brain	25 μm/210 μm, 4 mm x 4 mm field size	312, 1000 *6, 19*	No changes in cerebral blood volume or vascular density by 3 months post-MRT. Temporary blood-brain barrier disruption in 1000 Gy group.
Dilmanian *et al*., 2007	Expt. 1 – Bovine endothelial cells in culture	27 μm wide, 6 mm long, 2 mm separation	24 *Valley dose not stated*	Path of microbeam visible as straight row of dying cells, characteristic of apoptosis.
	Expt. 2 – Rat spinal cord	270 μm wide, 2 mm high, 2 mm separation	750 *Valley dose not stated*	Cell loss of oligodenrocytes, astrocytes and myeline 2 weeks post-MRT, repopulation and re-myelination by 3 months. Postulate existence of 'beneficial' bystander effect.

Figure 2.5: Summary of MRT normal tissue studies: 2000 - 2007

showed the normal developing porcine cerebellum could tolerate very high radiation doses, when delivered as planar microbeams. There was minimal damage to normal tissue, despite application of much higher doses than those used in conventional radiotherapy. In addition, there appeared to be rapid repair of acute microscopic lesions by adjacent, minimally irradiated cells. Histological staining showed, quite remarkably, that 15 months post-irradiation, the path of the microbeams through the cerebellum remained 'imprinted'as visible tracks or stripes (Figure 2.6). Their interpretation of the results, they felt, gave credence to the idea of MRT as a treatment option for agressive and fatal paediatric brain tumours.

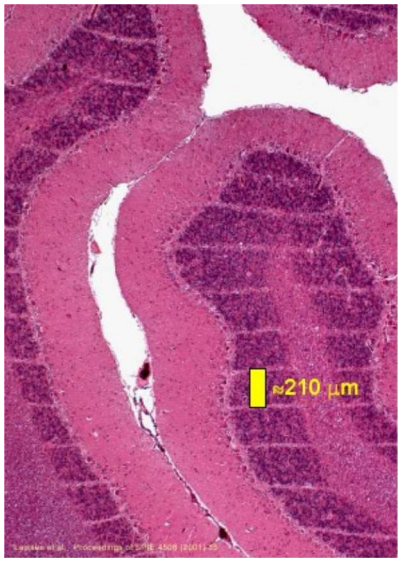

Figure 2.6: Histological stain of pig cerebellum 15 months post-irradiation reprinted from the paper by Laissue et al. (2001). The path of the beams through the tissue is clearly visible as regions of less dense cells. Copyright (2001) SPIE. Image used with permission.

Zhong et al. (2003) reported histological results from irradiated rat skin and postulated that the high tolerance of rat skin to MRT and the rapid regeneration of the damaged segments of skin were due to surviving clonogenic cells (stem cells) located between the microbeams (that is, in low dose regions). The authors also noted that the characteristic MRT tracks, seen in the cerebellum (Figure 2.6) by Laissue et al. (2001) and Slatkin et al. (1995), were not visible in skin using conventional histol-

ogy.

Blattmann et al. (2005) described the rapid formation of new capillaries in the microbeam-damaged vasculature of living chick embryo chorio-allontic membrane (CAM) (Figure 2.7). Blattmann et al.'s results are intriguing. However, care should be taken in interpreting these results. The developing vessels in the CAM may be much more sensitive to radiation than adult vessels because they are actively growing. However, because of the active growth, they may well also repair much more easily. ie: the CAM is a vasculogenesis/angiogenesis model, and is not necessarily representative of typical adult organs, where vessels are more stable (Peter A.W. Rogers, personal communication). Hence it is possible that the effects seen in the CAM would not be seen in other adult organs, such as brain or skin, where different tissue-specific responses might exist. More experimental data on a range of normal tissues and tumour types are required.

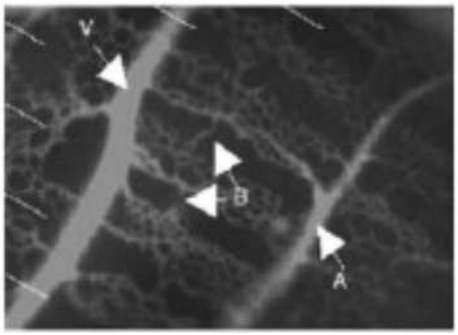

Figure 2.7: Capillaries forming vascular bridges (shown by white arrows labelled B) in MRT-irradiated chorio-allontic membrane, reprinted from Blattmann et al. (2005). Copyright (2005), with permission from Elsevier.

Dilmanian et al. (2006) described three experiments in which the CNS of normal rats were irradiated with microbeams as wide as 680 μm. Their experimental setup is shown in Figure 2.8. Note the microplanar nature of the incident beams; the dimensions may be tens or hundreds of μm in one direction but tens of mm in the other direction.

These experiments by Dilmanian et al. (2006) represent a departure from the

Figure 2.8: Irradiation setup for three experiments reproduced from Dilmanian et al. (2006); (a) Tolerance of the spinal cord of rats to thick microbeams, (b) Tolerance of the rat brain to thick microbeam arrays, (c) Dose localisation using interlaced thick microbeams. Copyright (2006), National Academy of Sciences, USA. Image used with permission.

more traditional MRT experiments, which used beams no wider than 90 μm. The authors reasoned that if animals could tolerate these wider microbeams (or mini-beams), it might then be feasible to deliver similar beams using a non-synchrotron X-ray source. In one experiment, the authors irradiated rats with an orthogonal pair of interlaced, thick microbeams (Figure 2.8c). The beams resembled broad beams in the interlaced region and perhaps unsurprisingly, the authors reported notable damage to brain tissue in this region (including atrophy, oedema and enlarged ventricles) when in-beam doses of 150 Gy were delivered.

Dilmanian et al. (2006) claimed that this interlaced, thick microbeam technique might have clinical implications and applications. However, the interlaced method does not provide a conformally-shaped distribution (which the authors admit), rather, an almost seamless cube of high dose in three dimensions is generated. This might ablate any tumour but may cause unacceptably high normal tissue toxicity. The interlaced method at such doses may not be appropriate for an irregularly-shaped tumour.

In another experiment (reported in the same paper), Dilmanian et al. (2006) exposed the spinal cord of normal rats to doses of 400 Gy and beam widths of 680 μm (Figure 2.8a). The damage imparted to the cord was only moderate, reminiscent of the spinal cord work described by Hopewell et al. (1987) and van der Kogel (1993) (but at higher doses) and may be a good example of the volume effect and functional response, discussed in section 2.1.4.

The work by Dilmanian et al. (2006) further highlights the need for more exper-

imental work on different beam widths. It is quite likely that different tissue types and tissue architectures will have different responses and this too requires further investigation.

Dilmanian et al. (2007) postulated the existence of a "beneficial" bystander effect in MRT, leading to normal tissue restoration. Signals between hit cells and neighbouring, bystander cells may be either transmitted by cytokines or growth factors, or via direct cell-cell communication. They postulate the microbeam effect, may be a type of tissue recovery process. Dilmanian et al. (2007) also described the migration of the endothelial cells post-irradiation into the spaces once occupied by the directly irradiated cells. They then speculated that repopulation of glial cells could have been due to the migrating cells subsequently undergoing proliferation, differentiation and producing new glial cells and myelin. They hypothesise the bystander effect initiates these events. Unfortunately, there are no concrete data to support or refute this hypothesis yet. Dilmanian et al. (2007) noted that the stimulation of cell proliferation has yet to be studied, but that it could be verified experimentally with bromodeoxyuridine-labelled cells. Such a test would certainly prove useful, especially if it were possible to visualise the irradiated cells and discriminate them from unirradiated, or minimally-irradiated cells.

2.4 Synchrotron MRT: Tumour Studies

Laissue et al. (1998) at the Brookhaven National Laboratory (BNL) performed the first synchrotron microbeam radiation therapy on tumours (9L gliosarcoma in rats). Rats were irradiated with either a single array (uni-directional) of parallel microbeams or two orthogonally crossed arrays (Bi-directional) of microbeam radiation. MRT to the gliosarcoma slowed the growth of these aggressive and usually fatal tumours, and in more than half the rats, eliminated them. Analysis of tissue structure showed severe damage only within well demarcated, orthogonally cross-irradiated regions, never in uni-directionally irradiated regions. Only minor damage was ob-

served in regions of rat brain irradiated unidirectionally. This paper was a landmark paper, because it was the first to show actual tumour ablation by MRT and not just normal tissue damage/repair. Some histology data was included in the paper, but it would have benefited from immunohistochemistry techniques comparing normal and tumour tissue.

Since the paper of Laissue et al. (1998), there have been at least 5 more papers describing the effects of MRT on tumours. The papers can be divided into MRT to 9L gliosarcoma in rats, or, MRT to other tumours in mice. Figure 2.9 tabulates a selection of the 9L gliosarcoma studies in rats, and as in figure 2.8 for normal tissue studies, summarises parameters such as beam geometry, dose and principal findings.

Author, Date	**Subject**	**Beam geometry**	**Peak Dose(s)/ Gy**	**MeST/days**† (no. of rats)	**Principal Findings**
Laissue *et al.*, 1998	9L glioma in Fisher rats	25 µm/100 µm, 12 mm high 101 parallel beams	0, Control 312 bi-directional 625 unidirectional 625 bi-directional	20 (9) 116 (11) 44 (11) 159 (14)	Tumours completely ablated in over half of the rats
Dilmanian *et al.*, 2002	9L glioma in Fisher rats	27 µm/50 µm 27 µm/75 µm 27 µm/100 µm 9 mm x 10.4 mm field size	150, 250, 300 250, 300, 500 500 0, Control	98, 136, 55 (5) 171, 62, 31 (6) 170 (3) 19 (17)	Smaller beam spacings causes increased toxicity to brain owing to increased valley doses.
Smilowitz *et al.*, 2006	9L glioma in Fisher rats	27 µm/211 µm 11 mm x 10.1 mm field size	0, Control 625 unidirectional 625 uni + IMPR 625 uni + GMIMPR	9 (14) 39 (25) 39 (14) 46 (14)	GMIMPR + MRT improves survival *c.f.* MRT alone. Immunologically-based mechanisms responsible for synergy?
Regnard *et al.*, 2008	9L glioma in Fisher rats	25 µm/100 µm 25 µm/200 µm	625 unidirectional 625 unidirectional 0, Control	67 40 20	200 µm spacing protocol provides better sparing of healthy tissue, but reduced MeST

† Median Survival Time in days, post-inoculation
IMPR – Immunoprophylaxis
GMIMPR – Gene-mediated immunoprophylaxis

Figure 2.9: Summary of MRT glioma tumour studies, 1998-2008

Dilmanian et al. (2002) irradiated rats bearing 9L gliosarcoma tumours to assess the dependence of tumour control and normal tissue damage on beam spacing and dose. The authors contrasted this with the work of Joel et al. (1990) who performed single exposure, broad beam irradiations of 9L gliosarcomas at 22.5 Gy and noted

a median survival time of only 34 days with severe depletion of neurons. Statistical analysis suggested that MRT at 75 micron beam spacing and 250 Gy, increased survival for the rats compared to the other groups. The authors also showed that the 27 μm beam width, 50 μm spacing, geometry (27/50 μm) gave reduced animal survival with higher MRT doses (200 and 300Gy in-beam doses) when compared to 27/75 μm with 250Gy. The valley dose as a percentage of the peak dose in the centre of the array was estimated (Monte Carlo simulation) to be 20%, 10% and 6% for the 50 μm, 75 μm and 100 μm groups respectively. These workers concluded that, at 27/50 μm, significant radiotoxicity was occurring in the brain, thus providing the first evidence for a minimum functional spacing and dose combination for MRT. Importantly, in histological studies, no tumour residues were visualised in eight samples where the tumours were ablated with MRT. Also, the brain tissue showed remarkably low levels of damage and for some configurations of beam spacing and dose, it was impossible to demonstrate any differences between the MRT-irradiated normal tissue and the unirradiated control.

The paper by Dilmanian et al. (2002) was an important paper in the field, because it reported a systematic attempt to identify physical parameters (in this case, the microbeam spacing) which would lead to differential biological outcomes. The limited MRT studies published to date have used collimator configurations that typically produced microbeams of 20-30 μm width, with centre to centre beam spacing in the range of 50-300 μm. Two further studies have compared different collimator configurations within the same set of published experiments (Miura et al., 2006; Regnard et al., 2008).

In Dilmanian et al. (2003), the authors compared the therapeutic efficacies of single fraction, unidirectional co-planar microbeams, cross-planar microbeams and broad beams from a synchrotron source. Figure 2.10, redrawn from Dilmanian's 2003 paper, illustrates the differences between co-planar and cross-planar microbeam.

Dilmanian et al. (2003) irradiated mice, inoculated in their hind leg with the

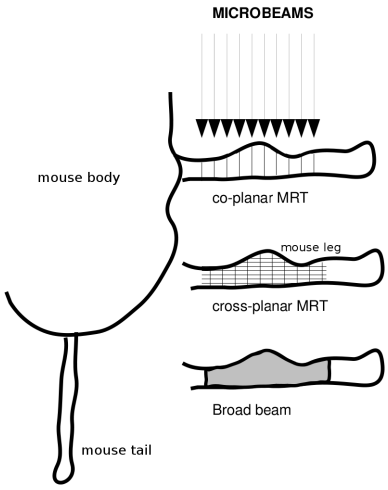

Figure 2.10: Schematic diagram, adapted from Dilmanian et al. (2003) illustrating the differences between co-planar and cross-planar MRT.

EMT-6 tumour (a type of mammary tumour). The microbeam width was 90 μm wide with a peak-to-peak spacing of 300 μm. The valley doses in the centre of the array were approximately 2% and 4% of the peak dose for the co-planar and cross-planar irradiations respectively. Tumour ablation rates were 4/8, 4/8 and 6/7 for incident cross-planar microbeam doses of 410, 520 and 625 Gy respectively. Tumour ablation rates were 1/8, 3/8, 6/8 for incident broad beam doses of 23, 30, 38 and 45 Gy respectively. However, the incidence of acute and delayed normal tissue toxicity was significantly lower for cross-planar microbeams compared to that from broad beams. In addition, severe leg dysfunction was reduced for the microbeam group compared to the broadbeam group post-irradiation.

The findings of Dilmanian et al. (2003) showed that spatially fractionated microbeams can ablate tumours at high rates with little normal tissue toxicity. Additionally, the authors noted that, cross-planar MRT gave a more favourable balance between tumour control and tissue toxicity compared to co-planar and broad beam. At the highest dose of cross-planar MRT (650 Gy), 86% of tumours were controlled (6/7), yet none of these animals developed leg complications.

Dilmanian et al. (2003) presented the first MRT tumour studies in an organ other

than the brain. The central nervous system (including the brain) is a unique and highly specialised organ, composed of neurons, glial cells, oligodendrocytes and astrocytes . A subcutaneous mammary tumour in the leg of a mouse is very different tissue to the CNS and may have a different response to ionising radiation than the brain. Dilmanian's 2003 study on the EMT-6 tumour in a mouse leg, could also have benefited from histology or immunohistochemistry data.

Miura et al. (2006) reported radiosurgical palliation of a squamous cell carcinoma inoculated into the hind legs of mice. The doses used in Miura's research were 442 Gy, 625 Gy or 884 Gy from 35 μm wide beams, or 442 Gy from 70 μm wide beams. Increased normal tissue damage occurred in the 70/200 compared to the 35/200 μm treatment groups. The authors also performed conventional radiotherapy studies using a kilovoltage generator and delivered 25 Gy or 35 Gy broadbeams to SCCVII-inoculated mice (squamous cell carcinoma, a very agressive tumour). The median survival time for the 35 Gy group was 20 days. By comparison, the median survival times for the 884 Gy/35 μm and 442 Gy/70 μm groups were 41 days and 38 days respectively.

The authors concluded that MRT gave better palliation of the tumour than broad beams. The authors did not attempt to explain the radiobiological mechanisms of MRT. Again, there was no histology or immunohistochemistry performed on the irradiated tissue sections.

Numerous hypotheses have been suggested to explain the unusual response of tissue to synchrotron MRT. However, no firm and conclusive evidence has yet appeared in the literature. Laissue et al. (2001) described the peak-valley-dose ratio as being a radiobiologically crucial parameter, dependent on the width and spacing of the microbeams, the energy spectrum and the depth in tissue of the point of interest. Dilmanian et al. (2002) postulated the tumouricidal effect of MRT was due to the failure of the tumour microvasculature to recover from the MRT, (in contrast to the microvasculature of normal tissue, which presumably does recover) leading to loss of tumour blood perfusion and ultimately, to death of the tumour. Spatial fractiona-

tion of synchrotron-generated X-rays into an array of microbeams may allow normal tissue to repair itself. Despite peak microbeam doses of hundreds of Gy, the significantly lower doses between adjacent microbeams may cause little if any damage and may in fact promote repair through a biological process such as the bystander effect (Dilmanian et al., 2007) or a stem cell recovery process (Zhong et al., 2003). More detailed histological/immunohistochemical studies are clearly required in an attempt to tease out the cellular responses of normal and malignant tissue to MRT.

In a recent paper, Serduc et al. (2008) irradiated nude mice which had been inoculated with rat 9L gliosarcomas. The authors wanted to characterise the effect of MRT on the microvascular parameters of the apparent diffusion coefficient, tumour blood volume and vessel size, using MRI scanning techniques. Some novel immunohistochemistry data were also presented. The MRT parameters were; 25 μm beam width, 211 μm spacing and in-beam dose 500 Gy. Serduc et al. (2008) showed that "MRT increased the mean survival time by a factor of 1.34". However collagen IV immunohistochemistry (a blood vessel marker) and magnetic resonance imaging (MRI) data showed that MRT did not reduce the tumour blood volume as one would have expected if the hypothesis outlined in Dilmanian et al. (2002) were true, thereby indicating that "the action mechanism of MRT may involve more than the previously hypothesized vascular effect (Laissue et al., 1998; Dilmanian et al., 2002)".

Serduc et al. (2008) concluded that the MRI and histological results indicated the increase in the survival time may have been due to cytoreduction (cell loss) rather than to an acute effect of ionising radiation on the tumour blood vessels. Tumor vessels appeared perfused up to 28 days post-irradiation, and the measured microvascular parameters did not seem to be predictive of treatment outcome. The authors stated that (in their particular experiment) the action mechanism of MRT on 9L gliosarcoma tumor did not involve a significant microvascular component and that the cellular processes implied should be further investigated.

In this thesis, such an investigation is reported. The data shown in Chapters 5 and 6 of the thesis exploit immunohistochemical techniques to explore the biological

response of normal and malignant tissue sections post-MRT. The next chapter (Chapter 3) provides background information on synchrotrons and why they are essential for MRT. It also describes some fundamental radiation dosimetry for MRT, and the physical properties of radiochromic film.

CHAPTER 3

Physics and Dosimetry for MRT

3.1 On Synchrotrons

What is it about synchrotrons that make them so useful for MRT? Could MRT be performed usefully on a hospital kilovoltage or megavoltage X-ray generator? The purpose of this section is to provide some background on the properties of synchrotron X-radiation and to explain what makes synchrotrons so suitable, indeed critical, to implement MRT.

Conventional X-ray sources such as radiology and radiotherapy units produce radiation by colliding charged particles (electrons) with a high atomic number target such as tungsten. The electrons decelerate and part of their kinetic energy is emitted as X-radiation. Radiation produced in this manner is referred to as *bremsstrahlung*, from the German word for braking. X-rays can also be produced by causing transitions between different atomic orbitals and is termed *characteristic* radiation.

Synchrotron radiation (SR for short) is produced in a different but related manner. SR refers to electromagnetic radiation emitted by relativistic, charged particles following a curved trajectory in free space under the influence of a magnetic field (Podgorsak, 2005). SR is produced on an enormous scale by astrophysical objects

such as pulsars in supernova remnants. Terrestrial SR was first observed in 1947 in the electron synchrotron particle accelerator at the General Electric research laboratory in the USA. Since the effect occurs in the presence of strong magnetic fields which maintain the charged particles in a circular trajectory, it is sometimes referred to as *magnetic bremsstrahlung*.

Developments in SR production continue apace today. The most modern machines, called third-generation machines, are designed to deliver high intensity, compact, highly focussed beams with a very small source size. Synchrotrons such as the ESRF in France, the APS in the USA and SPring-8 in Japan are the world's biggest third generation synchrotron sources.

The important components in a synchrotron are shown schematically in figure 3.1, (courtesy of the Australian Synchrotron). Electrons are emitted by an electron gun, are accelerated down the linear accelerator to an energy of the order of 100 MeV where they are transmitted to a booster synchrotron which accelerates the electrons to an energy of 3 GeV. From the synchrotron, the electrons are then moved to the large storage ring which they orbit *in vacuo* for many hours.

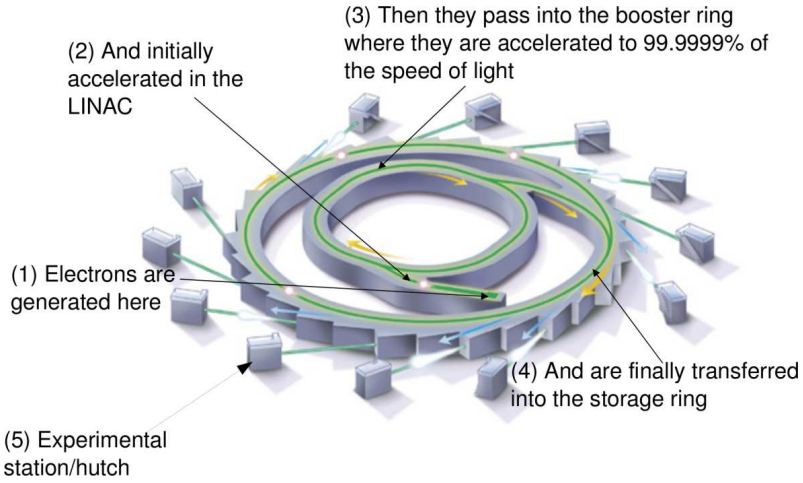

Figure 3.1: The important components in a synchrotron, courtesy of the Australian Synchrotron. Image used with permission.

Sextupole and quadrupole magnets correct and focus the electron beam to a narrow pencil beam, and dipole bending magnets, positioned at discrete locations produce synchrotron radiation tangential to the path of the orbiting electrons. The electrons lose energy during each turn in the storage ring, at the location of the bending magnets, so energy must be returned to them through the form of electromagnetic, radiofrequency pulses. These pulses as well as the variation in time of the magnetic field are synchronised (hence the term synchrotron) to match the energy losses of the electrons and thus keep the orbiting radius and energy constant.

At non-relativistic energies, electrons in circular motion radiate electromagnetic waves in a dipole pattern (doughnut-shaped). At relativistic energies however, the pattern becomes sharply peaked in the direction of motion of the electron (Lewis, 1997), as shown in figure 3.2.

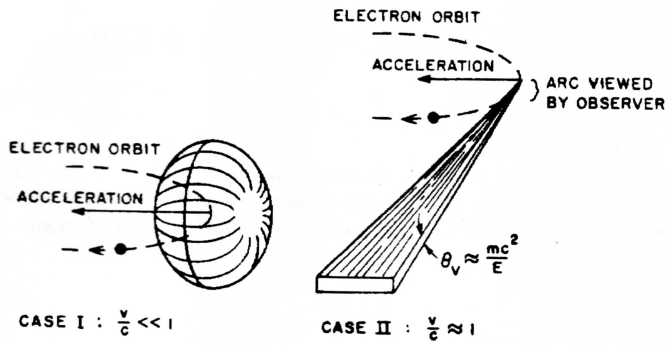

Figure 3.2: Radiation emission pattern of electrons in a circular motion: Case I, non-relativistic electrons, case II, relativistic electrons. Reproduced from Chapter 2 of Winick (1980). Copyright (1980). Image used with the kind permission of Springer Science and Business Media.

Electrons in a synchrotron must be treated using Einstein's theory of special relativity. The energy of a relativistic electron with velocity v is (Nielsen and McMorrow, 2001);

$$E = \gamma \cdot m_0 \cdot c^2, \tag{3.1}$$

where m_0 is the electron's rest-mass and γ is the Lorentz contraction factor, given by

$$\gamma = \frac{1}{\sqrt{1 - \frac{v^2}{c2}}}. \tag{3.2}$$

It can be shown that SR is emitted within a naturally collimated cone of angle $\theta \approx \frac{1}{\gamma} = \frac{m_0 \cdot c^2}{E}$ in the vertical direction. This angle is typically around 10^{-4}, or 0.1 milliradians (Winick, 1980). Each bending magnet in the storage ring therefore produces a fan beam, highly collimated in the vertical direction, with a broad spectrum ranging from the far infra-red to hard X-rays, which can be directed to a beamline hutch for experimental purposes. Large synchrotron facilities such as SPring-8 in Japan have over 40 beamlines all operating simultaneously.

There is also the means to produce more intense beams than those produced by a bending magnet source. So-called insertion devices (termed wigglers and undulators) can increase the brilliance of the X-ray beam by several orders of magnitude compared to bending magnets. Figure 3.3 illustrates the relative brilliance spectrum of a variety of radiation sources. Brilliance is a useful parameter to compare the quality of radiation from different sources. The brilliance is given by

$$Brilliance = \frac{Photons/sec}{(mrad)^2 \cdot (mm^2 source area) \cdot (0.1\% bandwidth)}. \tag{3.3}$$

The brilliance, a function of photon energy, is a figure of merit that rolls the flux, the collimation and source size and the spectral distribution into one single quantity (Nielsen and McMorrow, 2001). The maximum brilliance for 3rd generation undulators is about 10 orders of magnitude greater than that for a rotating anode-style X-ray generator that one might find in a hospital radiology department. Such dramatic improvements has led to a paradigm shift for performing experimental X-ray science. Experiments deemed impossible 20 years ago are now performed on synchrotrons on an almost routine basis.

In a 1980 textbook on SR, Winick (1980) summarised the properties of SR as follows;

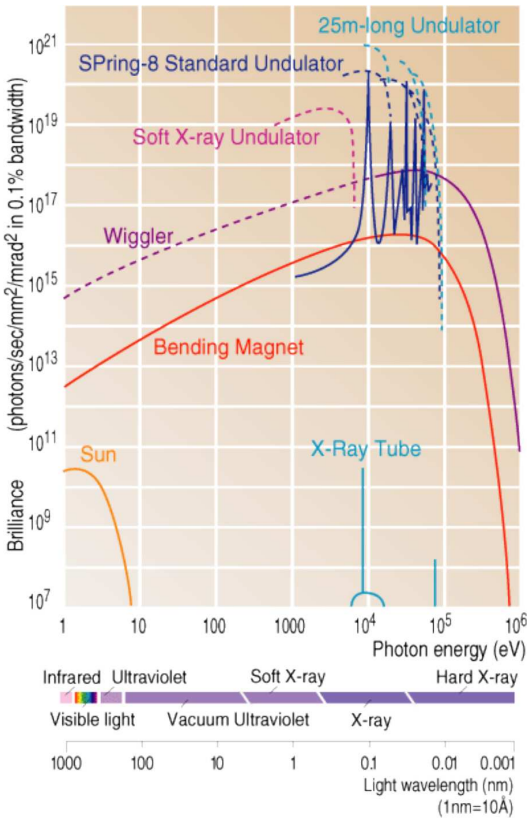

Figure 3.3: Brilliance of various radiation sources. Copyright (2008), Japan Synchrotron Radiation Research Institute. Image used with permission.

1. Very high intensity
2. Broad spectral range
3. High polarisation
4. Pulsed time structure
5. Natural collimation

In addition, Winick notes that the SR produced by storage rings offers;

1. High vacuum environment
2. Small source size
3. Stability

In a detailed review of the medical applications of SR from 1997, Robert Lewis stated that it was the combination of these properties that make SR a unique and very powerful source for a wide range of scientific and technical applications in biology and medicine, including angiography, mammography, computed tomography, diffraction enhanced imaging and radiotherapy (Lewis, 1997).

From the perspective of radiotherapy applications, a synchrotron produces very intense X-rays with a photon flux (number of photons per unit area, per unit time) several orders of magnitude greater than for x-rays produced by megavoltage linear accelerators for radiotherapy. The useful mean energy of synchrotron X-rays for therapy purposes is approximately 100 keV. At this energy the probability of Compton scattering events in tissue is low, and the distance travelled by secondary electrons is only of the order of tens of microns, as the photoelectric effect dominates (Nielsen and McMorrow, 2001). In addition, the minimally divergent x-rays (approximately 0.1 milliradians) allow a quasi-parallel beam to travel a distance of more than 40 metres in air. This technique permits an array of microbeams to be delivered, where a high peak dose relative to a low valley dose can be maintained. Such radiation fields can be delivered deep in tissue with microscopically sharp absorbed dose gradients at the field edges (Laissue et al., 1999). Importantly, the very high beam intensity achieved on a synchrotron mean that very high doses can be delivered in a very short period of time to objects on the dimensional scale of a cell (tens of μm). The synchrotron is therefore an ideal X-ray source for a technique such as microbeam radiation therapy.

3.2 Fundamentals of Radiation Dosimetry

Ionising radiation causes measurable changes when it interacts with matter. The science of dosimetry is concerned with ways to measure these changes. It is of tremendous importance to radiotherapy and human health. There are numerous textbooks on dosimetry which describe the subject in great detail. Examples include; Johns &

Cunningham's *The Physics of Radiology*, Khan's *The Physics of Radiation Therapy*, Attix's *Introduction to Radiological Physics & Radiation Dosimetry*, and Greening's *Fundamentals of Radiation Dosimetry*. The purpose of this chapter is not to give a detailed overview of radiation dosimetry, rather to review those aspects of dosimetry relevant to microbeam radiation therapy (MRT).

3.2.1 Description of a radiation beam

There are two different facets to dosimetry; describing the properties of the radiation, and describing the amounts of energy deposited by that radiation in matter. Looking firstly at how one might describe the radiation beam, there are a number of quantities and units to be considered. These have been formally defined by the International Commission on Radiological Units (ICRU) in for example, *Report 33*, *Radiation Quantities and Units*, published in 1980.

1. The fluence (Φ) of photons is defined as the quotient dN by da, where dN is the number of photons that enter an imaginary cross-sectional area da.

$$\Phi = \frac{dN}{da}. \tag{3.4}$$

2. The fluence rate, or flux density (ϕ) is the fluence per unit time.

$$\phi = \frac{d\Phi}{dt} \tag{3.5}$$

3. The energy fluence (Ψ) describes the amount of energy crossing unit area for photons with energy hν and is given by

$$\Psi = \frac{dN \cdot h\nu}{da}. \tag{3.6}$$

4. The energy fluence rate, or flux density, or intensity (ψ) is the energy fluence per unit time

$$\psi = \frac{d\Psi}{dt}. \tag{3.7}$$

The above identities and definitions mask a complexity; most radiation beams are composed of photons of different energies, they are 'polychromatic'. To describe a

polychromatic beam one needs to know both the number *and* the energy of all the photons in the beam and this information is not easy to obtain experimentally. A distribution of photons of a given energy is referred to as a spectrum.

3.2.2 Measurement of ionising radiation: exposure, electronic equilibrium & the free-air ionisation chamber

A radiation beam may also be described in terms of exposure, a measure of the ability of a radiation beam to ionise air. The units of exposure are the roentgen (R).

In 1928, the ICRU formally adopted the roentgen, R, as the unit for measuring the exposure from X and γ radiation. The exposure (X) was more recently (1980) defined as "the quotient of dQ by dm where dQ is the absolute value of the total charge of the ions of one sign produced in air when the electrons (negatrons & positrons) liberated by photons in air of mass dm are completely stopped in air " (ICRU, 1980),

$$X = \frac{dQ}{dm}. \tag{3.8}$$

The exposure is thus a measure of the ability of the radiation to ionise air. The SI unit of exposure is coulomb per kilogram. The roentgen, R, is a special unit ($1R = 2.58x10^{-4}Ckg^{-1}$) which is still in use for dosimetry purposes and indeed was used for exposure and dose measurements in the MRT experiments described in the next chapter.

In order to more fully appreciate the requirements of the definition of exposure, consideration must be given to the concept of electronic (or charged particle) equilibrium, and a description of the free-air ionisation chamber.

Figure 3.4 is a schematic diagram illustrating electronic equilibrium in a free-air chamber and is useful to define the roentgen. An X-ray beam passes through an aperture of known area, enters a metal box and passes through a hole on the far side of the box, without striking anything in the box other than the air it contains. As it interacts with the air, the X-ray beam will set in motion secondary electrons, which in turn will produce ionisation along their tracks. The separation of the electrodes in the

chamber are such that the vast majority of electrons released in the shaded volume in figure 3.4 lose all their energy before they can reach the electrodes or chamber walls. A high potential difference between the collecting electrode (of length L) and the high voltage electrode sweeps the ions (produced in the shaded area), to the collecting electrode over time Δ t. $\frac{\Delta Q}{\Delta t}$ constitutes a current, which can be measured by an electrometer.

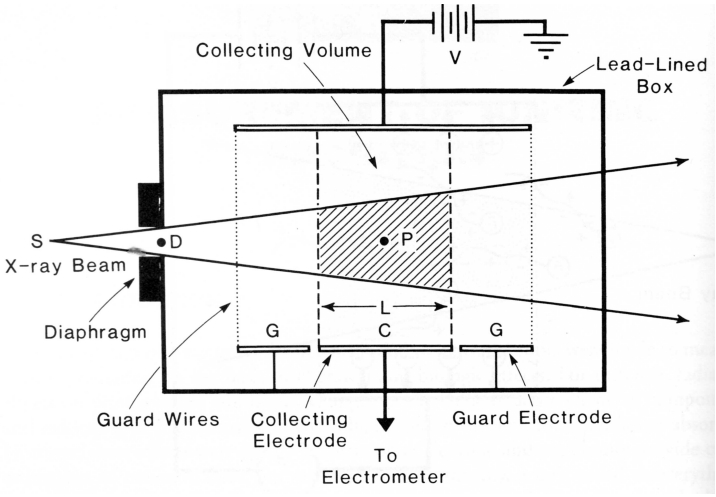

Figure 3.4: Electronic equilibrium & the free-air ionisation chamber. Reproduced from Khan (2003). Copyright (2003) Lippincott Williams & Wilkins. Image used with permission.

For the free-air ionisation chamber in figure 3.4, a high voltage (of the order of 2000 V) is applied across the plates to collect ions produced between the plates. This ionisation is measured over a length, L, which is determined by guard wires and guard electrodes, The ions are therefore collected from a defined volume. Importantly, some electrons produced in the specified volume deposit their energy outside the region of ion collection and thus are not measured. However, electrons produced outside the specified (shaded) volume may enter the ion-collecting region and produce ionisation there. If the number of ions lost is compensated by the number of ions gained, then a condition of electronic (or charged particle) equilibrium exists. Under this condition, the definition of the roentgen is satisfied and this is the principle behind the free-air ionisation chamber.

If ΔQ is the charge collected in coulombs, ρ is the density of air $(kgm^{-3}$, then the exposure, X_p at the centre of the specified volume (point p) is

$$X_p = \frac{\Delta Q}{\rho \cdot A_p \cdot L} \times \frac{1}{2.58 \times 10^{-4}}\, roentgens \tag{3.9}$$

Where A is the cross-sectional area (m^2) of the beam at point p and L is the length (m) of the collecting volume. A similar approach was used for exposure and dose measurements in the MRT experiments described in the next chapter.

The condition of electronic equilibrium can only exist if the range of electrons liberated by the incident photon beam is less than the distance between each plate and the specified, interaction volume. As the X-ray beam energies increase, the range of the electrons liberated in air increases (Khan, 2003). For example, a 3 MeV photon propagating in air can produce electron tracks 1.5 metres long (Johns and Cunningham, 1983) which gives some idea of the size of the air chamber required to measure the exposure from such radiation. Large plate separations create problems of ion recombination, photon scatter and air attenuation. These problems place an upper limit on the photon energy above which the roentgen cannot be measured accurately, and indeed this limit occurs at approximately 3 MeV (Johns and Cunningham, 1983; Khan, 2003).

In practice however, simply because of size, the free-air chamber is limited to radiation beams with energies of approximately 300 keV, the realm of kilovoltage and orthovoltage radiotherapy and diagnostic radiology. The free-air chamber is not suitable for use in megavoltage radiotherapy primarily for the practical reasons outlined in the previous paragraph. However, it is a very useful standard of exposure and a related concept, kerma, which will be described in the next section. Free-air chambers are predominantly used by national standards laboratories and synchrotron facilities. They are not routinely used in hospital radiotherapy departments, where the thimble-shaped, Farmer chambers and parallel plate chambers, are the norm (Khan, 2003).

3.2.3 Measurement of absorbed dose: the relationship between exposure, kerma and dose

The transfer of energy from a photon beam to the medium with which it interacts is a two-stage process. Stage (a) involves the photon interacting with an atom, causing one primary, and many secondary electrons, to be set in motion. The photon transfers some or all of its energy to an electron, imparting it with kinetic energy. Stage (b) involves the transfer of energy, from the energetic electron to the medium, through excitation and ionisation. These stages are illustrated in figure 3.5. The electron in turn will give up its energy along its track. The transfer of energy at Stage (a) is called 'Kerma'and along (b) is 'Absorbed Dose'. Kerma occurs at a point, whereas absorbed dose occurs further 'downstream', over a range equal to the range of the electron (Johns and Cunningham, 1983). The ICRU have defined KERMA (Kinetic

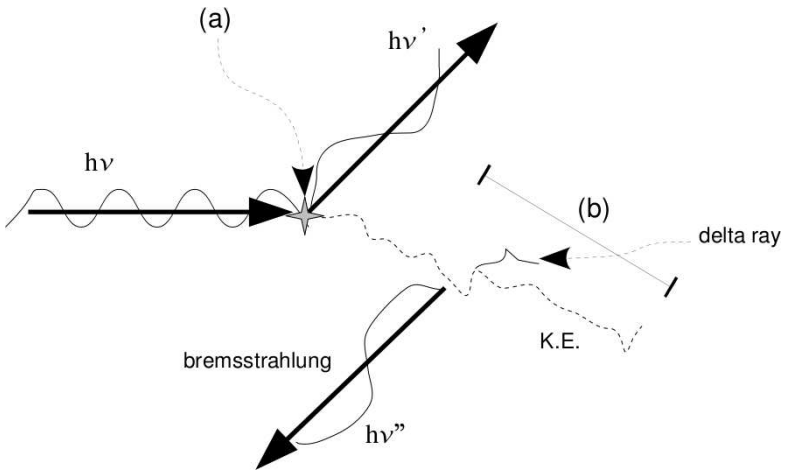

Figure 3.5: Air kerma, energy transfer and dose. Refer to the text for an explanation of (a) and (b). Adapted from Chapter 7 in Johns and Cunningham (1983).

Energy Released in the Medium) as the quotient of $d\overline{E_{tr}}$ by dm, where $d\overline{E_{tr}}$ is the kinetic energy transferred from photons to electrons in a volume element of mass dm (ICRU, 1980).

$$K = \frac{d\overline{E_{tr}}}{dm} \tag{3.10}$$

The unit of Kerma is the Gray (Gy). 1 Gy = 1 J/kg. For a monoenergetic beam of energy $h\nu$, the kerma is given by

$$K = \Phi \cdot (\frac{\mu}{\rho}) \cdot \overline{E_{tr}}, \tag{3.11}$$

where $\frac{\mu}{\rho}$ is the mass attenuation coefficient for the medium and $\overline{E_{tr}}$ is the average energy transferred to electrons of the medium at each interaction. For a spectrum of energies, the Kerma is defined as

$$K = \int_{h\nu_{min}}^{h\nu_{max}} \frac{d\Phi(h\nu)}{d(h\nu)} \cdot (\frac{\mu(h\nu)}{\rho}) \cdot \overline{E_{tr}}(h\nu) dh\nu \tag{3.12}$$

which is the integral of the kermas from the photons at each energy in the spectrum (Johns and Cunningham, 1983).

Exposure and kerma are closely related. The exposure is related to the part of the kerma associated with ionisation, but not bremsstrahlung production, and is termed the collision kerma, K^{col}. The collision kerma in air can be calculated from the ionisation charge produced per unit of energy deposited by photons. The mean energy required to produce an ion pair in dry air is virtually constant for all electron energies and has a value of $\overline{W}$ = 33.97 eV/ion pair (Greening, 1985; Khan, 2003). If e is the charge on the electron (1.602 x 10^{-19} C, then $\frac{\overline{W}}{e}$ is the average energy required to produce unit charge of ionisation and hence, $\frac{\overline{W}}{e} = 33.97 J/C$. The exposure is given by

$$X = (K^{col})_{air} \cdot (\frac{e}{\overline{W}}). \tag{3.13}$$

Because $\frac{\overline{W}}{e}$ is a well-defined numerical parameter, it can be seen that the free-air ion-chamber can act as a standard of air kerma as well as exposure (Greening, 1985).

In the presence of electronic equilibrium, the dose at a point in a medium is equal to the collision kerma (Khan, 2003). The dose in air, D_{air} is given by

$$D_{air} = (K^{col})_{air} = X \cdot (\frac{\overline{W}}{e}). \tag{3.14}$$

This is the relationship used to calculate the in-air entrance dose for the MRT experiments at the SPring-8 synchrotron, described in Chapters 4 and 6.

The absorbed dose D_m, in some other medium is given by (Greening, 1985)

$$D_m = X \cdot \frac{\overline{W_{air}}}{e} \cdot \frac{(\frac{\mu_{en}}{\rho})_m}{(\frac{\mu_{en}}{\rho})_{air}}, \tag{3.15}$$

where $\frac{\mu_{en}}{\rho}$ is the so-called mass-energy absorption coefficient. Values of $\frac{\mu_{en}}{\rho}$ for various materials are published in textbooks and on internet websites, for example, the website of the National Institute of Standards & Technology (Hubbell and Seltzer, 1996).

The ratio $\frac{(\frac{\mu_{en}}{\rho})_m}{(\frac{\mu_{en}}{\rho})_{air}}$ varies slowly with energy for materials with an atomic number close to air. The values of this ratio for water and air only vary by a few percent between 100 keV and about 10 MeV (Greening, 1985). As a consequence, the photon energy does not need to be known very accurately in order to determine the absorbed dose to water from an exposure measurement, providing the conditions of electronic equilibrium are satisfied.

It is important to note that there is an assumption inherent in our calculations of peak dose, based on the ionisation chamber readings, which deserves further consideration. Calculation of dose requires knowledge of the measured cross-section of the beam. We have assumed that the microbeam intensity profiles are perfect rectangles or top-hats, and the valley dose is zero Gy (perfect attenuator). The ionisation chamber records charge from the ionised air volume which inevitably must include a valley dose component. The dose calculation does not take into account the valley dose and dose from the penumbral regions of the beam. As will be reported in Chapter 4, the contribution from these regions are less than 5% of the maximum dose and is sufficiently low to be ignored.

Knowledge of the energy spectrum allows one to calculate the kerma, using equation 3.12. The energy spectrum of the X-ray beam on beamline BL28B2 at SPring-8, after 3 mm Cu filtration, is shown in figure 3.6, plotted on a log-log scale. The spectrum was generated using the computer program, SPECTRA (version 7.2), described in Tinaka and Kitamura (2001). The calculated spectrum in this instance incorporates the actual slit sizes used in our experiments at SPring-8. A beam width of 8.3

mm and a beam height of 0.9 mm, 36 metres from the source was selected, to produce a beam of approximately 10 mm x 1 mm at 44 metres from the source, the level of the sample stage. A calculation for air kerma based on the calculated energy spectrum and equation 3.12, produced an air kerma of 200 J/kg, which can be expressed as 200 Gy/sec. Synchrotron radiation is very well chacterised and often used as a standard for X-rays, therefore the calculation method certainly has validity.

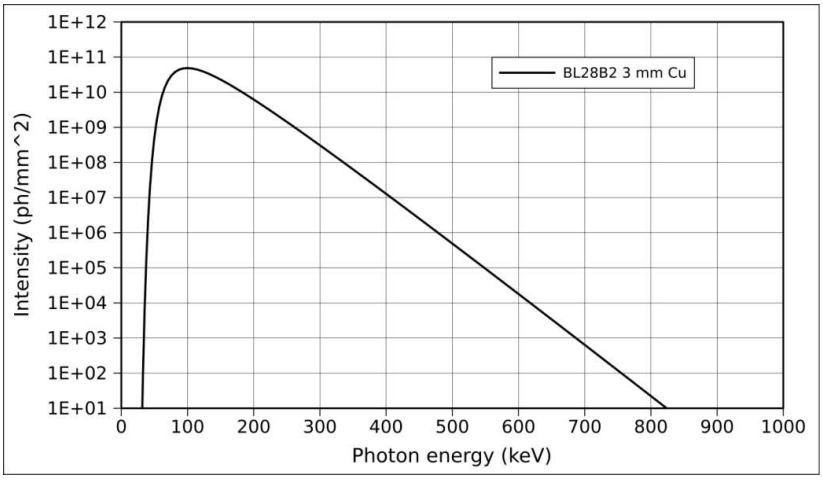

Figure 3.6: Energy spectrum from beamline Bl28B2 at SPring-8, calculated using the SPECTRA program of Tinaka and Kitamura (2001)

Lastly, some consideration is given to the range of secondary electrons in water. As charged particles travel through matter, the interactions cause the particles to slow down and change direction, eventually losing all kinetic energy and coming to rest. There is a finite distance beyond which there will be no charged particles, and this distance is called the range of the particle (Johns and Cunningham, 1983). As the electron slows down it starts to lose energy more quickly, and the Continuous Slowing Down Approximation (CSDA) is used to calculate the range of charged particles in a medium (Johns and Cunningham, 1983). The CSDA range emerged from Hans Bethe's stopping power theory in the 1930's, and can be expressed as follows;

$$R_{CSDA} = \int_0^{E_{k_i}} \frac{dE}{S_{tot}(E)}, \tag{3.16}$$

where R_{CSDA} is the CSDA range (mean path length) of the charged particle in the absorber, E_{k_i} is the initial kinetic energy of the charged particle and $S_{tot}(E)$ is the total stopping power of the charged particle as a function of energy, E_k. The CSDA and stopping power theory are described in greater detail in Podgorsak (2005).

The National Institute of Standards & Technology (NIST) have produced a useful database (Berger et al., 2005) which allows calculation of the CSDA range for electrons with energies ranging from 10 keV to 1 GeV, travelling in various media. The CSDA range for electrons with energies between 10 keV and 1000 keV, travelling in liquid water, is plotted in figure 3.7. Summing the product of the SPring-8 energy spectrum of figure 3.6 and the CSDA range plot of figure 3.7 (a crude convolution), yielded a maximum range in water, for dose-depositing electrons, of 180 μm. Podgorsak (2005) states "For heavy charged particles, the CSDA range is a very good approximation to the average range R of the charged particle in the absorbing medium, because of the essentially rectilinear path of the charged particle in the absorber. For light charged particles such as electrons, the CSDA range is up to twice the range of charged particles in the absorber, because of the very tortuous path that the light charged particles experience in the absorbing medium". Therefore, the average range in water, of secondary electrons from the X-ray beam at beamline BL28B2 at SPring-8, is 90 μm. The curve in Figure 3.7 shows why diagnostic energies are vital for MRT. Megavoltage energies will not work because the CSDA range of the secondary electrons produced (by megavoltage photons) would be too large, resulting in valley doses which are a significant fraction of the peak doses.

3.3 On Monte Carlo Simulations of MRT

Synchrotron MRT poses considerable difficulties for accurate, measurement-based dosimetry. Dose gradients on the order of tens of Gray per micron are required in MRT. No current dosimeter possesses the spatial resolution and dynamic range to accurately and simultaneously measure the dose in the microbeam peaks, and the

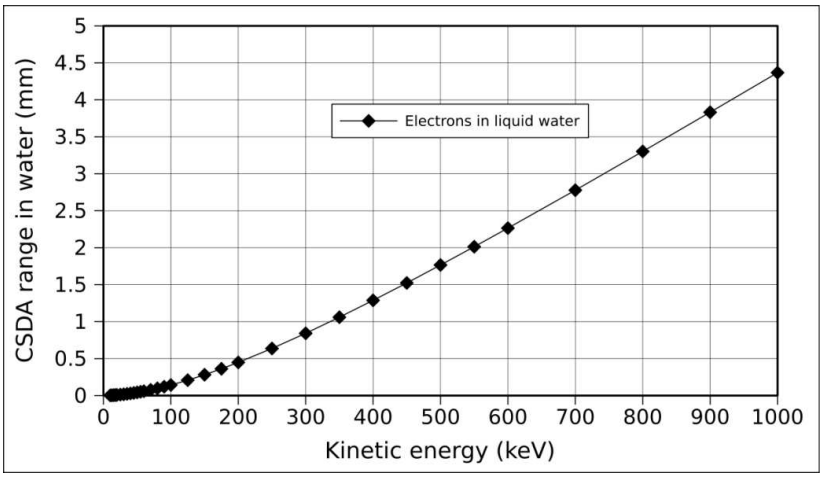

Figure 3.7: CSDA range for electrons in liquid water, calculated using the database of Berger et al. (2005)

dose in the valleys between the microbeams, for typical MRT energy ranges (50-250 keV). Consequently, the majority of publications pertaining to MRT dosimetry employ Monte Carlo computer simulations to model the radiation transport and dose deposition in water (Company and Allen, 1998; Orion et al., 2000; De Felici et al., 2005; Siegbahn et al., 2006). Some experimenters have performed measurements using Metal Oxide Semiconducting Field Effect Transistors (MOSFET) as an X-ray microbeam dosimeter (Rosenfeld et al., 1999; Kaplan et al., 2000) and have compared them with Monte Carlo simulation results (Orion et al., 2000; Brauer-Krisch et al., 2003; De Felici et al., 2005) and reported acceptable agreement on a micron scale. However, the use of MOSFETs can be problematic; there are stabilty and saturation concerns and they are difficult to align (Brauer-Krisch et al., 2003).

Monte Carlo simulation is a statistical approach to the modelling of various physical phenomena, for example the interaction of ionising radiation with matter. In a typical Monte Carlo simulation, a beam of virtual particles are “launched ”into a medium, they travel certain distances, determined by a probability distribution, to the site of a collision and scatter into another energy and/or direction, possibly producing new particles that have to be transported as well. This procedure is continued until all particles are absorbed or leave the geometric volume under consid-

eration (Kawrakow and Rogers, 2003). The Monte Carlo method is an extremely useful computational tool for radiation dosimetry. However, it is critical for novel radiotherapy techniques to have measurement-based dosimetry which can be used to benchmark computer simulations. This is particularly so if a new form of radiation therapy is ever to be implemented clinically.

To date, there are about a dozen papers in the literature on Monte Carlo simulations for MRT dosimetry. The original paper by Slatkin et al. (1992) used the EGS4 (Nelson et al., 1985) and the Persliden codes (Persliden and Carlsson, 1984), as well as an un-published, in-house code. Since then, a variety of other codes including EGS5 (Company, 2007), PSI-GEANT (Stepanek et al., 2000), PENELOPE (Siegbahn et al., 2006) and GEANT4 (Spiga et al., 2007) have been used to simulate X-ray microbeam dose distributions in a phantom. Numerous authors have used the same phantom as appeared in Slatkin's paper, namely a 16 cm long cylinder of water with a 16 cm diameter. The X-ray beam is transported along the cylinder's central axis. These papers typically describe the characteristics of both cylindrical (rod-shaped) and planar (wafer-shaped) microbeams. The cylindrical microbeams give very high peak-to-valley dose ratios compared to the planar microbeams, however there are no publications which describe a collimator to produce rod-shaped microbeams, only planar microbeams. The symmetry of cylindrical (rods) microbeams make them easier to simulate and analyse and this may explain their popularity in the literature. A recent paper by Spiga et al. (2007) described Monte Carlo simulations of cylindrical microbeams only. There was no equivalent experimental data to compare the simulated dose distributions, because no cylindrical microbeam-generating collimator exists as yet.

In view of the fact that detailed Monte Carlo simulations had already been performed and published by several authors using different codes, further Monte Carlo study was not deemed useful. Instead, it was decided to pursue experimental measurements of the absorbed dose distribution using radiochromic film and microdensitometry. This is the subject of the next chapter and some of the shortcomings of

Monte Carlo simulations, as well as directions for future work are discussed there. We did perform Monte Carlo simulations, using the GEANT4 code, to investigate the depth dose characteristics of the synchrotron X-ray microbeam at the SPring-8 synchrotron in Japan. However, a complete simulation of peak & valley doses at different depths was not performed, rather, our efforts were directed to measuring the dose distributions and then comparing our measured peak-to-valley dose ratios with previously published Monte Carlo simulations.

3.4 Radiochromic Film Dosimetry & Microdensitometry

X-rays blacken radiographic film by causing a chemical reaction within crystals of silver bromide on the film. The degree of blackening depends on the amount of free silver deposited, which is related to the radiation energy absorbed (Khan, 2003). X-ray film, or radiographic film, has been used for many years as a dosimeter. The dose can be related to the optical density, or blackening, of the film by the relation

$$OD = \log_{10} \frac{I_0}{I_t}. \tag{3.17}$$

Where I_0 is the intensity of light incident on a region of film and I_t is the intensity of light transmitted through the region (Williams and Thwaites, 2000). The optical density is measured with a densitometer, which consists of a light source on one side of the film and a detector on the other side to measure the relative transmitted light intensity.

Ideally, there would be a linear relationship between optical density and dose, but this is not often the case. In order to use film for dosimetry purposes, it is necessary to determine the relationship by delivering known, graded doses of radiation to film and plotting the net optical density to obtain a characteristic curve. The net optical density is obtained by subtracting the reading for the base fog, that is the optical density of unirradiated film, from the measured optical density. Too high a dose and the film saturates, and cannot blacken further.

Radiochromic film is chemically quite different to radiographic film. Radiochromic film consists of monomer crystals in a gel bound to a mylar substrate. The monomer undergoes partial polymerisation upon irradiation and the film changes colour (hence the name radiochromic) from a light blue colour to a dark blue (Williams and Thwaites, 2000). Radiochromic film has been investigated as a dosimeter since the 1960's. William L. McLaughlin from the National Institute of Standards and technologies (NIST) in the US is credited with doing some of the first research with radiochromic film, mostly for industrial applications. The era of modern radiochromic film dosimetry began in the the mid-1980's, when David Lewis described the first GafChromic film which was an order of magnitude more sensitive to radiation than previous generations of radiochromic film, as reported by Soares (2006). This new film, now known as HD-810, was sensitive enough for some medical applications [1].

The active component in GafChromic radiochromic dosimetry films is a long chain fatty acid, similar to stearic acid and belonging to a class of molecules known as diacetylenes. When exposed to radiation, active diacetylenes undergo a solid-state polymerisation reaction, producing a dye polymer known as polydiacetylene characterised by a cyan blue colour in the transmitted light spectrum. A technical paper describing the physical and chemical properties of HD-810 GafChromic film is available from the ISP website (ISP, 2008).

Like radiographic film (silver halide film), radiochromic film provides a two-dimensional map of the incident dose distribution. The spatial resolution of radiographic film is high, limited only by the grain size. In the case of GafChromic films, the resolution is limited by the dimensions of the polymer and is better than 1 micron, based on modulation transfer function measurements (David Lewis, personal communication). Niroomand-Rad et al. (1998) quote the spatial resolution of radiochromic film to be of the order of 600 line pairs/mm. There are a number of

[1] GafChromic is the trade name for a type of radiochromic film manufactured by International Specialty Products, NJ, USA

important differences between radiochromic and radiographic film, as outlined in Williams and Thwaites (2000);

1. Radiochromic film is self developing and requires no post-exposure processing in a developer.

2. Radiochromic film may be handled in visible light, although it is sensitive to long periods of exposure to ultra-violet radiation.

3. The composition of radiochromic film is more tissue-equivalent than radiographic film, with an effective atomic number close to 6.5.

4. Radiochromic film response is less energy dependent than radiographic film, especially over low energy ranges (< 100 keV), where radiographic film demonstrates a very strong energy dependence.

5. Radiochromic film continues to 'develop' post-irradiation, that is, the optical density increases for at least 6 hours post-irradiation.

6. Radiochromic film is temperature dependent and needs to be stored in a cool, dark environment.

GafChromic radiochromic films can be handled in normal room light for several hours without noticeable effects, according to the manufacturers (ISP, 2008). However, ISP recommended leaving the films in dark conditions when not being handled, and ideally, storing the films in a refrigerator to prolong the film's shelf life. The films can be cut or trimmed to size, they can be marked with a pen and can even be immersed in water for short periods of time (less than 1 hour) (Butson et al., 2003). The density of radiochromic film is 1.08 g/cm^3 (Hubbell and Seltzer, 1996).

GafChromic films are the most commonly used type of radiochromic film media. The most popular forms of GafChromic film for medical applications are HD-810, MD-55 and EBT. EBT film has become increasingly popular in radiotherapy centres, largely as a result of centres going filmless and abandoning their film processor and

also owing to needing a method of performing fast quality assurance tests for patients who are having intensity modulated radiation therapy.

An overview is provided in the following two subsections, on the properties of GafChromic HD-810 and EBT films since these films were used in the research described in this thesis. The information is not intended to be comprehensive; emphasis is placed on particular properties pertinent to this research. The American Association of Physicists in Medicine (AAPM) published a comprehensive task group report on radiochromic film dosimetry (Niroomand-Rad et al., 1998). The task group report described properties of HD-810 and MD-55 film, but not EBT film. However, Soares (2006) and Fuss et al. (2007), describe EBT film in some detail.

3.4.1 Properties of GafChromic HD-810 Radiochromic Film

HD-810 film is designed for the measurement of absorbed dose photons with energy > 100 keV. Sensitometric studies have shown the film to be linear for doses up to 250 Gy (ISP, 2008). The recommended dose range for this film is between 10 and 400 Gy (ISP, 2008), however higher dose ranges can be used but require appropriate dose calibrations to be used. Structurally, the film has a 7 μm thick active layer coated on a 100 μm polyester base. There is also a cover layer approximately 1 μm thick, coated to the surface. The schematic configuration of HD-810, and its sensitometric curve are shown in figures 3.8 and 3.9 respectively.

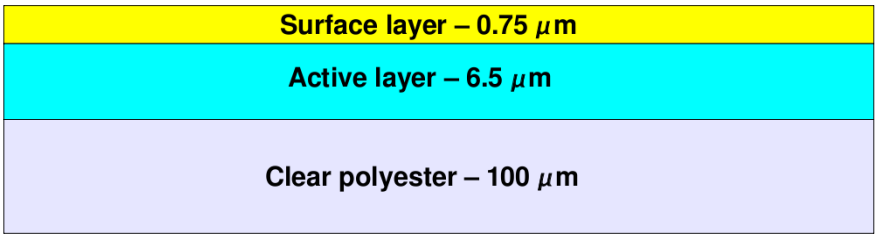

Figure 3.8: Structure of GafChromic HD-810 radiochromic film

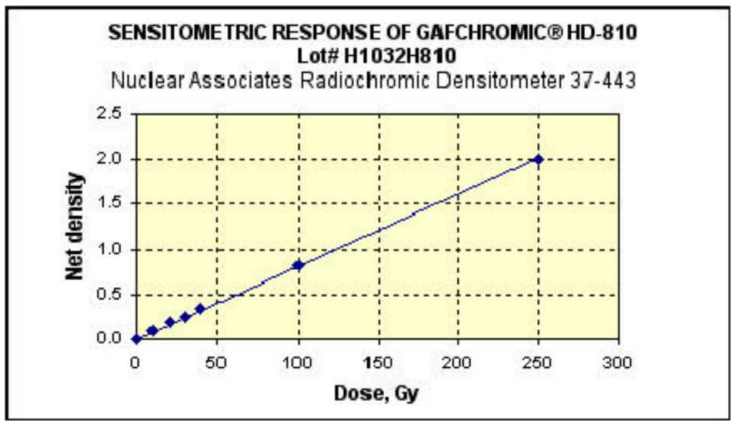

Figure 3.9: Dose response of GafChromic HD-810 radiochromic film, from ISP's 2008 technical report on HD-810 film. Copyright (2008) ISP. Image used with permission.

When the active component in HD-810 film is irradiated, it reacts to form a blue coloured polymer, with absorption maxima at about 615 nm and 675 nm. The response of the film is optimised therefore by densitometric measurement using red light. Studies have shown the response of HD-810 film to be largely independent of X-ray energy for energies > 100 keV. Muench et al. (1991) showed the response of GafChromic HD-810 film decreased by about 30% when the effective (or mean) photon energy decreased from 1720 keV (4 MV X-rays) to 28 keV (60 kVp X-rays). In contrast, the response of silver-halide, radiographic film was observed to increase by almost 1000% over the same energy range. Muench et al. (1991) did not proffer any reasons for the drastic increase in sensitivity of radiographic film at low energies.

Studies have also shown no measurable effects in HD-810 film from the dose rate, in the range 0.02 Gy/min to 200 Gy/min from a Co^{60} source (Saylor et al., 1988). With synchrotron MRT, the dose rates are more like 200 Gy/sec. Nariyama (2005) investigated the use of GafChromic films at synchrotron dose rates as high as 60 kGy/s in order to confirm maximum measurable doses. No dose rate effects however were reported in this paper. It appears there is not enough data in the literature to determine whether dose rate effects in GafChromic film are significant for synchrotron MRT. HD-810 film does exhibit post-exposure growth and the manufac-

turers recommend waiting 24 hours post-irradiation before performing densitometric measurements. Figure 3.10 is a plot of the post-exposure density growth curve of HD-810 film exposed to different doses of X-rays. The curve in figure 3.10 has been normalised to the density value at 24 hours post-exposure and is essentially independent of dose. The density changes by approximately 8% between 1 hour and 24 hours post-exposure, but the rate of density growth decreases and the density changes by less than 2% over the next 96 hours.

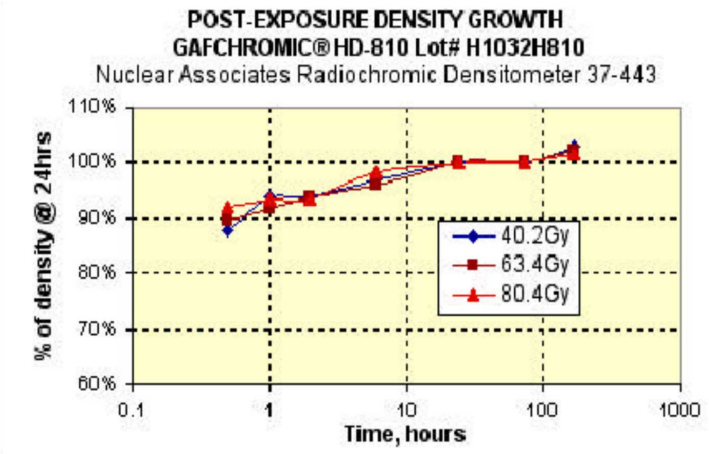

Figure 3.10: Normalised post-exposure optical density growth curve of GafChromic HD-810 radiochromic film, measured with a Nuclear Associates Radiochromic Densitometer 37-443, from ISP's 2008 technical report on HD-810 film. Copyright (2008), ISP. Image used with permission.

Lot-to-lot variations and roll-to-roll uniformity on HD-810 film can be as much as 5%, largely a result of it being made in smaller production volumes than other varieties of GafChromic film (Dr. David Lewis, ISP, personal communication).

3.4.2 Properties of GafChromic EBT film

In 2004, ISP Corporation introduced a new type of radiochromic film known as EBT film. This film featured a more sensitive emulsion than previously available. The useful dose range of EBT film is from about 0.1 Gy to 8 Gy. Below 2 Gy the response is linear with dose. The structure of EBT film is shown schematically in figure 3.11. The sensitive emulsion is in two active layers, each one being 17 μm thick. Each

active layer is sandwiched between a surface layer and a polyester base. Each of these layers in turn are glued with an adhesive layer to a polyester layer in the film's centre. The total thickness of the film is almost 300 μm. A 'white paper' describing the physical properties of EBT film is available from the ISP website (ISP, 2007a).

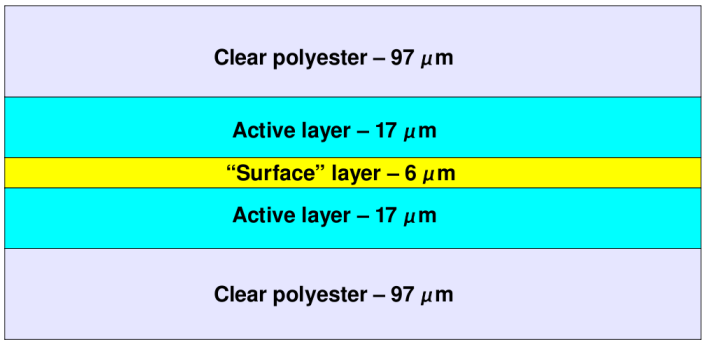

Figure 3.11: EBT GafChromic film configuration

EBT film is clearly more sensitive to dose than HD-810. EBT film has been adopted quite rapidly by radiotherapy departments as a direct replacement for radiographic film such as Kodak X-OMAT film, which requires a chemical processor to develop the film. EBT film exhibits a more uniform response with spatial position than HD-810 film. In the twenty production lots since 2005, the roll-to-roll variance of uniformity within a lot has been < 2% (Dr. David Lewis, ISP, personal communication). Figure 3.12 is a plot of the uniformity profiles (variations in spatial position response) of EBT film, the expressions cross-web and down-web refer to directions orthogonal and parallel to the coating direction of the emulsion. Assuming the values are random and normally distributed (and the results are representative of the entire roll), the overall uniformity of a production roll is typically $\pm$ 1.5% (Dr. David Lewis, ISP, personal communication).

Rink et al. (2007) investigated the response of GafChromic EBT film for dependence on X-ray beam energy using X-rays with effective energies ranging from 34 keV (75 kVp X-rays) to 5650 keV (18 MV X-rays). All responses were normalised to that obtained for Co^{60} irradiations (essentially monoenergetic at approximately

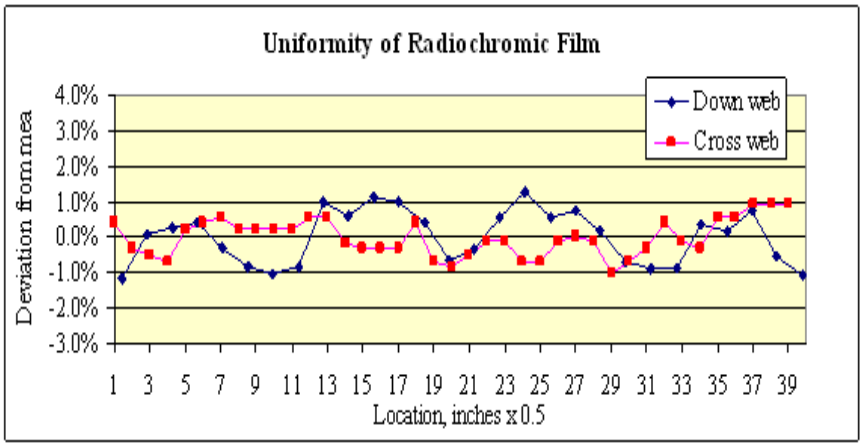

Figure 3.12: EBT GafChromic film uniformity, from personal communication with Dr. David Lewis, ISP. Copyright (2008), ISP. Image used with permission.

1.2 MeV). The mean change in optical density of EBT film remained within 3% of that of Co^{60} over the entire energy range. Figure 3.13 is a plot of the optical density versus dose curve for different beam qualities, three kilovoltage beams and a megavoltage, Co^{60} beam. There is less than 5% difference in response between the beam qualities, illustrating the low energy dependency of EBT film.

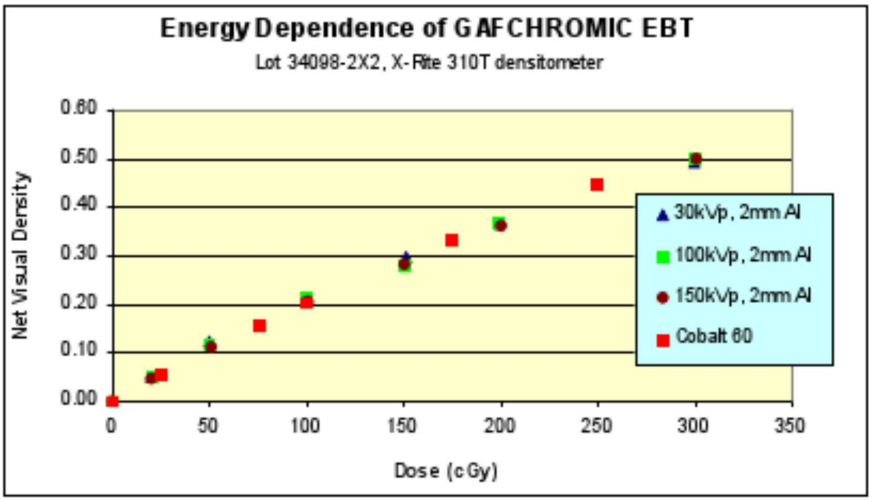

Figure 3.13: Response of EBT film to different kilovoltage and megavoltage beam qualities, from ISP's 2007 white paper on EBT radiochromic film. Copyright (2008), ISP. Image used with permission.

The peak absorption of EBT film occurs at 636 nm. Like HD-810 film, the

response of EBT film is (quite naturally) improved if the spectral response of the light source is matched to the absorption of the film. Consequently, EBT's response is optimised by measurements with red light such as a Helium-Neon laser light source (633 nm).

The effective atomic number of EBT film is almost 7. This value is greater than that of HD-810 ($\sim$ 6.5) and also closer to that of water (7.3). The presence of a moderate Z element, chlorine, in EBT film may increase photoelectric absorption of low (< 50 keV) energy photons and this, according to the manufacturers, may explain why EBT film is not as energy dependent as other types of GafChromic radiochromic film at low energies.

At present, there is no published evidence of a dose rate dependent sensitivity effect with EBT film. The manufacturers however, cite unpublished observations and personal communications that there are no dose rate effects provided there is sufficient time allowed for polymerisation to occur (a few hours). The manufacturers have investigated the post-exposure density growth of EBT film and found it to be less than previous types of GafChromic films. ISP state that the growth, is "essentially complete by 2 hours post-exposure"(ISP, 2007b).

Many of the environmental considerations for handling HD-810 film also apply to EBT. EBT film can be handled in normal room light for several hours without any serious effects, although the film should be stored in dark conditions when not being handled, nor should it be exposed to direct sunlight. EBT film is not as temperature sensitive as HD-810 film and can withstand temperatures in excess of 70^0C for a few seconds without compromising the film. GafChromic films can also be immersed in water for maximum periods of 1 hour (Butson et al., 2003).

3.4.3 Microdensitometry

The traditional approach to densitometry is to use a small light source and detector and to translate the object being scanned. This approach was used in the present MRT

dosimetry research, and is described in detail in Chapter 4. Densitometry, according to Niroomand-Rad et al. (1998), consists of a light transmission measurement averaged over the area of the defining aperture of the light source, and also over the absorbance spectrum of the sample being measured, weighted by the wavelength spectrum of the light source and the efficiency of the light detector. The spatial resolution of such translational systems is governed by the size of the light source used and by the distance between successive measurements.

A more modern approach is to use a two-dimensional imaging system. In this method, a uniform light source illuminates the object being scanned and a position-sensitive detector, is used to measure light transmission from many points on the object simultaneously. The spatial resolution of the scan is determined by the pixel size of the detector. The great advantage of this method is the speed of measurement compared to the more traditional, stepped method. Many low-cost, desktop scanners have been used for GafChromic film densitometry in radiotherapy. However, microbeam radiation therapy (MRT) places far greater demands on spatial resolution and accurate intensity measurements than conventional radiotherapy. For these reasons, it was decided to use a microdensitometer (Joyce-Loebl 3CS, Gateshead, UK) which was made available to the School of Physics at Monash University by the Photography Department of the Royal Melbourne Institute of Technology, and is shown in figure 3.14.

The spatial resolution of an imaging system is typically quantified by the number of resolvable line pairs per mm. The light source size and the distance between successive readings will strongly influence the spatial resolution. For the densitometry work presented in this thesis, the limiting factor for determining spatial resolution is the microdensitometer, not the GafChromic film. ISP quote spatial resolutions of greater than 600 line pairs per mm for GafChromic film. The spatial resolution of the 3 CS microdensitometer was evaluated using a projector, line pair test pattern, as shown in figure 3.15. The Modulation Transfer Function (MTF) value was 81% at a spatial frequency of 20 line pairs/mm (Figure 3.16). For a perfect system, in the

Figure 3.14: Joyce-Loebl 3CS Microdensitometer. Photograph by Mr. Steve Morton, School of Physics, Monash University.

absence of noise, the relationship between the spatial frequency F, and the object width Δ, can be expressed as (Bushberg et al., 2001)

$$F = \frac{1}{2 \cdot \Delta}. \tag{3.18}$$

Therefore a square object of width Δ, can be thought of as corresponding to the spatial frequency given by equation 3.18. So ideal objects that are 25 μm wide correspond to a spatial frequency of 20 lp/mm (Bushberg et al., 2001) .

Lastly, one must consider environmental factors for accurate densitometry. Temperature is probably the most important factor when scanning GafChromic films and it is recommended not to subject the film to temperatures significantly above room temperature ($> 50^0$ C) because this can cause spurious changes in optical density readings. Long exposure to UV radiation from fluorescent lights should be minimised, according to the manufacturers, which includes light emitted from the densitometer itself.

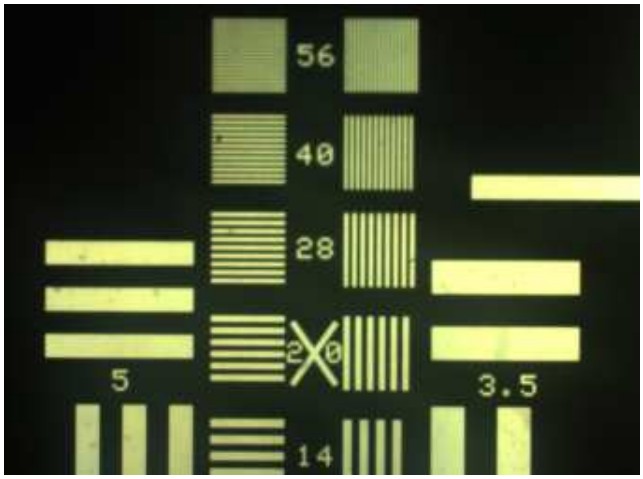

Figure 3.15: High resolution line pair test pattern

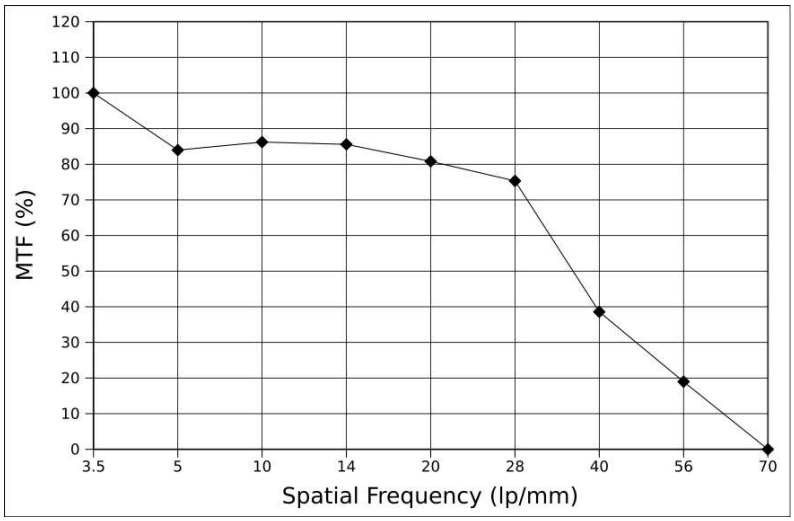

Figure 3.16: MTF for microdensitometer. The data were normalised to the 3.5 lp/mm test pattern

CHAPTER 4

A Method of Dosimetry for Synchrotron Microbeam Radiation Therapy using Radiochromic Films of Different Sensitivity

4.1 Introduction

This chapter reproduces in full, a paper published in the Journal *Physics in Medicine & Biology* (Crosbie et al., 2008). The paper contains its own bibliography, and reference styles, separate from the rest of the thesis. The figures appear at the end of the chapter, in the version presented in this thesis chapter. The published, electronic version of the paper is included at the back of the thesis, reproduced with the permission of Institute of Physics Publishing.

4.2 Declaration by Candidate for Thesis Chapter 4

In the case of Chapter 4, the nature and extent of my contribution to the work was the following: Conception, planning and study design, initiation & execution of experimental research, analysis and interpretation of the data, including statistical analysis, drafting and revising the submitted manuscript.

I estimate the extent of my contribution to this paper was 75%.

The following co-authors contributed to the work.

Name	Nature of Contribution
Dr. Imants Svalbe	Planning experiments & revising manuscript
Dr. Stewart Midgley	Technical assistance/advice on beamline & revising manuscript
Dr. Naoto Yagi	Technical assistance/advice on beamline & revising manuscript
Prof. Peter Rogers	Planning experiments & revising manuscript
Prof. Robert Lewis	Planning experiments & revising manuscript

Co-authors who are students at Monash University must also indicate the extent of their contribution in percentage terms. Since there were no other student co-authors on the paper (apart from myself, the candidate), this requirement is not applicable.

Candidate's Signature:

Date:

4.3 Declaration by Co-authors

The undersigned hereby certify that:

1. the above declaration correctly reflects the nature and extent of the candidate's contribution to this work, and the nature of the contribution of each of the co-authors.
2. they meet the criteria for authorship in that they have participated in the conception, execution, or interpretation, of at least that part of the publication in their field of expertise;
3. they take public responsibility for their part of the publication, except for the responsible author who accepts overall responsibility for the publication;
4. there are no other authors of the publication according to these criteria;
5. potential conflicts of interest have been disclosed to (a) granting bodies, (b) the editor or publisher of journals or other publications, and (c) the head of the responsible academic unit; and
6. the original data are stored at the following location(s) and will be held for at least five years from the date indicated below:

Location: School of Physics, Monash University, Clayton, VIC 3800, Australia

Name	Signature	Date
Imants Svalbe	[redacted]	03/12/08
Stewart Midgley	[redacted]	03/12/08
Peter Rogers	[redacted]	4/12/8
Robert Lewis	[redacted]	12-4-2008
Naoto Yagi	[redacted]	24/11/2008

4.4 Paper 1: A Method of Dosimetry for Synchrotron Microbeam Radiation Therapy using Radiochromic Films of Different Sensitivity

A method of dosimetry for synchrotron microbeam radiation therapy using radiochromic films of different sensitivity

J C Crosbie[1, 2, 5], I Svalbe[1], S M Midgley[1,2], N Yagi[3] , P A W Rogers[4] & R A Lewis[1, 2]

[1]School of Physics, [2]Monash Centre for Synchrotron Science, and [4]Monash Institute of Medical Research, Monash University, Melbourne, Victoria 3800, Australia.

[3]Japan Synchrotron Radiation Research Institute (SPring-8), Hyogo, 679-5198, Japan.

[5]The William Buckland Radiotherapy Centre, Alfred Hospital, Melbourne, Victoria 3004, Australia.

Running Title: Film Dosimetry for Synchrotron Microbeam Radiation Therapy

Address for Correspondence; Jeffrey Crosbie, School of Physics, Monash University, Clayton, VIC 3800, Australia, Ph: + 61 3 9905 8063, Fax: + 61 3 9905 3637

E-mail: Jeffrey.Crosbie@sci.monash.edu.au

Abstract

This paper describes a method of film dosimetry, used to measure the peak-to-valley dose ratios for synchrotron microbeam radiation therapy (MRT). Two types of radiochromic film (manufactured by International Specialty Products, NJ, USA) were irradiated in a phantom and also flush against a microbeam collimator (beam width 25 μm, centre-to-centre spacing 200 μm) on beamline BL28B2 at the SPring-8 synchrotron. Four experiments are reported; 1. The HD-810 and EBT varieties of radiochromic film were used to record 'peak' dose and 'valley' (regions in between peaks) dose respectively. 2. A stack of HD-810 film sheets was microbeam-irradiated and analysed to investigate a possible dose build-up effect. 3. A very high MRT dose was delivered to HD-810 film to elicit a measurable valley dose to compare with the result obtained using broad beam radiation. 4. The half value layer of the beam with and without the microbeam collimator was measured to investigate the effect of the collimator on the beam quality. The valley dose obtained for films placed flush against the collimator was approximately 0.2% of the peak dose. Within the water phantom, the valley dose had increased to between 0.7 – 1.8% of the peak dose, depending on the depth in the phantom. We also demonstrated, experimentally and by Monte Carlo simulation, that the dose is not maximal on the surface and that there is a dose build-up effect. The microbeam collimator did not make an appreciable difference to the beam quality. The values of peak-to-valley ratio reported in this paper are higher than those predicted by previously published Monte Carlo simulation papers.

Key words: Microbeam Radiation Therapy, Dosimetry, Radiochromic Film, Microdensitometry

PACS: 87.53.Bn

Published in Physics in Medicine & Biology

1. Introduction

In 1995, scientists at the Brookhaven National Laboratory, USA, reported on a novel form of radiation therapy (Slatkin *et al.*, 1995). This technique, known as microbeam radiation therapy, or MRT, delivered microplanar arrays of synchrotron-generated X-rays to the cerebellum of normal rats. The incident X-ray beam was segmented spatially by a collimator to create beam widths less than 40 μm and centre-to-centre spacings of 200 μm.

Synchrotron MRT has also been developed at the European Synchrotron Radiation Facility in Grenoble, France. A publication in 2001 by Laissue *et al.* reported the irradiation of the cerebellum of weaning piglets at the ESRF (Laissue *et al.*, 2001). Since 2005, a program of research into synchrotron microbeam radiation therapy (MRT) has been carried out by Japanese and Australian research groups at the SPring-8 synchrotron in Japan.

MRT has several peculiar and beguiling properties, which appear to challenge many of the current paradigms in conventional radiation therapy; normal tissue appears exceptionally resistant to hundreds of Grays of peak, in-beam MRT doses (Zhong *et al.*, 2003). In addition, malignant tissue mass appears to respond to MRT by significant growth delay and, in some cases, complete tumour ablation. This is despite the small fraction of the tumour mass irradiated with the high dose microbeams (Laissue *et al.*, 1998; Dilmanian *et al.*, 2002; Dilmanian *et al.*, 2003; Miura *et al.*, 2006). The ratio between dose in the peaks of the microbeams to the dose in the valleys between the microbeams has strong biological significance (Laissue *et al.*, 1998; Laissue *et al.*, 2001; Dilmanian *et al.*, 2003; Zhong *et al.*, 2003; Siegbahn *et al.*, 2006).

The optimal geometrical configuration or the optimal peak-to-valley dose ratio for successful MRT (maximal tumour control and minimal normal tissue toxicity) is not yet known. Moreover it is likely to vary depending on the tissue and cell types being irradiated. A number of different MRT studies have shown that tumour types experience growth delay when irradiated with peak doses ranging from 150 Gy to 884 Gy, with beam widths and spacings, ranging from 25 to 90 μm-wide beams and 50 to 300 μm spacings respectively. The tumours have included 9L gliosarcoma (Laissue et al., 1998, Dilmanian et al. 2002, Smilowitz et al., 2006), EMT-6.5 (Dilmanian et al. 2003) and SCCVII (Miura et al., 2006). In addition, tumour growth delay has been reported for uni-directional, bi-directional and cross-planar irradiations.

Synchrotron MRT poses several fundamental radiobiological challenges. It also poses dosimetric challenges due to the very high dose gradients (hundreds of Gray) over short distances (tens of μm). No current dosimeter can accurately measure simultaneously, the dose in the microbeam peaks and the dose in the valleys between the microbeams for the typical MRT energy range (50-250 keV). Consequently, the majority of publications pertaining to MRT dosimetry have relied on Monte Carlo simulations to model the radiation transport and dose deposition in water (Slatkin *et al.*, 1992; Company and Allen, 1998; Orion *et al.*, 2000; Stepanek *et al.*, 2000; De Felici *et al.*, 2005; Siegbahn *et al.*, 2006).

The one dosimeter that is perhaps best suited to the task is also one of the oldest; photographic film. The type of film used in this work is GafChromic radiochromic film, manufactured by ISP Technologies, New Jersey, USA. This is a relatively new type of film dosimeter that undergoes a dose proportional colour change upon exposure to X-radiation. Some of the more popular varieties of GafChromic

radiochromic film for dosimetric purposes include HD-810, MD-55 and more recently, EBT.

Radiochromic film dosimetry is an established technique in medical radiation physics. There are several review articles describing the properties and applications of radiochromic film dosimetry for clinical use (McLaughlin *et al.*, 1996; Niroomand-Rad *et al.*, 1998; Butson *et al.*, 2003; Soares, 2006). A Task Goup report (TG55) by the American Association of Physicists (AAPM), is perhaps the most comprehensive review of radiochromic film dosimetry available (Niroomand-Rad *et al.*, 1998).

Used individually for MRT dosimetry, neither HD-810 nor EBT film is particularly efficient at measuring peak dose and valley dose simultaneously. An accurate measure of dose across this range is unrealistic using a single film.

In this paper, we test the hypothesis that it is possible to irradiate parallel sheets of radiochromic films of different sensitivity, and record the peak doses with HD-810 film (low sensitivity) and the valley doses with the EBT film (high sensitivity). We also test the hypothesis that the dose is not maximal on the surface of a water phantom but builds up rapidly to a peak, tens of μm below the surface.

2. Materials & Methods

2.1 Synchrotron X-ray beam

All irradiations were carried out on beamline BL28B2 at the SPring-8 synchrotron, Hyogo, Japan (SPring-8, 2008). This beamline uses a bending magnet to produce polychromatic x-rays from 8 GeV electrons with a circulating beam current of approximately 100 mA. The synchrotron x-ray beam was filtered using a 3 mm thick copper filter to preferentially absorb low energy x-rays and hence increase its mean energy. The resulting X-ray beam spectrum had a mean energy of 125 keV (Ohno *et al.*, 2008). The energy spectrum of the filtered x-ray beam from the bending magnet on BL28B2 was simulated using the SPECTRA program (Tinaka and Kitamura, 2001) and is shown plotted on a log-log scale in Figure 1(a).

2.2 Free air ionization chamber beam monitor

The experimental dose from the incident beam was estimated by careful measurements of the ion current, recorded by a free-air ionisation chamber (OKEN S-1194, Tokyo, Japan) and compensating for the beam cross section. The charge recorded by the ionisation chamber was converted to exposure through the following relationship (Greening, 1985);

$$X = \frac{\Delta Q}{\rho \times A \times L} \times \frac{1}{2.58 \times 10^{-4}}\ Roentgens \qquad (1)$$

Where ΔQ is the charge collected in Coulombs, ρ is the density of air at standard temperature and pressure (kg/m^3), A is the cross-sectional area of the beam (m^2) and L is the length (m) of the collecting volume in the ionisation chamber. The relation 1R = 2.58×10^{-4}C/kg was used (Johns and Cunningham, 1983). No correction was made for ion recombination because the ion chamber was operating in the flat portion of the

efficiency saturation curve where the chamber collection efficiency is taken to be unity. Corrections were required for ambient temperature and pressure.

At this energy range we assume that the air kerma is composed almost entirely of its so-called collisional component, K_{col}, and is equivalent to dose in air (Khan, 2003). The air kerma is calculated from the following relationship;

$$K = \left(\frac{W}{e}\right) X \qquad (2)$$

Where W/e is the average energy required to produce an ion pair in dry air and has a value of 33.97 eV/ion pair (Khan, 2003).

2.3 Microbeam collimator

A fixed geometry tungsten/kapton multislit collimator was used to segment the broad beam into an array of planar microbeams. The incident X-ray beam is collimated by 175 μm thick planes of high-Z tungsten, spatially separated by 25 μm thick sheets of low density kapton, a type of plastic. The collimator design is described in greater detail by Ohno *et al. (Ohno et al., 2008)*. The thickness of the tungsten/kapton collimator in the direction of the beam was approximately 10mm. The nominal, collimated beam width was 25 μm with a centre-to-centre spacing of 200 μm. The exposure time was adjusted by varying the opening and closing time of an upstream shutter, which blocked the x-ray beam. The minimum opening time of the shutter was 100msec.

2.4 Radiochromic film dosimetry

Radiochromic film consists of monomer crystals in a gel bound to a mylar substrate. The monomer undergoes partial polymerisation upon irradiation which leads to a colour change from a light to a dark blue. The active component in GafChromic

radiochromic dosimetry films is a long chain fatty acid, similar to stearic acid and belonging to the diacetylene class of molecules (ISP, 2008). These films have different physical properties (thickness, composition, sensitivity) and respond over different dose ranges. The thickness of the HD-810 and EBT films are approximately 110 μm and 290 μm respectively.

The dose range for GafChromic HD-810 film is between 10 Gy and 400 Gy and below 250 Gy, the response of the film is essentially linear with dose (ISP, 2008). However, HD-810 can also be used at higher doses provided the results are interpreted with appropriate dose calibration curves. The TG55 report states that the nominal dose range of HD-810 is between 50-1000 Gy (Niroomand-Rad *et al.*, 1998). ISP state that EBT film is sensitive to doses in the range 0.01 Gy to 8 Gy (ISP, 2007) whereas Soares states that the useful range of EBT is from 0.05 Gy to-8 Gy (Soares, 2006). The sensitive material in radiochromic films is quite similar to water in terms of mass energy absorption coefficients and electron mass stopping powers (Niroomand-Rad *et al.*, 1998; Butson *et al.*, 2003).

Radiochromic film continues to 'develop' or polymerise for several hours post-exposure before reaching chemical completion and most practical radiochromic film analysis is done the day after exposure. ISP recommend waiting at least 24 hours post-irradiation before analysing HD-810 film and at least 6 hours before analysing EBT film. Post-exposure density growth curves for both films are available (ISP, 2007b, 2008). For other varieties of GafChromic film, slight increases (up to 4%) in the absorbance of MD-55 have been reported after 24 hours out to 2 weeks post-exposure and there have no appreciable changes in absorbance between 40 and 165 days post-exposure (Niroomand-Rad *et al.*, 1998).

The manufacturers state that HD-810 film is energy independent for photons with energies above about 200 keV (ISP, 2008). Muench *et al* showed the response of GafChromic HD-810 film decreased by approximately 30% when the effective photon energy decreased from 1720 keV (4 MV X-rays) to 28 keV (60 kVp X-rays) (Muench *et al.*, 1991). Considering our mean photon energy is 125 keV, any energy dependencies of the HD-810 film are sufficiently small to be ignored. The EBT film is essentially energy independent across all therapeutic energy ranges (Rink *et al.*, 2007).

2.4.1 Microdensitometry. After irradiation, the films were placed in aluminium foil (to exclude light) for transport to and analysis in Australia. Broadbeam and microbeam-irradiated films were scanned on a Joyce-Loebl microdensitometer (3CS Mark II, Joyce-Loebl, Gateshead, UK). The spatial resolution of GafChromic HD-810 radiochromic film is extremely high, better than 600 line pairs/mm (Niroomand-Rad *et al.*, 1998). The microdensitometer however is a more limiting factor for spatial resolution. We measured the microdensitometer's spatial resolution, using a line-pair test pattern and recorded a Modulation Transfer Function (MTF) value of 81% for a spatial frequency of 20 line pairs/mm, This corresponds to an object width of 25 μm, the nominal width of the microbeams.

The microdensitometer outputs a voltage, proportional to the optical density of the film, which we verified using a step-wedge film. We also independently checked the response of HD-810 film using a hand-held densitometer (data not shown). Calibration curves of absorbed voltage versus dose are shown in Figure 2 for both HD-810 (a) and EBT (b) films. Three scans were performed perpendicular to the microbeam direction across the centre and the two edges of the microbeams. The readings were then averaged across the three profiles to obtain a mean reading with

associated uncertainty (two times the standard error of the mean). The digitised voltage values from the MRT profiles were then converted to dose (in water) using the broad beam voltage-dose calibration curves. A quadratic curve was fitted to the data, a technique similar to that performed by commercial radiotherapy film dosimetry software packages.

2.5 Experiment 1 – Peak & valley dose measurements

The principal objective of the experiment was to measure the peak-to-valley dose ratio at the collimator and as a function of depth in a tissue equivalent, solid water phantom, downstream of the collimator. To this end, two parallel sheets of HD-810 and EBT radiochromic film were placed at various depths in the phantom and irradiated with an in-beam entrance dose of 160 Gy. Films were also positioned flush against the beam exit side of the collimator. The HD-810 films were placed in front of the EBT films. The experimental setup for the solid water phantom irradiations is shown schematically in Figure 3. The films were positioned between the solid water slabs at the surface and subsequently at 1 mm, 5 mm, 10 mm, 30 mm, 50 mm and 70 mm thickness.

A set of dose calibration films for the two film types were also acquired, in which known broad beam doses of synchrotron radiation were delivered to the HD-810 and EBT films. Calibration doses of between 20 Gy and 320 Gy were delivered to the HD-810 film and doses between 0.2 Gy and 6 Gy were delivered to the EBT film. The calibration films were placed at a depth of 1 mm in the solid water stack. The air kerma, corrected for ambient temperature and pressure, was converted to dose to water at 1 mm depth by multiplying the kerma by the ratio of the mass energy absorption coefficients for water and air. A simple exponential attenuation factor, to adjust the

dose for a depth of 1mm, was also applied.

It was necessary to attenuate the broad beam in order to accurately deliver calibration doses of less than 1 Gy to EBT film due to the limitations of the upstream lead shutter. The flux rate was attenuated by placing high purity, metallic absorbers (11.5 mm Cu, 1 mm Fe, 7 mm Al) in the path of the beam. The effect of beam hardening on the EBT calibration was considered negligible owing to the energy independence of EBT film (Rink *et al.*, 2007).

2.6 Experiment 2 – Investigation of the dose build-up effect

Preliminary film dosimetry work hinted at a dose build-up effect for the MRT beam. That is to say, the dose did not appear to be maximal on the surface. To further investigate this, a stack of thirty strips of HD-810 film, sandwiched together, was irradiated. This provided measurements of the relative dose distribution at 110 μm depth increments, instead of the 1000 μm (1 mm) increments of the thinnest solid water slab. The percentage depth dose curve of this polyenergetic X-ray beam was simulated using the GEANT4 Monte Carlo code (Agostinelli *et al.*, 2003).

The stack was irradiated at four locations; at the level of the collimator, in front of the ionisation chamber, at the sample stage and a further position, 1.1 metres downstream of the sample stage. Films were scanned on the microdensitometer in a manner similar to that described in Experiment 1.

2.7 Experiment 3 – Accurate valley dose measurements

A single piece of HD-810 film was irradiated with a peak MRT dose of 3000 Gy, as measured using the ionisation chamber. A separate piece of HD-810 film was irradiated with broad beam radiation across a range of dose values, chosen to be similar to the valley dose of the MRT-irradiated film. The purpose of this experiment

was to scale the valley dose up into the HD-810 film's sensitivity range. This acted as a 'cross check' of the EBT valley dose data. These films were scanned on the microdensitometer and a calibration curve of dose versus voltage (optical density) was generated from the broad beam films. This curve was used to estimate the dose in the valley region of the very high dose MRT film, based upon a microdensitometer scan of the valley region.

2.8 Experiment 4 - Measurement of beam quality

In order to determine whether the microbeam collimator changed the beam quality, we measured the first three Half Value Layers (HVL) for copper for (A) the beam transmitted through the microbeam collimator, (B) no microbeam collimator present and (C) the microbeam collimator and ion chamber placed beside each other. The predicted HVLs were obtained by analysis of the predicted primary beam energy spectrum (SPECTRA) .

3. Results

3.1 Experiment 1- Peak & valley dose measurements

A single broad beam, measuring 1 mm in the vertical plane, produced five horizontal microbeams after collimation. Figure 1(b) is a scan of HD-810 radiochromic film exposed to five such microbeams. An example of the one-dimensional dose profile is shown in figure 1(c). This is a sample line profile across the film and is typical of the profiles obtained on the microdensitometer. Note the low sensitivity of the film in the valley region despite the in-air, entrance peak dose of 160 Gy. The peak regions of HD-810 film showed an obvious, measurable change in optical density but the valley regions did not, the HD-810 film being insensitive to

doses below 10 Gy (ISP, 2008). The peak regions of the EBT film were saturated yet the valley regions showed a measurable change in optical density.

The percentage depth dose curves for both peak and valley dose are plotted in figure 4(a). The peak and valley doses were obtained from microdensitometry scans of the HD-810 & EBT films respectively for each depth in the phantom. The plots are normalised to the maximum peak dose, which was not maximal at the surface. There was a rapid build-up effect with the maximum peak dose observed at a depth of 1 mm (limit of solid water slab thickness). The typical exponential-like attenuation was observed beyond 1 mm. The variation in valley dose is not readily apparent from figure 4(a), since the profiles are normalised to the maximum peak dose. The valley dose increased slowly, to a maximum at a depth of 10 mm in water, and then decreased slowly with depth. A similar variation in peak and valley doses, computed by Monte Carlo simulations, was reported by Siegbahn *et al.* (Siegbahn *et al.*, 2006).

The variation in peak-to-valley dose ratio (PVDR) with depth in the solid water phantom is shown in figure 4(b). This is a dimensionless quantity, and in these results, the uncertainty in PVDR is expressed as a percentage of that ratio. The PVDR on the surface of the phantom was 65 ± 35%. It then increased to a maximum, mean PVDR of 144 ± 29%, at a depth of 1 mm. The PVDRs then decreased with depth down to 10 mm and were then observed to be rather stable; 67 ± 27% at 10 mm, 76 ± 26% at 30 mm and 60 ± 29% at 50 mm depth.

The mean PVDR at 70 mm depth was 85±18%. The peak-to-valley dose ratio for the films placed flush against the collimator was 388 ± 21%. The uncertainty in PVDR was calculated by expressing the uncertainties in peak and valley dose as a percentage and summing them in quadrature according to equation (3) below. The PVDR uncertainty is dominated by that of the valley dose.

$$\delta_{PVDR} = \sqrt{(\delta_{peak})^2 + (\delta_{valley})^2} \qquad (3)$$

Closer inspection of the percentage depth dose curve for the peak doses (as measured with HD-810 film) showed a distinct build-up effect. The dose was not maximal on the surface, but rather at a depth of 1mm in solid water, the thinnest slab. This is the dose 'build-up' effect; dose depositing secondary electrons are set in motion when an X-ray photon beam bombards a medium (Johns and Cunningham, 1983; Khan, 2003). This build-up effect explains the large differences between the PVDR recorded on the surface and the PVDR recorded at a depth of 1 mm.

The Monte Carlo simulated depth dose curve also reproduces this build-up effect. The measured and simulated depth dose curves are shown superimposed in figure 5(a). The experimental film data were normalised to the maximum value at 1 mm depth. The Monte Carlo simulated depth dose curve was performed using a 100 µm step size and was normalised to the peak dose. The simulation was performed in liquid water. At a depth of 100 µm, the simulated depth dose curve was already 95% of its maximum dose. Figure 5(b) shows a Monte Carlo depth dose simulation using 1 µm step sizes. This plot shows the dose builds up very rapidly, approaching its maximum value after only 20 µm. There are fluctuations in the simulated data which make it difficult to quote a precise value of the depth of maximum dose other than to say the dose is not maximal on the surface but builds up rapidly after a depth of some

tens of μm. At the depth of 10 mm, the agreement between experiment and simulation is not as strong as at the other depths in figure 5(a). The experimental uncertainty in the film data is the most likely explanation for the difference.

3.2 Experiment 2 – Investigation of a dose build-up effect

Figure 5(c) shows the percentage depth dose curve in the thirty film stack of HD-810 films. These films were irradiated at the level of the free-air ionisation chamber, situated approximately 400 mm downstream of the collimator. The combined thickness of the sandwich was 3.3 mm (or 3300 μm) since each film was approximately 110 μm thick. At all four irradiation positions, the relative surface dose (first film in the sandwich) was significantly less than the relative dose recorded from the second film, approximately 110 μm deep in the sandwich. The GEANT4 Monte Carlo simulated depth dose from Figure 4a is included in figure 5(c) for comparison. The film sandwich experiment confirmed that the dose was not maximal on the surface.

There was quite a degree of experimental uncertainty (expressed as two times the standard error of the mean) in the film data presented in figure 5(c). In addition, the experimental curve was arbitrarily normalised to the second film at a depth of 110 μm. The Monte Carlo simulation of depth dose is the same curve from (a) albeit at a shallower depth, and the simulation was carried out in liquid water and not film material.

3.3 Experiment 3 – Accurate measurement of valley doses

Figure 6 shows a colour comparison on HD-810 film between a broad beam entrance dose of 47.8 Gy and the valley region of HD-810 film, irradiated with a peak, MRT dose of 3000 Gy. The optical density in the valley region was qualitatively

comparable to that of the broad beam. The dose in the valley region of the MRT-irradiated film was found to be 56 ± 4 Gy, after scanning with the microdensitometer and converting to dose using the equation of fit. An extrapolation was required from the equation of fit as the maximum broad beam dose delivered was 47.8 Gy. The 'colour change', i.e. optical density (dose) in the valley region of the MRT-irradiated film was greater than in the broad beam film. The peak-to-valley dose ratio from this experiment was 55 ± 9%. This value is comparable to the lower end of PVDRs obtained in experiment 1 (Figure 4(b)). The uncertainty in PVDR was lower in this experiment than in experiment 1, most likely a result of stronger signal-to-noise ratio from the HD-810 film scans using the 'colour change' method.

3.4 Beam quality measurements

The beam quality, as measured by successive half value layers, of both the beam transmitted by the microbeam collimator and the broad beam were very similar and in good agreement with the predictions from the SPECTRA program. The HVL measurements and predictions are summarised in Table 1.

HVL	**A (mm Cu)**	**B (mm Cu)**	**C (mm Cu)**	**Predicted (mm Cu)**
1	0.198	0.200	0.198	0.198
2	0.243	0.240	0.245	0.246
3	0.270	0.283	0.290	0.290

Table 1. Half Value Layer (HVL) measurements of X-ray beam transmitted through microbeam collimator (A), with the collimator removed (B) and with the ion chamber close to the collimator (C). The predicted HVLs are also shown.

We calculated the photon flux rate to be 1.96 x 10^{12} and 2.44 x 10^{12} ph/s/mm^2 with and without the microbeam collimator. The 10 mm of kapton attenuates the flux rate by approximately 20%. The air kerma rate, as measured by the free-air ion chamber, for the microbeam and broadbeam conditions was approximately 85 Gy/s and 105 Gy/s respectively.

4. Discussion

Our results demonstrate that it is possible to use radiochromic films of different sensitivities to record the peak-to-valley dose ratio for synchrotron MRT and to track PVDR changes at various depths in a water phantom. The peak-to-valley dose ratio obtained for films placed flush against the collimator was almost 400. Combining the solid water phantom (experiment 1) and 'colour change' (experiment 3) data, a peak-to-valley dose ratio of between 145 and 55 was recorded, depending on the depth in the phantom.

It has also been demonstrated, both experimentally and by computer simulation that the dose is not maximal on the surface but builds up rapidly with depth after distances of some tens of μm. Other authors have shown a build-up effect via Monte Carlo simulation (Siegbahn *et al.*, 2006). Considering the dose builds up so rapidly with depth, over a distance of two or three cell diameters, it may not have a significant implication for MRT studies in biological tissue.

A distinct advantage to radiochromic film is its ease of use as a dosimeter. Other MRT dosimetry techniques have reported difficulties. For example, the alignment and stability concerns of MOSFET (Metal Oxide Semiconductor Field Effect Transistor) detectors (Brauer-Krisch *et al.*, 2003) do not apply to film. The combination of radiochromic film and microdensitometer provides sufficient spatial

resolution for the measurements (section 2.4.1). We emphasise that the results obtained here are of real measurements and not simulated doses. It is important for MRT to have measurement-based dosimetry which can be used to benchmark computer simulations. The results presented here were for a fixed-geometry, multi-slit collimator, but it should be possible to use the same technique on a variable width collimator, such as the collimators used at the National Synchrotron Light Source in the USA and at the ESRF in France.

The PVDR obtained for films placed flush against the collimator was significantly greater than the PVDRs in the solid water phantom (Figure 4(b)). The sample stage for the phantom was approximately 1 metre downstream of the collimator. The biggest difference between the collimator films and the phantom films was the dose in the valley region. The valley dose was observed to increase from approximately 0.2% of the peak dose at the level of the collimator, to approximately 2% of the peak dose in the water phantom.

It is possible there occurs angular, multiple scattering and reflection of the x-ray beam from the tungsten/kapton borders into the valley regions, immediately beyond the collimator. This is illustrated schematically in Figure 7. Scattered photons and characteristic radiation from tungsten may be generated inside the collimator as the incident X-ray beam is collimated by 175 μm thick planes of high-Z tungsten, spatially separated by 25 μm thick sheets of low density plastic. Our HVL data (Table 1) obtained in the presence of and in the absence of the microbeam collimator were very similar, indicating that the microbeam collimator is not in fact producing significant amounts of secondary radiation. The microbeams from a collimator are not perfectly precise; they possess ‘tails’ of valley dose, which may contribute dose to adjacent microbeams.

The interaction of the incident X-rays with the tungsten/kapton collimator and the propagation of the segmented microbeams through air, prior to reaching the target, requires more detailed modelling and measurement. A more realistic simulation, for example, would be to model a 25 μm thick sheet of kapton, sandwiched between two tungsten plates, and also to model a 'detector' of variable thickness and distance from the collimator face. The detector material could be more accurately modelled as film using the relative elemental constituents rather than simply liquid water

The ‘colour change’ experiment on the HD-810 film (Figure 6) provides convincing evidence that the dose in the valley region is between 1 and 2% of the peak dose, as observed at the level of the sample stage. Most of the Monte-Carlo simulated PVDRs (for microplanar beams) published in the literature are lower than those reported in this paper. We obtained a maximum PVDR of 144 ± 29% at 1 mm depth in water and a minimum PVDR of 60 ± 29% at 50 mm depth. The Monte Carlo papers of Siegbahn *et al.*, De Felici *et al.*, Stepanek *et al.* and Slatkin *et al.* report PVDRs closer to 30. That is, a valley dose which is approximately 3% of the peak dose. In general, the literature on Monte Carlo simulations of MRT is rather consistent; the different radiation transport codes produce PVDRs which agree with each other reasonably well.

Table 2 lists the PVDR reported by a sample of authors in articles on MRT dosimetry, which used Monte Carlo simulations. In the tabulated references, the quoted PVDR was for 25 μm wide beams at 200 μm centre-to-centre separations.

Author	Code	PVDR	Depth/cm
Slatkin *et al.,* 1992	CPE	35 15	0 – 1 7 - 8
(Stepanek *et al.*, 2000)	PSI-GEANT	29 (centre of field) 44 (field edge)	0 - 1
*(*De Felici *et al., 2005)*	EGS4	29 (centre of field) 33 (field edge)	7 – 8
(Brauer-Krisch *et al.*, 2005)	Penelope	53	0 – 1 in PMMA
(Siegbahn *et al.*, 2006)	Penelope	29 14	0 – 1 7 - 8

Table 1. The Monte Carlo simulated peak-to-valley dose ratios as reported by a selection of authors for a 25 μm wide beam with a 200 μm wide centre-to-centre separation.

The Monte Carlo simulations do not fully simulate the synchrotron X-ray source or downstream features such as slits. Perhaps the major shortcoming of the simulations is that they do not actually simulate a collimator. Multiple, planar microbeams have been simulated as individual microbeams, propagating through a phantom and then positioned at 200 μm intervals. As a consequence, multiple, angular scattering events occurring inside and immediately beyond the collimator (illustrated schematically in Figure 7), have not been adequately modelled.

In one publication (Siegbahn *et al.*, 2006), the X-ray source is assumed to originate on the surface of the water phantom, neglecting the effect of scatter into the valley region within the collimator, immediately post-collimator and pre-water

phantom. Slight manufacturing imperfections (on a μm scale) in a real collimator will also affect the PVDR but would be difficult to simulate.

There is a paucity of synchrotron MRT studies with the emphasis on experimentally obtained data. An exception being MOSFET dosimetry for planar microbeams as described by Brauer-Krisch *et al.* The authors reported a measured PVDR of approximately 60 using MOSFET dosimetry averaged across different depths in a PMMA phantom (Brauer-Krisch *et al.*, 2003). This value is closer to our experimentally derived PVDRs than the Monte Carlo simulation data.

In general, film is not used for absolute dosimetry purposes in radiotherapy but rather for relative dosimetry. An ionisation chamber at different depths in water would be the preferred dosimeter, but ultimately an alternative dosimeter may be required. Whereas ionisation chamber dosimetry can give an estimate of the dose in the peaks, there is no easy way to measure the dose in the valley region. From a radiobiological standpoint, being able to quantify the peak dose to within an accuracy of 3% may not be so critical when delivering hundreds of Gray of radiation, since it is already a lethal dose to the irradiated cells. Accurate measurement of the valley dose on the other hand, is essential, as this may be the limiting biological factor in MRT (Laissue *et al.*, 1998; Laissue *et al.*, 2001; Dilmanian *et al.*, 2003; Zhong *et al.*, 2003; Siegbahn *et al.*, 2006).

Trying to simultaneously measure the peak and valley doses, to obtain the PVDR, has proven difficult, until now. The strength of our paper lies in a simple and straightforward way to measure the PVDR for synchrotron MRT. A distinct advantage to the technique described in this paper is that one can measure fine spatial variations in the dose distribution within a bulk material. The MOSFET technique, as well as in-air ion chambers typically only measure entrance dose distributions at a point. Inside a

material, a significant contribution from scattered x-rays comes from all directions. Film is probably the only way to measure this.

Acknowledgements

We thank the reviewers of this article for helpful comments and suggestions which have been incorporated into the text. The authors thank the following individuals for their assistance with this study; Dr. Marian Cholewa, Dr. Toby Beveridge and Dr. John Gillam, Monash Centre for Synchrotron Science, Monash University, Mr. Steve Morton and Mr. Peter Oliver, School of Physics, Monash University, Dr. Duncan Butler, Australian Radiation Protection and Nuclear Safety Agency, Dr. David Lewis, ISP, New Jersey, USA and Mr. Andrew Campbell, Royal Perth Hospital, Western Australia. The authors have received funding from the following agencies; Cancer Council Victoria Venture Grant to PAWR, RAL & IS, Australian Nuclear Science and Technology Organisation (ANSTO) travel grants to JCC & PAWR, Monash University postgraduate scholarship to JCC, National Health and Medical Research Council of Australia (Fellowship Grant Number 143805) to PAWR.

The authors declare that conflicts of interest do not exist.

References

Agostinelli S, et al. 2003 G4--a simulation toolkit *Nuclear Instruments and Methods in Physics Research Section A: Accelerators, Spectrometers, Detectors and Associated Equipment* **506** 250-303

Brauer-Krisch E, Bravin A, Lerch M, Rosenfeld A, Stepanek J, Di Michiel M and Laissue J A 2003 MOSFET dosimetry for microbeam radiation therapy at the European Synchrotron Radiation Facility *Med Phys* **30** 583-9

Brauer-Krisch E, et al. 2005 New irradiation geometry for microbeam radiation therapy *Phys Med Biol* **50** 3103-11

Butson M J, Yu P K N, Cheung T and Metcalfe P 2003 Radiochromic film for medical radiation dosimetry *Materials Science and Engineering: R: Reports* **41** 61-120

Company F Z and Allen B J 1998 Calculation of microplanar beam dose profiles in a tissue/lung/tissue phantom *Phys Med Biol* **43** 2491-501

De Felici M, Felici R, Sanchez del Rio M, Ferrero C, Bacarian T and Dilmanian F A 2005 Dose distribution from x-ray microbeam arrays applied to radiation therapy: an EGS4 Monte Carlo study *Med Phys* **32** 2455-63

Dilmanian F A, et al. 2002 Response of rat intracranial 9L gliosarcoma to microbeam radiation therapy *Neuro-oncol* **4** 26-38

Dilmanian F A, Morris G M, Zhong N, Bacarian T, Hainfeld J F, Kalef-Ezra J, Brewington L J, Tammam J and Rosen E M 2003 Murine EMT-6 carcinoma: high therapeutic efficacy of microbeam radiation therapy *Radiat Res* **159** 632-41

Greening J R 1985 *Fundamentals of Radiation Dosimetry*: Taylor & Francis)

ISP 2007 GafChromic EBT Product Brief ISP Technologies http://online1.ispcorp.com/_layouts/Gafchromic/index.html

ISP 2007b GafChromic EBT, Self developing film for radiotherapy dosimetry ISP Technologies http://online1.ispcorp.com/_layouts/Gafchromic/index.html

ISP 2008 GAFCHROMIC HD-810 radiochromic dosimetry film and D-200 pre-formatted dosimeters for high energy photons. Configuration, specifications and performance data International Specialty Products (ISP) Technologies http://online1.ispcorp.com/_layouts/Gafchromic/index.html

Johns H E and Cunningham J R 1983 *The Physics of Radiology,* (Springfield, Illinois, USA: Charles C Thomas)

Khan F M 2003 *The Physics of Radiation Therapy*: Lippincott Williams & Wilkins)

Laissue J A, Blattmann H, Di Michiel M, Slatkin D N, Lyubimova N and Guzman R 2001 The weaning piglet cerebellum: a surrogate for tolerance to MRT (microbeam radiation therapy) in paediatric neuro-oncology. *Proc. SPIE, Penetrating radiation systems & applications III* **4508** 65-73

Laissue J A, et al. 1998 Neuropathology of ablation of rat gliosarcomas and contiguous brain tissues using a microplanar beam of synchrotron-wiggler-generated X rays *Int J Cancer* **78** 654-60

McLaughlin W L, Puhl J M, Al-Sheikhly M, Christou C A, Miller A, Kovács A, Wojnarovits L and Lewis D F 1996 Novel Radiochromic Films for Clinical Dosimetry *Radiat Prot Dosimetry* **66** 263-8

Miura M, Blattmann H, Brauer-Krisch E, Bravin A, Hanson A L, Nawrocky M M, Micca P L, Slatkin D N and Laissue J A 2006 Radiosurgical palliation of aggressive murine SCCVII squamous cell carcinomas using synchrotron-generated X-ray microbeams *Br J Radiol* **79** 71-5

Muench P J, Meigooni A S, Nath R and McLaughlin W L 1991 Photon energy dependence of the sensitivity of radiochromic film and comparison with silver

halide film and LiF TLDs used for brachytherapy dosimetry *Med Phys* **18** 769-75

Niroomand-Rad A, et al. 1998 Radiochromic film dosimetry: recommendations of AAPM Radiation Therapy Committee Task Group 55. American Association of Physicists in Medicine *Med Phys* **25** 2093-115

Ohno Y, Torikoshi M, Suzuki M, Umetani K, Imai Y, Uesugi K and Yagi N 2008 Dose distribution of a 125 keV mean energy microplanar x-ray beam for basic studies on microbeam radiotherapy *Med Phys* **35** 3252-8

Orion I, Rosenfeld A B, Dilmanian F A, Telang F, Ren B and Namito Y 2000 Monte Carlo simulation of dose distributions from a synchrotron-produced microplanar beam array using the EGS4 code system *Phys Med Biol* **45** 2497-508

Rink A, Vitkin I A and Jaffray D A 2007 Energy dependence (75 kVp to 18 MV) of radiochromic films assessed using a real-time optical dosimeter *Med Phys* **34** 458-63

Siegbahn E A, Stepanek J, Brauer-Krisch E and Bravin A 2006 Determination of dosimetrical quantities used in microbeam radiation therapy (MRT) with Monte Carlo simulations *Med Phys* **33** 3248-59

Slatkin D N, Spanne P, Dilmanian F A, Gebbers J O and Laissue J A 1995 Subacute neuropathological effects of microplanar beams of x-rays from a synchrotron wiggler *Proc Natl Acad Sci U S A* **92** 8783-7

Slatkin D N, Spanne P, Dilmanian F A and Sandborg M 1992 Microbeam radiation therapy *Med Phys* **19** 1395-400

Soares C G 2006 New developments in radiochromic film dosimetry *Radiat Prot Dosimetry* **120** 100-6

SPring-8 2008 http://www.spring8.or.jp/wkg/BL28B2/instrument/lang-en/INS-0000000374/instrument_summary_view?q=BEwH&f=

Stepanek J, Blattmann H, Laissue J A, Lyubimova N, Di Michiel M and Slatkin D N 2000 Physics study of microbeam radiation therapy with PSI-version of Monte Carlo code GEANT as a new computational tool *Med Phys* **27** 1664-75

Tinaka T and Kitamura H 2001 SPECTRA: a synchrotron radiation calculation code *J Synch Rad* **8** 1221-8

Zhong N, Morris G M, Bacarian T, Rosen E M and Dilmanian F A 2003 Response of rat skin to high-dose unidirectional x-ray microbeams: a histological study *Radiat Res* **160** 133-42

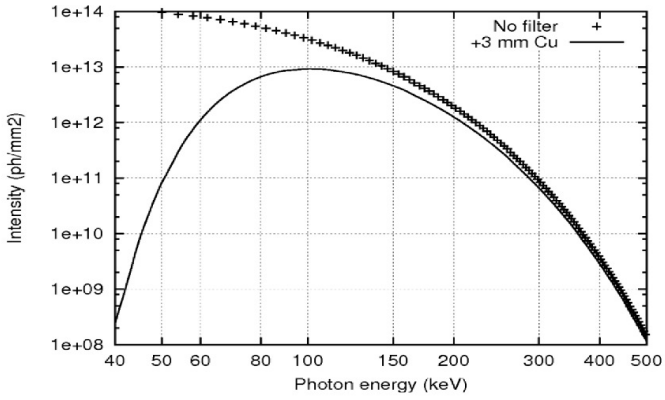

(a)

(b)

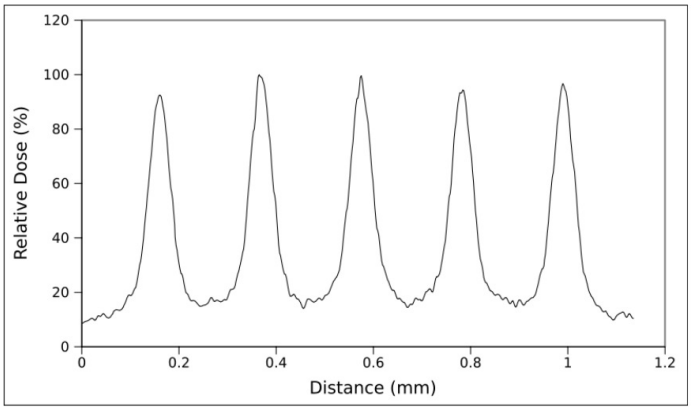

(c)

Figure 1. The energy spectrum (a) of the polychromatic x-ray beam produced by the bending magnet source for beamline BL28B2 at SPring-8. The spectrum was estimated using the SPECTRA computer program of Tanaka and Kitamura. A section of radiochromic film which has been exposed to MRT is shown in (b) and a line profile is shown in (c). The 1 mm high beam contains 5 microbeams, each one spaced 200

µm from its neighbour.

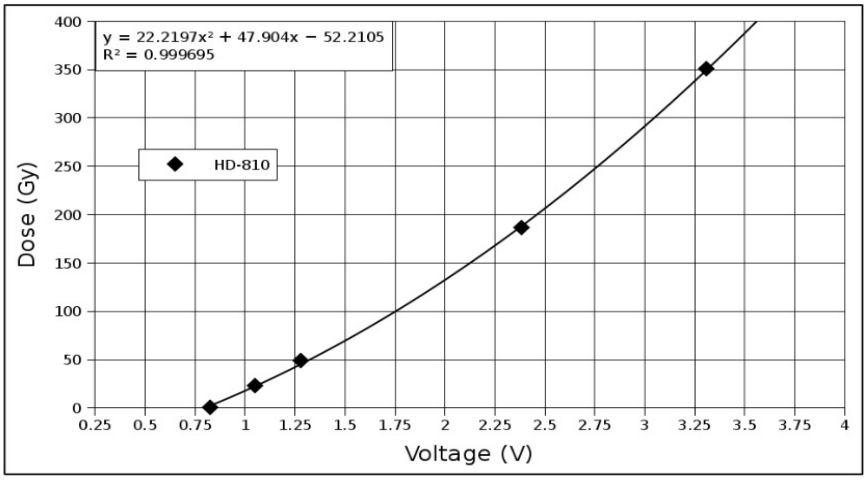

(a)

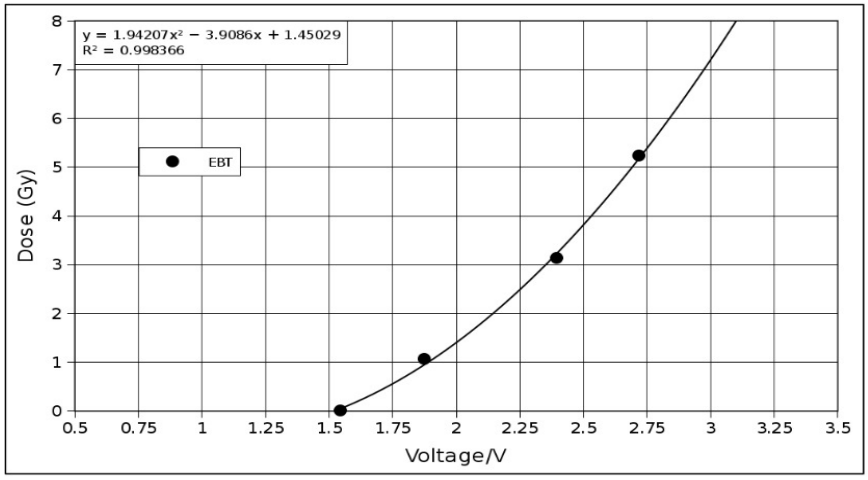

(b)

Figure 2. Typical voltage-dose calibration curves for high dose, low sensitivity HD-810 film (a) and low dose, high sensitivity EBT film (b) film subjected to broad beam radiation and analysis based upon microdensitometer scans.

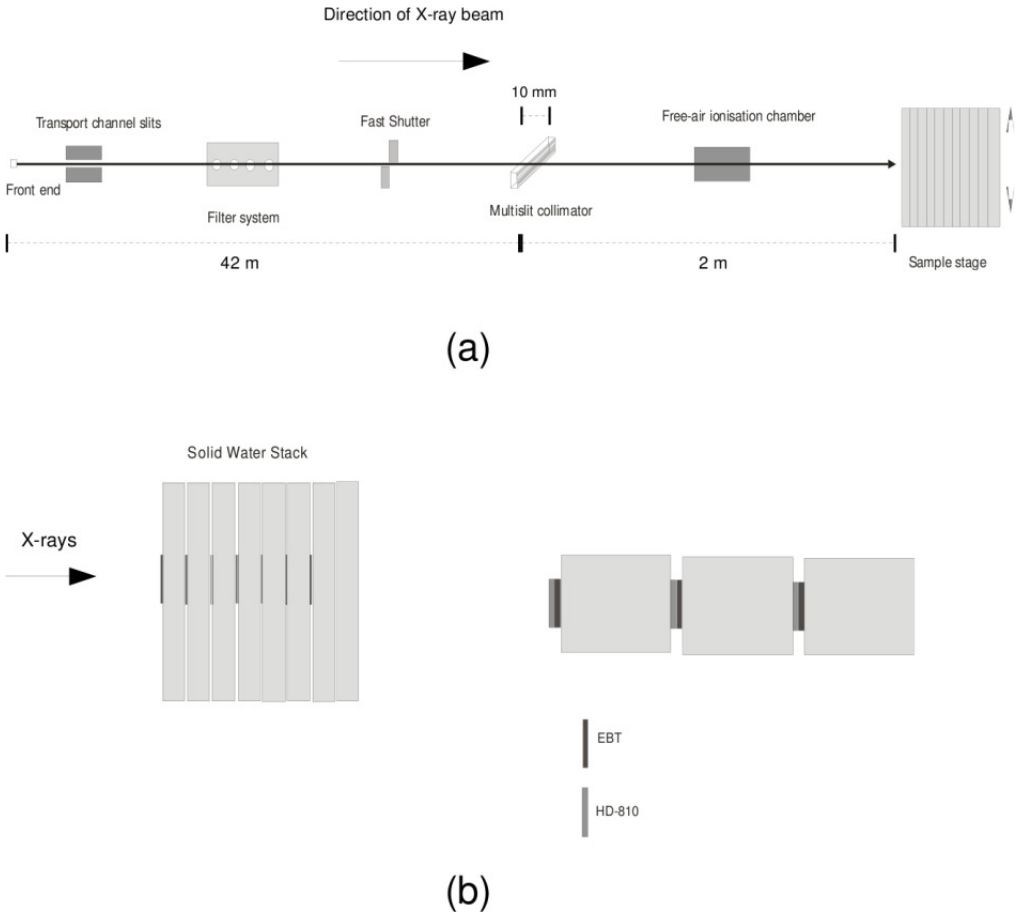

Figure 3. (a) Schematic of apparatus on beamline BL28B2 at SPring-8 for MRT film dosimetry. Figure 3(b) shows the stack of solid water slabs and sandwiched radiochromic films Each solid water slab measured 300 mm x 300 mm x 10 mm.

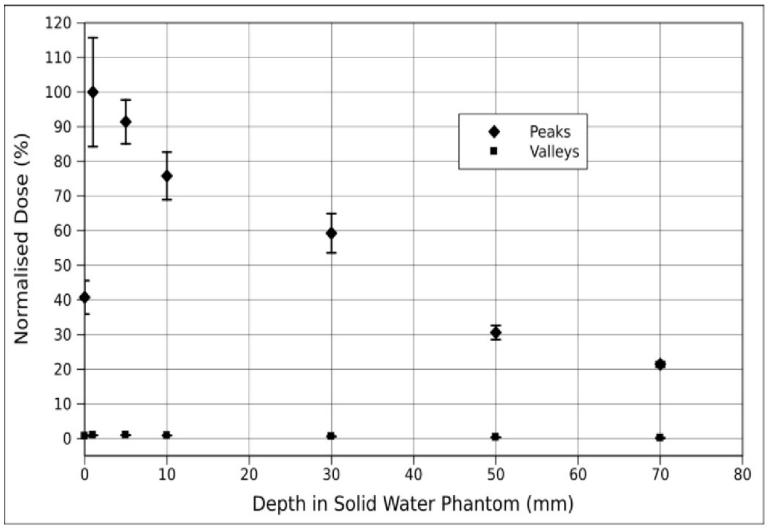

(a)

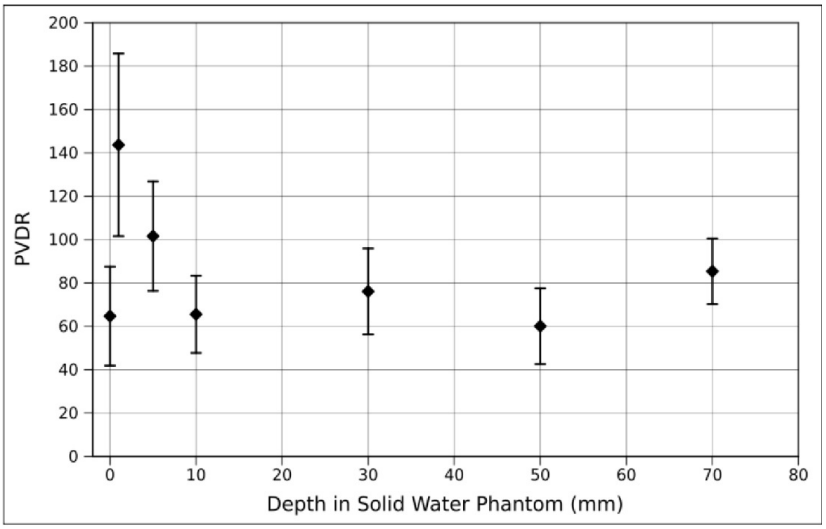

(b)

Figure 4. (a) Measured peak and valley dose at various depths in a water phantom, normalized to the peak dose at 1 mm depth. The uncertainties (error bars) represent two times the standard error of the mean across the left, centre and right sides of the film. Plot 4(b) shows the change in peak-to-valley dose ratio (PVDR) with depth. The data points were obtained by dividing the mean peak dose by the mean valley dose. The uncertainties (error bars) represent the uncertainty in peak dose plus the uncertainty in valley dose summed in quadrature.

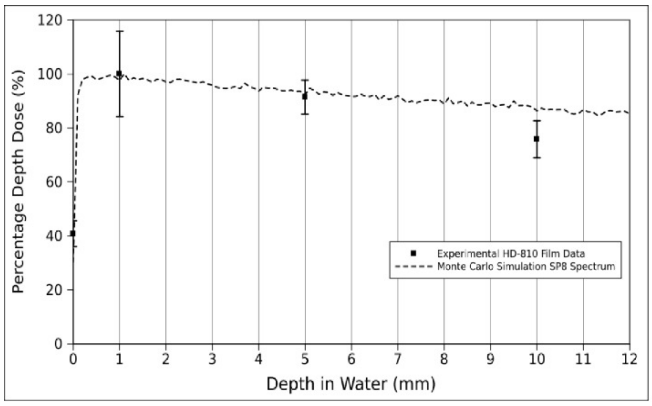

(a)

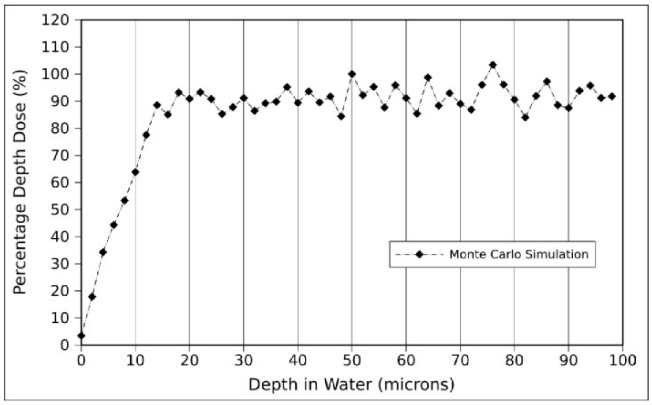

(b)

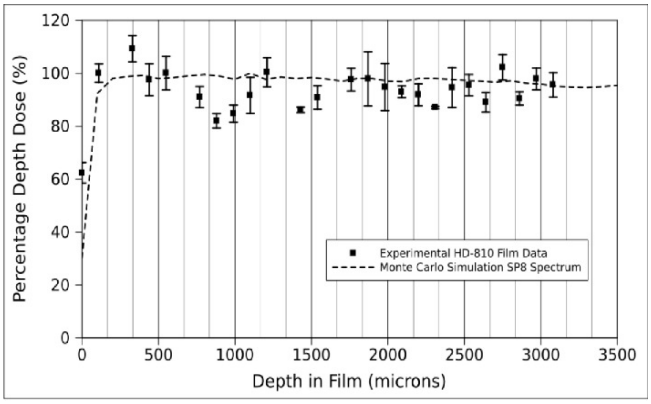

(c)

Figure 5. Percentage depth dose measurements compared against Monte Carlo simulations; (a) coarse measurements every 5 mm in solid water, (b) Monte Carlo depth dose simulations using a fine 1 µm step and (c) fine measurements every 110 µm in a stack of HD-810 films.

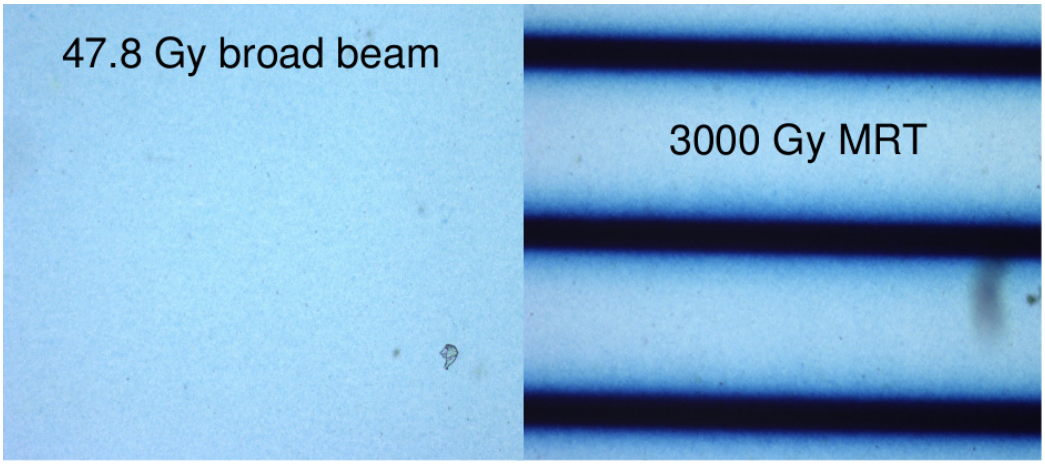

Figure 6. A visual comparison of HD-810 film exposed to 47.8 Gy of broad beam radiation (left-hand side) and HD-810 film exposed to MRT with an in-beam, peak dose of 3000 Gy (right-hand side). The change in optical density (proportional to dose) elicited in the valley region of the MRT-irradiated film is comparable to the change in optical density in the broad beam-irradiated film.

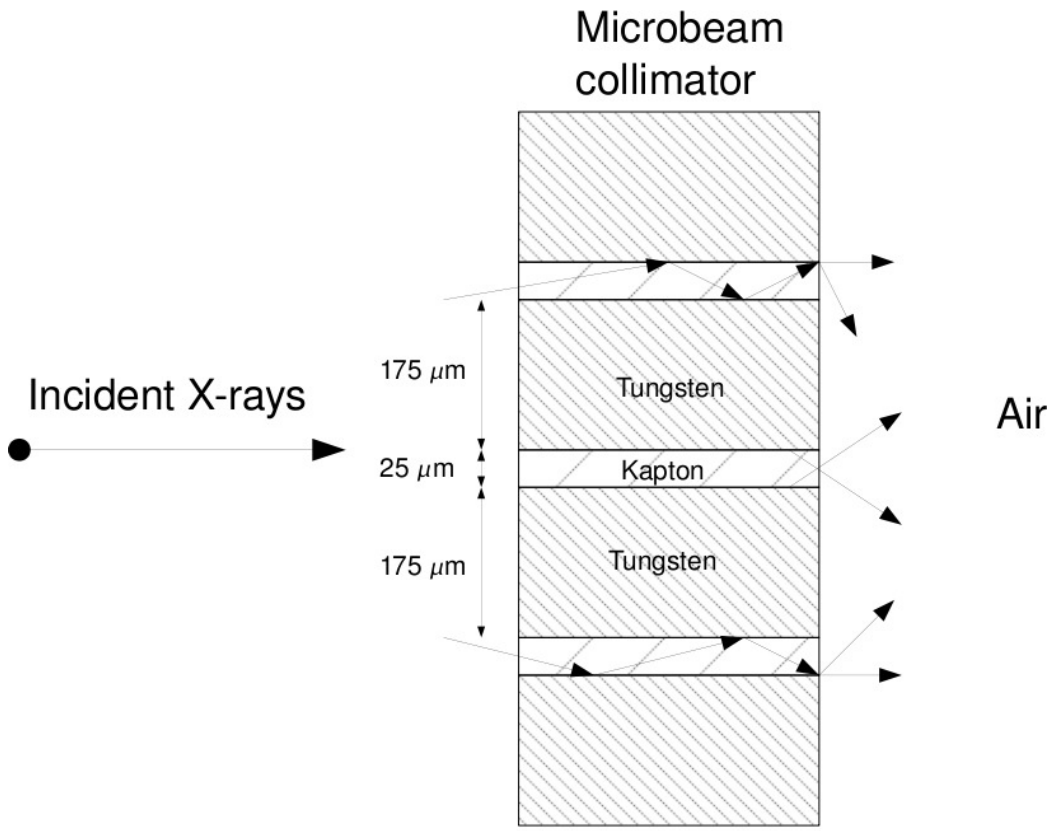

Figure 7. Schematic diagram of tungsten/kapton collimator at SPring-8, illustrating the potential for the collimator to produce secondary radiation (e.g. scattered photons and tungsten characteristic radiation).

CHAPTER 5

The Search for Immunohistochemical Markers for MRT

This chapter is written in the style of a scientific paper. It is envisaged that significant portions of this chapter will be submitted to a peer-reviewed journal for publication, hence it has been prepared in a pre-submission form.

5.1 Introduction

Synchrotron microbeam radiation therapy (MRT) is an experimental treatment which has been performed in a number of pre-clinical studies on tumour-bearing rodents (Laissue et al., 1998; Dilmanian et al., 2002, 2003; Miura et al., 2006). The high flux, X-ray beam from a synchrotron is segmented into micro-planar arrays of very narrow beams, typically 25 μm wide, with peak-to-peak separations of 200 μm. Normal tissue appears exceptionally resistant when hundreds of Grays of peak, in-beam dose are delivered by MRT (Zhong et al., 2003). Such doses are an order of magnitude more than are delivered during conventional radiotherapy. Furthermore, MRT has been shown to cause significant tumour growth delay and in some cases complete

tumour ablation (Laissue et al., 1998).

It is not known why normal tissues can tolerate such high doses of microplanar-delivered radiation, nor is it known how tumours respond to MRT when only a fraction of the tumour volume is irradiated. Clearly, the radiobiological response of tissue, at a cellular level, to MRT is of interest. Knowledge of such tolerance and repair mechanisms may inform current radiotherapy paradigms and dramatically alter the existing treatment regimens used for tumour control.

Using conventional histology, it is not possible to determine where the microbeams traversed most tissues. The distinctive stripes of radiation damage to neural cells in the cerebellum, as reported by Laissue et al. (1998) and others, are not observed in skin using conventional histological methods. This was noted by Zhong et al. (2003) in their histological investigation of the effects of MRT on rat skin. This causes difficulties when trying to describe, at a cellular level, the effect of MRT on skin tissue, especially in the acute stages (hours and days) following MRT.

The aim of this study was to identify an immunohistochemical marker of MRT which would allow us to visualise the path of the microbeams through the tissues in the hours and days following irradiation. Four assays in particular were of interest (apart from routine H & E). These were immunohistochemical assays of DNA double strand breaks (γ-H2AX), leukocytic infiltration (indicative of radiation-induced inflammation), proliferation (associated with tissue repair), and radiation-induced apoptosis (a mechanism of cell death). The hypothesis tested was that the ionising energy deposited in skin tissue by MRT would cause spatially localised regions of DNA double strand breaks, leukocytic infiltration, proliferation, and apoptosis.

5.2 Materials & Methods

5.2.1 Synchrotron radiation source & microbeam generation

All irradiations were carried out on beamline BL28B2 at the SPring-8 synchrotron, Hyogo, Japan. This beamline utilises a bending magnet to produce polychromatic

x-rays from electrons travelling at relativistic speeds around a storage ring with energies of 8 GeV and a stable beam current of approximately 100 mA. The synchrotron x-ray beam was filtered by passing through a 3 mm thick copper filter that preferentially absorbs low energy x-rays and hence increases its mean energy. The resulting x-ray beam had a mean energy of 125 keV (Ohno et al., 2008). A fixed geometry, tungsten/kapton collimator was used to segment the broad beam into an array of planar microbeams. The collimator design is described in more detail elsewhere (Ohno et al., 2008). The thickness of the tungsten/kapton collimator in the direction of the beam was approximately 10mm. The nominal beam width was 25 μm, with a centre-to-centre spacing of 200 μm. The peak-to-valley dose ratio for this collimator was measured using radiochromic films of different sensitivity. In a solid water phantom, the dose in the valley region is typically between 1 and 2 percent of the dose in the peaks. A complete description of the dosimetry employed for this MRT research is described in Chapter 4 of the thesis.

5.2.2 Mouse Preparation

The dorsal skin flap of normal mice was selected as an appropriate target because it is accessible tissue and is easily harvested when the animal has been culled. The skin is composed of different tissue types, or compartments; epidermis, dermis, fat and muscle layers. These tissue types are also of varying radiosensitivity; typically, the epidermis is the site of early radiation reactions and the dermis is the site of late radiation reactions (Hall, 2000).

Adult, female mice (ddY strain) aged 11 weeks, were used for this study. All experimental protocols were approved by the animal welfare committees of the Japanese Synchrotron Radiation Research Institute (SPring-8) and Monash University. The animals were fed a standard rodent diet and given water *ad libitium* in the animal house of the biomedical imaging centre on the SPring-8 synchrotron campus. The animals were anaesthetized using a 1:10 dilution of pentobarbitone (Nembutal,

Sigma Aldrich, St Louis, MO, USA) at a dose rate of approximately 50 mg/kg and a concentration of approximately 5 mg/ml.

The hair along the animals back was shaved using a standard electric rodent shaver. A skin flap was raised along the animals' back and pre-cut lengths of radiochromic film (Gafchromic HD-810, ISP Corp, New Jersey, USA) were placed on both sides of the skin flap to demarcate the entrance and exit radiation fields. The mice were secured on a perspex jig by placing them inside a 50 ml vial with a cut-away made to expose the raised skin flap for irradiation.

5.2.3 Mouse Irradiation

A total of sixty eight mice were used in the study. Two mice did not recover from the anaesthesia. A set of mice (n = 27) were irradiated with three fields, of different doses, of unidirectional, MRT. The peak, in-beam doses were 200 Gy, 400 Gy and 800 Gy. A further set of mice (n = 27) were irradiated with broad beam (BB) radiation doses of 200 Gy, 400 Gy and 800 Gy. The experimental arrangement is shown in figure 5.1. Six mice were used as sham-irradiated controls. These un-irradiated mice were prepared, anaesthetized and positioned on the treatment jig in an identical fashion to the irradiated mice.

We took significant measures to accurately outline the irradiated tissue for this experiment. This was based on our experiences from pilot studies which showed the difficulties of accurately identifying irradiated tissue 5 days post-irradiation when all markings have vanished from the animal and the fur has begun to grow back. Immediately post-irradiation, a fine gauge needle containing Evan's Blue dye (Sigma Aldrich, St Louis, MO, USA) was used to mark the corners of the irradiated fields on the mice skin using the exposed radiochromic film as a visual guide. The overall irradiated region was marked with permanent marker (Figure 5.2). The mice recovered from the anaesthesia and were returned to the animal facility in the biomedical imaging centre at SPring-8.

Figure 5.1: Experimental setup for dorsal skin flap irradiation. The treatment fields were made visible using radiochromic film to demarcate the radiation fields.

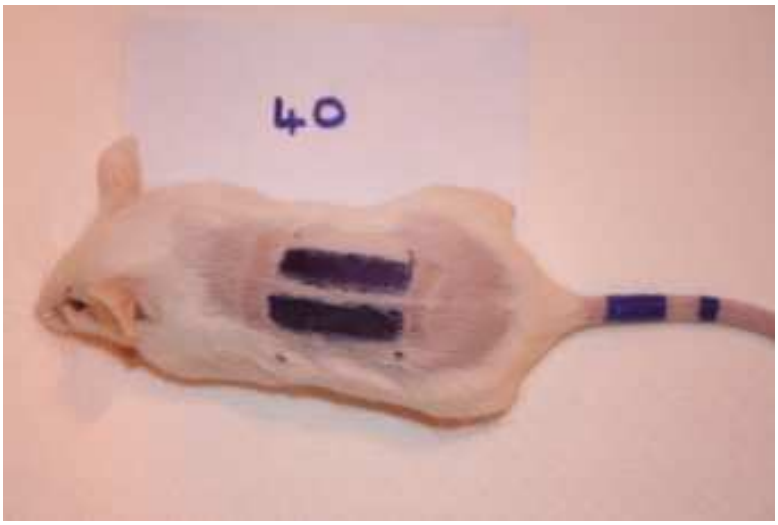

Figure 5.2: Skin markings on mouse to outline the radiation fields. Such markings were made using a permanent marker to ensure accurate tissue harvesting.

5.2.4 Tissue Harvesting

Mice were culled by cervical dislocation at 6 hours, 12 hours, 24 hours, 48 hours or 5 days post irradiation. There were six mice in each group (MRT or BB) at each culling time, with the exception of the 6 hour point, for which there were three mice in the MRT group and three in the BB group. The skin flap was excised from the mouse, flattened and fixed in formalin for at least six hours (Figure 5.3). Small sections of unequivocally-irradiated tissue, perpendicular to the path of the microbeams for each of the three delivered doses, were then removed and placed into histology cassettes. The tissue sections were returned to Australia in phosphate-buffered saline for analysis.

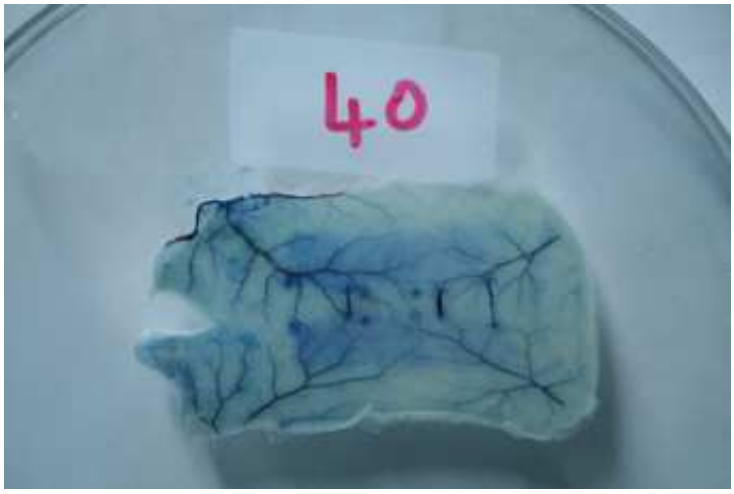

Figure 5.3: Harvested mouse skin from a mouse irradiated with MRT. The excised tissue was flattened and formalin fixed for 6 hrs. The skin markings enabled us to unequivocally harvest irradiated tissue.

5.2.5 Histology & Immunohistochemistry

Haematoxylin & Eosin (H&E)

All tissue sections were embedded into paraffin wax blocks to enable sectioning on a microtome. A routine H & E staining protocol was used to stain control, microbeam and broadbeam-irradiated tissue sections. The section thickness for all histological

and immunohistochemical sections was 5 μm, unless otherwise stated. All histology and immunohistochemistry was performed by Ms. Leonie Cann, Centre for Women's Health Research, Monash Institute of Medical Research, unless otherwise stated.

DNA double strand breaks using γ-H2AX assay

γ-H2AX immunohistochemistry was performed at the Gray Cancer Institute in the UK. Antigen retrieval was performed for the γ-H2AX assay by immersing slides in 250 ml of 10mM citric acid (pH adjusted to 6.0) and subjected to microwave heating for 4 min at high power (850W). The samples were incubated at 37^0 C for 20 mins. The primary antibody was a 1:200 dilution of γ-H2AX, mouse monoclonal, (Upstate, Temecula, CA, USA). This was applied to the sections and allowed to sit for 60 minutes at room temperature. This primary antibody was detected using the DAKO Envision kit, as per the manufacturer's instructions (DAKO Corporation, Carpenteria, CA, USA). Sections were counterstained using haematoxylin.

Apoptosis using TUNEL assay

Detection of apoptosis in tissue sections was achieved using an Apoptag Peroxidase in situ Apoptosis Detection kit according to the manufacturer's instructions (Chemicon International, Temecula, USA) and a previously published protocol (Ruwanpura et al., 2008). The TUNEL stain was performed by Dr. Saleela Ruwanpura from Prince Henry's Institute of Medical Research, Melbourne. In brief, tissues were incubated with a mixture containing digoxigenin (Dig)-conjugated nucleotide and terminal deoxynucleotidyl transferase at 37^0 C for 1 hour. Tissue sections were incubated with anti-Dig horseradish peroxidase for 30 minutes. Diaminobenzidine (DAKO, Carpenteria, USA) was added for 2-3 minutes to reveal sites of anti-Dig binding. Sections were counterstained with Mayer's Haematoxylin.

Leukocyte Common Antigen (CD-45)

The primary antibody applied was a 1:1000 dilution of rat anti-mouse CD45 (Leukocyte Common Antigen, LCA) monoclonal antibody (Becton Dickinson Pharmingen, San Diego, CA, USA). Samples were incubated for 1 hour at 37 degrees. The secondary antibody was a 1:200 dilution of biotinylated goat anti-rat IgG (Chemicon, Temecula, CA, USA) in a 1% solution of BSA and tris-buffered saline. The secondary antibody was applied to the sections and allowed to sit for 20 minutes at room temperature. Sections were then covered with an alkaline phosphatase enzyme, available commercially as the Vectastain ABC elite kit (Vector Laboratories, Burlingame, CA, USA). The chromogen, diaminobenzidine (Sigma-Aldrich, St Louis, MO, USA) was applied to the sections and left for 5 minutes at room temperature before rinsing with distilled water. Sections were counterstained with Mayer's haematoxylin.

Proliferating Cell Nuclear Antigen (PCNA)

The primary antibody was a 1:200 dilution of mouse monoclonal anti-PCNA dissolved in a 1% BSA and PBS (NovoCastra Laboratories, Newcastle Upon Tyne, UK). Samples sat at room temperature for 30 mins, whereupon they were washed with tris-buffered saline. The primary antibody was detected using the Envision anti-mouse HRP kit (Dako Corporation, Carpenteria, CA, USA). This was applied to the sections and allowed to sit for 30 minutes at room temperature. The chromogen, diaminobenzidine was applied to the sections and left for 5 minutes at room temperature before rinsing with distilled water. Sections were counterstained with 1:10 dilution of Harris's haematoxylin.

5.2.6 Microscopy & Image Analysis

General Remarks

Colour images of the stained skin sections were acquired from a Fuji HC-1000 digitising camera (Fuji Photo Film Co., Minato-ku, Tokyo, Japan) connected to a Zeiss

Axioskop light microscope (Carl Zeiss GmbH Gottingen, Germany). A calibrated graticule was used to perform a distance calibration (pixels/μm) for the software in order to accurately record scale and the distance between two points. The software used to acquire, analyse and save the images was the Advanced Imaging System v3.0 software (Interfocus Europe, Cambridge, UK).

γ-H2AX

For the analysis of the γ-H2AX assay, we quantified immunohistochemical information observed under the microscope. We acquired digital, colour photographs within a known irradiated area. The AIS software possesses an automatic target detection algorithm. This software allows the user to input target criteria based on a combination of colour information (hue, saturation and intensity) and physical size. The algorithm then segments structures (cells typically) in the region of interest which match the target criteria. The program returns statistical information from the analysed images, such as the proportional area (area of detected structures relative to the whole image), the cell (grain) count and colour information.

The automatic target detection was performed on the 800 Gy MRT sections only. The total count (i.e. number of identifiable cells satisfying target criteria) was recorded for those mice irradiated with MRT and culled at 6 hrs, 12 hrs, 24 hrs or 48 hrs post-irradiation. The analysis was not performed on broad beam-irradiated sections because the emphasis of the research was to identify an immunohistochemical marker for MRT. Figure 5.4 is a screenshot from the AIS program showing an example of the automatic target detection segmenting structures on an image which match the target criteria.

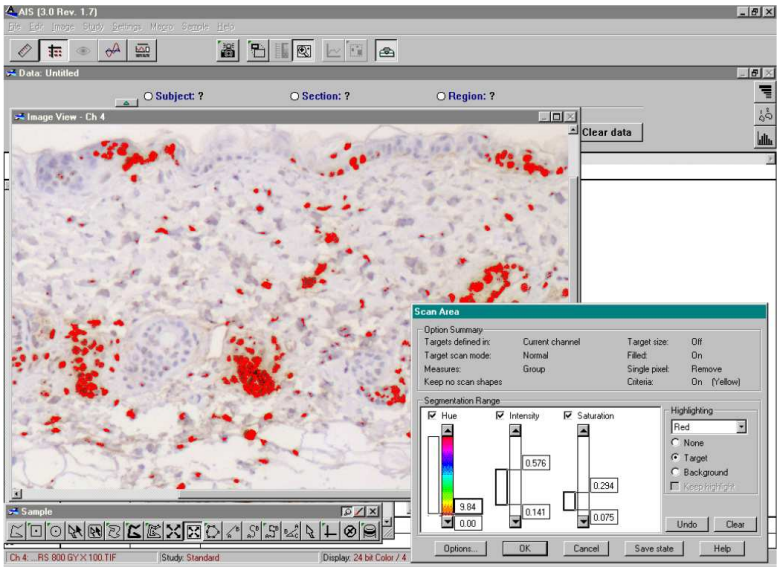

Figure 5.4: AIS autmatic target detection of structures on a microscopy image of MRT-irradiated mouse skin

TUNEL & Apoptosis quantification

For this study, the quantification of apoptosis in MRT and BB-irradiated sections was performed on the 800 Gy section only. A total of six digital images were acquired from each 800 Gy section. The aim was to examine and quantify apoptotic activity within the sections. The tissue sections were from mice culled 6 hrs, 12 hrs, 24 hrs and 48 hrs post-irradiation. Images were saved in a numbered format which prevented the observer knowing to which experimental group the section belonged during the scoring process. Counting of TUNEL-labelled cells (identified by deep brown nuclear staining) was performed manually by another researcher blinded to the image file naming system.

LCA & PCNA

For the analysis of these assays, the aim was to quantify the relative degree of proliferation, and the proportional area of LCA-positive regions. The photographed region was known to be within an irradiated area. Target criteria were established using control tissue sections. The AIS automatic target detection algorithm was used

to quantify the proportional area of LCA-positive regions with hue, saturation and intensity values preset to a threshold condition, to assist with the target detection. For the leukocyte common antigen analysis, the automatic target detection was performed over the entire image and the proportional area of leukocytes recorded. For the PCNA analysis, the proportional area and the intensity was recorded over a region of interest based around the epidermis and upper dermis. For both the LCA and PCNA sections, automatic target detection was performed for the three different doses (200 Gy, 400 Gy and 800 Gy) for mice irradiated and culled 48 hrs or 5 days post-irradiation.

H&E

Digital photographs of the H & E sections were obtained in order to report basic, qualitative morphology on MRT and BB-irradiated mouse skin tissue at the different time intervals post-irradiation.

5.3 Results

Outcome 1

In normal skin, γ-H2AX is a high resolution marker that distinguishes between tissues that have received peak compared to valley doses of microbeam radiation. Figure 5.5 shows MRT tracks identified by γ-H2AX immunostaining of mouse skin irradiated with a peak-in-beam dose of 800 Gy and culled at 6 hrs (b), 12 hrs (c), 24 hrs (d) and 48 hrs (e) post-irradiation. An un-irradiated, control section (a) shows the absence of γ-H2AX-positive staining. The different tissue compartments of skin and objects such as hair follicles and sebaceous glands are labelled on selected images. We did not perform detailed analysis on γ-H2AX sections 5 days post-irradiation because there were large amounts of non-specific, background staining visible which interfered with the auto-detection algorithm. The width of the γ-H2AX positive regions fluctuated from approximately 60 μm 6 hrs post-irradiation, to approximately

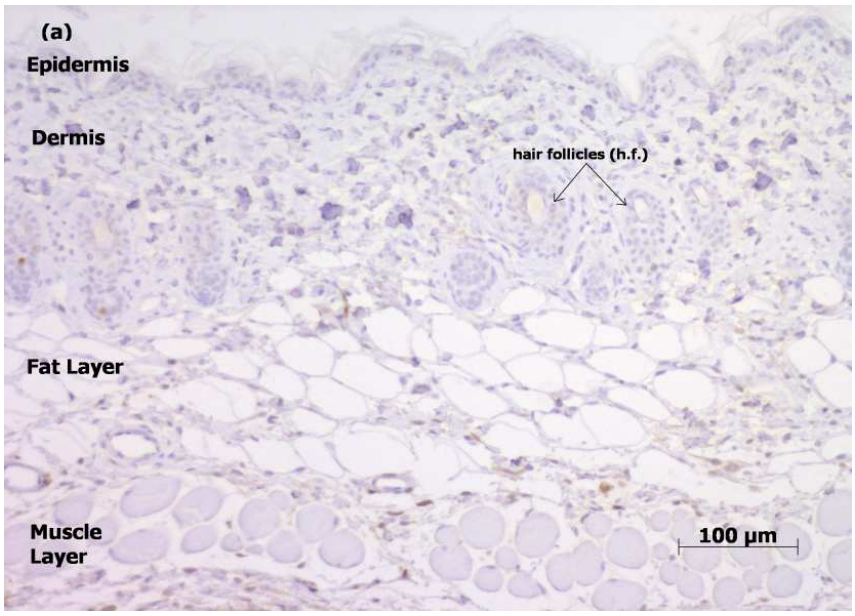

(a)

Figure 5.5: γ-H2AX assay on unirradiated, control skin.

30 μm 48 hrs post-irradiation. The stripes did not always appear perfectly straight, possibly due to movement of different skin layers as a result of stretching the skin flap for irradiation.

Epithelial cells, such as those found in the epidermis and in hair follicles, stained strongly for γ-H2AX, indicating the sites of DNA double strand breaks (5.5(b)). Endothelial cells in irradiated blood vessels were also positive for γ-H2AX, as were cells in the muscle layer. Fibroblast-like cells in the dermis were predominantly negative for γ-H2AX.

The immunohistochemical staining in normal skin was maximal 6 hrs postirradiation with MRT (in-beam, entrance dose 800 Gy), as revealed by plotting the mean cell count (cells/nuclei positive for γ-H2AX per mm^2) in MRT-irradiated skin tissue (Figure 5.5(f)). A one-way Analysis of Variance (ANOVA) [1] was performed on the γ-H2AX count data with a significant difference ($p < 0.0001$) observed between the different time points. Whilst phosphorylated γ-H2AX decreased rapidly, it was still

[1] Statistical analysis, such as ANOVA calculations, were performed using the SPSS v.15 statistical software package. SPSS Inc., Chicago, IL, USA

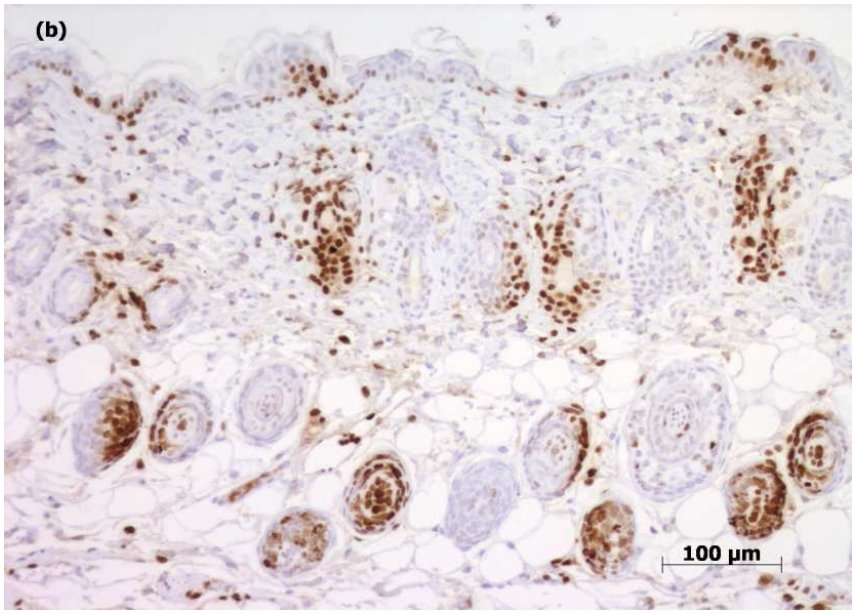

(b)

Figure 5.5: (cont'd) γ-H2AX in mouse skin 6 hrs post-irradiation.

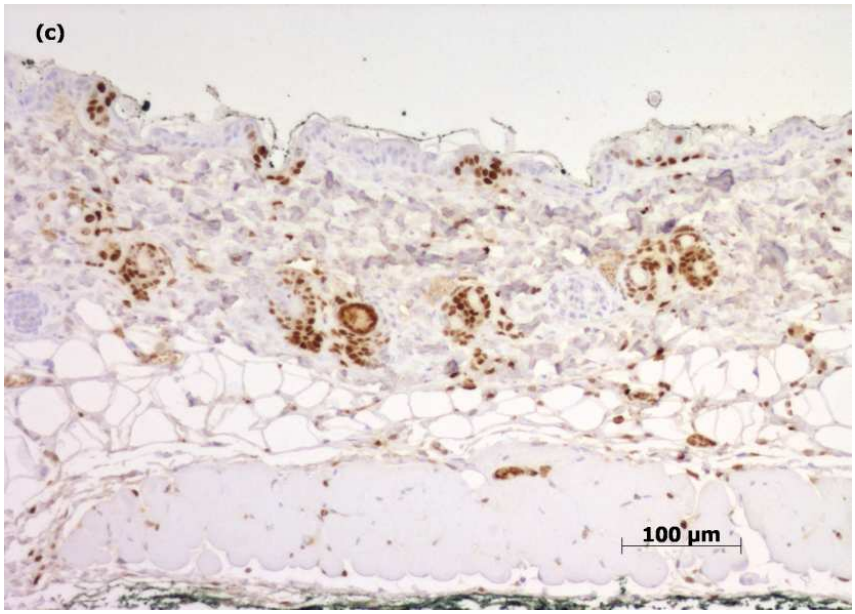

(c)

Figure 5.5: (cont'd) γ-H2AX assay on mouse skin 12 hrs post-irradiation.

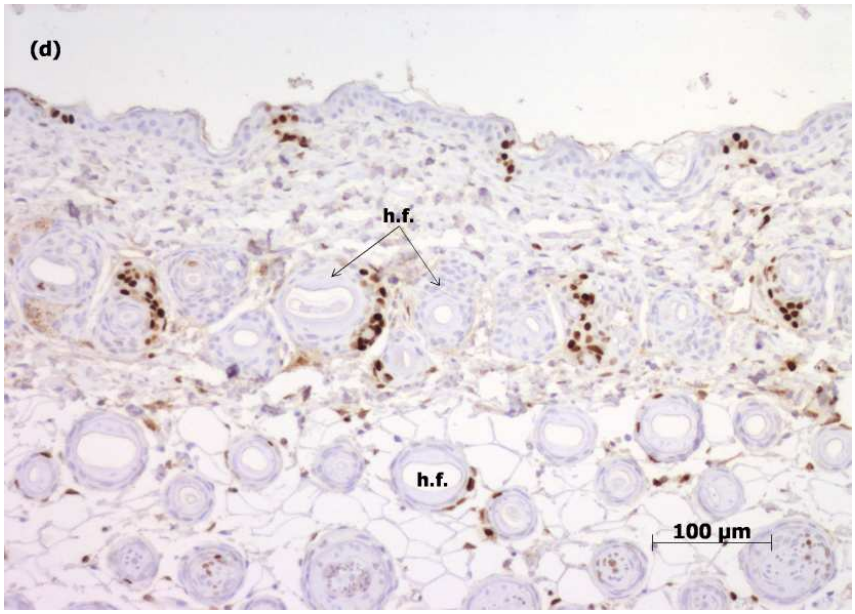

(d)

Figure 5.5: (cont'd) γ-H2AX assay on mouse skin 24 hrs post-irradiation.

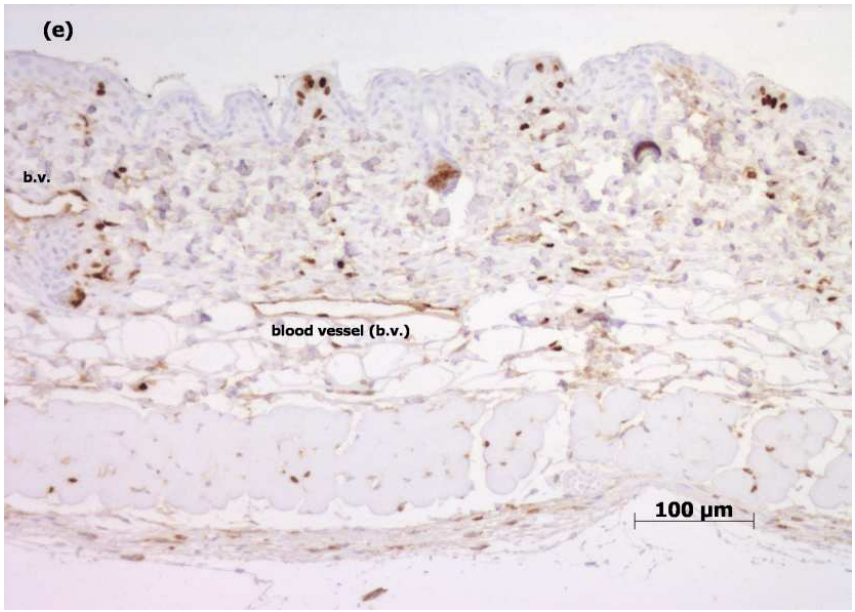

(e)

Figure 5.5: (cont'd) γ-H2AX assay on mouse skin 48 hrs post-irradiation.

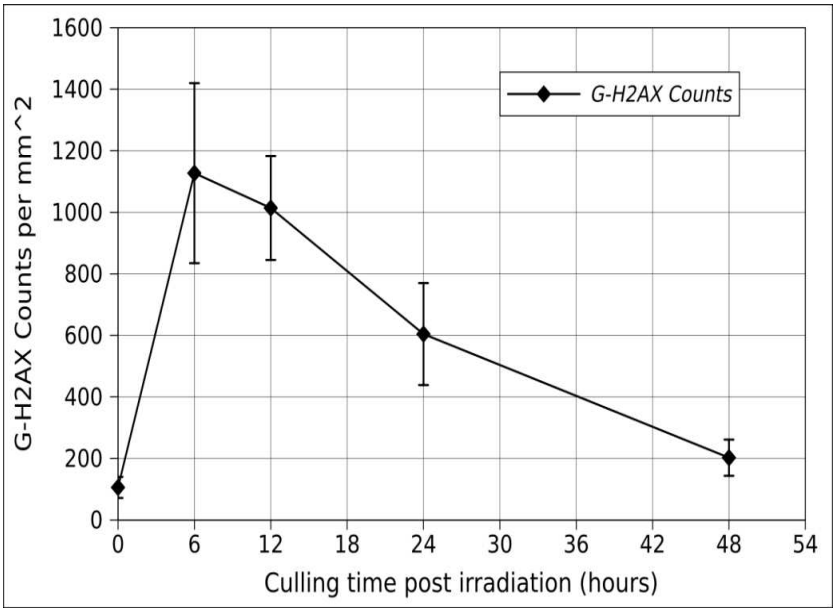

(f)

Figure 5.5: (cont'd) Quantitative plots of γ-H2AX in MRT-irradiated mouse skin. Zero hours post-MRT corresponds to unirriadiated, control tissue. Error bars correspond to two times the standard error of the mean (SEM) γ-H2AX count.

evident at 48 hours.

Outcome 2

Virtually all epithelial cells stained positive for PCNA, including cells in unirradiated, control sections, casting doubt on the PCNA data and its usefulness as a cellular marker of MRT (Figure 5.6).

Given the unexpectedly high levels of PCNA positive staining in the control sections, we did not pursue quantification of this marker in the MRT-treated samples. However, we did observe interesting phenomena on the PCNA sections which we pursued using standard H & E stains.

Outcome 3

H & E, morphology and epidermal thickness measurements show high dose broad beam radiation causes severe tissue damage compared to microplanar delivered radiation. Upon examination of H & E-stained sections under light microscopy, it was

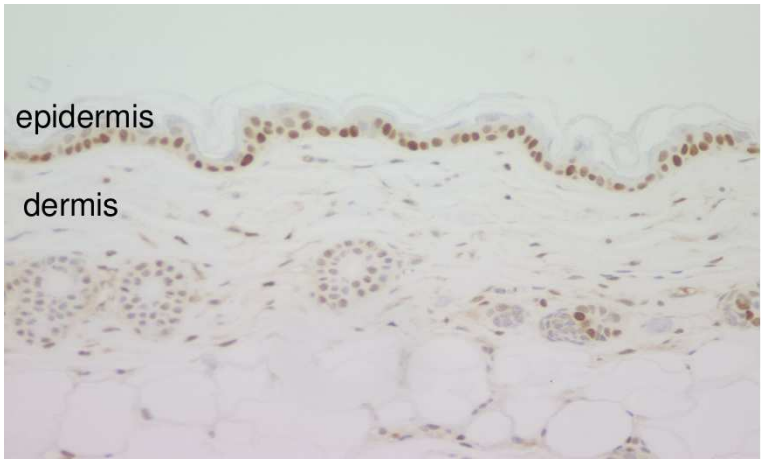

Figure 5.6: Unirradiated control skin section, showing epithelial cells staining positive for PCNA

clear that high dose broad beam radiation caused catastrophic damage to the skin compared to high dose MRT. The characteristic stripes or tracks of MRT damage reported by various authors in the cerebellum of rats were not at all visible in skin, hence our motivation for finding a marker such as γ-H2AX. Therefore, phenomena such as epidermal swelling were clues to the zones of irradiated tissue. Epidermal thickening was noticeable in BB-irradiated tissue by 24 hrs post-irradiation, especially for the 400 Gy and 800 Gy sections. Epidermal swelling was noticeable only in the 800 Gy MRT irradiated sections by 48 hrs post-irradiation.

The damage caused by BB radiation was most pronounced by 5 days post-irradiation. Prior to culling the mice, hair epilation and skin blistering were noted in animals which received 400 Gy and 800 Gy doses. A dose of 400 Gy of BB radiation caused epidermal denuding (Figure 5.7(b)). In addition, sebaceous glands and entire hair follicles had vanished. Large, necrotic cavities which made identifying the tissue type quite difficult were observed in 400 Gy and 800 Gy sections (f). The 200 Gy sections displayed gross epidermal swelling, leukocytic infiltration and morphological damage to hair follicles and sebaceous glands (d).

The effects on skin tissue 5 days post-irradiation with MRT were less pronounced than with BB. The 200 Gy sections (c) appeared very similar to sham-irradiated con-

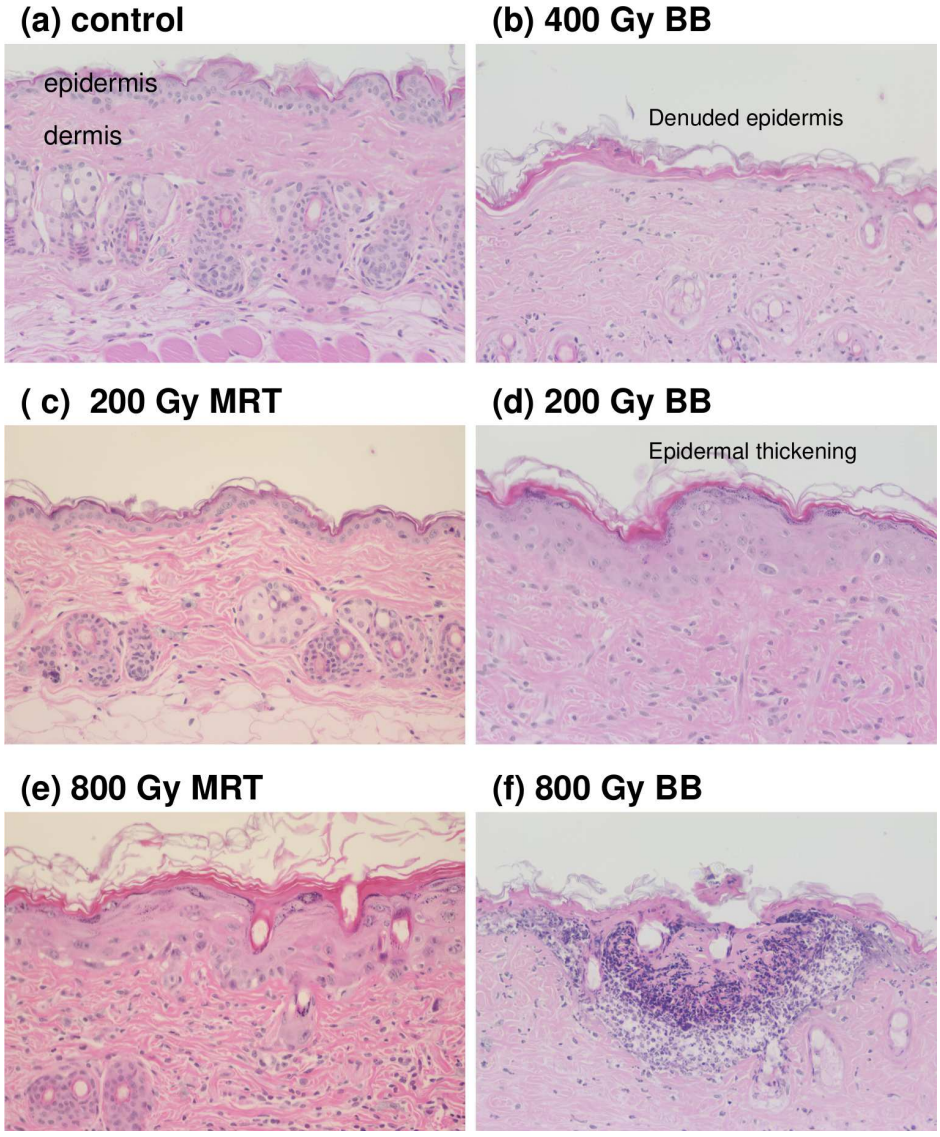

Figure 5.7: Images of H & E stained mouse skin sections showing more severe damage to BB-irradiated skin than MRT-irradiated skin; (a) unirradiated, control, (b) 400 Gy broad beam, (c) 800 Gy broad beam, (d) 200 Gy broad beam, (e) 200 Gy MRT, and (f) 800 Gy MRT Images (b)-(f) are from mice culled 5 days post-irradiation.

trols (a). The 400 Gy sections showed epidermal swelling and increased presence of leukocytes, but structures such as hair follicles and sebaceous glands appeared relatively normal. The damage caused by a dose of 800 Gy of MRT was more noticeable, with considerable epidermal swelling observed (e). Basal cells within the epidermal layer appeared morphologically damaged with evidence of hypertrophy. Hair follicles also appeared morphologically damaged.

The epidermal thickness measurements are plotted in figure 5.8. It was not possible to measure epidermal thickness for 800 Gy BB by 48 hrs post-irradiation. Nor was it possible to measure epidermal thickness for 400 Gy sections by 5 days post-irradiation. The epidermal layers for these sections had been largely denuded by the broad beam of high dose radiation. The treatment modality, dose and cull times post-irradiation is indicated on the x-axis.

A one-way ANOVA was performed on control and MRT sections for the 48 hrs and 5 day post-irradiation samples. There was a statistically significant difference in epidermal thickness ($P < 0.0005$) between the four groups (control, 200 Gy, 400 Gy and 800 Gy MRT) at both the 48 hr and the 5 day cull point. Post-hoc analysis (Tukey's Highest Significant Difference) showed significance at the 0.05 level for the 800 Gy sections only at 48 hrs post-irradiation, and significance at the 0.05 level for the 400 Gy and 800 Gy sections at 5 days post-irradiation.

Outcome 4

High-dose, broad beam radiation reduced proliferation by destroying epithelial cells. Figures 5.9(a-d) show H & E-stained sections for mouse skin. Images are shown for (a) control, (b) BB 800 Gy, mid-treatment field, 5 days post-irradiation, (c) MRT 800 Gy, mid-treatment field, 5 days post-irradiation and (d) BB 400 Gy (field edge) 5 days post-irradiation.

By 48 hrs post-irradiation with a BB field, the skin proliferation appeared to decrease compared to the control group, with epithelial cells destroyed (5.9b). Immediately outside the field, proliferation appeared to increase substantially before

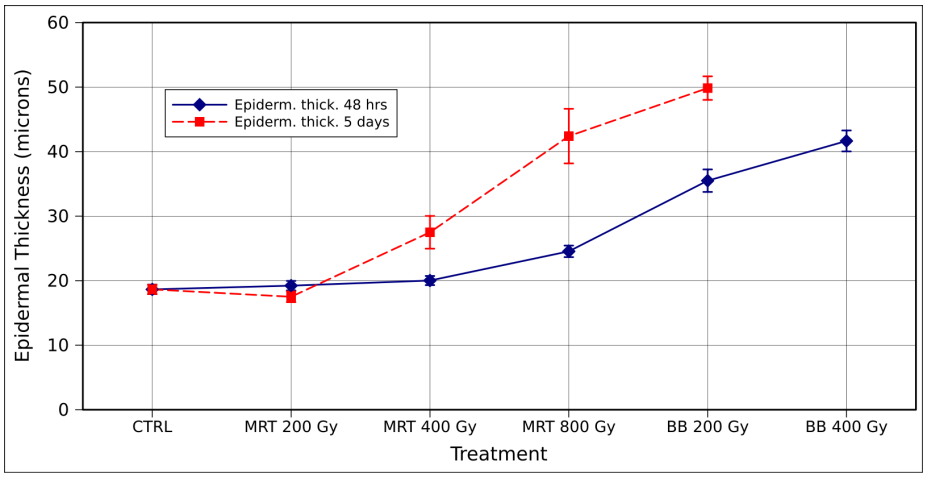

Figure 5.8: Epidermal thickness (in μm) of MRT and BB-irradiated mouse skin tissue at different time points post-irradiation. The error bars correspond to two times the standard error of the mean epidermal thickness.

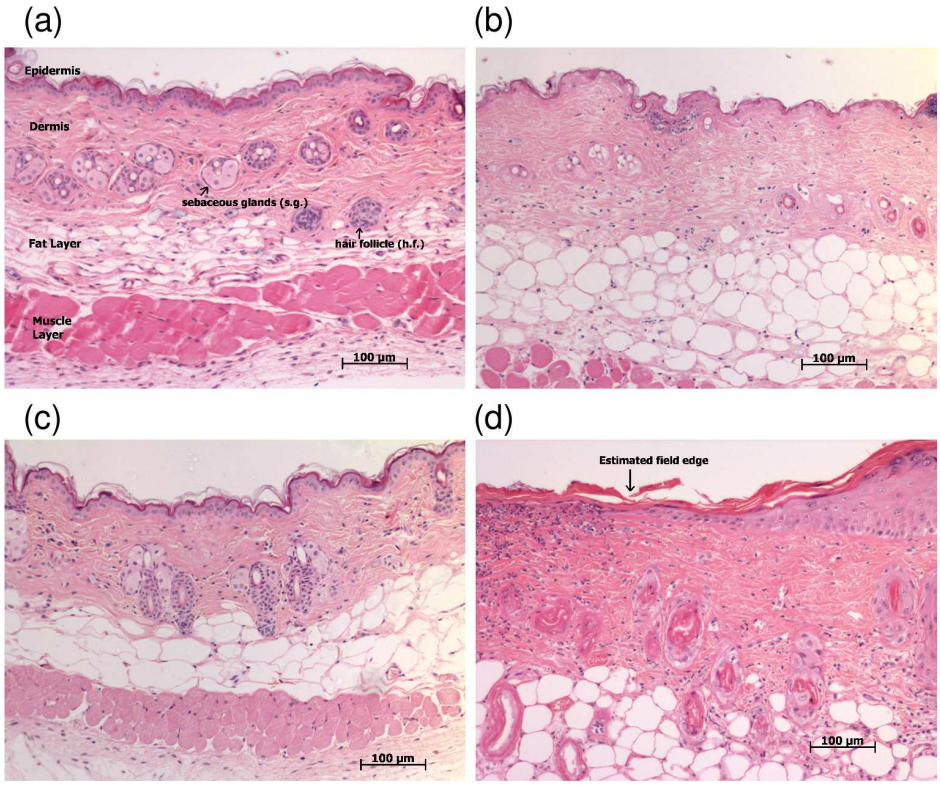

Figure 5.9: Images of H & E-stained skin sections for (a) unirradiated control, (b) BB 800 Gy, 5 days post-irradiation, (c) MRT 800 Gy, 5 days post-irradiation and (d) BB 400 Gy 5 days post-irradiation. The field edges are not identifiable in MRT-irradiated skin.

returning to control levels further from the field edge (d). The field edge and penumbral regions are indicated by arrows in (d). Epidermal thickening and (presumably) increased proliferation are obvious on the right hand side of (d).

The epidermal thickening at the edge of the broad beam field returned to control levels approximately 1 mm from the estimated field edge as shown in figure 5.10, a montage of three H & E images. No such behaviour was observed in MRT-irradiated skin.

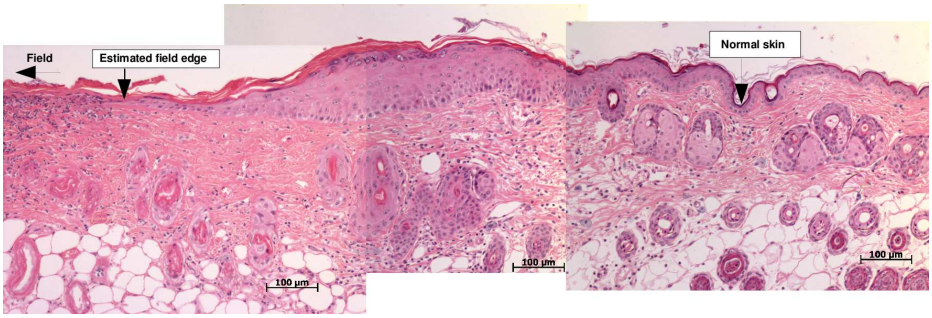

Figure 5.10: Montage of three separate H & E images, tiled together, to illustrate the effects of the edge of a 400 Gy broad beam on skin, 5 days post-irradiation. The irradiated regions are to the left of the estimated field edge and essentially out of the picture. The epidermal thickness returns to normal, control levels approximately 1 mm from the estimated field edge.

Outcome 5

Apoptosis was elevated in the first 6 hrs post-irradiation with MRT, but there-after returned to control levels. Figure 5.11(a) is a representative image of TUNEL-stained mouse skin section from a mouse culled 6 hrs post-800 Gy MRT. The TUNEL-positive cells are shown with a dark brown nuclear stain as seen in the inset (b). The path of the microbeams through the skin tissue (evident with γ-H2AX) was not visible using the TUNEL assay. Figure 5.11(c) is a plot of the number of TUNEL positive cells in MRT-irradiated tissue at different time points post-irradiation. The maximum number of TUNEL positive cells appeared maximal 6 hours post-irradiation, albeit with large variability between the time points and no statistically significant differences. There was no obvious trend in apoptosis, but by 120 hours (5 days) post-MRT

the number of apoptotic cells was at unirradiated, control levels. The broad beam TUNEL data is not shown because cell counting was only performed out to 48 h post-irradiation.

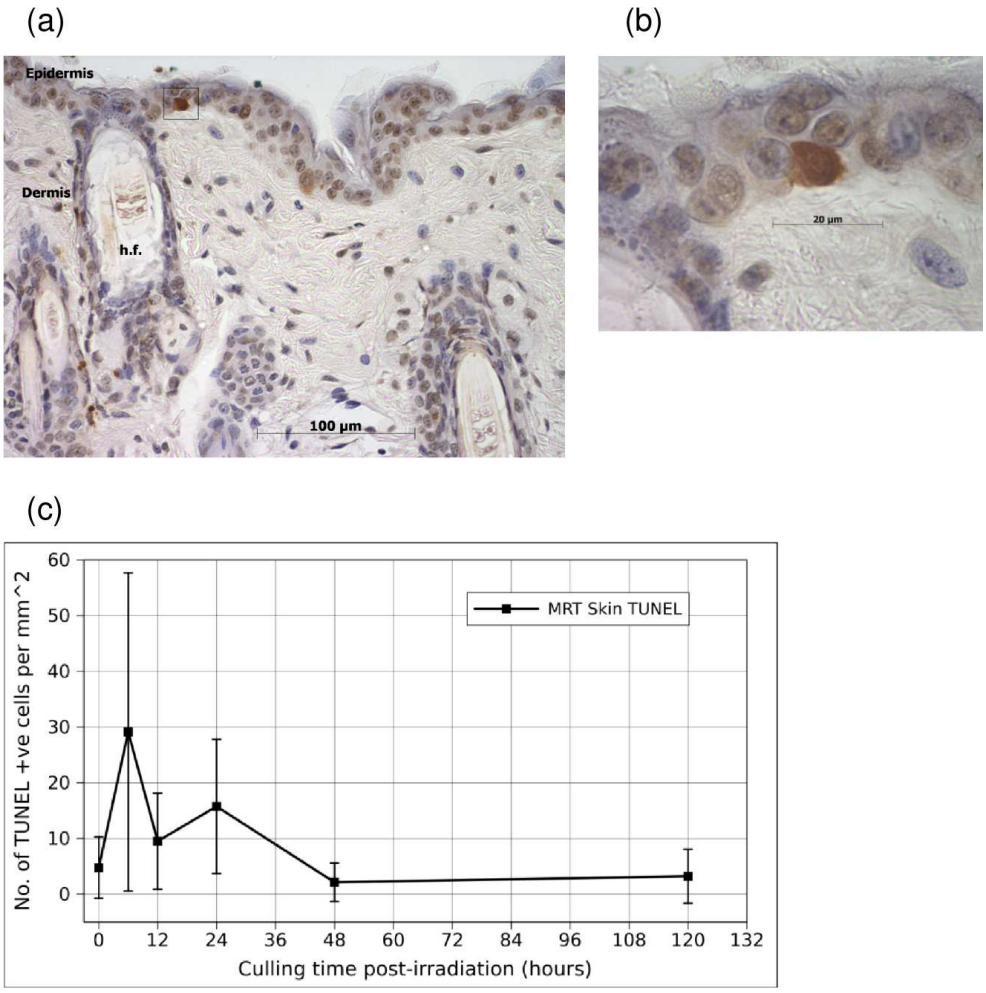

Figure 5.11: TUNEL assay on mouse skin (a) 6 hrs post-irradiation, TUNEL positive cells appear with a dark brown nuclear stain. (b) magnified version of (a) showing a TUNEL-positive cell. (c) Quantitative plots for manual TUNEL counts. Error bars correspond to two times the standard error of the mean TUNEL-positive cell count

Outcome 6

Treatment modality (MRT/BB) caused a significant change ($p < 0.05$) in the proportional area of leukocytic infiltration (i.e. population of leukocytes) but increasing the dose (for both MRT and BB) did not. There was no clear indication of the paths of

individual microbeams through the tissue with the CD45 assay. Representative photographs from the LCA immunohistochemistry assay are shown in figures 5.12(a-c). Regions positive for leukocytic activity are shown in brown. Leukocytic infiltration was apparent in the MRT-irradiated sections by 48 hrs post-irradiation.

Figure 5.13 is a plot of the proportional area for the different treatment modalities and doses for irradiated skin sections 48 hrs and 5 days post-irradiation. Post-hoc statistical analysis (Tamhane method) showed a statistically significant difference ($p < 0.05$) in the proportional area of leukocytic infiltration between control and MRT samples for the 400 Gy and 800 Gy groups. This was true by both 48 hrs and 5 days post-irradiation. There was also a significant difference ($p < 0.05$) in proportional area between control and BB, and between MRT and BB by both 48 hrs and 5 days post-irradiation, for all three doses. Increasing the dose within a treatment modality, did not cause statistically significant changes in the proportional area of the LCA positive regions. The modality (control, MRT, BB), but not the dose, was the significant factor for changes in proportional area.

5.4 Discussion

The results of this study show that the γ-H2AX immunohistochemistry assay provides spatial localisation of DNA double strand break repair in MRT-irradiated tissue. The γ-H2AX marker distinguishes between tissues that have received peak compared to valley doses of microbeam radiation. Histological assays (H & E) and immunohistochemical assays such as CD45, PCNA and TUNEL, failed to locate MRT-irradiated zones in mouse skin. Single stain TUNEL, LCA and PCNA assays did not identify spatially-localised regions of apoptosis, leukocytic infiltration or proliferation as initially hypothesised.

The γ-H2AX immunohistochemistry assay has been used as a quantitative biomarker of radiation-induced DNA double strand breaks and their repair, (Sedelnikova et al., 2002; Rothkamm et al., 2003; Rothkamm and Lobrich, 2003) and (Qvarnstrom et al.,

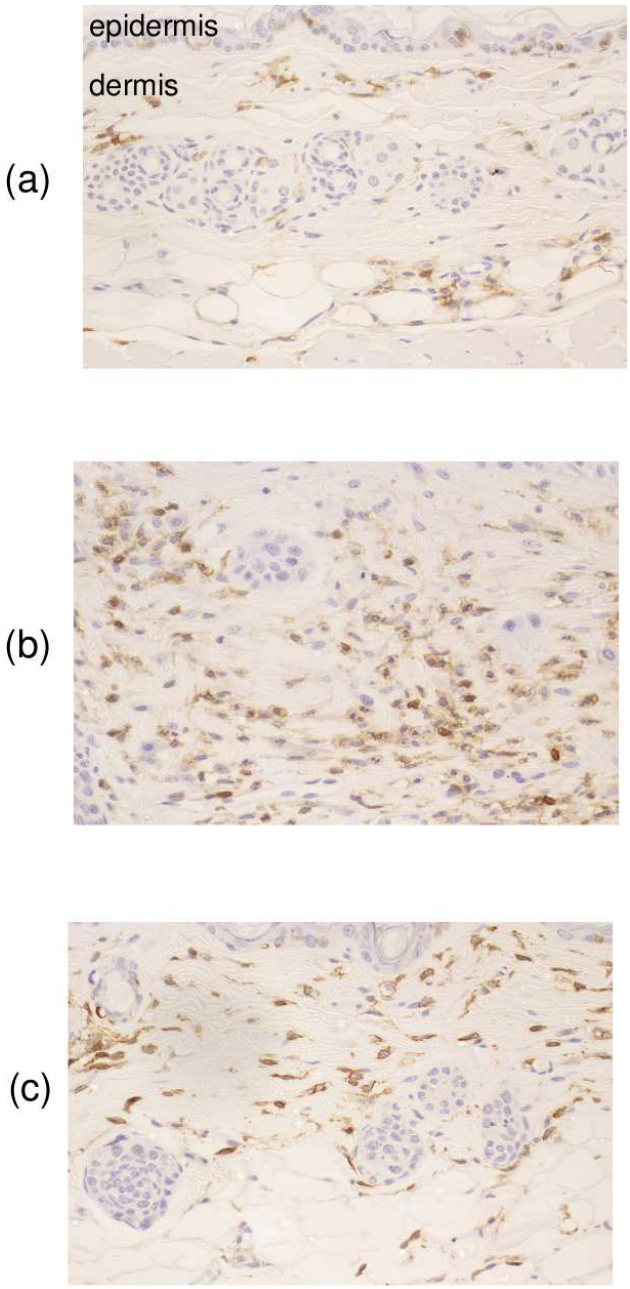

Figure 5.12: Images of LCA-stained skin sections for (a) unirradiated control, (b) MRT 800 Gy, 5 days post-irradiation and (c) Broadbeam, 800 Gy, 5 days post-irradiation .

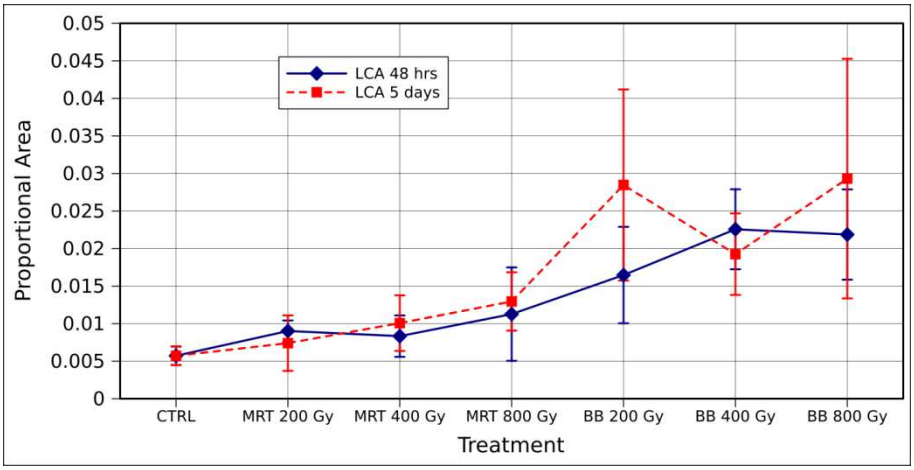

Figure 5.13: plot of CD45/LCA proportional area in MRT and BB-irradiated mouse skin, as detected by AIS automatic detection algorithm. Error bars correspond to two times the standard error of the mean proportional area.

2004; Lobrich et al., 2005; Rothkamm et al., 2007). Exposure to ionising radiation results in the formation of DNA double strand breaks. A downstream event is the phosphorylation of the histone, H2AX, on Ser139 of the carboxyl tail after irradiation. Upstream DNA damage kinases include ataxia telangiectasia mutated protein (ATM), ataxia telangiectasia Rad3-related protein (ATR) and DNA-dependent protein kinase catalytic subunit (DNA-PKcs,) as reviewed in Kao et al. (2006). These events are important for our understanding of the underlying biochemistry of γ-H2AX.

In this study, we observed that not all cell types in the different compartments were positive for γ-H2AX. We do not know the reasons for this heterogeneity. The differences could reflect tissue compartment heterogeneity in H2AX expression or in phosphorylation capacity. There may also be differences in the upstream DNA damage kinases; ATM, ATR and DNA-PKcs (Kai Rothkamm, personal communication).

The single stain immunohistochemical assays of leukocytic infiltration, apoptosis and proliferation did contain useful biological information in their own right. In the case of the PCNA assay, it was hypothesised that the pattern of proliferation at the very edge of a broad beam would resemble the pattern of proliferation between two

adjacent microbeams when the same in-beam dose was delivered. However, this was not the case.

The differences in proliferation between a BB-irradiated field and a MRT-irradiated field are clearly evident in the H & E images shown in figure 5.7. Large amounts of proliferating cells were observed 'massing at the borders'of the BB sample (Figure 5.7(d)), as if trying to migrate into the irradiated zones and promote repair and proliferation. Repair was not possible however, owing to the catastrophic damage to the tissue over distances of several millimetres. This phenomenon was not observed in the case of MRT-irradiated tissue.

Normal tissue appears to possess the ability to tolerate high doses of radiation when it is delivered in a microplanar fashion. The ability of epithelial cells to proliferate is not substantially affected, at least in the first 5 days post-irradiation. When the radiation is delivered uniformly as a broad beam, the ability of cells to proliferate appears compromised owing to widespread tissue damage. Such findings may be an important contribution to the debate on how normal skin tissue tolerates high doses of microplanar-delivered radiation compared to high dose broad beam radiation. This phenomena is clearly also of interest to radiation therapy for cancerous tissue. However, there is still much that remains unknown and more work is required.

The findings presented here are consistent with the theory of Zhong et al. (2003), who postulated that the unique skin-sparing effect of MRT is related to the survival of stem cells located close to hair follicles and lying in the valley region between adjacent microbeams. Zhong et al. (2003) also noted that in the epidermis, clonogenic cells in the hair folicular epithelium, appeared to play a key role in the regenerative process.

These findings are also consistent with Hopewell's ideas on the anatomical and structural response of tissue having more to do with migration and absolute field sizes than on a volume effect *per se*, as outlined in Section 2.1.3 of this thesis. It may be informative to perform an isoeffect study, similar to the pig skin work of Hopewell et al. (1986) and Hopewell (1990), but using smaller and smaller field

sizes, down to 25 μm. In Hopewell's work, it was observed that for a particular biological effect (moist desquamation in skin), the dose required to cause this effect increased dramatically as the field size was reduced from tens of cms to less than 5 mm.

We observed that all epithelial cells (including control sections) appeared to stain positive for PCNA. This indicates that PCNA is not in fact a useful marker of proliferation in this tissue and the proliferation results achieved must be treated with suspicion. Quantitative PCNA data is not shown as a result. A more specific marker such as bromodeoxyuridine (BrdU), which is incorporated into the DNA of replicating cells, is required. Unfortunately, BrdU staining cannot be performed retrospectively. With this approach, the treated animal is injected with BrdU solution four hours before culling, in order that it can be incorporated into the replicating DNA. A BrdU experiment was performed by our research group in a subsequent field trip to SPring-8 and is reported in the next chapter.

It is clear that any attempt to understand the radiobiological effects of MRT on a cellular level requires an immunohistochemical assay such as γ-H2AX which can discriminate between peak and valley irradiated sections on a cellular level. In skin at least, the conventional histological assays such as H & E provide limited information on MRT zones, but not broad beam fields.

In conclusion, γ-H2AX is an excellent cellular marker of microbeam radiation therapy. The spatial localisation of the microbeams with γ-H2AX was so precise that the path of the radiation through an individual hair follicle bulb could be visualised, as shown in figure 5.14. This remarkable image is testament not only to γ-H2AX as a marker of radiation damage/repair, but also to the precision and spatial resolution of synchrotron microbeam radiation therapy.

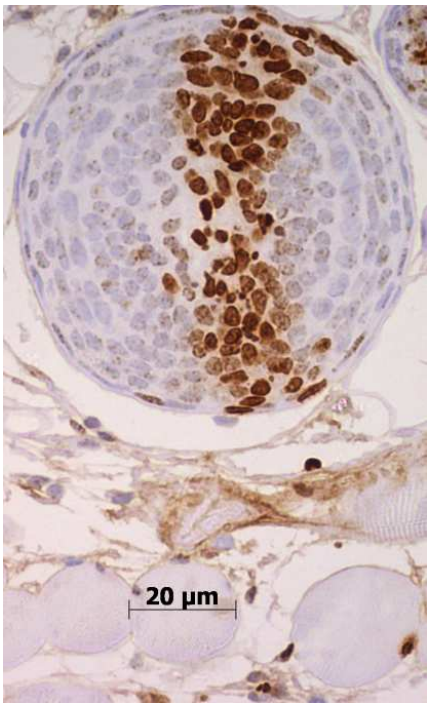

Figure 5.14: The central portion of a hair follicle bulb appears positive for γ-H2AX indicating the path of an X-ray microbeam. The skin section was from a mouse culled 6 hrs post-irradiation. Epithelial cells in the outer portions of the follicle were not positive and thus were spared the high dose microbeam (800 Gy).

CHAPTER 6

Acute Cellular Response of Normal & Malignant Tissue to High Dose Synchrotron Microbeam Radiation Therapy

6.1 Introduction

This chapter appears as a complete paper, which was submitted to the *Journal of the National Cancer Institute*. However the journal's editorial board did not accept it for publication. It is currently being re-formatted for submission to another journal. The paper, as it appears here, contains its own bibliography, and reference styles, separate from the rest of the thesis. The figures appear at the end of the paper. Since this chapter is intended as a stand-alone publication, there is some repetition of material from other chapters in this thesis.

6.2 Declaration by Candidate for Thesis Chapter 6

In the case of Chapter 6, the nature and extent of my contribution to the work was the following:

Conception, planning and study design, Initiation & Execution of experimental research, Analysis and interpretation of the data, including statistical analysis, Drafting and revising the submitted manuscript.

I estimate the extent of my contribution to this paper was 50%.

The following co-authors contributed to the work.

Name	Nature of Contribution
Dr. Robin Anderson	Planning experiments & revising manuscript
Dr. Kai Rothkamm	Planning experiments & revising manuscript
Ms. Leonie Cann	Planning & executing experiments, immunohistochemical staining, revising manuscript
Ms. Christina Restall	Tumour inoculation & growth measurements, Executing conventional radiotherapy experiments, revising manuscript
Dr. Saleela Ruwanpura	Immunohistochemical staining, cell counting & revising manuscript
Dr. Sarah Meachem	Revising manuscript
Dr. Naoto Yagi	Technical assistance/advice on beamline & revising manuscript
Dr. Imants Svalbe	Planning experiments & revising manuscript
Prof. Bryan Williams	Revising manuscript
Prof. Robert Lewis	Planning experiments & revising manuscript
Prof. Peter Rogers	Planning & executing experiments, advising on data analysis, revising manuscript

Co-authors who are students at Monash University must also indicate the extent of their contribution in percentage terms. Since there were no other student co-authors on the paper (apart from myself, the candidate), this requirement is not applicable.

Candidate's Signature:

Date:

6.3 Declaration by Co-authors

The undersigned hereby certify that:

1. the above declaration correctly reflects the nature and extent of the candidate's contribution to this work, and the nature of the contribution of each of the co-authors.

2. they meet the criteria for authorship in that they have participated in the conception, execution, or interpretation, of at least that part of the publication in their field of expertise;

3. they take public responsibility for their part of the publication, except for the responsible author who accepts overall responsibility for the publication;

4. there are no other authors of the publication according to these criteria;

5. potential conflicts of interest have been disclosed to (a) granting bodies, (b) the editor or publisher of journals or other publications, and (c) the head of the responsible academic unit; and

6. the original data are stored at the following location(s) and will be held for at least five years from the date indicated below:

Location(s): School of Physics & Centre for Women's Health Research, Monash University, Clayton, VIC 3800, Australia

Name	Signature	Date
Robin Anderson	[redacted]	Dec 3, 2008
Christina Restall	[redacted]	4 Dec 2008
Leonie Cann	[redacted]	4/12/2008
Saleela Ruwanpura	[redacted]	04/12/2008
Sarah Meachem	[redacted]	04 12 2008
Imants Svalbe	[redacted]	03/12/08
Bryan Williams	[redacted]	25 Nov 2008
Robert Lewis	[redacted]	12- 4- 2008
Peter Rogers	[redacted]	4/12/8
Kai Rothkamm	[redacted]	26 November 2008
Naoto Yagi	[redacted]	24/11/2008

6.4 Paper 2: Acute Cellular Response of Normal & Malignant Tissue to High Dose Synchrotron Microbeam Radiation Therapy

Acute Cellular Response of Normal and Malignant Tissue to High Dose Synchrotron Microbeam Radiation Therapy

Jeffrey C. Crosbie, Robin L. Anderson, Kai Rothkamm, Christina M. Restall, Leonie Cann, Saleela Ruwanpura, Sarah Meachem, Naoto Yagi, Imants Svalbe, Robert A. Lewis, Bryan R. G. Williams, Peter A. W. Rogers

Affiliations of authors: School of Physics (JCC, IS, RAL), Monash Centre for Synchrotron Science (JCC, RAL), and Monash Institute of Medical Research (LC, SR, BRGW, PAWR), Monash University, Clayton,Victoria, Australia; Health Protection Agency, Radiation Protection Division, Chilton, Didcot, Oxfordshire, United Kingdom (KR); Prince Henry's Institute of Medical Research, Clayton, Victoria, Australia (SM); Research and Utilisation Division, JASRI (Japan Synchrotron Radiation Research Institute), SPring-8, Mikazuki-cho, Sayo-gun, Hyogo, Japan (NY); The William Buckland Radiotherapy Centre, Alfred Hospital, Melbourne, Victoria, Australia (JCC); PeterMacCallum Cancer Centre, East Melbourne, Victoria, Australia (RLA, CMR); Department of Pathology, The University of Melbourne, Victoria, Australia (RLA).

Correspondence to: Prof. Peter A. W. Rogers, Centre for Women's Health Research, Monash Institute of Medical Research, Monash Medical Centre, 246

Clayton Road, Clayton, Victoria 3168, Australia

(e-mail: Peter.Rogers@med.monash.edu.au).

Ph: (+ 61) 3 95945370

Fax: (+61) 3 95946389

ABSTRACT

Background Synchrotron microbeam radiation therapy (MRT) is a candidate for clinical use following demonstration of efficacy in tumor-bearing rodent models with remarkable sparing of normal tissue. The underlying cellular mechanisms are poorly understood.

Methods MRT irradiations were performed using X-rays of mean energy 125 keV, segmented into an array of 25 μm-wide, planar microbeams, with peak-to-peak separations of 200μm. Planar (560 Gy) or cross-planar (2x280 Gy or 2x560 Gy) irradiations were delivered to mice bearing mammary tumors. Immunohistochemical staining of DNA double strand breaks, proliferation and apoptosis was performed on irradiated tissue sections. The MRT response was compared to conventional radiotherapy at 11, 22 or 44 Gy.

Results This study provides the first evidence for a differential tissue response at a cellular level between normal and tumor tissues following synchrotron MRT. Within 24 h of MRT to tumor, obvious cell migration occurred into and out of irradiated zones. MRT-irradiated tumor showed significantly less

proliferative capacity by 24h post-irradiation (P= 0.002). Median survival times for EMT-6.5 and 67NR tumor bearing mice following MRT (2x560 Gy) and conventional radiotherapy (22 Gy) increased significantly compared to unirradiated controls (P< 0.0005). However, there was markedly less normal tissue damage from MRT than from conventional radiotherapy.

Conclusions MRT-treated normal skin mounts a more coordinated repair response than tumors. Our studies did not find evidence of a microvascular effect in MRT-irradiated tumors. Cell-cell communication of death signals from directly irradiated, migrating cells, may explain why tumors are less resistant to high dose MRT than normal tissue.

Abbreviations:

MRT – Microbeam Radiation Therapy

BrdU – Bromodeoxyuridine

TUNEL – Terminal deoxynucleotidyl Transferase Biotin-dUTP Nick End Labelling

JASRI - Japan Synchrotron Radiation Research Institute

Synchrotron Microbeam Radiation Therapy (MRT) has been used in a number of pre-clinical studies on tumor-bearing rodent models (1-4). A high flux, X-ray beam from a synchrotron is segmented into micro-planar arrays of narrow beams, typically 25 μm wide and with peak-to-peak separations of 200 μm. Normal tissue is reported to be exceptionally resistant to hundreds of Grays of peak, in-beam dose delivered by MRT (5). Such doses are 1-2 orders of magnitude greater than those delivered using conventional radiotherapy. MRT has been shown to cause significant tumor growth delay and in some cases, tumor ablation (3).

It is not known why normal tissues can tolerate such high doses of microplanar-delivered radiation, or why tumors respond so well to MRT when only a fraction of their volume is irradiated. Knowledge of the radiobiological response to MRT at a cellular level is important since the tolerance and repair mechanisms may inform current radiotherapy paradigms and dramatically alter the existing treatment regimens used for tumor control.

Using conventional histology, it is not possible to determine where the microbeams traversed most tissues. The distinctive stripes of radiation damage to neural cells in the cerebellum, as reported by Laissue *et al.* (3, 6) and others, are not observed in skin for example, using conventional histological methods (5). To allow investigation of the cellular mechanisms underlying MRT, we have used immunohistochemistry of γ-H2AX as a quantitative bio-marker of radiation-induced DNA double strand breaks and repair (7-12) to reveal the

path of the microbeams through tissue sections in the hours and days following irradiation.

The aims of this study were to demonstrate an anti-tumor effect with relative normal tissue sparing using MRT compared to conventional radiotherapy, and to quantify cell proliferation, apoptosis and DNA repair, in normal skin and malignant tissue, in the hours and days following high dose synchrotron MRT. We hypothesise that differences in proliferation, apoptosis and DNA repair between normal tissue and tumor may explain the relative resistance of normal tissue to microplanar generated X-rays.

Materials and Methods

Synchrotron Radiation Source

Beamline BL28B2 at the SPring-8 synchrotron, Hyogo, Japan was used for microbeam irradiation. Information on this beamline is available from the SPring-8 website (13). The beamline utilises a bending magnet to produce polychromatic X-rays from 8 GeV electrons, with a stable beam current of 100 mA. The synchrotron X-ray beam was hardened to a mean energy of 125 keV using a 3 mm thick copper filter that preferentially absorbs low energy X-rays (14). The energy spectrum of the open X-ray beam from the bending magnet on BL28B2 was simulated using the SPECTRA program of Tanaka and Kitamura (15) and is shown in Figure 1, A.

Microbeam Generation

The electron beam in the bending magnet produces a virtually parallel beam of X-rays with minimal vertical divergence. The high flux produced by synchrotron radiation permits the beam to be split or segmented into an array of parallel microbeams each several orders of magnitude more intense than the flux from conventional X-ray sources with a low flux between the beams. A fixed geometry tungsten/kapton collimator, as described in (14), was used to segment the broad beam into an array of planar microbeams. The thickness of the tungsten/kapton collimator in the direction of the beam was approximately 10 mm. The nominal beam width was 25 μm, with a centre-to-centre spacing of 200 μm. Figure 1, B shows a small piece of radiochromic film exposed to MRT to illustrate the spatially fractionated geometry of MRT. The exposure time was adjusted by varying the opening time of an upstream lead shutter, which blocked the X-ray beam.

Dosimetry

The experimental dose from the incident beam was estimated by careful measurements of the ion current, recorded by a free-air ionisation chamber (OKEN S-1194, Tokyo, Japan) and compensating for the beam cross section. The energy liberated by the measured charge and the mass of air ionized was calculated to determine the dose in air. Accurate dosimetry for MRT is not trivial, with most groups relying on Monte Carlo computer simulations of absorbed dose distribution (16-18). We have developed a method of

measurement-based dosimetry for MRT using radiochromic films of different sensitivity, analysed using a microdensitometer, to determine the peak-to-valley dose ratio at different depths in tissue equivalent material. The range of peak-to-valley dose ratios between depths in tissue up to 10 mm (comparable to the mouse leg thickness) was 144 to 65. A complete description of the dosimetry employed for this MRT research is described in Crosbie *et al.*[1]. For treatment of both normal skin and tumors, radiochromic film (GafChromic HD-810, ISP Corp, New Jersey, USA) was placed on both sides of the skin flap or the leg bearing the tumor to permit in situ visualisation of the entrance and exit radiation fields.

Cell Lines, Mice and Tumor Growth

The EMT6.5 and 67NR mouse mammary tumor lines were cultured in alpha minimal essential medium (α-MEM) supplemented with 5% fetal calf serum and 1% penicillin/streptomycin at 37°C in 5% CO2 in air. Adult, female ddY mice (JASRI/SPring-8, Japan) and Balb/c mice (Animal Resource Centre, Perth, Australia) were used for the normal tissue studies, whilst female Balb/c mice (6-8 weeks of age) were used for the tumor studies. EMT6.5 and 67NR mammary tumor cells (50,000), both syngeneic to Balb/c mice, were injected subcutaneously into one or both hind legs, depending on the experiment, 7-10 days prior to the scheduled access time to the synchrotron. Based on pilot studies, this allowed small (1-2mm diameter) but palpable tumors to be

[1] J Crosbie, *et al.*, A method of dosimetry for synchrotron microbeam radiation therapy using radiochromic films of different sensitivity. Accepted for publication in *Physics in Medicine & Biology* September 2008.

identified on the outside of the leg at the time of MRT treatment. Mice were transported from Australia to Japan for treatment at the synchrotron after tumor inoculation, and returned to Australia for monitoring of tumor growth and normal tissue toxicity following treatment. Animals were culled when the thickness of the tumor plus leg reached 11 mm. For irradiation, the mice were anaesthetised with sodium pentobarbital (approximately 10 ml/kg). All experimental protocols were approved by the animal welfare committees of JASRI/SPring-8 and Monash University.

Irradiation of mice

Uni-directional synchrotron irradiation of normal and tumor tissues. For investigation of cellular responses to MRT, mice were irradiated with a single fraction of unidirectional, microbeam radiation with an in-beam, entrance dose of either 800 Gy (ddY mice) or 560 Gy (Balb/c mice). Dorsal hair was shaved, a skin flap was raised along the back and radiochromic film was placed on both sides of the skin flap to demarcate the entrance and exit radiation fields. The irradiation field size was 6 mm x 6 mm for the 800 Gy dose and 10mm (horizontal) x 6mm (vertical) for the 560 Gy dose. For sham-irradiated controls, six mice were anaesthetised and positioned on the treatment jig in an identical fashion to the irradiated mice. In some short term experiments, Balb/c mice that received the dorsal dose of 560 Gy were also subjected to a 560 Gy exposure to the right hind leg, which had

previously been inoculated with the EMT-6.5 tumor, using an irradiation field size of 10 mm x 10mm.

Cross-hatched synchrotron irradiation of tumors. Cross-hatched MRT was delivered to the mouse leg by rotating the jig by 90 degrees in the plane orthogonal to the incident beam and delivering a second MRT dose (2). A photograph of the setup and the cross-hatch pattern on radiochromic film is shown in Figure 1, D. The total irradiation field size was 10 x 10 mm. Nine 1mm increments of a goniometer-driven sample stage were required to deliver the beam in a 'step and shoot' manner. 67NR and EMT-6.5 tumor-bearing mice were randomised into MRT high dose, low dose and zero dose (control) groups, with ten animals in each group. The peak in-beam doses for the high and low dose groups were 560 Gy and 280 Gy respectively. Where the microbeams overlapped, the delivered entrance dose was as high as 1120 Gy. The valley dose was between 8 Gy and 17 Gy, assuming maximum and minimum peak-to-valley dose ratios of 144 and 65 respectively across the relevant tissue depths . Tumor growth was monitored and mice culled if the combined thickness of the leg plus tumor reached 11mm.

Broadbeam irradiation. Balb/c mice (10 per group) bearing EMT6.5 tumors on the right hindlimb were subjected to 0, 11, 22 or 44 Gy using a Varian 2100C linear accelerator (Varian Medical Systems, Palo

Alto, CA, USA), seven days after tumor cell inoculation. The dose rate was 20 Gy/min in a 6 MeV electron beam. The field size was 25 mm x 25 mm, with lead shielding to allow exposure only to the tumor-bearing leg. The mice were monitored for tumor growth and radiation toxicity and culled when the leg plus tumor thickness reached 11 mm or earlier if the tumor became ulcerated, or if the mouse showed signs of distress due to swelling or skin damage resulting from the radiation.

Response of cultured tumor cells to irradiation. Known numbers of EMT6.5 and 67NR cells were plated into triplicate 6cm Petri dishes for 6h prior to exposure to graded doses (up to 12.5 Gy) of radiation at a dose rate of 0.59 Gy/min using a Cs-137 gamma irradiator (Gammacell 40, Atomic Energy of Canada, Limited). Clonogenic survival was measurement by colony formation 8-9 days after the radiation exposure.

Tissue Harvesting. To obtain tissues for investigating cellular mechanisms, mice were culled by cervical dislocation at timed intervals up to 5 days post-irradiation. In some experiments, the mice were injected with bromodeoxyuridine (BrdU) (40 mg/kg) 4h before being culled. The skin flap and tumor were excised and fixed in formalin for 4-6h for subsequent histology and immunohistochemistry.

Histology. Formalin fixed tissues were embedded in paraffin and sections used for conventional haematoxylin & eosin staining, for apoptosis detection and for immunohistochemistry.

Apoptosis. *In situ* detection of apoptosis in tissue sections was achieved using an Apoptag Peroxidase *in situ* Apoptosis Detection kit according to the manufacturer's instructions (Chemicon International, Temecula, USA) and a previously published protocol (19). In brief, tissues were incubated with a mixture containing digoxigenin (Dig)-conjugated nucleotide and terminal deoxynucleotidyl transferase at 37°C for 1 hour. Tissue sections were incubated with anti-Dig horseradish peroxidase for 30 minutes. Diaminobenzidine (DAKO, Carpenteria, USA) was added for 2-3 minutes to reveal sites of anti-Dig binding. Sections were counterstained with Mayers Haematoxylin.

DNA Double Strand Breaks & Proliferation. Immunohistochemical detection of γ-H2AX required antigen retrieval by microwaving sections in a citrate buffer for 10 minutes. Sections were incubated overnight at 4°C with antibody (Anti-phospho-Histone H2AX (Ser139) Clone JBW301, Upstate, Temecula, CA, USA) diluted 1:1000 in a mouse-on-mouse diluent. Mouse-on-mouse biotinylated secondary antibody kit, conjugated with a Vectastain ABC kit (Vector Laboratories Inc., Burlinghame, CA, USA) was applied at room

temperature for 10 min, followed by chromogen (diaminobenzidine, Sigma-Aldrich, St Louis, MO, USA) for 5 min at room temperature.

For BrdU localisation, antigen retrieval was achieved using pepsin digestion, followed by sheep anti-BrdU (Biodesign International, Saco, Maine, USA) diluted 1:1000 in 10% donkey serum overnight at 4°C. A biotinylated donkey anti-sheep secondary antibody (Jackson Immuno Research, West Grove, PA, USA) conjugated with alkaline phosphatase streptavidin (Vector Laboratories Inc., Burlinghame, CA, USA), was applied at room temperature for 30 min, with Vector Blue chromogen (Vector Laboratories Inc., Burlinghame, CA, USA) to identify cells undergoing DNA replication. Both single and double immunohistochemical staining was achieved using antibodies for γ-H2AX and BrdU.

Image Analysis

Images of immunostained skin and tumor sections were acquired using a Zeiss ICc3 digital camera connected to a Zeiss Axioskop light microscope (Carl Zeiss GmbH, Gottingen, Germany). A calibrated graticule was used for software-driven distance calibration (pixels/μm). The software used to acquire and analyse the images was Axiovision v.4.2 (Carl Zeiss GmbH, Gottingen, Germany).

Digital images were acquired in areas corresponding to the irradiated regions, covering peaks and valleys Manual cell counting (number of cells per

mm^2) was performed for the images acquired from the TUNEL and γ-H2AX/BrdU assays on normal skin tissue and the TUNEL assay on tumors on a total of six images per mouse using a x20 objective lens.

For the quantification of γ-H2AX and BrdU in tumors, the automatic target detection algorithm of the Axiovision software was used to segment cells based upon the criteria of colour information (hue, saturation and intensity) and their physical size. The γ-H2AX and BrdU counts were obtained from a single image using a x10 objective lens. Statistical information was extracted from the analysed images, such as the proportional area, the cell (grain) count and colour information. The number of automatically detected cells per mm^2 was recorded for mice irradiated and culled at the different time points post-irradiation and for unirradiated mice. Automatic target detection was carried out on single-stain immunohistochemistry sections of γ-H2AX and BrdU, rather than the double-stained sections, to improve the accuracy of the cell detection.

Statistical Methods

All statistical analyses were performed using the SPSS 15.0 software system, (SPSS, Chicago, IL, USA). Differences in proliferation between irradiated and unirradiated tumor groups were analyzed with a two-sided, unpaired Student t test. Log-rank, Breslow and Tarone-Ware tests of equality of survival distributions were all significant to < 0.0005. Plots of γ-H2AX, BrdU and TUNEL counts are shown as means with 95% confidence intervals.

Results

Differential cellular responses of normal and tumor tissue to MRT.

DNA damage: γ-H2AX was used as a marker at cellular dimensions,for damage to tissue from the microbeam radiation. MRT tracks were identified by γ-H2AX immunostaining of mouse skin irradiated with a peak-in-beam entrance dose of 560 Gy and culled 4 hours later (Figure 2, A). Persistent but reduced immunostaining was also seen at 24 hours (2, B) and 84 hours (2, C) post-irradiation. An unirradiated skin section (2, D), showed practically no γ-H2AX-positive staining. Epithelial cells in the epidermis and hair follicles appeared most sensitive to the radiation, as indicated by strong γ-H2AX immunostaining (Figure 3, A). Endothelial cells in irradiated blood vessels were positive for γ-H2AX (3, B) as were cells in the muscle layers (3, C) while fibroblasts in the dermis were predominantly negative for γ-H2AX (3, A). The spatial localisation of the γ-H2AX immunostaining was precise enough to allow the path of a microbeam through an individual hair follicle bulb to be visualised (3, D).

In irradiated tumors harvested 4 hours post-MRT, γ-H2AX immunostaining produced a pattern of positive cells that corresponded precisely to the spatial arrangement of the MRT beam (Figure 4, A). Unlike skin, EMT-6.5 tumor cells were highly migratory in the hours following MRT, with obvious movement of γ-H2AX positive cells out of peak radiation zones by 12 hours (4, B), and complete intermixing of peak and valley irradiated

cells by 24-48 hours post-irradiation (4, C, 4, E). Double immunostaining for γ-H2AX and BrdU confirmed that tumor cells were migrating both into and out of the peak irradiated zones, resulting in close apposition of peak and valley irradiated cells throughout the tumor (4, B, 4, C and 4, E). Non-irradiated tumors showed no evidence of γ-H2AX immunostaining (4, D).

Phosphorylated γ-H2AX immunostaining was maximal in both normal skin and tumor 30 minutes post-irradiation with MRT (Figures 5, A, B). H2AX immunostaining decreased significantly up to 24 hours, but was still evident at 84 hours in both tissue types. From 24-84 hours post-MRT, γ-H2AX positive cell numbers continued to drop in normal skin, but remained relatively constant in tumors. The different tissue compartments within skin (e.g. epidermis, muscle, glands and connective tissue) expressed variable levels of γ-H2AX at four hours post-irradiation (5, C).

Proliferation: There were virtually no BrdU-positive cells in MRT-treated skin until 48 hours post-irradiation, when proliferation commenced (5, D). There were clear differences in BrdU staining of different cell types within the skin, with epithelial cells showing the most proliferation at 84 hours (Figure 6, A) and the dermis (connective layer) and muscle layers the least (5, E). There was also evidence of epithelial cell migration in MRT-irradiated skin in and around hair follicles, sebaceous glands and in the epidermis (6, A). Muscle tissue immediately underneath irradiated dermis displayed damage and disruption that was not repaired by 84 hours (6, B).

The proliferative response to MRT was markedly different in the tumors. As expected, the majority of cells in non-irradiated tumors were BrdU-positive (Figure 4, D). At 4 hours post-MRT, BrdU-positive tumor cells were located in the valley regions between adjacent microbeams (4, A). There was a significant decrease in proliferation by 24 hours post-irradiation compared to non-irradiated tumors ($P = 0.002$) (Figure 5, F), and proliferation levels remained significantly lower than in non-irradiated tumors until at least 84 hours post-irradiation ($P = 0.001$).

Apoptosis: We observed a differential persistence of apoptosis in normal skin and tumor following MRT. Representative images of TUNEL-stained mouse skin sections (Figures 7, A and B) from mice culled 6 hours post-800 Gy MRT and 4 hours post-560 Gy-MRT respectively reveal TUNEL-positive cells with a dark brown nuclear stain. In normal skin, the number of TUNEL-positive cells was elevated by 6 hours post-irradiation, but by 48 and 120 hours post-MRT, the number of apoptotic cells had returned to unirradiated skin levels (7, C). In MRT-treated tumors, apoptosis levels were significantly higher than in untreated tumors and increased until at least 84 hours post-irradiation (7, D). TUNEL positive cells in MRT-irradiated tissue did not appear in lines, or tracks, as observed with γ-H2AX.

Tumor growth delay achieved using cross-hatched MRT. Minimal normal tissue toxicity.

MRT increased survival times for Balb/C mice inoculated with the

EMT-6.5 and 67NR tumor cells with minimal radiation toxicity. The median survival times for EMT-6.5 and 67NR tumor bearing Balb/C mice following MRT (2 x 560 Gy) increased from 16 to 29 and 27 to 42 days respectively, compared to unirradiated controls ($P < 0.0005$, Figure 8, A, B). Two mice with EMT-6.5 tumors in the MRT high dose group and one mouse in the low dose group were still alive at the end of the study (day 49) with no palpable tumor.

By 28 days post-irradiation, some skin reddening and keratinous crust was observed on the legs of the irradiated non-tumor bearing mice. We noted hair epilation and some temporary impairment of leg movement in mice irradiated with 2 x 560 Gy. These side effects were most noticeable at the beam exit point on the mouse leg. By 46 days post-irradiation, the only noticeable effect of the radiation in the high dose group was epilation and scaly skin.

Tumor growth delay using conventional radiotherapy. Significant normal tissue toxicity.

The median survival times following broadbeam radiotherapy for EMT-6.5 tumor-bearing Balb/C mice increased from 19 days (unirradiated controls) to 27 days for 11 Gy and to 33 days for the 22 Gy exposure ($P < 0.0005$) (Figure 8, C). However, this was accompanied by notable radiation toxicity including swelling of the leg and hair loss at the two higher doses. The 44 Gy group is not shown on the Kaplan-Meier survival plot since all mice had to be culled

due to distress from normal tissue damage before the designated endpoint was reached. These mice suffered from hair loss, reddened, thin and fragile skin and severe swelling of the leg.

Intrinsic tumor cell response to radiation. The clonogenic survival of the EMT-6.5 and 67NR tumor cell lines following exposure to increasing doses of Cs-137 gamma radiation was assessed. The results (8, D) showed that the response was similar between the two lines, with the EMT-6.5 tumor cell line being slightly more resistant than 67NR.

Discussion

MRT promises a new approach to radiation therapy. However, there are only a limited number of reports using rodent tumor models and mechanistic studies have not been forthcoming. This study provides the first evidence for a differential tissue response at a cellular level between normal and tumor tissues following irradiation with synchrotron generated MRT. These observations have been made possible by the use of γ-H2AX as an immunohistochemical marker to identify MRT irradiated cells, thus allowing spatial resolution of tissue response at the cellular level.

γ-H2AX immunohistochemistry showed that in mouse skin the tissue geometry is largely retained post-MRT, with stripes of γ-H2AX positive cells visible for at least three and a half days after irradiation. In complete contrast,

in the EMT-6.5 tumor γ-H2AX positive cells rapidly inter-mix with non-positive cells, such that despite the presence of γ-H2AX positive cells 24 hours post-MRT, there is no recognizable spatial organisation into stripes. This rapid intra-tumoral migration of irradiated cells is a novel observation, and has significant implications for understanding tumor response to MRT. The extent of migration in non-irradiated tumors remains unclear, however it has been reported that only 1-5% of cells within the tumor are motile (20).

The post-MRT tumor cell migration or 'washing machine' effect results in peak dose and valley dose irradiated tumor cells thoroughly intermixing by 24 hours post-MRT (Figure 4, E). Cells irradiated with 100's of Gray are destined to die, but this process may take several hours or days. This mixing results in close apposition of lethally irradiated and normal cells. If the lethally irradiated cells are releasing toxic death signals, a localised 'bystander effect' between adjacent cells may help to explain the reduction in tumor cell proliferation.

While γ-H2AX induction occurs within minutes of DNA damage, the dephosphorylation and/or removal of γ-H2AX foci by phosphatases occurs over hours to days and is closely related to double strand break repair proteins such as Rad50 and BRCA1 (21). It is unclear why many skin and tumor cells in our MRT study retain γ-H2AX positivity for long periods post-irradiation, but a correlation between increased γ-H2AX persistence, unrepaired DNA damage and cell death has been observed in some studies, as reviewed in (21).

Normal human fibroblasts can remain metabolically active for several weeks following exposure to supra-lethal doses (80 Gy) of X-rays (Kai Rothkamm, unpublished data). However, DNA double strand break repair in the presence of thousands of double strand breaks induced by high dose (80 Gy) X-rays is often faulty and most repair events produce large-scale genomic rearrangements, which are likely to prevent successful mitotic cell division (reviewed in (22)).

In contrast to tumor cells, the number of γ-H2AX-positive cells per unit area in skin decreases with time to at least 84 hours post-irradiation (Figure 5, A). The number of γ-H2AX-positive cells per unit area in the EMT6.5 tumor remained constant between 24 hours and 84 hours post-irradiation (5, B). This supports our proposal that the mechanisms for removal of damaged cells and for tissue repair are different in normal skin and tumor.

Cell proliferation in skin (as detected by BrdU incorporation) showed a co-ordinated increase from 24-84 hours post MRT, presumably reflecting organised tissue repair. This increase in proliferation coupled with the observed decrease in γ-H2AX positive cells demonstrates the ability of an organised tissue to respond to radiation damage. In contrast, there was decreased tumor cell proliferation by 12 hours post-irradiation and this remained low out to 84 hours (5, F). As with the γ-H2AX positive cell clearance, this is consistent with a failure to mount a normal repair response to radiation damage in the tumor. It is likely that the disorganised architecture of

the EMT-6.5 tumor impedes a competent repair response to eliminate and replace radiation-damaged cells.

Based on research in the 1950s and 1960s using a deuteron beam incident on the cerebellum of rodents, it was hypothesized that blood vessels irradiated with high dose MRT may be repaired through the migration of endothelial cells over distances comparable to physical beam width (20-30 μm) (23, 24). This microvascular hypothesis was restated by Slatkin *et al.* (25) in the first animal studies of synchrotron MRT and also by other MRT investigators. Serduc *et al.* (26) published glioma-inoculated mouse data indicating that the mechanism of action of MRT did not involve a significant microvascular component, and postulated on cytoreduction mechanisms in their mouse brain tumor model (26). Our double immunohistochemical staining of irradiated EMT-6.5 tumors using γ -H2AX and CD-31, a marker of blood vessels, did not appear to show evidence of a microvascular effect in MRT-irradiated tumors (Supplementary data). Irradiated blood vessels within EMT-6.5 tumors appeared functional and patent until 84 hours post-irradiation and were comparable to the vasculature within unirradiated tumors.

It was somewhat surprising that the TUNEL assay was not more effective at identifying the irradiated zones in the same way that γ-H2AX did. That apoptosis was not preferentially occurring in the MRT tracks could only be expected if its induction was dose dependent between ~10 Gy in valleys and hundreds of Gy in MRT tracks. However, apoptosis induction tends to

increase steeply with dose at low doses (<1Gy) and plateaus at higher doses, both in lymphocytes and tumour cell lines (27, 28). We are not aware of any studies comparing apoptosis at tens and hundreds of Gray.

Dilmanian *et al.* (2) described the palliative effects of MRT on the EMT-6 mouse model using the cross-hatched technique. They used a 90 μm wide beam with a 300 μm centre-to-centre spacing with peak, in-beam entrance doses of 2 x 410 Gy, 2 x 520 Gy and 2 x 650 Gy. The valley dose was estimated to be 4% of the peak dose. Complete tumor ablation was reported in four of eight mice in both the 2 x 410 Gy and 2 x 520 Gy groups with complete tumor ablation in six of seven mice in the 2 x 650 Gy group. In contrast, only 2/9 mice in our high dose group and 1/9 in our low dose group had their tumors ablated by the end of the study. A limitation of our study was a lack of pre-treatment imaging to localise the tumor. Our results may have been different had we been able to confirm that we irradiated the margins of the tumor. Further MRT studies need to include pre-treatment verification images of the target volume.

MRT includes an inherent, broad beam dose, termed the valley dose. The 11 Gy and 22 Gy dose regimens in our broad beam study were chosen deliberately to reflect our initial estimate of the mean valley dose in the MRT arrangement, assuming a peak-to-valley dose ratio of 50 for uni-directional irradiation. However, subsequent and more precise investigations of this ratio showed it was closer to 65 at minimum and varied with depth. Therefore, in

our cross-hatched MRT study, there were parts of the mouse leg that received a maximum valley dose of 17 Gy. However, these mice did not show the same levels of radiotoxicity as did the mice that received 22 Gy on a conventional, linear accelerator, despite a much larger integrated dose (1280 Gy x 25 μm /200μm = 70 Gy). Dilmanian *et al.* noted that there was a unique biological effect distinct from a volume effect with MRT (2).

Our tumor migration data may have implications for temporal fractionation, in addition to spatial fractionation. Fractionating the dose in time may only lead to a smeared broad beam effect, as the tumor cells will have migrated by the time of the next fraction. This is especially true for a bi-directional, inter-leafing technique, requiring micron precision. However, if one were to fractionate with weekly intervals between fractions, the normal tissue should have repaired itself (extrapolating from Figure 5, A), the overall dose to the tumor would still be cumulative and the prospect of a cure would increase.

In conclusion, by using immunohistochemistry of γ-H2AX to identify cells that have received peak doses of synchrotron generated MRT radiation, we have been able to demonstrate a differential cellular response between tumor and normal tissues. Tumors showed extensive cell migration post-MRT resulting in a complete mixing of MRT peak and valley dose irradiated cells within 24 hours. By contrast, in normal skin peak dose irradiated cells showed minimal evidence of migration up to 3.5 days post irradiation. There were also

significant differences in cell proliferation and γ-H2AX-positive cell clearance dynamics in the days following MRT. These data provide the first insights into biological mechanisms that may explain why normal tissues, but not tumors, are relatively resistant to spatially fractionated radiation.

References

1. Dilmanian FA, Button TM, Le Duc G, Zhong N, Pena LA, Smith JA, et al. Response of rat intracranial 9L gliosarcoma to microbeam radiation therapy. Neuro-oncol 2002;4(1):26-38.

2. Dilmanian FA, Morris GM, Zhong N, Bacarian T, Hainfeld JF, Kalef-Ezra J, et al. Murine EMT-6 carcinoma: high therapeutic efficacy of microbeam radiation therapy. Radiat Res 2003;159(5):632-41.

3. Laissue JA, Geiser G, Spanne PO, Dilmanian FA, Gebbers JO, Geiser M, et al. Neuropathology of ablation of rat gliosarcomas and contiguous brain tissues using a microplanar beam of synchrotron-wiggler-generated X rays. Int J Cancer 1998;78(5):654-60.

4. Miura M, Blattmann H, Brauer-Krisch E, Bravin A, Hanson AL, Nawrocky MM, et al. Radiosurgical palliation of aggressive murine SCCVII squamous cell carcinomas using synchrotron-generated X-ray microbeams. Br J Radiol 2006;79(937):71-5.

5. Zhong N, Morris GM, Bacarian T, Rosen EM, Dilmanian FA. Response of rat skin to high-dose unidirectional x-ray microbeams: a histological study. Radiat Res 2003;160(2):133-42.

6. Laissue JA, Blattmann H, Di Michiel M, Slatkin DN, Lyubimova N, Guzman R. The weaning piglet cerebellum: a surrogate for tolerance to MRT (microbeam radiation therapy) in paediatric neuro-oncology. Proc. SPIE 2001;4508(Penetrating radiation systems & applications III).

7. Lobrich M, Rief N, Kuhne M, Heckmann M, Fleckenstein J, Rube C, et al. In vivo formation and repair of DNA double-strand breaks after computed tomography examinations. Proc Natl Acad Sci U S A 2005;102(25):8984-9.

8. Qvarnstrom OF, Simonsson M, Johansson KA, Nyman J, Turesson I. DNA double strand break quantification in skin biopsies. Radiother Oncol 2004;72(3):311-7.

9. Rothkamm K, Balroop S, Shekhdar J, Fernie P, Goh V. Leukocyte DNA damage after multi-detector row CT: a quantitative biomarker of low-level radiation exposure. Radiology 2007;242(1):244-51.

10. Rothkamm K, Kruger I, Thompson LH, Lobrich M. Pathways of DNA double-strand break repair during the mammalian cell cycle. Mol Cell Biol 2003;23(16):5706-15.

11. Rothkamm K, Lobrich M. Evidence for a lack of DNA double-strand break repair in human cells exposed to very low x-ray doses. Proc Natl Acad Sci U S A 2003;100(9):5057-62.

12. Sedelnikova OA, Rogakou EP, Panyutin IG, Bonner WM. Quantitative detection of (125)IdU-induced DNA double-strand breaks with gamma-H2AX antibody. Radiat Res 2002;158(4):486-92.

13. http://www.spring8.or.jp/wkg/BL28B2/instrument/lang-en/INS-0000000374/instrument_summary_view?q=BEwH&f=. 1/08/2008.

14. Ohno Y, Torikoshi M, Suzuki M. Dose distribution of a 125 keV mean energy microplanar x-ray beam for basic studies on microbeam radiotherapy.

Med Phys 2008;35(7):3252-3258.

15. Tinaka T, Kitamura H. SPECTRA: a synchrotron radiation calculation code. Journal of Synchrotron Radiation 2001;8:1221-1228.

16. Orion I, Rosenfeld AB, Dilmanian FA, Telang F, Ren B, Namito Y. Monte Carlo simulation of dose distributions from a synchrotron-produced microplanar beam array using the EGS4 code system. Phys Med Biol 2000;45(9):2497-508.

17. De Felici M, Felici R, Sanchez del Rio M, Ferrero C, Bacarian T, Dilmanian FA. Dose distribution from x-ray microbeam arrays applied to radiation therapy: an EGS4 Monte Carlo study. Med Phys 2005;32(8):2455-63.

18. Siegbahn EA, Stepanek J, Brauer-Krisch E, Bravin A. Determination of dosimetrical quantities used in microbeam radiation therapy (MRT) with Monte Carlo simulations. Med Phys 2006;33(9):3248-59.

19. Ruwanpura SM, McLachlan RI, Matthiesson KL, Meachem SJ. Gonadotrophins regulate germ cell survival, not proliferation, in normal adult men. Hum Reprod 2008;23(2):403-11.

20. Pinner S, Sahai E. Imaging amoeboid cancer cell motility in vivo. J Microsc 2008;231(3):441-5.

21. Kao J, Milano MT, Javaheri A, Garofalo MC, Chmura SJ, Weichselbaum RR, et al. gamma-H2AX as a therapeutic target for improving the efficacy of radiation therapy. Curr Cancer Drug Targets 2006;6(3):197-205.

22. Rothkamm K, Lobrich M. Misrepair of radiation-induced DNA double-strand breaks and its relevance for tumorigenesis and cancer treatment (review). Int J Oncol 2002;21(2):433-40.

23. Zeman W, Curtis HJ, Baker CP. Histopathologic effect of high-energy-particle microbeams on the visual cortex of the mouse brain. Radiat Res 1961;15:496-514.

24. Curtis HJ. The use of deuteron microbeam for simulating the biological effects of heavy cosmic-ray particles. Radiat Res Suppl 1967;7:250-7.

25. Slatkin DN, Spanne P, Dilmanian FA, Gebbers JO, Laissue JA. Subacute neuropathological effects of microplanar beams of x-rays from a synchrotron wiggler. Proc Natl Acad Sci U S A 1995;92(19):8783-7.

26. Serduc R, Christen T, Laissue J, Farion R, Bouchet A, Sanden B, et al. Brain tumor vessel response to synchrotron microbeam radiation therapy: a short-term in vivo study. Phys Med Biol 2008;53(13):3609-22.

27. Torudd J, Protopopova M, Sarimov R, Nygren J, Eriksson S, Markova E, et al. Dose-response for radiation-induced apoptosis, residual 53BP1 foci and DNA-loop relaxation in human lymphocytes. Int J Radiat Biol 2005;81(2):125-38.

28. Baierlein SA, Distel L, Sieber R, Weiss C, Rodel C, Sauer R, et al. Combined effect of tumor necrosis factor-alpha and ionizing radiation on the induction of apoptosis in 5637 bladder carcinoma cells. Strahlenther Onkol 2006;182(8):467-72.

Funding

This work was supported by a Cancer Council Victoria Venture Grant to PAWR, RAL, IS, BW; an Australian Nuclear Science and Technology Organisation (ANSTO) grant to JCC and PAWR; a Monash University postgraduate scholarship to JCC; a Cancer Research UK grant (C14504/A6116) to KR; and a National Health and Medical Research Council of Australia Fellowship (Grant No. 143805) to PAWR.

The authors declare that a conflict of interest does not exist.

Acknowledgements

We are grateful to Mr. William Lanigan, Monash Animal Services, for his assistance with the logistics of transporting the mice to and from Japan. The authors acknowledge Ms. Frances M. Daley, Gray Cancer Institute, University of Oxford, UK for performing initial γ-H2AX immunohistochemistry staining on the skin sections.

We thank Dr. Duncan Butler, Australian Radiation Protection and Nuclear Safety Agency, Dr. Tomasz Wysokinski, Canadian Light Source, Saskatoon, Canada, Dr. Chris Hall, Dr. Toby Beveridge and Mr. Ivan Williams, Monash University, Victoria, Australia, for providing technical assistance during the various experiments at SPring-8. We are also grateful to Dr. Keiji Umetani and Dr. Yashuiko Imai, SPring-8/JASRI, for technical assistance and advice during the experiments. Finally, we thank Dr. Jim Hagekyriakou from the

Dept. of Physical Sciences at the Peter MacCallum Cancer Centre, Melbourne, Australia, for his assistance with the conventional radiotherapy study.

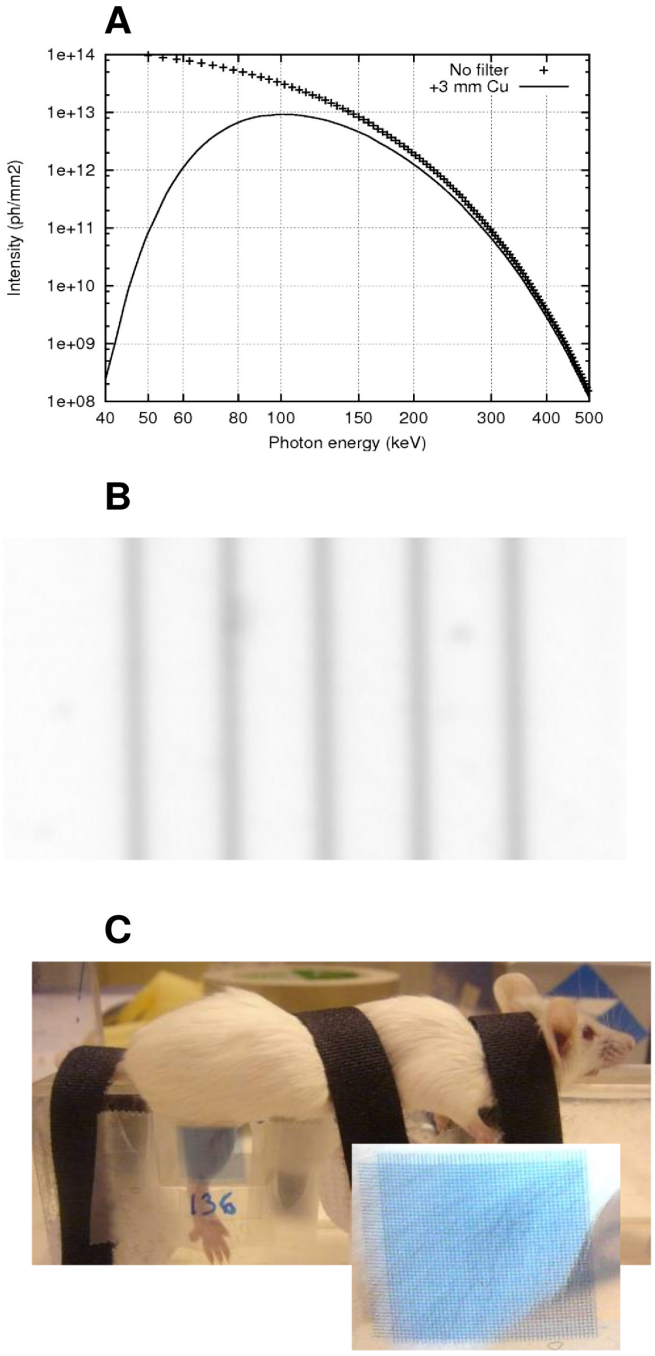

Figure 1. **A**) The energy spectrum (on a log-log scale) of the X-ray beam produced by the bending magnet source for beamline BL28B2 at the SPring-8 synchrotron. The spectrum with and without 3 mm of Cu absorber is plotted.

B) Section of radiochromic film which has been exposed to MRT. **C**) Photograph of mouse irradiation setup for survival studies. The mouse and jig were rotated 90 degrees by hand (orthogonal to the beam) after the first microbeam irradiation. The inset shows the cross-hatched pattern delivered to radiochromic film that was attached to the leg of the mouse.

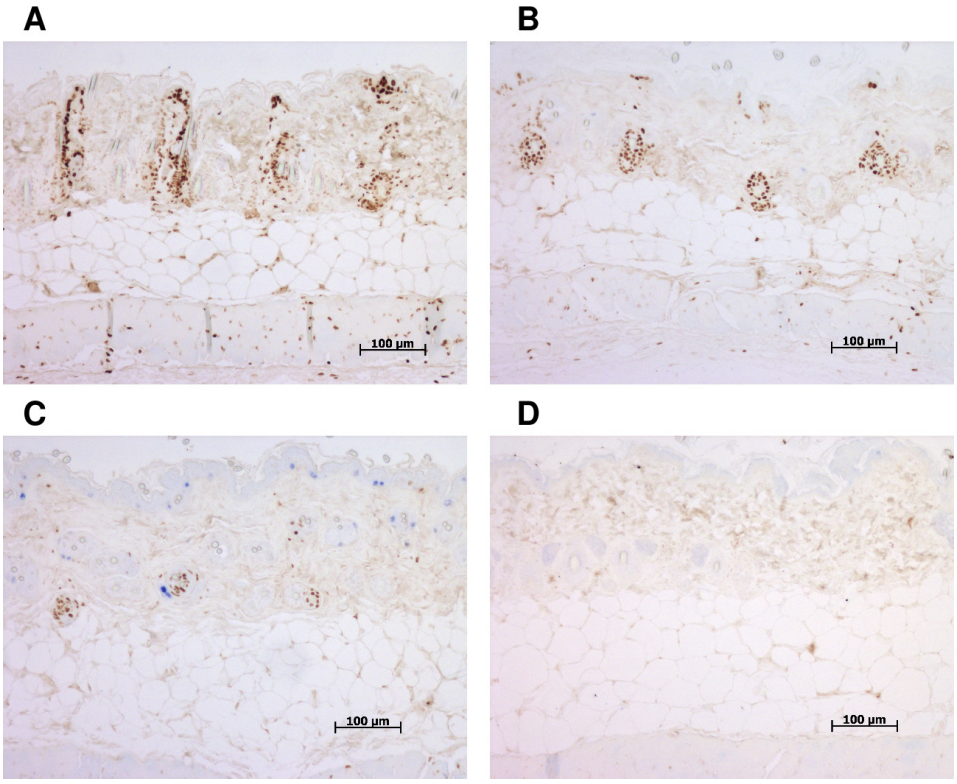

Figure 2. Representative images of γ-H2AX/BrdU-stained sections from mouse skin at 4 hours (**A**), 24 hours (**B**) and 84 hours (**C**) post-irradiation, with a peak entrance dose of 560 Gy. The path of the microbeams through the tissue is visible as brown stripes of cells positive for γ-H2AX. **D**) Image of a γ-H2AX-stained section from unirradiated mouse skin. BrdU-positive cells appear blue and are epithelial cells in the epidermis layer and in hair follicles (**C**).

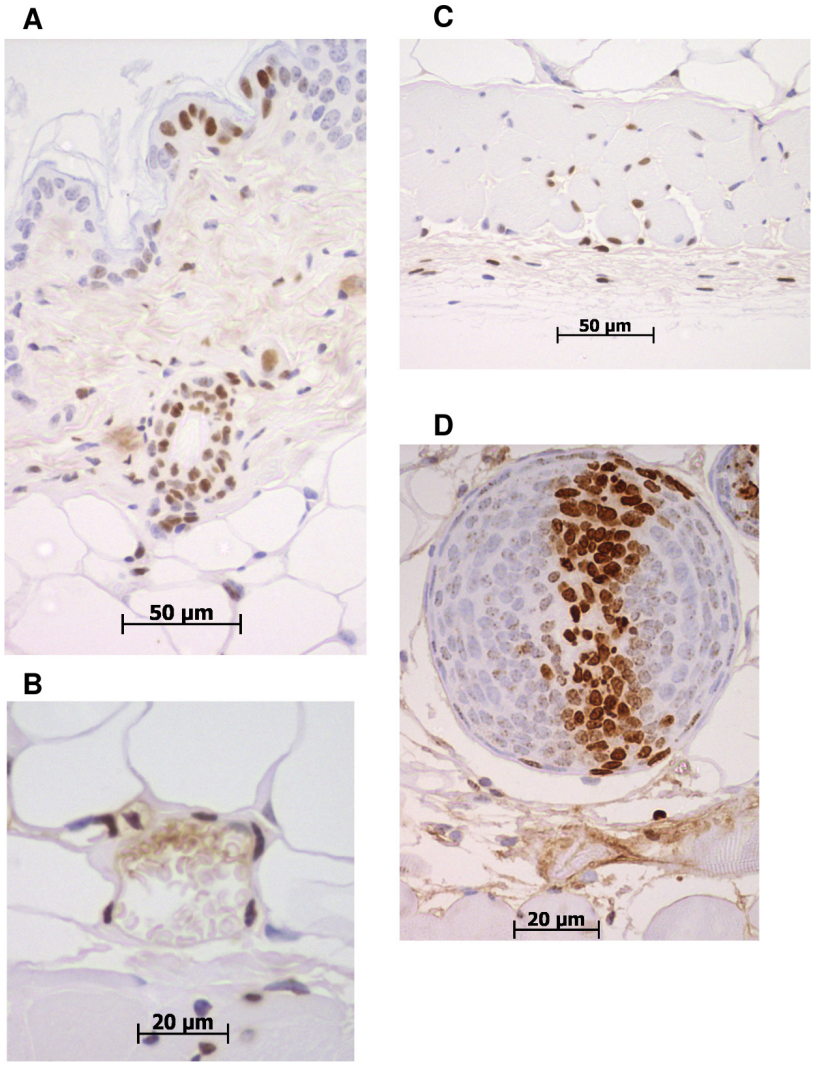

Figure 3. Epithelial cells (**A**), endothelial cells (**B**) and muscle cells (**C**) in normal skin are positive for γ-H2AX post 560 Gy MRT. **D**) The central portion of a hair follicle bulb is positive for γ-H2AX indicating the path of an X-ray microbeam. This skin section was from a mouse culled 6 hours post-irradiation. Epithelial cells in the outer portions of the follicle were not positive and thus were spared the high dose microbeam.

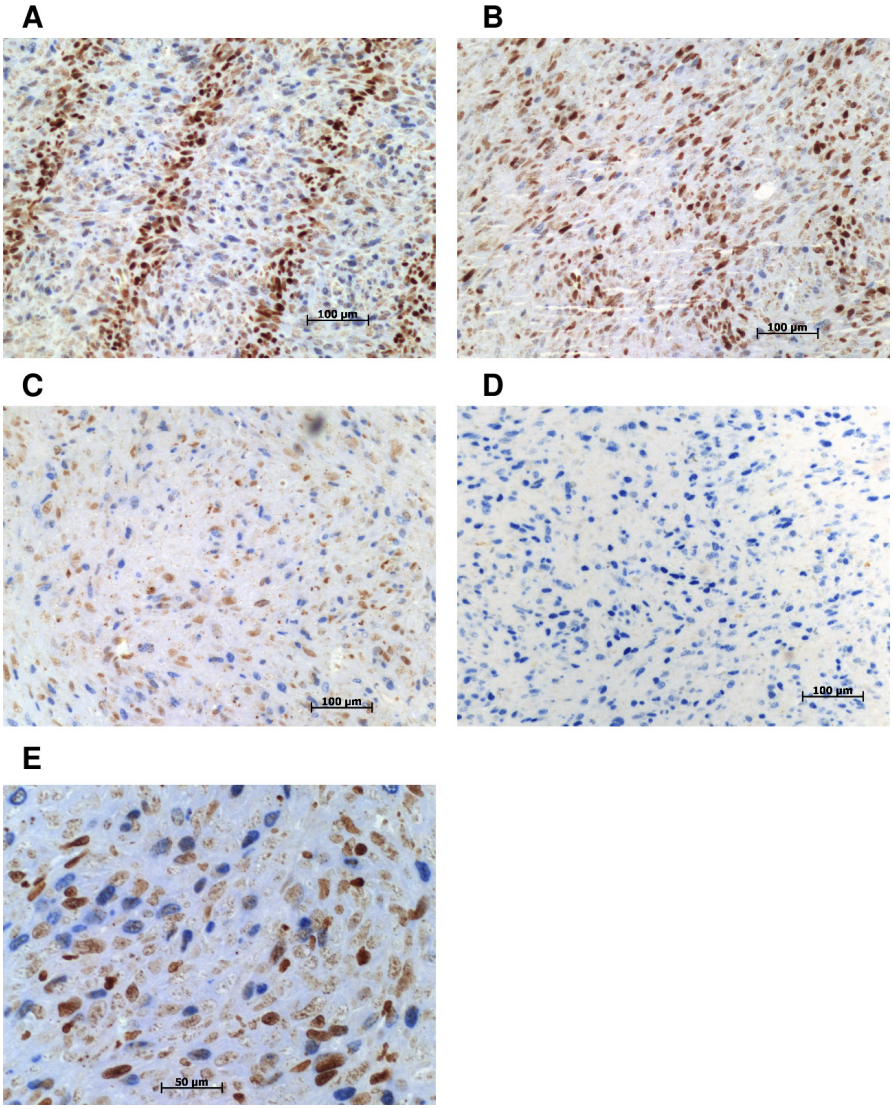

Figure 4. Representative images of γ-H2AX/BrdU-stained sections of EMT-6.5 tumors from mice culled at 4 hours (**A**), 12 hours (**B**) and 48 hours (**C**) post-irradiation with a peak entrance dose of 560 Gy. Cells undergoing histone phosphorylation at DNA double strand breaks are stained brown and cells replicating their DNA are shown in blue. Cell migration is obvious by 12 hours and by 48 hours the cells have completely intermixed. **D**) An

unirradiated tumor section. **E**) At higher magnification, complete cell migration and intermixing was observed in some regions by 24 hours post-migration.

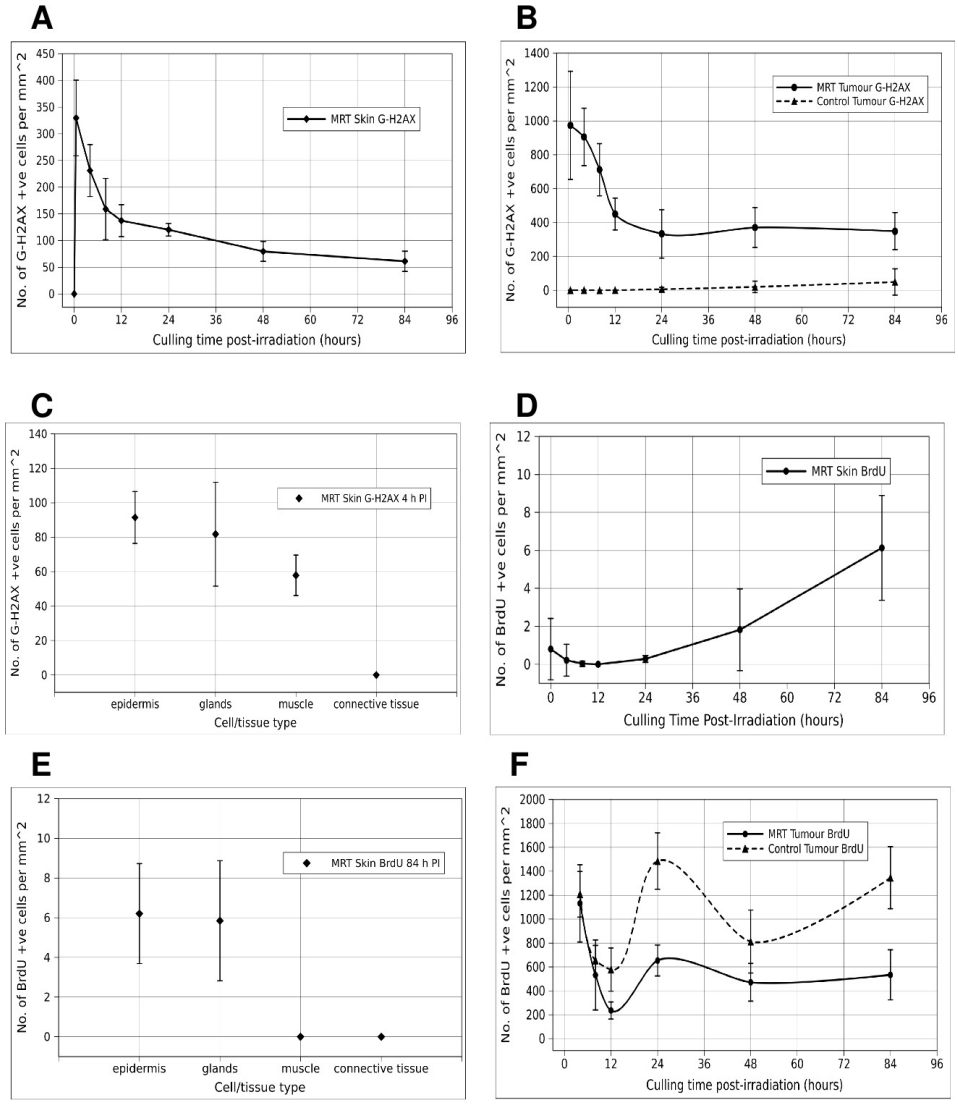

Figure 5. Quantitative analysis of γ-H2AX counts in MRT-irradiated skin (**A**), tumor (**B**), and different skin compartments (**C**). Quantitative measurements of BrdU counts in skin (**D**), skin tissue compartments (**E**) and tumor (**F**). For the skin plots, 0 hours post-irradiation corresponds to unirradiated tissue. Plots (**C** & **E**) were weighted to account for the total cell count in each compartment. In all plots, the uncertainties (error bars) are

expressed as the 95% confidence interval.

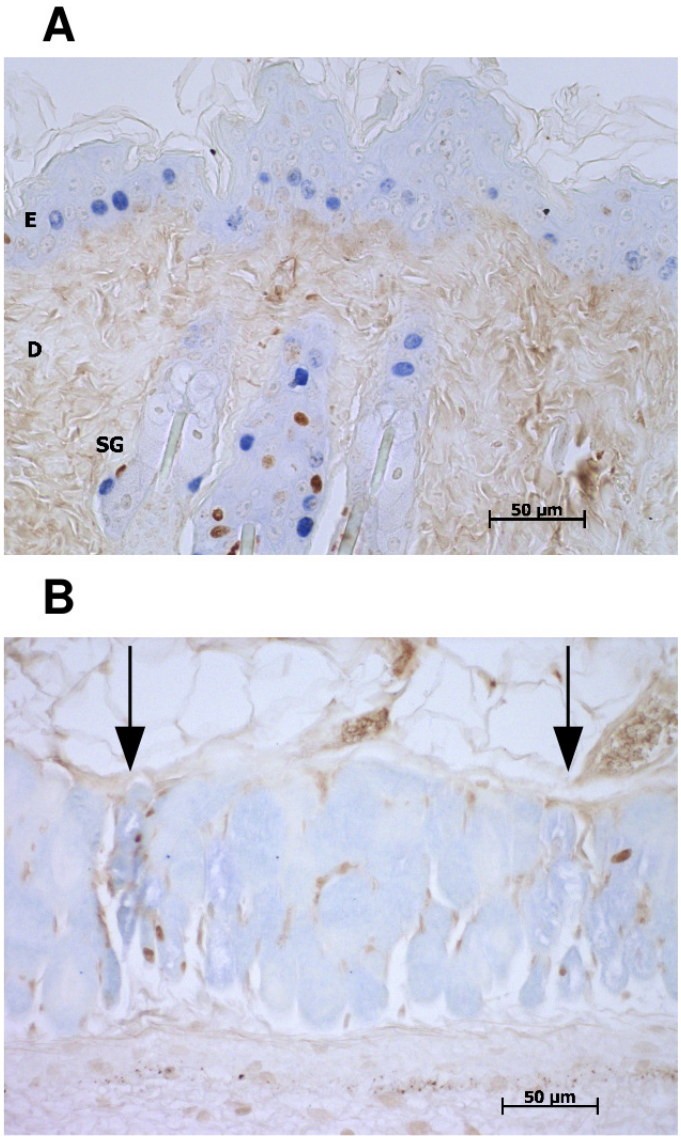

Figure 6. **A**) Epithelial cells (blue) in normal skin stain positive for BrdU 84 hours post-irradiation. (**B**) Proliferation was not observed in the muscle layer post-irradiation, and radiation damage and disruption of the muscle tissue had not been repaired by 84 h. The arrows indicate the path of the microbeams as

inferred by positive γ-H2AX staining in epithelial cells above the muscle layer.

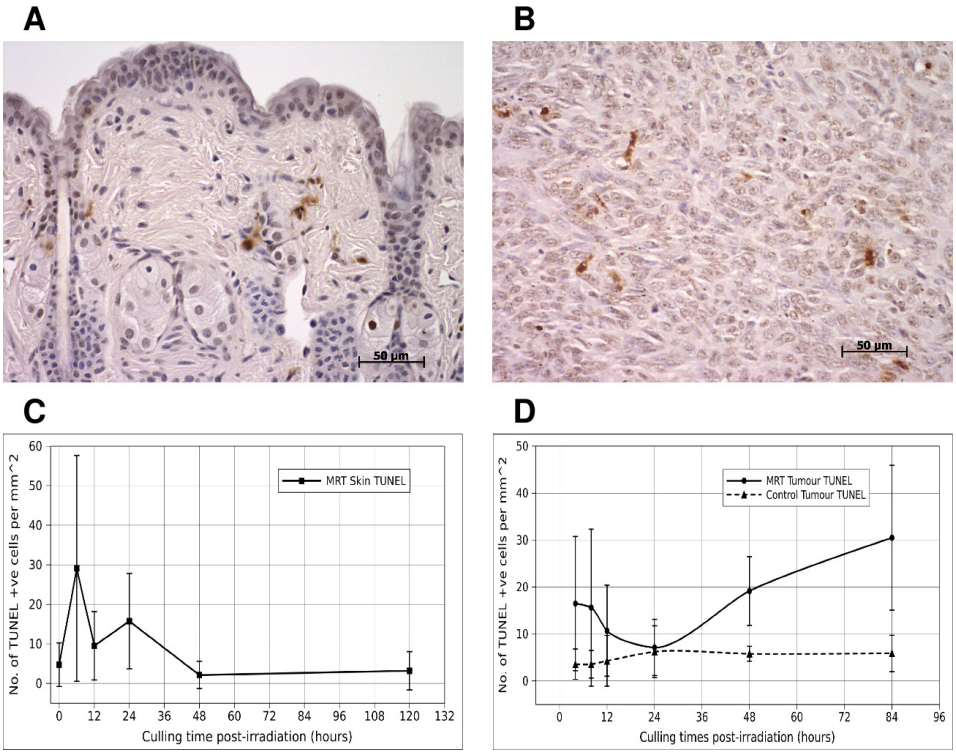

Figure 7. Representative images of TUNEL-stained sections from mouse skin 6 hours post-irradiation with MRT at an in-beam dose of 800 Gy (**A**) and from a tumor 4 hours post-irradiation with 560 Gy MRT (**B**). A TUNEL-positive cell (apoptotic) is characterised by a dark brown colour in the nucleus. Quantitative plots of TUNEL counts in skin (**C**) and tumor (**D**). The uncertainties are expressed as the 95% confidence interval.

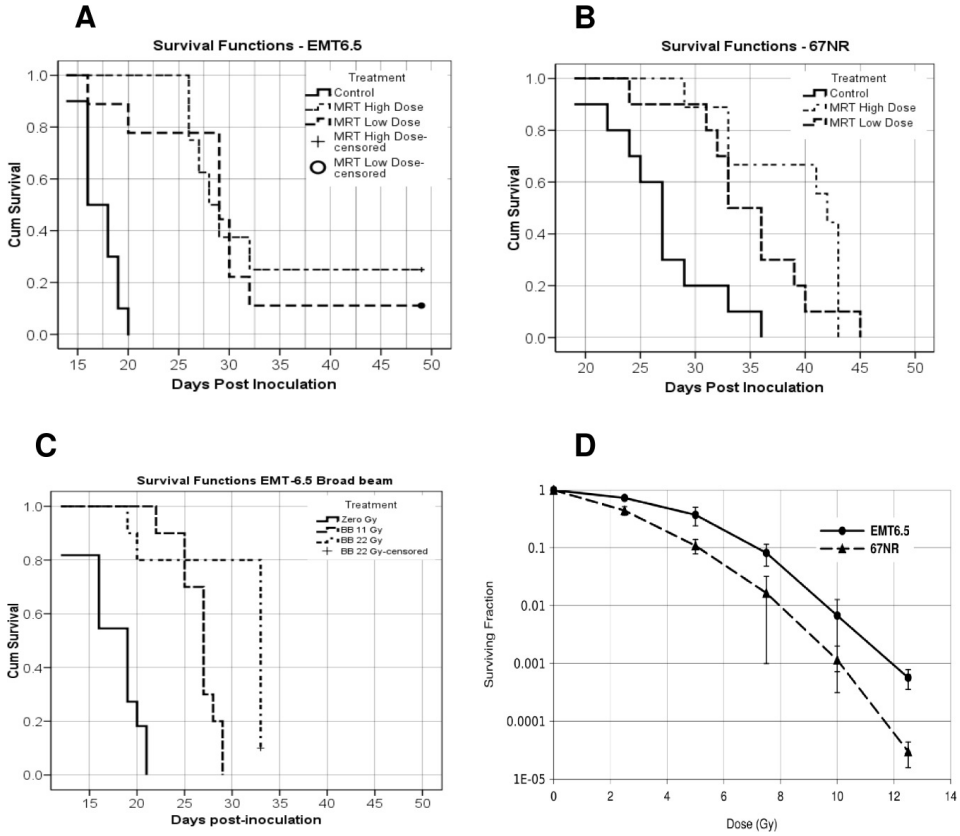

Figure 8. Kaplan-Meier survival curves for mice inoculated with the EMT-6.5 (**A**) and 67NR (**B**) tumor cells. Mice were treated with high dose, cross-hatched MRT (2 x 560 Gy) or low dose (2 x 280 Gy). **C**) Kaplan-Meier survival curves for EMT-6.5 tumor bearing mice treated with conventional radiotherapy (11 Gy or 22 Gy). **D**) *In vitro* clonogenic survival of EMT-6.5 and 67NR tumor cells to increasing doses of radiation from a Cs-137 gamma radiation source.

CHAPTER 7

Works in Progress

7.1 Introduction

The purpose of this section is to describe works still in progress, that is, related projects that were started but not completed within the time-frame of the PhD. Some of these projects are now the subject of a major grant application.

7.2 Bidirectional MRT, Gel Dosimetry & Treatment Planning

The cross-hatch, (or cross-planar) irradiations described in chapter 6 of the thesis, and by Dilmanian et al. (2003) deliver radiation in such a way that the entrance and exit of the two fields are the same. In chapter 6, the mouse and jig were rotated in the plane orthogonal to the beam, the clinical equivalent of rotating the treatment couch on a linac before delivering the second field (Figure 7.1(A)). An alternative is to rotate in the plane of the beam, the clinical equivalent of rotating the gantry on a linac before delivering the second field (B).

The advantage to method (B) with MRT, is that the entrance and exit of the two fields would be different. The dose distribution in 3D would resemble a wine rack shape as the beams intersected. The PVDR should be lower at the intersections but

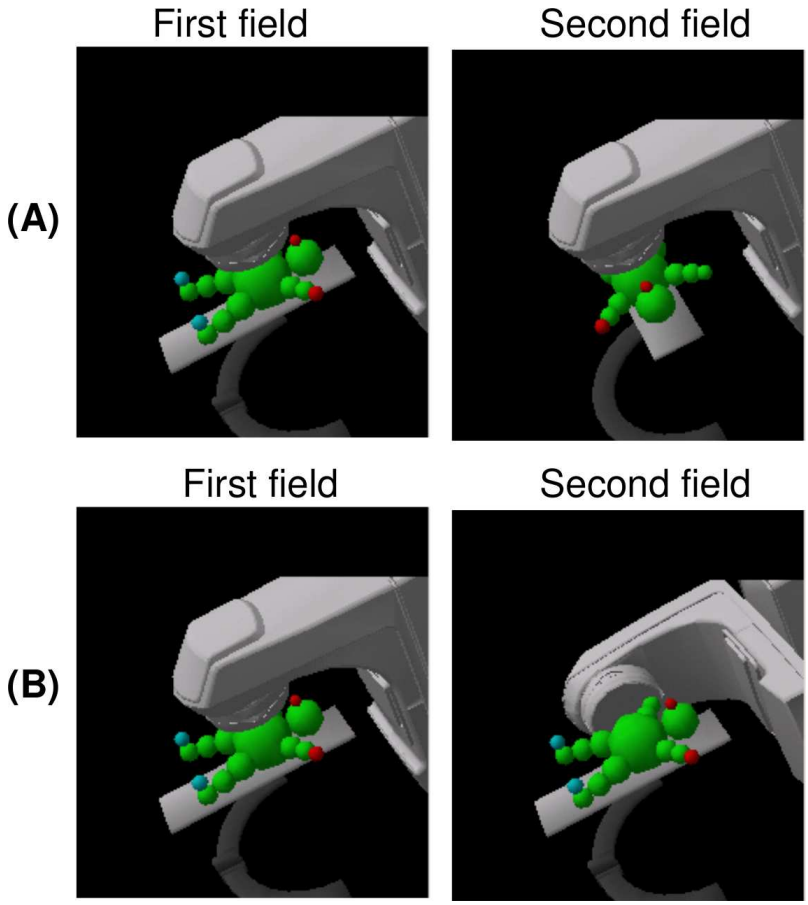

Figure 7.1: Rotating a linear accelerator patient treatment couch (A) and gantry (B) by 90 degrees. Rotating the gantry (B) by 90 degrees means the X-ray beam entry and exit points are different, thus reducing the total dose to normal tissue along the beam paths.

higher for the entrance and exits of the two fields. Assuming the centre of the target is an isocentric point in space means in theory, a larger dose could be delivered to the target region with sparing of normal tissue along the entrance/exit paths of the beam. Since it is not possible to rotate the synchrotron source around the target in the way one would rotate a linac gantry, it is necessary to find a way to rotate the target in the correct plane instead.

We attempted this on beamline BL28B2 at SPring-8, using a cylindrical glass vial filled with a normoxic gel to simulate a mouse leg. We also modified the treatment stage by using an extra goniometer that allowed fast rotation in the plane of the

beam via stepper motor control. Figure 7.2 shows the goniometer setup (a) which is magnified schematically in (b). We used a CCTV camera with a gridded display to minimise movements in the gel's centre of rotation as it rotated from -45^0 to +45^0. We delivered various doses to the gels ranging from 500 Gy to 2000 Gy. The gel polymerises upon irradiation, depending on the dose and oxygen concentration. A collaboration with Royal Melbourne Institute of Technology is investigating the use of gels and Raman spectroscopy (to read the gels) for dosimetry purposes [1].

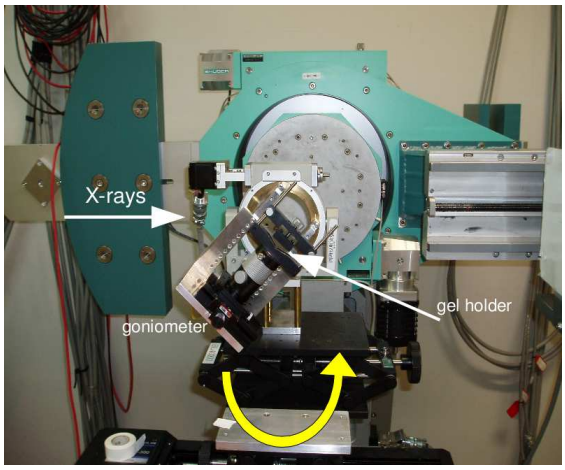

(a)

Figure 7.2: Bi-directional MRT using a gel positioned in a goniometer. The goniometer rotates the gel 90 degrees about its central axis of rotation, normal to the page. An arrow indicates the location of the gel holder in the goniometer, however, there is no actual gel in the photograph

Figure 7.3 shows the 'wine rack'effect in the gel, proof of principle that such a bi-directional MRT technique can be delivered to the target. A difficulty of using gels to detect the dose distribution is the inability to subsequently analyse the dose in 3D owing to the high spatial resolution demands of MRT, which exceeds the capability of, for example, standard magnetic resonance imaging. Optical tomography is being considered for this in the future.

It is likely that the tissue toxicity would be reduced if we were to use this bi-

[1] C.J. Wong, J.C. Crosbie, C.E. Powell et al. Gel dosimetry & Raman spectroscopy applied to high dose synchrotron microbeam radiation therapy. Paper submitted to *Australasian Physical & Engineering Sciences in Medicine*, August 2008

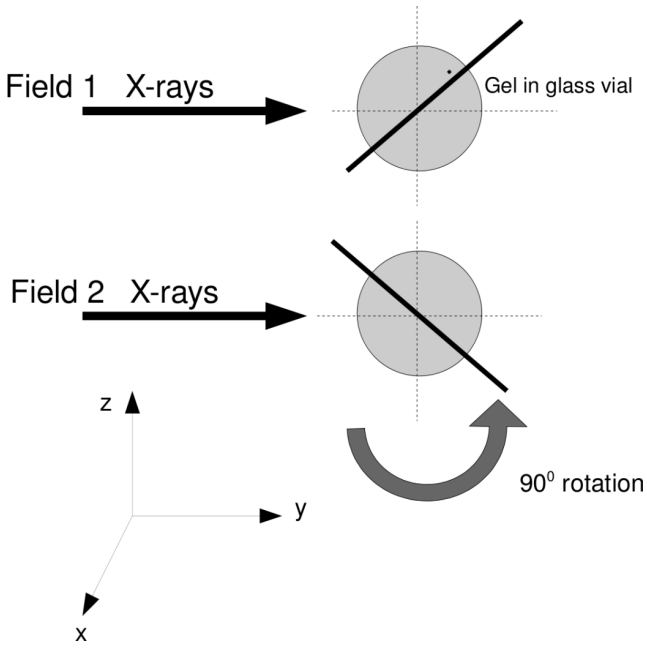

(b)

Figure 7.2: (cont'd) magnified version of (a), showing schematically how the gel was rotated 90 degrees about its central (z-y) axis between the first and second field. The x-axis is into the page.

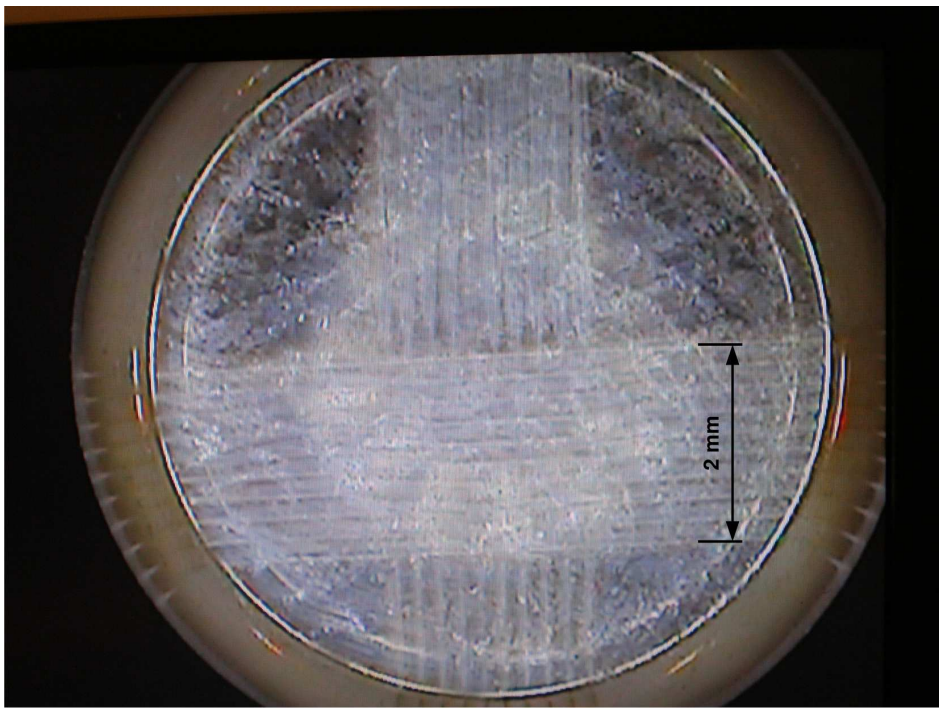

Figure 7.3: Bi-directional MRT captured in a gel

directional approach on a tumour-inoculated mouse leg. The mouse leg is quite an irregular shape and attempting to irradiate from two directions is challenging. It would be feasible to rotate the mouse on a turntable-style platform between irradiations, much like the mouse and rat brain irradiations at the ESRF are done (Figure 7.4) (Serduc et al., 2008). However, this method may be more difficult to do on a mouse leg because objects such as bone and/or abdominal tissue may be in the direct path of a beam, hence our motivation to find an alternative method.

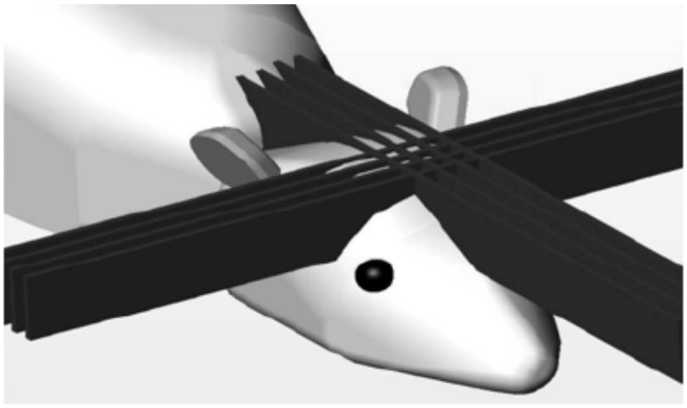

Figure 7.4: Schematic representation of the MRT irradiation geometry used at the ESRF on rodent brain tumours. Reproduced from Serduc et al. (2008), Copyright (2008) Institute of Physics Publishing. Image used with permission.

The above discussions highlight the need for an MRT treatment planning system that incorporates pre-treatment imaging of the target, localisation, simulation and dose delivery/calculation, tasks with standardised protocols in conventional radiotherapy. The development of an MRT treatment planning system is yet another example of future work which would be extremely useful for all MRT research groups.

7.3 GEANT4 Monte Carlo Simulation of a Microbeam Collimator

Some of the deficiencies in Monte Carlo modelling of MRT were pointed out in the Discussion section of Chapter 6. One shortcoming is that the simulations in the liter-

ature do not model a collimator, rather a pencil beam that is propagated through air into a water phantom. As a result, no account is taken of scattered photons, secondary electrons and characteristic tungsten radiation generated within the collimator. The data presented in chapter 6 showed much higher PVDRs at the collimator face (approximately 400) than at the sample stage (approximately 65).

It is proposed to use the GEANT4 Monte Carlo code to more accurately model the conditions in MRT, and indeed, some progress has already been made. A tungsten-kapton-tungsten material has been modelled and the narrow, pencil-beam of photons has been given horizontal and vertical dimensions. The detector material has always been of arbitrary dimension but can now be modelled and arbitrary distance from the collimator. In this way it should be possible to simulate X-ray interactions at different distances from the collimator. It should also be possible to look at the scatter profile as a function of depth within the actual collimator itself and perhaps optimise its thickness. Finally, the detector material itself will be modified to resemble the elemental constituents of radiochromic film, instead of liquid water.

Figure 7.5 shows the revised geometry of collimator and EBT film detector. Figure 7.6 is a plot of a GEANT4 Monte Carlo simulated X-ray microbeam incident on EBT film. Suitable histogramming of the data file is still required in order to obtain the radial microbeam profiles. Superposing these profiles at appropriate spacing intervals would build up an array of microbeams, and enable determination of simulated PVDRs, which could be compared to experimentally-obtained PVDRs. This work is being actively pursued at present.

7.4 Gamma-H2AX-based Biological Dosimetry for MRT

It was apparent after the first attempts at γ-H2AX staining in skin that a sufficiently large valley dose was present to show low-level γ-H2AX foci formation (in epithelial cells) in the valley region between the peaks, which persisted up to about 12 h post-exposure (Figure 7.7).

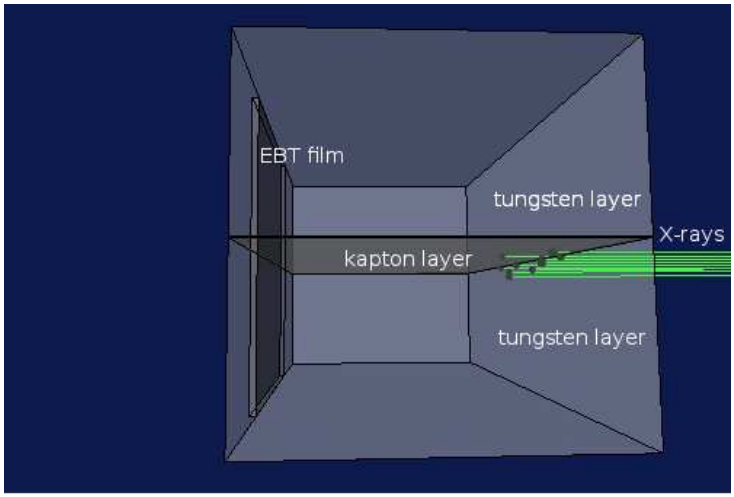

Figure 7.5: New Monte Carlo simulations of a tungsten-kapton collimator. Collimated X-rays are detected by a sheet of EBT film

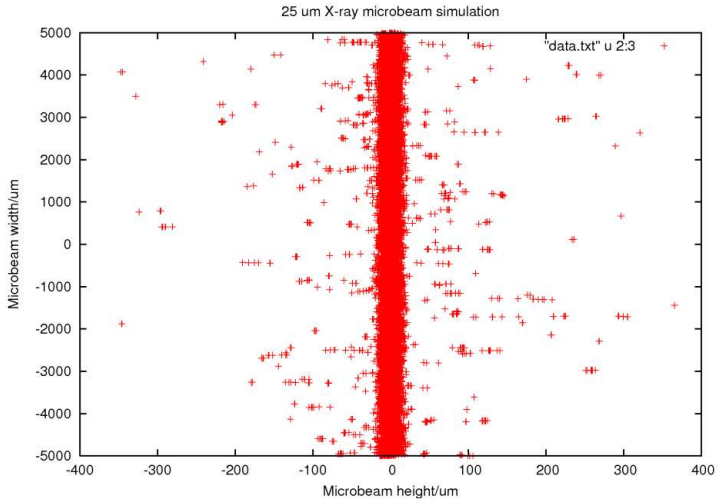

Figure 7.6: Simulated X-ray microbeam (25 μm x 10 mm) on EBT film. The red crosses correspond to locations of deposited energy

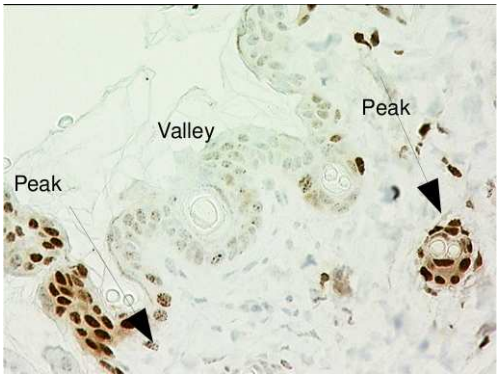

Figure 7.7: γ-H2AX staining in murine skin following microbeam radiotherapy

In collaboration with Dr. Kai Rothkamm, formerly of the Gray Cancer Institute, UK, now Health Protection Agency, UK, we proposed the use of γ-H2AX as a biological dosimeter for MRT. γ-H2AX has previously been used as a biodosimeter in other studies, for example Rothkamm and Lobrich (2003) used γ-H2AX foci formation in X-irradiated human fibroblasts, and showed a linear relationship between the number of DNA double strand breaks per cell and the delivered dose. Rothkamm et al. (2007) performed γ-H2AX-based biological dosimetry on tissue which had been CT-scanned, with low dose (mGy) radiation.

In a pilot study, we irradiated flasks of human fibroblast cultures with peak, entrance doses of 8, 10, 20, 50 and 100 Gy MRT on beamline BL28B2 at SPring-8. At the time we assumed a PVDR of 50 that is, the valley dose was 2% of the peak dose. This was based on pilot film dosimetry measurements. A PVDR of 50 meant the lowest valley dose (8 Gy case) was approximately 160 mGy. We also delivered low dose (0.5, 1.0 and 2.0 Gy), broadbeam calibration doses to flasks of cell cultures, in order to generate a calibration curve which we could then use to quantify the valley dose of MRT-irradiated cultures. Extra metal absorbers were used to attenuate the broad beam photon flux in order to deliver a dose lower than that permitted by the physical limitations of the lead shutter.

The flasks were transported to the Gray Cancer Institute at the Mount Vernon Hospital site, outside London, in the UK. The cells were stained using a fluorescent

γ-H2AX antibody and analysed under fluorescent microscopy. All data and images presented in this subsection are from analysis performed by Dr. Kai Rothkamm. Figure 7.8 shows the γ-H2AX staining in the fibroblast cultures post-MRT with entrance doses of 100 Gy (top images) and 50 Gy (bottom images). Cell migration in the cultures was observed during 2 h incubation.

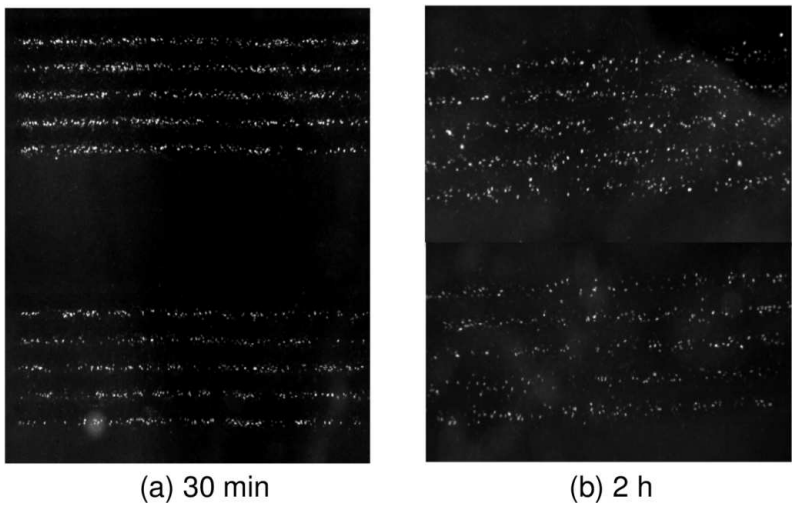

Figure 7.8: γ-H2AX staining in human fibroblast cultures post-MRT. (a) cells formalin-fixed 30 minutes post-MRT, (b) cells fixed 2 hrs post-MRT

Figure 7.9 is a plot of the broadbeam calibration curve of the number of γ-H2AX foci per cell versus entrance dose (Gy). The dose deposited in the valley region of MRT-irradiated cells is shown in figure 7.10 as a percentage of the peak dose. At a distance of 80 - 100 μm from the peak, the mid-point of the valley region, the dose is approximately 3% of the peak dose, in other words a biological PVDR of approximately 30. The γ-H2AX intensity profiles across MRT tracks in the cell cultures reflected the physical geometry of the beam (Figure 7.11), although the valleys were narrower than was observed with film. It was also noted that there were only 2-3 times more γ-H2AX foci for five times the dose, that is, the foci induction adjacent to MRT tracks was non-linear.

The use of bio-dosimetry in MRT could be a powerful way to quantify the biological dose and may lead to new insights into cellular response mechanisms post-MRT.

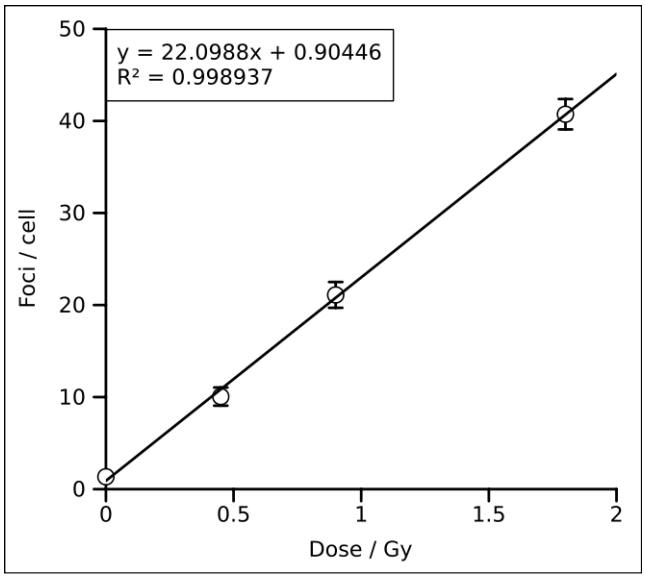

Figure 7.9: Foci yield in broadbeam reference samples. This curve served as a dose calibration curve, analogous to the film calibration curves in Chapter 4

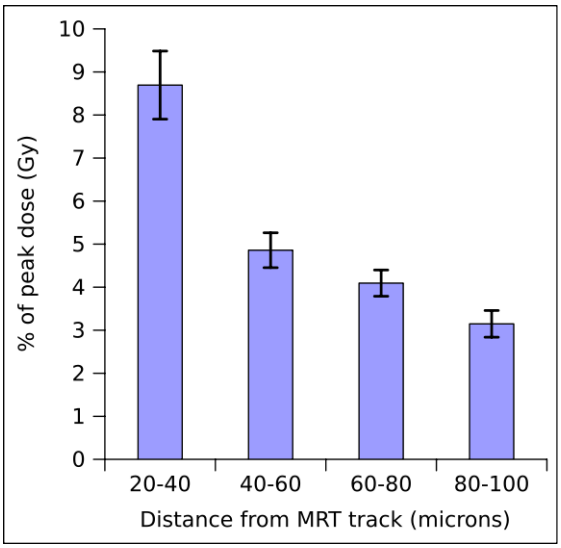

Figure 7.10: Dose deposited in MRT valleys as a percentage of peak dose. In the mid-point of the valley region, the biological valley dose is approximately 3% of the biological peak dose

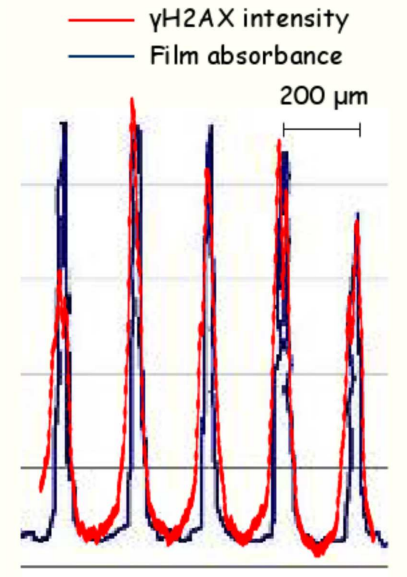

Figure 7.11: γ-H2AX intensity profiles vs radiochromic film. The two profiles were superimposed on one another for comparsion and they are clearly very similar, although the γ-H2AX valleys are narrower than the film valleys

We have also collected data for *in vivo* bio-dosimetry by delivering MRT and low dose broadbeam irradiations to mouse skin. The analysis of these data is ongoing.

7.5 Quantitative assessment of microvascular effects in MRT-irradiated tissue

The pioneers of deuteron microbeam therapy in the late 1950's and 1960's hypothesised that blood vessels irradiated with microplanar beams of radiation could be repaired via migration of minimally-irradiated endothelial cells over distances comparable to the microbeam width. This was restated by Slatkin et al. (1995) and others with regard to synchrotron MRT. Further, Dilmanian et al. (2002) hypothesised that this repair mechanism is faulty in tumours and the tumour might collapse because of a lack of functioning vasculature. Our own MRT research group have performed immunohistochemical staining on MRT-irradiated tumour sections (EMT-6.5) using single and double stain markers for CD31 (a blood vessel marker) and γ-H2AX (Fig-

ure 7.12 and Figure 7.13).

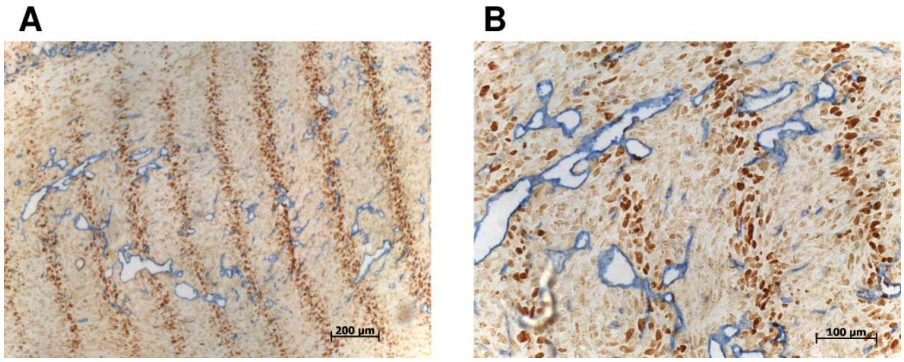

Figure 7.12: CD31 and γ-H2AX double stain immunohistochemistry of MRT-irradiated EMT-6 tumour. The entrance dose was 560 Gy and the tissue section was from a mouse culled 4 h post-irradiation. **A** Low power microscopy image showing the microbeam tracks (stained brown) and vessels (stained blue). **B** Higher power microscopy image showing directly irradiated vessels.

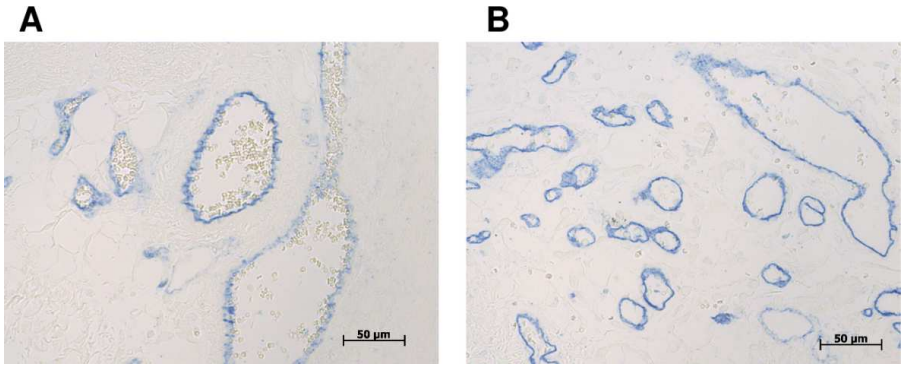

Figure 7.13: Lack of evidence for a microvascular effect in MRT-irradiated tumours. CD31 single stain immunohistochemistry of MRT-irradiated tumour. The entrance dose was 560 Gy and the tissue section was from (A) control and (B) a mouse culled 84 h post-irradiation. Blood vessels are stained blue.

Prof. P. Rogers, Director, Centre for Women's Health Research, Monash Institute of Medical Research & Mr. J. Crosbie, the candidate, examined the sections 4, 24 and 84 hours post-MRT and observed no qualitative differences between irradiated and unirradiated tumours. The microvasculature in the irradiated tumour sections appeared as patent and functional as the microvasculature in the unirradiated control tumour sections. The staining did not appear to show any microvascular effects,

however, further quantitative study could be carried out. Blood vessel counting and measurement of vessel surface area could be performed for example, to search for differences between irradiated and unirradiated tumours.

The immunohistochemistry data presented in this thesis provides strong evidence that the underlying radiobiological mechanisms of MRT in a tumour are dominated by the cellular processes of migration, proliferation, DNA repair and apoptosis, rather than a microvascular effect.

CHAPTER 8

Discussion & Conclusions

8.1 Summary and Discussion of Major Findings

The major findings of this thesis are;

1. Radiochromic films of different sensitivity, in conjunction with microdensitometry, allow experimental determination of the peak and valley doses for MRT.

2. The X-rays produced on beamline BL28B2 at the SPring-8 synchrotron exhibit a dose build-up effect in tissue-equivalent material; the dose is not maximal on the surface, but builds up to a peak rapidly after depths of tens of microns.

3. Measurements of the half value layer with and without the tungsten/kapton collimator in place showed the collimator did not appreciably alter the beam energy spectrum.

4. γ-H2AX is a high resolution cellular marker for MRT, identifying the path of the beam through tissue. Other immunohistochemical markers including TUNEL, PCNA, CD45 and H & E did not delineate the path of the beam through the tissue.

5. MRT has been shown to have a palliative effect on two types of breast tumours inoculated in a mouse model. Significant tumour growth delay was observed with minimal normal tissue toxicity.

6. Conventional RT at doses approximately equal to the valley dose in MRT, has also shown a palliative effect but with increased normal tissue toxicity.

7. Normal skin tissue and EMT-6.5 tumour tissue respond to MRT very differently, with normal skin seemingly capable of mounting an effective repair response to MRT damage, compared with a reduced capacity in the tumour.

8. EMT-6.5 tumour cells are highly migratory (compared to skin cells) by 24 hours post-irradiation.

9. MRT causes a reduction in tumour cell proliferation. Cell-cell communication (the bystander effect) may explain this reduction in tumour cell proliferation.

10. Persistnent γ-H2AX staining (unrepaired DNA) remains up to 84 hours post-irradiation and apoptosis is elevated in tumours post-MRT compared to normal skin.

11. There does not appear to be a microvascular effect in EMT-6 tumours with MRT. Irradiated blood vessels in tumours appear no different than unirradiated blood vessels.

That normal skin and tumour behaves differently to MRT is perhaps the most important and novel result in the thesis and is an important new finding for the field of MRT. The vital biological processes of cell migration, DNA repair, proliferation and apoptosis occurred in normal skin and EMT6.5 tumour in a wholly different manner, as can be seen from the quantitative plots in figure 5 of Chapter 6. Normal skin appeared to mount a competent repair response to the radiation damage, unlike tumour, which appeared less capable of mounting an effective response to the irradiation.

The observations of these processes were made possible by applying the γ-H2AX immunohistochemical assay to MRT-irradiated sections. It was shown in Chapter 3 that the immunohistochemical assays of apoptosis (TUNEL), leukocytic infiltration (CD-45/LCA), proliferation (PCNA) and conventional H & E alone did *not* delineate the path of the beams through the tissue.

γ-H2AX allowed precise spatial localisation of peak-irradiated cells The 'washing machine effect'of minimally and maximally-irradiated cells inter-mixing and migrating 24 hours post-irradiation, is a novel and significant observation in MRT. Cell-cell communication (bystander effect) of toxic, signals (proteins) from directly irradiated tumour cells to minimally irradiated cells adjacent, may explain the reduced proliferation observed in the tumour. The results presented in this thesis are the first detailed immunohistochemical study of biological processes of normal and tumourous tissue post-MRT.

MRT proposes not just one, but several paradigm shifts for the delivery of radiation to treat tumours. Gone is the need to treat the whole tumour to a uniform dose distribution, only a fraction of the tumour volume is maximally irradiated. Gone is the requirement for temporal fractionation, with hundreds of Gy of in-beam dose being delivered in a single fraction in a matter of seconds, and normal tissue displaying an extraordinarily high tolerance to MRT. Gone is the requirement to deliver megavoltage (MV) energy beams. MRT would not be suitable for deep-seated tumours in the pelvis, owing to its shallower depth dose characteristics compared with MV beams, but it could be adapted to more superficial tumours in the head and neck or chest region. Gone also is the requirement to uniformly contour a target volume with a particular isodose, as is the norm in conventional radiotherapy. To people working in the field of clinical radiotherapy, these observations are clearly paradigm shifts, flying in the face of conventional wisdom. Nevertheless, there is now substantial evidence that MRT causes tumour growth delay (and in some cases tumour ablation) and that normal tissue can tolerate doses of radiation two orders of magnitude greater than is delivered in conventional radiotherapy.

In Chapter 6, it was stated there was little evidence of a microvascular effect in MRT-irradiated tumours and the relevant data was shown in chapter 7. Our qualitative, analysis of MRT-irradiated tumour sections using an immunohistochemical marker of blood vessels (CD-31) did not indicate the presence of a differential microvascular degeneration/repair effect. Further confirmation work is required, but our

immunohistochemical tumour blood vessel data is an important contribution to MRT radiobiology, casting doubt on a hypothesis which has prevailed for 50 years.

The work in Chapter 6 also showed that MRT had a palliative effect on two types of breast tumour inoculated into the legs of mice, with minimal normal tissue toxicity. Conventional radiotherapy, whilst also palliative, did cause increased and severe normal tissue toxicity. The doses delivered in the conventional study were selected on the basis that they were equal to the initial estimate of the valley dose in the cross-hatched MRT study, assuming a peak-to-valley dose ratio of 50. The justification was that, if MRT includes a broad beam dose as part of the valley region, could this valley dose alone be sufficient to obtain the desired biological effect? The mice receiving 11 Gy did experience some growth delay, but not as much as those that received 22 Gy. However, the 22 Gy mice experienced increased normal tissue toxicity. The 2 x 560 Gy MRT-irradiated mice, on the other hand, may have had a valley dose as high as 17 Gy, but their integrated dose, i.e. the total dose averaged over the area irradiated was much higher (approximately 70 Gy, assuming perfect attenuation by the collimators and 'top hat'intensity profiles) than the 17 Gy valley dose. Although the median survival time in days for the 22 Gy conventional RT study was comparable to the 2 x 560 Gy MRT study, the mice in the conventional group experienced more severe normal tissue toxicity than the mice in the MRT group.

The MRT and conventional RT survival studies are confirmatory rather than original, since Dilmanian et al. (2003) published similar results using the EMT-6.5 breast tumour model. However, the MRT response for the 67NR tumour which we describe, has not previously been reported in the MRT literature. Our mouse survival data from this experiment are important in light of the immunohistochemical data (migration, proliferation, DNA repair and apoptosis). It is likely the long-term effects observed weeks and months post-MRT are shaped by what occurs in the hours post-treatment.

In our survival study, we also inoculated mice with a third tumour line, the highly metastatic tumour, 4T1.2. These mice were transported to SPring-8, were irradiated and monitored at the same time as the mice inoculated with EMT-6.5 and 67NR.

However, MRT did not cause any tumour growth delay, with the survival of irradiated mice no different to unirradiated (Figure 8.1)

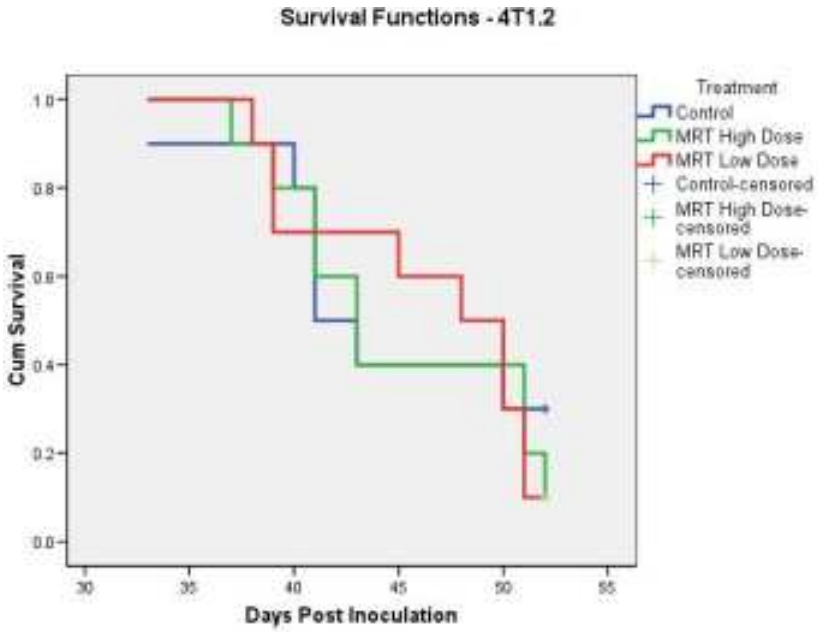

Figure 8.1: Kaplan-Meier survival curve for mice inoculated with the 4T1.2 tumour line and irradiated with cross-planar MRT

We do not know exactly why 4T1.2 did not respond to MRT, however, we noted that at the time of irradiation there were no palpable tumours, unlike EMT6 and 67NR, which were palpable in the mouse leg. In other words, the 4T1.2 tumour may not have been established at the time of irradiation. Comparisons with earlier, pilot studies of 4T1.2 tumour growth also showed discrepancies; the growth of our unirradiated 4T1.2 tumours was slower than tumour growth in the pilot studies, when they should have been very similar. *In vitro* irradiations of the three tumour cell lines also showed the response of 4T1.2 cells to ionising radiation was comparable to the response of EMT-6 and 67NR.

One explanation for the slower growth of the 4T1.2 tumours (and their failure to respond to MRT) is technical (human) error at the time of inoculation. We suspect the mice may have been inoculated with too few, viable 4T1.2 cells and this is why the tumour growth was slow. The mice were eventually culled owing to the leg and

tumour thickness exceeding 11 mm. Considering the difficulties we had locating a palpable tumour, it is possible that the radiation missed 4T1.2 cells and they migrated from the radiation zone and re-established a tumour towards the top of the mouse's leg.

A common feature in scientific publications is a bias towards only publishing positive results. This is unfortunate since negative results can also be very informative. The TUNEL, PCNA and CD-45 immunohistochemical data shown in Chapter 5 were negative results in a sense, because the assays did not show the path of the microbeams through the tissue. However, a supposedly negative result may be an important finding for other workers in the field. The 4T1.2 tumour survival data was omitted from Chapter 6, not because MRT 'didn't work'on this tumour line, but because we felt that technical (human) error during the inoculation of 4T1.2 was the reason for the poor response of 4T1.2 to MRT. Ideally, the experiment should be repeated. The advent of the medical imaging and therapy beamline on the new Australian Synchrotron will greatly facilitate MRT experiments on a variety of inoculated tumours.

Naturally, one draws conclusions from the published literature. However, the negative result with 4T1.2 makes one question the lack of contrary findings in the MRT literature. It is conceivable that other experimenters in the field have also achieved 'less than perfect' findings in their MRT experiments, which have not been published.

To our knowledge, our MRT survival data is the first reported MRT survival study performed on a synchrotron other than the National Synchrotron Light Source (NSLS) at Brookhaven National Laboratory, New York, USA or the European Synchrotron Radiation Facility (ESRF) in Grenoble, France. This extends the evidence of MRT's robustness as an experimental procedure. The X-ray source on the BL28B2 beamline at SPring-8 is a bending magnet, whereas the NSLS and ESRF sources are wigglers. The X-rays produced on BL28B2 at SPring-8 are two orders of magnitude lower in flux rate than is achievable at the ESRF. At SPring-8, we use a fixed geom-

etry, tungsten/kapton microbeam collimator. The NSLS and the ESRF use a variable width, tungsten/gas collimator, to obtain similar outcomes.

Further work is required to compare MRT to conventional RT; is there a threshold broadbeam dose whereby the dose gives adequate tumour control and acceptable normal tissue toxicity? One suspects that this was the very same question the pioneers of clinical radiotherapy faced in the 1920's. Their solution of course, was temporal fractionation; split the total dose into smaller daily doses to permit normal tissue repair. However temporal fractionation only partly solved the problem, and indeed the problem still remains today but is being tackled in an iterative manner, with advances in 3-D conformal, intensity modulated and image-guided radiotherapy and experimental fractionation regimens.

One could speculate that with improved imaging and localisation of the tumour before treatment (i.e. treatment planning), coupled with temporal fractionation of the dose, the tumour control and normal tissue toxicity with MRT could be exceptionally good, based on our own work and other published survival study literature. These are the strategies required for progressing MRT from a scientific curiosity to clinical applications.

What conclusions can be drawn about threshold peak and valley doses for optimal MRT efficacy? Does it matter if we irradiate tumours with 5000 Gy or 500 Gy peak dose if the effect is the same on those cells in the direct path of the beam? Or, is the valley dose the important factor for tumour control and normal tissue toxicity? Considering the extensive cell migration which can and does occur, and the potential for cell-cell communication, it is possible the precise peak and valley doses are not so critical. The valley dose is however, likely to matter for normal tissue toxicity. It is likely a valley dose threshold exists for certain tissue types beyond which tissue toxicity is unacceptably high. That dose is not known and *in vivo* studies are required to establish it for a particular collimator geometry and a particular tissue type.

It was stated in Chapter 4 that the optimal geometrical configuration for MRT was not yet known, which immediately identifies a number of future experiments.

A variable width collimator, such as those at the National Synchrotron Light Source (NSLS) in the USA and the European Synchrotron Radiation Facility (ESRF) in France, is required for such experiments. The Japanese collimator at SPring-8 has fixed geometry, and would not be suitable for this experiment. The effect of increased normal tissue tolerance to microplanar radiation, presumably breaks down as the beam width increases and is likely to be very tissue-type dependent. Dilmanian et al. (2002) and Regnard et al. (2008) showed worsening toxicity by decreasing the microbeam separation distance in brain tissue and converging towards a broad beam. These effects may be related to Hopewell's ideas on volume effects, described in section 2.1.3. The various MRT design parameters and the lack of knowledge regarding peak-to-valley dose ratios highlights the need for a more systematic study of biological effects. The physical unknowns are combined with biological unknowns, such as the variety of tissues/animals studied, despite the strong evidence that MRT tumour control appears widespread, repeatable and highly significant. The study would ideally need to be carried out *in vivo* considering the tissue micro-environment available to cells is different *in vitro*. However, a mass-screening style *in vitro* experiment, may be informative for future *in vivo* experiments.

Changing the geometry of the collimator requires an accurate method of dosimetry to assess possible changes to the PVDR, which leads to another major finding reported in the thesis; the use of radiochromic films and microdensitometry to measure the peak and valley doses in MRT. The majority of MRT dosimetry to date has been Monte Carlo simulation-based. The experimental, measurement method outlined in Chapter 6 is simple and straight-forward, using a well-established medical physics technique and commercial film products. It could be applied to any collimator configuration. A feature of film as a dosimeter is its ability to measure the contributions of dose scattering from all directions and at different depths. Alignment of film with respect to the beam is not a big concern either. This gives film an advantage over MOSFETs, TLDs and ion chambers.

A dose build-up effect was confirmed experimentally using a stack of GafChromic HD-810 films, each one 110 μm thick. The build-up effect was also predicted using Monte Carlo simulations. The dose builds up over depths of tens of microns. This finding is consistent with Continuous Slowing Down Approximation (CSDA) range calculations for charged particles (secondary electrons). The HVL measurements performed with and without the collimator present showed that the kapton did not alter the energy spectrum in an appreciable way.

It was shown in Chapter 6 that the PVDR measured directly at the collimator face was almost 400. At the level of the sample stage, the PVDR was less than 100, the decrease in PVDR possibly due to scatter from the collimator causing a larger valley dose. Further experimental work and Monte Carlo computer simulations need to be carried out. This would be of importance for future collimator design and application. The limitations and shortcomings of the published Monte Carlo simulations were also discussed in Chapter 6 and this is a topic of future work, described in Chapter 7.

8.2 Concluding Remarks

The thesis presents the first, detailed and quantitative immunohistochemical data on MRT-irradiated tumours and normal tissue, and proposes mechanisms of the radiobiology effect. It also describes a straight-forward method of measurement-based dosimetry using radiochromic films.

Appendix

On Immunohistochemistry

Immunohistochemistry (IHC) is a very powerful tool to visualise the distribution and localisation of specific cellular components within a cell or tissue. Much use was made of IHC in the research presented in this thesis (see Chapters 5 and 6) and therefore a brief description and overview of the technique is appropriate. The basic principle of IHC techniques is that a specific antibody will combine with its specific antigen to give an antibody-antigen complex tagged with a visible label (Boenisch, 2001). For example, IHC has become a routine and extremely useful tool in the practice of surgical pathology. Pathologists rely on IHC to assist in the diagnoses and classifications of malignant tissue Hsi (2001).

Some additional definitions may be useful.

Antibody: The pivotal reagent common to all IHC techniques is the antibody. Antibodies belong to a group of proteins called immunoglobulins (Ig), the most common being immunoglobulin G (IgG). The shape and structure of immunoglobulin resembles the letter Y (Figure 1).

Antigen: The classic definition of an antigen is any foreign substance that elicits an immune response, such as the production of a specific antibody molecule, when introduced into the tissue of a susceptible animal and is capable of combining with specific antibodies formed. Antigens are generally of high molecular weight and are commonly proteins or polysaccharides, although many other molecules (polypep-

tides, nucleic acids) can also function as antigens. Antigens may be present in their native cellular environment or extracted and purified. In their natural form, they may be cytoplasmic, intracellular or extracellular (Boenisch, 2001). Examples of commonly used antigens in the field of IHC include Proliferating Cell Nuclear Antigen (PCNA), and Ki67. These proteins are expressed by proliferating cells at particular stages of their cell cycle.

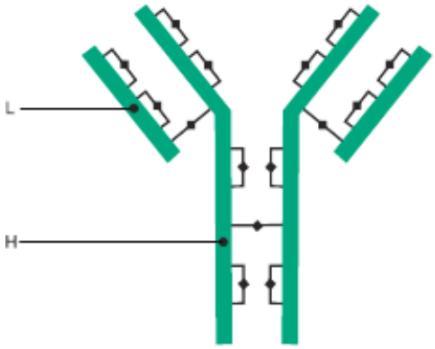

Figure 1: Diagram showing the structure of an immunoglobulin molecule. It comprises two identical heavy (H) chains and two identical light (L) chains. From Boenisch (2001).

Polyclonal antibodies are produced by various types of cells and are immunochemically dissimilar. Monoclonal antibodies, on the other hand, are produced by clones of cells and are immunochemically identical. Monoclonal antibodies (as opposed to polyclonal) are directed against a single site (called an epitope) on the antigen molecule. Rabbits are most commonly used for raising polyclonal antibodies, although donkeys, goats and sheep are also used. Mice are generally used to raise monoclonal antibodies (Boenisch, 2001). Figure 2 shows a monoclonal antibody clone reacting with a specific epitope on an antigen molecule.

Indirect Immunohistochemistry There are numerous IHC staining methods which can be used to localise antigens. The most common method of immunohistochemical staining is the so-called ABC method, or Avidin-Biotin Complex method (Hayat, 2002). At the Centre for Women's Health Research, Monash Institute of Medical Research, a two-step indirect method, similar to the ABC method, known as the

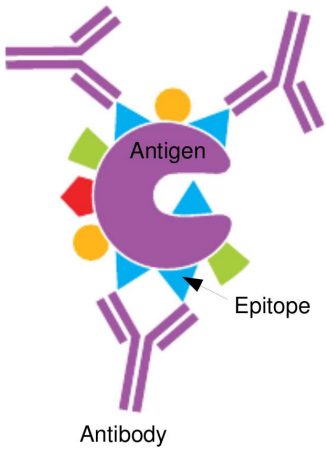

Figure 2: A monoclonal antibody clone reacts with a specific epitope on an antigen from Boenisch (2001).

Labelled Streptavidin-Biotin (LSAB) indirect method of immunohistochemistry, is commonly used. For this method, a primary antibody binds to the antigen (Figure 3, Step 1). An enzyme-labelled secondary antibody, directed against the primary antibody-antigen molecule is then applied, followed by the substrate, or chromogen. The LSAB method requires the secondary antibody to be covalently bonded to a protein known as biotin (Figure 3, Step 2). This biotinylated secondary antibody can then be bound to enzyme-labelled streptavidin (Figure 3, Step 3). The aim is ultimately to increase the staining intensity by increasing the number of enzyme molecules bound to the tissue. Streptavidin is a protein molecule with a high affinity for biotin. The binding sites between the biotinylated secondary antibodies and streptavidin molecules produce this amplification, thus leading to an increase in signal intensity.

Commonly used enzymes to label with streptavidin are horseradish peroxidase and alkaline phosphotase. The chromogen, (or substrate) which is converted by the enzyme to a coloured precipitate, depends on the enzyme itself. For horseradish peroxidase, commonly used chromogens are diaminobenzidine (DAB) which stains brown and 3-amino 9-ethylcarbozole (AEC) which stains red. For alkaline phosphatase, AP-Blue and Vector Blue are often used.

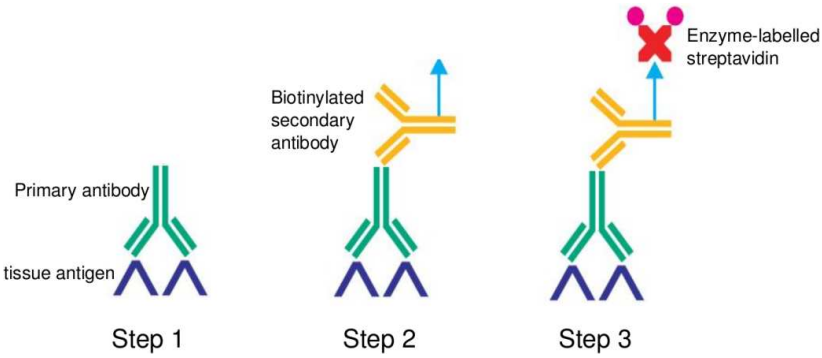

Figure 3: The three steps of the LSAB technique consist of the primary antibody (step 1), biotinylated secondary antibody (step 2) and enzyme-labelled streptavidin (step 3). From Boenisch (2001)

Figure 4 is a camera image, obtained from the light microscope, of mouse brain, immunostained for blood vessels using CD31. The image shows a cross section of a blood vessel with blue staining around the endothelial cell layer and red blood cells (erythrocytes) visible within the vessel itself.

Figure 4: CD31 immunohistochemical stain of a blood vessel in mouse brain

For this immunohistochemistry protocol, the tissue sample was incubated with the CD31 primary antibody (rat monoclonal anti-mouse) and left to incubate for 1 hour at 37^0C. Tissue slides were then washed in buffered-saline and covered in biotinylated secondary antibody (goat anti-rat IgG). Slides were washed in saline again

and sections were then covered with the alkaline phosphatase enzyme, conjugated (bound) with streptavidin. Slides were left at room temperature for 15 minutes and were then washed with saline. The sections were then covered with Vector Blue chromagen and left for 10 minutes before draining and washing with distilled water. Slides were covered with a mounting medium, and a glass coverslip placed over the tissue section, ready for microscopy.

Bibliography

Barcellos-Hoff, M. H., Park, C., and Wright, E. G. (2005). Radiation and the microenvironment - tumorigenesis and therapy. *Nat Rev Cancer*, 5(11):867–875.

Bentzen, S. M. (2006). Preventing or reducing late side effects of radiation therapy: radiobiology meets molecular pathology. *Nat Rev Cancer*, 6(9):702–713.

Berger, M., Coursey, J., Zucker, M., and Chang, J. (2005). Stopping-power and range tables for electrons, protons, and helium ions. Technical report, Ionizing Radiation Division, Physics Laboratory, National Institute of Standards and Technology, Gaithersburg, MD, USA.

Bernier, J., Hall, E. J., and Giaccia, A. (2004). Radiation oncology: a century of achievements. *Nat Rev Cancer*, 4(9):737–47.

Blattmann, H., Gebbers, J. O., Brauer-Krisch, E., Bravin, A., LeDuc, G., Burkhard, W., Di Michiel, M., Djonov, V., Slatkin, D. N., Stepanek, J., and Laissue, J. A. (2005). Applications of synchrotron x-rays to radiotherapy. *Nuclear Instruments and Methods in Physics Research Section A Accelerators Spectrometers Detectors and Associated Equipment*, 548:17.

Boenisch, T. (2001). Handbook of immunochemical staining methods, 3rd edition. DakoCytomation, Carpinteria, California.

Brauer-Krisch, E., Bravin, A., Lerch, M., Rosenfeld, A., Stepanek, J., Di Michiel,

M., and Laissue, J. A. (2003). Mosfet dosimetry for microbeam radiation therapy at the european synchrotron radiation facility. *Med Phys*, 30(4):583–9.

Bushberg, J., Seibert, J., Leidholdt, E., and Boone, J. (2001). *The Essential Physics of Medical Imaging*, chapter 10. Lippincott Williams & Wilkins.

Butson, M. J., Yu, P. K. N., Cheung, T., and Metcalfe, P. (2003). Radiochromic film for medical radiation dosimetry. *Materials Science and Engineering: R: Reports*, 41(3-5):61–120.

Clifford Chao, K., Ozyigit, G., Low, D. A., Wippold, F., and Thorstad, W. (2002). *Intensity Modulated Radiation Therapy for Head and Neck Cancers*. Lippincott Williams & Wilkins.

Company, F. Z. (2007). Calculation of dose profiles in stereotactic synchrotron microplanar beam radiotherapy in a tissue-lung phantom. *Australas Phys Eng Sci Med*, 30(1):33–41.

Company, F. Z. and Allen, B. J. (1998). Calculation of microplanar beam dose profiles in a tissue/lung/tissue phantom. *Phys Med Biol*, 43(9):2491–501.

Crosbie, J., Svalbe, I., Midgley, S., Yagi, N., Rogers, P., and Lewis, R. (2008). A method of dosimetry for synchrotron microbeam radiation therapy using radiochromic films of different sensitivity. *Phys Med Biol*, 53(23):6861–6877.

Curtis, H. J. (1967a). The interpretation of microbeam experiments for manned space flight. *Radiat Res Suppl*, 7:258–264.

Curtis, H. J. (1967b). The use of deuteron microbeam for simulating the biological effects of heavy cosmic-ray particles. *Radiat Res Suppl*, 7:250–7.

De Felici, M., Felici, R., Sanchez del Rio, M., Ferrero, C., Bacarian, T., and Dilmanian, F. A. (2005). Dose distribution from x-ray microbeam arrays applied to radiation therapy: an egs4 monte carlo study. *Med Phys*, 32(8):2455–63.

Dilmanian, F. A., Button, T. M., Le Duc, G., Zhong, N., Peña, L. A., Smith, J. A. L., Martinez, S. R., Bacarian, T., Tammam, J., Ren, B., Farmer, P. M., Kalef-Ezra, J., Micca, P. L., Nawrocky, M. M., Niederer, J. A., Recksiek, F. P., Fuchs, A., and Rosen, E. M. (2002). Response of rat intracranial 9l gliosarcoma to microbeam radiation therapy. *Neuro Oncol*, 4(1):26–38.

Dilmanian, F. A., Morris, G. M., Zhong, N., Bacarian, T., Hainfeld, J. F., Kalef-Ezra, J., Brewington, L. J., Tammam, J., and Rosen, E. M. (2003). Murine emt-6 carcinoma: high therapeutic efficacy of microbeam radiation therapy. *Radiat Res*, 159(5):632–41.

Dilmanian, F. A., Qu, Y., Feinendegen, L. E., Peña, L. A., Bacarian, T., Henn, F. A., Kalef-Ezra, J., Liu, S., Zhong, Z., and McDonald, J. W. (2007). Tissue-sparing effect of x-ray microplanar beams particularly in the cns: is a bystander effect involved? *Exp Hematol*, 35:69–77.

Dilmanian, F. A., Zhong, Z., Bacarian, T., Benveniste, H., Romanelli, P., Wang, R., Welwart, J., Yuasa, T., Rosen, E. M., and Anschel, D. J. (2006). Interlaced x-ray microplanar beams: a radiosurgery approach with clinical potential. *Proc Natl Acad Sci U S A*, 103(25):9709–9714.

Folkard, M., Schettino, G., Vojnovic, B., Gilchrist, S., Michette, A. G., Pfauntsch, S. J., Prise, K. M., and Michael, B. D. (2001). A focused ultrasoft x-ray microbeam for targeting cells individually with submicrometer accuracy. *Radiat Res*, 156(6):796–804.

Fuss, M., Sturtewagen, E., De Wagter, C., and Georg, D. (2007). Dosimetric characterization of gafchromic ebt film and its implication on film dosimetry quality assurance. *Phys Med Biol*, 52(14):4211–4225.

Greene, D. and Williams, P. (1997). *Linear Accelerators for Radiation Therapy*. Medical Science Series. Taylor and Francis, 2nd edition.

Greening, J. R. (1985). *Fundamentals of Radiation Dosimetry*. Taylor & Francis, 2 edition.

Hall, E. J. (2000). *Radiobiology for the Radiologist*, chapter 19. Lippincott Williams & Wilkins, 5th edition.

Hall, E. J. and Mitchell, S. A. (2003). How many bystander effects are there? Center for Radiological Research, Columbia University Medical Center, Annual Report.

Hayat, M. (2002). *Microscopy, Immunohistochemistry, and Antigen Retrieval Methods: For Light and Electron Microscopy*. Springer, 1st edition.

Herrmann, T., Baumann, M., Voigtmann, L., and Knorr, A. (1997). Effect of irradiated volume on lung damage in pigs. *Radiother Oncol*, 44(1):35–40.

Hopewell, J. W. (1990). The skin: its structure and response to ionizing radiation. *Int J Radiat Biol*, 57(4):751–773.

Hopewell, J. W., Coggle, J. E., Wells, J., Hamlet, R., Williams, J. P., and Charles, M. W. (1986). The acute effects of different energy beta-emitters on pig and mouse skin. *Br J Radiol Suppl*, 19:47–51.

Hopewell, J. W., Morris, A. D., and Dixon-Brown, A. (1987). The influence of field size on the late tolerance of the rat spinal cord to single doses of x rays. *Br J Radiol*, 60(719):1099–1108.

Hopewell, J. W. and Trott, K. R. (2000). Volume effects in radiobiology as applied to radiotherapy. *Radiother Oncol*, 56(3):283–288.

Hsi, E. (2001). A practical approach for evaluating new antibodies in the clinical immunohistochemistry laboratory. *Arch Pathol Med*, 125.

Hubbell, J. and Seltzer, S. (1996). Tables of x-ray mass attenuation coefficients and mass energy-absorption coefficients. Technical report, Ionizing Radiation

Division, Physics Laboratory, National Institute of Standards and Technology, Gaithersburg, MD, USA.

ICRU (1980). *Radiation Quantities and Units*. 33. ICRU Publications, Washington, DC.

ISP (2007a). Gafchromic ebt, product brief. Technical report, International Specialty Products.

ISP (2007b). White paper; gafchromic ebt, self developing film for radiotherapy dosimetry. Technical report, International Specialty Products.

ISP (2008). Technical report; gafchromic hd-810 radiochromic dosimetry film and d-200 pre-formatted dosimeter for high energy photons; configuration, specifications and performance data. Technical report, International Specialty Products.

Joel, D. D., Fairchild, R. G., Laissue, J. A., Saraf, S. K., Kalef-Ezra, J. A., and Slatkin, D. N. (1990). Boron neutron capture therapy of intracerebral rat gliosarcomas. *Proc Natl Acad Sci U S A*, 87(24):9808–9812.

Johns, H. E. and Cunningham, J. R. (1983). *The Physics of Radiology*. Charles C Thomas, Springfield, Illinois, USA, 4th edition.

Kaminski, J. M., Shinohara, E., Summers, J. B., Niermann, K. J., Morimoto, A., and Brousal, J. (2005). The controversial abscopal effect. *Cancer Treat Rev*, 31(3):159–172.

Kao, J., Milano, M. T., Javaheri, A., Garofalo, M. C., Chmura, S. J., Weichselbaum, R. R., and Kron, S. J. (2006). gamma-h2ax as a therapeutic target for improving the efficacy of radiation therapy. *Curr Cancer Drug Targets*, 6(3):197–205.

Kaplan, G. I., Rosenfeld, A. B., Allen, B. J., Booth, J. T., Carolan, M. G., and Holmes-Siedle, A. (2000). Improved spatial resolution by mosfet dosimetry of an x-ray microbeam. *Med Phys*, 27(1):239–44.

Kawrakow, I. and Rogers, D. (2003). The egsnrc code system: Monte carlo simulation of electron and photon transport. Technical report, National Research Council of Canada, PIRS-701.

Khan, F. M. (2003). *The Physics of Radiation Therapy*. Lippincott Williams & Wilkins, 3rd edition.

Laissue, J. A., Blattmann, H., Di Michiel, M., Slatkin, D. N., Lyubimova, N., and Guzman, R. (2001). The weaning piglet cerebellum: a surrogate for tolerance to mrt (microbeam radiation therapy) in paediatric neuro-oncology. *Proc. SPIE*, 4508(Penetrating radiation systems & applications III).

Laissue, J. A., Geiser, G., Spanne, P. O., Dilmanian, F. A., Gebbers, J. O., Geiser, M., Wu, X. Y., Makar, M. S., Micca, P. L., Nawrocky, M. M., Joel, D. D., and Slatkin, D. N. (1998). Neuropathology of ablation of rat gliosarcomas and contiguous brain tissues using a microplanar beam of synchrotron-wiggler-generated x rays. *Int J Cancer*, 78(5):654–60.

Laissue, J. A., Lyubimova, N., Wagner, T. H., Archer, D., Slatkin, D. N., and Di Michiel, M. (1999). Microbeam radiation therapy. In *SPIE Conference on medical applications of penetrating radiation*, volume 3770. SPIE.

Lewis, R. A. (1997). Medical applications of synchrotron radiation x-rays. *Phys Med Biol*, 42:1213–1243.

Lobrich, M., Rief, N., Kuhne, M., Heckmann, M., Fleckenstein, J., Rube, C., and Uder, M. (2005). In vivo formation and repair of dna double-strand breaks after computed tomography examinations. *Proc Natl Acad Sci U S A*, 102(25):8984–9.

Miura, M., Blattmann, H., Brauer-Krisch, E., Bravin, A., Hanson, A. L., Nawrocky, M. M., Micca, P. L., Slatkin, D. N., and Laissue, J. A. (2006). Radiosurgical palliation of aggressive murine sccvii squamous cell carcinomas using synchrotron-generated x-ray microbeams. *Br J Radiol*, 79(937):71–5.

Mothersill, C. and Seymour, C. (2001). Radiation-induced bystander effects: past history and future directions. *Radiat Res*, 155(6):759–767.

Mothersill, C. and Seymour, C. B. (2004). Radiation-induced bystander effects–implications for cancer. *Nat Rev Cancer*, 4(2):158–164.

Mothersill, C. E., Moriarty, M. J., and Seymour, C. B. (2004). Radiotherapy and the potential exploitation of bystander effects. *Int J Radiat Oncol Biol Phys*, 58(2):575–579.

Muench, P. J., Meigooni, A. S., Nath, R., and McLaughlin, W. L. (1991). Photon energy dependence of the sensitivity of radiochromic film and comparison with silver halide film and lif tlds used for brachytherapy dosimetry. *Med Phys*, 18(4):769–775.

Nariyama, N. (2005). Responses of gafchromic films for distribution of extremely high doses from synchrotron radiation. *Appl Radiat Isot*, 62(5):693–7.

Nelson, W., Hirayama, H., and Rogers, D. (1985). The egs4 code system report slac 265. Technical report, Stanford Linear Accelerator Centre, CA, USA.

Nielsen, J. and McMorrow, D. (2001). *Elements of Modern X-Ray Physics*, chapter 2. John Wiley and Sons, London.

Niroomand-Rad, A., Blackwell, C. R., Coursey, B. M., Gall, K. P., Galvin, J. M., McLaughlin, W. L., Meigooni, A. S., Nath, R., Rodgers, J. E., and Soares, C. G. (1998). Radiochromic film dosimetry: recommendations of aapm radiation therapy committee task group 55. american association of physicists in medicine. *Med Phys*, 25(11):2093–115.

Ohno, Y., Torikoshi, M., Suzuki, M., Umetani, K., Imai, Y., Uesugi, K., and Yagi, N. (2008). Dose distribution of a 125 kev mean energy microplanar x-ray beam for basic studies on microbeam radiotherapy. *Med Phys*, 35(7):3252–3258.

Orion, I., Rosenfeld, A. B., Dilmanian, F. A., Telang, F., Ren, B., and Namito, Y. (2000). Monte carlo simulation of dose distributions from a synchrotron-produced microplanar beam array using the egs4 code system. *Phys Med Biol*, 45(9):2497–508.

Persliden, J. and Carlsson, G. A. (1984). Energy imparted to water slabs by photons in the energy range 5-300 kev. calculations using a monte carlo photon transport model. *Phys Med Biol*, 29(9):1075–1088.

Podgorsak, E. B. (2005). *Radiation Physics for Medical Physicists*. Springer.

Prise, K. M., Schettino, G., Folkard, M., and Held, K. D. (2005). New insights on cell death from radiation exposure. *Lancet Oncol*, 6(7):520–528.

Qvarnstrom, O. F., Simonsson, M., Johansson, K. A., Nyman, J., and Turesson, I. (2004). Dna double strand break quantification in skin biopsies. *Radiother Oncol*, 72(3):311–7.

Regnard, P., Le Duc, G., Bräuer-Krisch, E., Troprès, I., Siegbahn, E. A., Kusak, A., Clair, C., Bernard, H., Dallery, D., Laissue, J. A., and Bravin, A. (2008). Irradiation of intracerebral 9l gliosarcoma by a single array of microplanar x-ray beams from a synchrotron: balance between curing and sparing. *Phys Med Biol*, 53(4):861–878.

Rink, A., Vitkin, I. A., and Jaffray, D. A. (2007). Energy dependence (75 kvp to 18 mv) of radiochromic films assessed using a real-time optical dosimeter. *Med Phys*, 34(2):458–63.

Rosenfeld, A. B., Kaplan, G. I., Kron, T., Allen, B. J., Dilmanian, F. A., Orion, I., Ren, B., Lerch, M., and Holmes-Siedle, A. (1999). Mosfet dosimetry of an x-ray microbeam. *IEEE Transactions on Nuclear Science*, 46(6):1774–1780.

Rothkamm, K., Balroop, S., Shekhdar, J., Fernie, P., and Goh, V. (2007). Leukocyte dna damage after multi-detector row ct: a quantitative biomarker of low-level radiation exposure. *Radiology*, 242(1):244–51.

Rothkamm, K., Kruger, I., Thompson, L. H., and Lobrich, M. (2003). Pathways of dna double-strand break repair during the mammalian cell cycle. *Mol Cell Biol*, 23(16):5706–15.

Rothkamm, K. and Lobrich, M. (2003). Evidence for a lack of dna double-strand break repair in human cells exposed to very low x-ray doses. *Proc Natl Acad Sci U S A*, 100(9):5057–62.

Ruwanpura, S. M., McLachlan, R. I., Matthiesson, K. L., and Meachem, S. J. (2008). Gonadotrophins regulate germ cell survival, not proliferation, in normal adult men. *Hum Reprod*, 23(2):403–11.

Saylor, M. C., Tamargo, T. T., McLaughlin, W. L., Khan, H. M., Lewis, D. F., and Schenfele, R. D. (1988). A thin film recording medium for use in food irradiation. *Int J Rad Applications and Instrumentation. Part C. Radiation Physics and Chemistry*, 31:529–536.

Sedelnikova, O. A., Rogakou, E. P., Panyutin, I. G., and Bonner, W. M. (2002). Quantitative detection of (125)idu-induced dna double-strand breaks with gamma-h2ax antibody. *Radiat Res*, 158(4):486–92.

Serduc, R., Christen, T., Laissue, J., Farion, R., Bouchet, A., Sanden, B. v. d., Segebarth, C., Bräuer-Krisch, E., Le Duc, G., Bravin, A., Rémy, C., and Barbier, E. L. (2008). Brain tumor vessel response to synchrotron microbeam radiation therapy: a short-term in vivo study. *Phys Med Biol*, 53(13):3609–3622.

Siegbahn, E. A. (2007). *Dosimetry for synchrotron X-ray microbeam radiation therapy*. PhD thesis, University of Munich.

Siegbahn, E. A., Stepanek, J., Brauer-Krisch, E., and Bravin, A. (2006). Determination of dosimetrical quantities used in microbeam radiation therapy (mrt) with monte carlo simulations. *Med Phys*, 33(9):3248–59.

Slatkin, D. N., Spanne, P., Dilmanian, F. A., Gebbers, J. O., and Laissue, J. A. (1995). Subacute neuropathological effects of microplanar beams of x-rays from a synchrotron wiggler. *Proc Natl Acad Sci U S A*, 92(19):8783–7.

Slatkin, D. N., Spanne, P., Dilmanian, F. A., and Sandborg, M. (1992). Microbeam radiation therapy. *Med Phys*, 19(6):1395–400.

Snyder, A. R. (2004). Review of radiation-induced bystander effects. *Hum Exp Toxicol*, 23(2):87–89.

Soares, C. G. (2006). New developments in radiochromic film dosimetry. *Radiat Prot Dosimetry*, 120:100–6.

Spiga, J., Siegbahn, E. A., Bräuer-Krisch, E., Randaccio, P., and Bravin, A. (2007). The geant4 toolkit for microdosimetry calculations: application to microbeam radiation therapy (mrt). *Med Phys*, 34(11):4322–4330.

Stepanek, J., Blattmann, H., Laissue, J. A., Lyubimova, N., Di Michiel, M., and Slatkin, D. N. (2000). Physics study of microbeam radiation therapy with psi-version of monte carlo code geant as a new computational tool. *Med Phys*, 27(7):1664–75.

Stewart, F. and Van der Kogel, A. (2002). *Basic Clinical Radiobiology*, chapter Volume Effects in Normal Tissue. Arnold, London, 3rd ed. edition.

Tinaka, T. and Kitamura, H. (2001). Spectra: a synchrotron radiation calculation code. *Journal of Synchrotron Radiation*, 8:1221–1228.

Turesson, I., Carlsson, J., Brahme, A., Glimelius, B., Zackrisson, B., and Stenerlöw, B. (2003). Biological response to radiation therapy. *Acta Oncol*, 42(2):92–106.

van der Kogel, A. J. (1993). Dose-volume effects in the spinal cord. *Radiother Oncol*, 29(2):105–109.

Van der Meeren, A., Monti, P., Vandamme, M., Squiban, C., Wysocki, J., and Griffiths, N. (2005). Abdominal radiation exposure elicits inflammatory responses and abscopal effects in the lungs of mice. *Radiat Res*, 163(2):144–152.

Williams, J. and Thwaites, D. (2000). *Radiotherapy physics in practice*. Oxford University Press.

Winick, H. (1980). *Synchrotron Radiation Research*. Springer.

Zeman, W., Curtis, H. J., and Baker, C. P. (1961). Histopathologic effect of high-energy-particle microbeams on the visual cortex of the mouse brain. *Radiat Res*, 15:496–514.

Zeman, W., Curtis, H. J., Gebhard, E. L., and Haymaker, W. (1959). Tolerance of mouse-brain tissue to high-energy deuterons. *Science*, 130:1760–1761.

Zhong, N., Morris, G. M., Bacarian, T., Rosen, E. M., and Dilmanian, F. A. (2003). Response of rat skin to high-dose unidirectional x-ray microbeams: a histological study. *Radiat Res*, 160(2):133–42.

IOP PUBLISHING PHYSICS IN MEDICINE AND BIOLOGY

Phys. Med. Biol. **53** (2008) 6861–6877 doi:10.1088/0031-9155/53/23/014

A method of dosimetry for synchrotron microbeam radiation therapy using radiochromic films of different sensitivity

J C Crosbie[1,2,3,6], I Svalbe[1], S M Midgley[1,2], N Yagi[4], P A W Rogers[5] and R A Lewis[1,2]

[1] School of Physics, Monash University, Melbourne, Victoria 3800, Australia
[2] Monash Centre for Synchrotron Science, Monash University, Melbourne, Victoria 3800, Australia
[3] The William Buckland Radiotherapy Centre, Alfred Hospital, Melbourne, Victoria 3004, Australia
[4] Japan Synchrotron Radiation Research Institute (SPring-8), Hyogo, 679-5198, Japan
[5] Monash Institute of Medical Research, Monash University, Melbourne, Victoria 3800, Australia

E-mail: Jeffrey.Crosbie@sci.monash.edu.au

Received 1 July 2008, in final form 13 October 2008
Published 12 November 2008
Online at stacks.iop.org/PMB/53/6861

Abstract

This paper describes a method of film dosimetry used to measure the peak-to-valley dose ratios for synchrotron microbeam radiation therapy (MRT). Two types of radiochromic film (manufactured by International Specialty Products, NJ, USA) were irradiated in a phantom and also flush against a microbeam collimator (beam width 25 μm, centre-to-centre spacing 200 μm) on beamline BL28 B2 at the SPring-8 synchrotron. Four experiments are reported: (1) the HD-810 and EBT varieties of radiochromic film were used to record 'peak' dose and 'valley' (regions in between peaks) dose, respectively; (2) a stack of HD-810 film sheets was microbeam-irradiated and analysed to investigate a possible dose build-up effect; (3) a very high MRT dose was delivered to HD-810 film to elicit a measurable valley dose to compare with the result obtained using broad beam radiation; (4) the half value layer of the beam with and without the microbeam collimator was measured to investigate the effect of the collimator on the beam quality. The valley dose obtained for films placed flush against the collimator was approximately 0.2% of the peak dose. Within the water phantom, the valley dose had increased to between 0.7 and 1.8% of the peak dose, depending on the depth in the phantom. We also demonstrated, experimentally and by Monte Carlo simulation, that the dose is not maximal on the surface and that there is a dose build-up effect. The microbeam collimator did not make an appreciable difference to the beam quality. The values of the

[6] Address for correspondence: Jeffrey Crosbie, School of Physics, Monash University, Clayton, Victoria 3800, Australia.

peak-to-valley ratio reported in this paper are higher than those predicted by previously published Monte Carlo simulation papers.

1. Introduction

In 1995, scientists at the Brookhaven National Laboratory, USA, reported on a novel form of radiation therapy (Slatkin *et al* 1995). This technique, known as microbeam radiation therapy, or MRT, delivered microplanar arrays of synchrotron-generated x-rays to the cerebellum of normal rats. The incident x-ray beam was segmented spatially by a collimator to create beam widths less than 40 μm and centre-to-centre spacings of 200 μm.

Synchrotron MRT has also been developed at the European Synchrotron Radiation Facility in Grenoble, France. A publication in 2001 by Laissue *et al* reported the irradiation of the cerebellum of weaning piglets at the ESRF (Laissue *et al* 2001). Since 2005, a program of research into synchrotron microbeam radiation therapy (MRT) has been carried out by Japanese and Australian research groups at the SPring-8 synchrotron in Japan.

MRT has several peculiar and beguiling properties, which appear to challenge many of the current paradigms in conventional radiation therapy; normal tissue appears exceptionally resistant to hundreds of Grays of peak, in-beam MRT doses (Zhong *et al* 2003). In addition, malignant tissue mass appears to respond to MRT by significant growth delay and, in some cases, complete tumour ablation. This is despite the small fraction of the tumour mass irradiated with the high dose microbeams (Laissue *et al* 1998, Dilmanian *et al* 2002, 2003, Miura *et al* 2006). The ratio between the dose in the peaks of the microbeams and the dose in the valleys between the microbeams has strong biological significance (Laissue *et al* 1998, 2001, Dilmanian *et al* 2003, Zhong *et al* 2003, Siegbahn *et al* 2006).

The optimal geometrical configuration or the optimal peak-to-valley dose ratio for successful MRT (maximal tumour control and minimal normal tissue toxicity) is not yet known. Moreover, it is likely to vary depending on the tissue and cell types being irradiated. A number of different MRT studies have shown that tumour types experience growth delay when irradiated with peak doses ranging from 150 Gy to 884 Gy, with beam widths and spacings ranging from 25 to 90 μm wide beams and 50 to 300 μm spacings, respectively. The tumours have included 9L gliosarcoma (Laissue *et al* 1998, Dilmanian *et al* 2002, Smilowitz *et al* 2006), EMT-6.5 (Dilmanian *et al* 2003) and SCCVII (Miura *et al* 2006). In addition, tumour growth delay has been reported for uni-directional, bi-directional and cross-planar irradiations.

Synchrotron MRT poses several fundamental radiobiological challenges. It also poses dosimetric challenges due to the very high dose gradients (hundreds of Gray) over short distances (tens of μm). No current dosimeter can accurately measure simultaneously the dose in the microbeam peaks and the dose in the valleys between the microbeams for the typical MRT energy range (50–250 keV). Consequently, the majority of publications pertaining to MRT dosimetry have relied on Monte Carlo simulations to model the radiation transport and dose deposition in water (Slatkin *et al* 1992, Company and Allen 1998, Orion *et al* 2000, Stepanek *et al* 2000, De Felici *et al* 2005, Siegbahn *et al* 2006).

The one dosimeter that is perhaps best suited to the task is also one of the oldest: photographic film. The type of film used in this work is GafChromic radiochromic film, manufactured by ISP Technologies, NJ, USA. This is a relatively new type of film dosimeter that undergoes a dose proportional colour change upon exposure to x-radiation. Some of

the more popular varieties of GafChromic radiochromic film for dosimetric purposes include HD-810, MD-55 and more recently, EBT.

Radiochromic film dosimetry is an established technique in medical radiation physics. There are several review articles describing the properties and applications of radiochromic film dosimetry for clinical use (McLaughlin *et al* 1996, Niroomand-Rad *et al* 1998, Butson *et al* 2003, Soares 2006). A Task Group report (TG55) by the American Association of Physicists (AAPM) is perhaps the most comprehensive review of radiochromic film dosimetry available (Niroomand-Rad *et al* 1998).

Used individually for MRT dosimetry, neither HD-810 nor EBT film is particularly efficient at measuring peak dose and valley dose simultaneously. An accurate measure of dose across this range is unrealistic using a single film.

In this paper, we test the hypothesis that it is possible to irradiate parallel sheets of radiochromic films of different sensitivity and record the peak doses with the HD-810 film (low sensitivity) and the valley doses with the EBT film (high sensitivity). We also test the hypothesis that the dose is not maximal on the surface of a water phantom but builds up rapidly to a peak, tens of μm below the surface.

2. Materials and methods

2.1. Synchrotron x-ray beam

All irradiations were carried out on beamline BL28 B2 at the SPring-8 synchrotron, Hyogo, Japan (SPring-8 2008). This beamline uses a bending magnet to produce polychromatic x-rays from 8 GeV electrons with a circulating beam current of approximately 100 mA. The synchrotron x-ray beam was filtered using a 3 mm thick copper filter to preferentially absorb low energy x-rays and hence increase its mean energy. The resulting x-ray beam spectrum had a mean energy of 125 keV (Ohno *et al* 2008). The energy spectrum of the filtered x-ray beam from the bending magnet on BL28 B2 was simulated using the SPECTRA program (Tinaka and Kitamura 2001) and is shown plotted on a log–log scale in figure 1(a).

2.2. Free-air ionization chamber beam monitor

The experimental dose from the incident beam was estimated by careful measurements of the ion current, recorded by a free-air ionization chamber (OKEN S-1194, Tokyo, Japan) and compensating for the beam cross section. The charge recorded by the ionization chamber was converted to exposure through the following relationship (Greening 1985):

$$X = \frac{\Delta Q}{\rho \times A \times L} \times \frac{1}{2.58 \times 10^{-4}} \text{ Roentgens} \tag{1}$$

where ΔQ is the charge collected in coulombs, ρ is the density of air at standard temperature and pressure (kg m^{-3}), A is the cross-sectional area of the beam (m^2) and L is the length (m) of the collecting volume in the ionization chamber. The relation $1R = 2.58 \times 10^{-4}$ C kg^{-1} was used (Johns and Cunningham 1983). No correction was made for ion recombination because the ion chamber was operating in the flat portion of the efficiency saturation curve where the chamber collection efficiency is taken to be unity. Corrections were required for ambient temperature and pressure.

At this energy range, we assume that the air kerma is composed almost entirely of its so-called collisional component, K_{col}, and is equivalent to dose in air (Khan 2003). The air

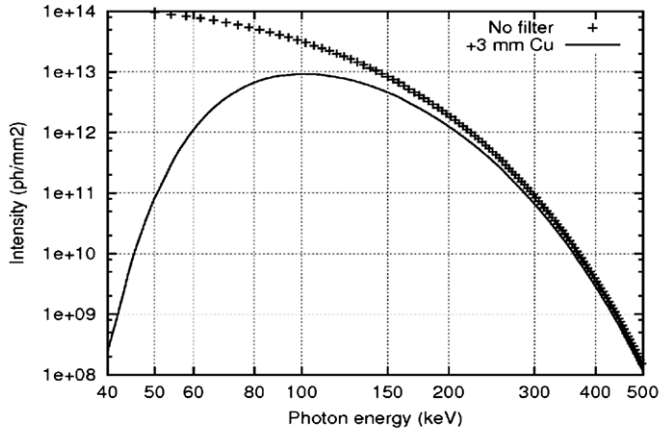

(a)

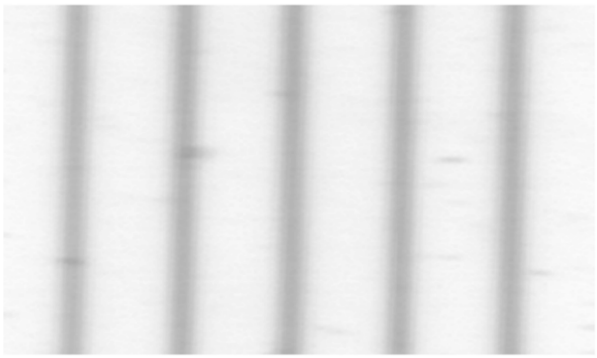

(b)

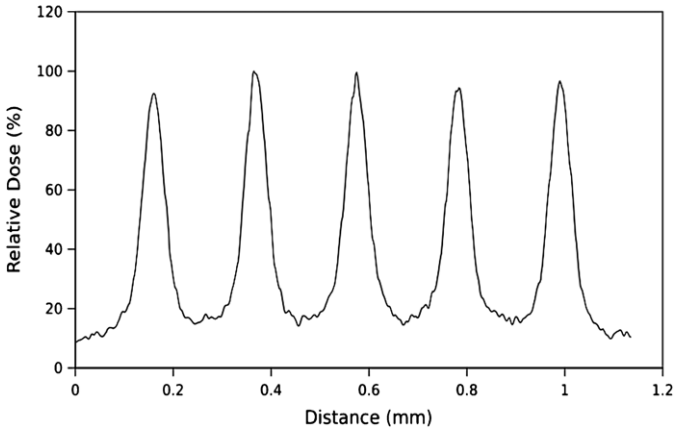

(c)

Figure 1. The energy spectrum (a) of the polychromatic x-ray beam produced by the bending magnet source for beamline BL28 B2 at SPring-8. The spectrum was estimated using the SPECTRA computer program of Tanaka and Kitamura. A section of radiochromic film which has been exposed to MRT is shown in (b) and a line profile is shown in (c). The 1 mm high beam contains five microbeams, each one spaced 200 μm from its neighbour.

kerma is calculated from the following relationship:

$$K = \left(\frac{W}{e}\right) X \tag{2}$$

where W/e is the average energy required to produce an ion pair in dry air and has a value of 33.97 eV/ion pair (Khan 2003).

2.3. Microbeam collimator

A fixed geometry tungsten/kapton multislit collimator was used to segment the broad beam into an array of planar microbeams. The incident x-ray beam is collimated by 175 μm thick planes of high-Z tungsten, spatially separated by 25 μm thick sheets of low density kapton, a type of plastic. The collimator design is described in greater detail by Ohno *et al* (2008). The thickness of the tungsten/kapton collimator in the direction of the beam was approximately 10 mm. The nominal, collimated beam width was 25 μm with a centre-to-centre spacing of 200 μm. The exposure time was adjusted by varying the opening and closing time of an upstream shutter, which blocked the x-ray beam. The minimum opening time of the shutter was 100 ms.

2.4. Radiochromic film dosimetry

Radiochromic film consists of monomer crystals in a gel bound to a Mylar substrate. The monomer undergoes partial polymerization upon irradiation which leads to a colour change from a light to a dark blue. The active component in GafChromic radiochromic dosimetry films is a long chain fatty acid, similar to stearic acid and belonging to the diacetylene class of molecules (ISP 2008). These films have different physical properties (thickness, composition, sensitivity) and respond over different dose ranges. The thicknesses of the HD-810 and EBT films are approximately 110 μm and 290 μm, respectively.

The dose range for GafChromic HD-810 film is between 10 Gy and 400 Gy, and below 250 Gy, the response of the film is essentially linear with dose (ISP 2008). However, HD-810 can also be used at higher doses provided the results are interpreted with appropriate dose calibration curves. The TG55 report states that the nominal dose range of HD-810 is between 50 and 1000 Gy (Niroomand-Rad *et al* 1998). ISP states that the EBT film is sensitive to doses in the range 0.01–8 Gy (ISP 2007) whereas Soares states that the useful range of EBT is from 0.05 Gy to 8 Gy (Soares 2006). The sensitive material in radiochromic films is quite similar to water in terms of mass energy absorption coefficients and electron mass stopping powers (Niroomand-Rad *et al* 1998, Butson *et al* 2003).

Radiochromic film continues to 'develop' or polymerize for several hours post-exposure before reaching chemical completion, and most practical radiochromic film analysis is done the day after exposure. ISP recommends waiting at least 24 h post-irradiation before analysing the HD-810 film and at least 6 h before analysing the EBT film. Post-exposure density growth curves for both films are available (ISP 2007b, 2008). For other varieties of GafChromic film, slight increases (up to 4%) in the absorbance of MD-55 have been reported after 24 h out to 2 weeks post-exposure, and there have been no appreciable changes in absorbance between 40 and 165 days post-exposure (Niroomand-Rad *et al* 1998).

The manufacturers state that the HD-810 film is energy independent for photons with energies above about 200 keV (ISP 2008). Muench *et al* showed the response of GafChromic HD-810 film decreased by approximately 30% when the effective photon energy decreased from 1720 keV (4 MV x-rays) to 28 keV (60 kVp x-rays) (Muench *et al* 1991). Considering that our mean photon energy is 125 keV, any energy dependence of the HD-810 film is

sufficiently small to be ignored. The EBT film is essentially energy independent across all therapeutic energy ranges (Rink *et al* 2007).

2.4.1. Microdensitometry. After irradiation, the films were placed in aluminium foil (to exclude light) for transport to and analysis in Australia. Broad beam- and microbeam-irradiated films were scanned on a Joyce–Loebl microdensitometer (3CS Mark II, Joyce–Loebl, Gateshead, UK). The spatial resolution of GafChromic HD-810 radiochromic film is extremely high, better than 600 line pairs mm^{-1} (Niroomand-Rad *et al* 1998). The microdensitometer however is a more limiting factor for spatial resolution. We measured the microdensitometer's spatial resolution using a line-pair test pattern and recorded a modulation transfer function (MTF) value of 81% for a spatial frequency of 20 line pairs mm^{-1}. This corresponds to an object width of 25 μm, the nominal width of the microbeams.

The microdensitometer outputs a voltage proportional to the optical density of the film, which we verified using a step-wedge film. We also independently checked the response of the HD-810 film using a hand-held densitometer (data not shown). Calibration curves of absorbed voltage versus dose are shown in figure 2 for both HD-810 (a) and EBT (b) films. Three scans were performed perpendicular to the microbeam direction across the centre and the two edges of the microbeams. The readings were then averaged across the three profiles to obtain a mean reading with associated uncertainty (two times the standard error of the mean). The digitized voltage values from the MRT profiles were then converted to dose (in water) using the broad beam voltage–dose calibration curves. A quadratic curve was fitted to the data, a technique similar to that performed by commercial radiotherapy film dosimetry software packages.

2.5. Experiment 1—peak and valley dose measurements

The principal objective of the experiment was to measure the peak-to-valley dose ratio at the collimator and as a function of depth in a tissue equivalent, solid water phantom, downstream of the collimator. To this end, two parallel sheets of HD-810 and EBT radiochromic films were placed at various depths in the phantom and irradiated with an in-beam entrance dose of 160 Gy. The films were also positioned flush against the beam exit side of the collimator. The HD-810 films were placed in front of the EBT films. The experimental setup for the solid water phantom irradiations is shown schematically in figure 3. The films were positioned between the solid water slabs at the surface and subsequently at 1 mm, 5 mm, 10 mm, 30 mm, 50 mm and 70 mm thicknesses.

A set of dose calibration films for the two film types were also acquired, in which known broad beam doses of synchrotron radiation were delivered to the HD-810 and EBT films. Calibration doses between 20 Gy and 320 Gy were delivered to the HD-810 film and doses between 0.2 Gy and 6 Gy were delivered to the EBT film. The calibration films were placed at a depth of 1 mm in the solid water stack. The air kerma, corrected for ambient temperature and pressure, was converted to dose to water at 1 mm depth by multiplying the kerma by the ratio of the mass energy absorption coefficients for water and air. A simple exponential attenuation factor, to adjust the dose for a depth of 1 mm, was also applied.

It was necessary to attenuate the broad beam in order to accurately deliver calibration doses of less than 1 Gy to the EBT film due to the limitations of the upstream lead shutter. The flux rate was attenuated by placing high purity, metallic absorbers (11.5 mm Cu, 1 mm Fe, 7 mm Al) in the path of the beam. The effect of beam hardening on the EBT calibration was considered negligible owing to the energy independence of the EBT film (Rink *et al* 2007).

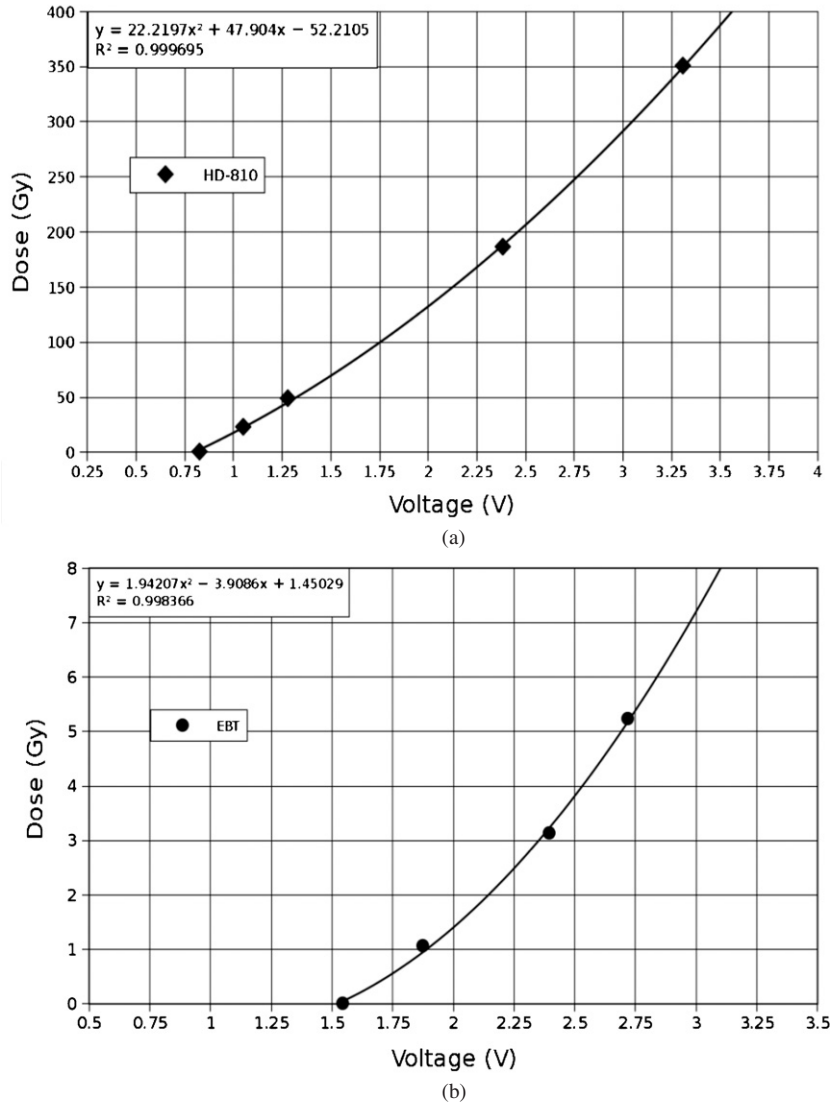

Figure 2. Typical voltage–dose calibration curves for the high dose, low sensitivity HD-810 film (a) and the low dose, high sensitivity EBT film (b) subjected to broad beam radiation and analysis based upon microdensitometer scans.

2.6. Experiment 2—investigation of the dose build-up effect

Preliminary film dosimetry work hinted at a dose build-up effect for the MRT beam. That is to say, the dose did not appear to be maximal on the surface. To further investigate this, a stack of 30 strips of the HD-810 film, sandwiched together, was irradiated. This provided measurements of the relative dose distribution at 110 μm depth increments, instead of the 1000 μm (1 mm) increments of the thinnest solid water slab. The percentage depth dose curve of this polyenergetic x-ray beam was simulated using the GEANT4 Monte Carlo code (Agostinelli *et al* 2003).

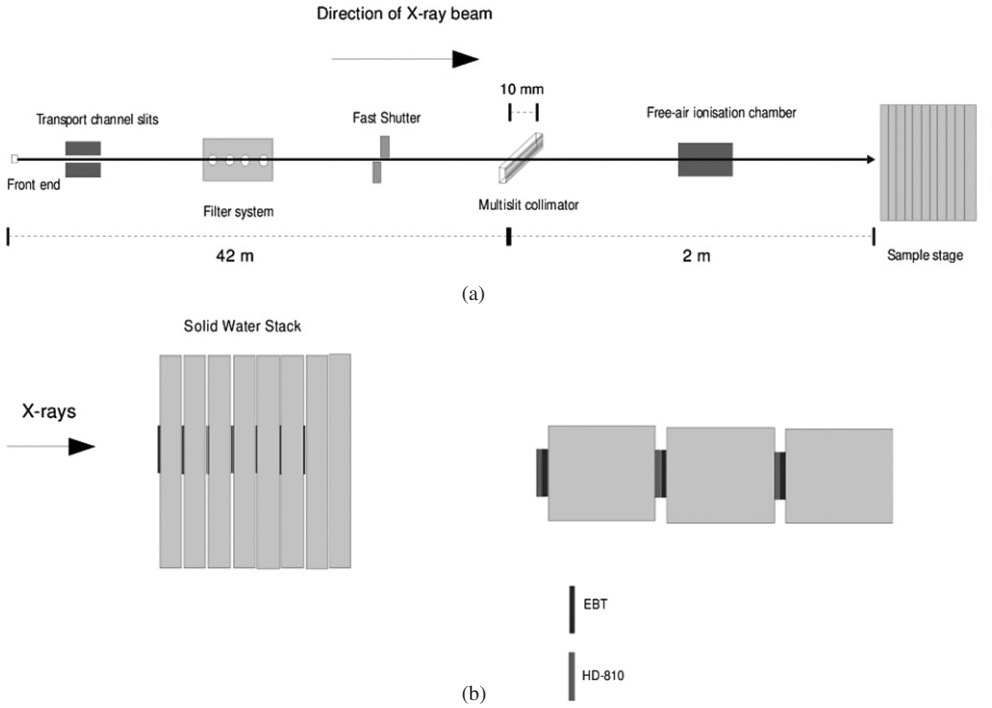

Figure 3. (a) Schematic of apparatus on beamline BL28 B2 at SPring-8 for MRT film dosimetry; (b) the stack of solid water slabs and sandwiched radiochromic films. Each solid water slab measured 300 mm × 300 mm × 10 mm.

The stack was irradiated at four locations: at the level of the collimator, in front of the ionization chamber, at the sample stage and a further position, 1.1 m downstream of the sample stage. Films were scanned on the microdensitometer in a manner similar to that described in experiment 1.

2.7. Experiment 3—accurate valley dose measurements

A single piece of HD-810 film was irradiated with a peak MRT dose of 3000 Gy, as measured using the ionization chamber. A separate piece of HD-810 film was irradiated with broad beam radiation across a range of dose values, chosen to be similar to the valley dose of the MRT-irradiated film. The purpose of this experiment was to scale the valley dose up into the HD-810 film's sensitivity range. This acted as a 'cross check' of the EBT valley dose data. These films were scanned on the microdensitometer and a calibration curve of dose versus voltage (optical density) was generated from the broad beam films. This curve was used to estimate the dose in the valley region of the very high dose MRT film, based upon a microdensitometer scan of the valley region.

2.8. Experiment 4—measurement of beam quality

In order to determine whether the microbeam collimator changed the beam quality, we measured the first three half value layers (HVL) for copper for (A) the beam transmitted through the microbeam collimator, (B) no microbeam collimator present and (C) the microbeam

collimator and ion chamber placed beside each other. The predicted HVLs were obtained by the analysis of the predicted primary beam energy spectrum (SPECTRA).

3. Results

3.1. Experiment 1—peak and valley dose measurements

A single broad beam, measuring 1 mm in the vertical plane, produced five horizontal microbeams after collimation. Figure 1(b) is a scan of HD-810 radiochromic film exposed to five such microbeams. An example of the one-dimensional dose profile is shown in figure 1(c). This is a sample line profile across the film and is typical of the profiles obtained on the microdensitometer. Note the low sensitivity of the film in the valley region despite the in-air, entrance peak dose of 160 Gy. The peak regions of the HD-810 film showed an obvious, measurable change in optical density but the valley regions did not, the HD-810 film being insensitive to doses below 10 Gy (ISP 2008). The peak regions of the EBT film were saturated yet the valley regions showed a measurable change in optical density.

The percentage depth dose curves for both peak and valley doses are plotted in figure 4(a). The peak and valley doses were obtained from microdensitometry scans of the HD-810 and EBT films respectively for each depth in the phantom. The plots are normalized to the maximum peak dose, which was not maximal at the surface. There was a rapid build-up effect with the maximum peak dose observed at a depth of 1 mm (limit of solid water slab thickness). Typical exponential-like attenuation was observed beyond 1 mm. The variation in valley dose is not readily apparent from figure 4(a), since the profiles are normalized to the maximum peak dose. The valley dose increased slowly, to a maximum at a depth of 10 mm in water, and then decreased slowly with depth. A similar variation in peak and valley doses, computed by Monte Carlo simulations, was reported by Siegbahn *et al* (2006).

The variation in peak-to-valley dose ratio (PVDR) with depth in the solid water phantom is shown in figure 4(b). This is a dimensionless quantity, and in these results, the uncertainty in PVDR is expressed as a percentage of that ratio. The PVDR on the surface of the phantom was 65 ± 35%. It then increased to a maximum, mean PVDR of 144 ± 29%, at a depth of 1 mm. The PVDRs then decreased with depth down to 10 mm and were then observed to be rather stable: 67 ± 27% at 10 mm, 76 ± 26% at 30 mm and 60 ± 29% at 50 mm depth. The mean PVDR at 70 mm depth was 85 ± 18%. The peak-to-valley dose ratio for the films placed flush against the collimator was 388 ± 21%. The uncertainty in PVDR was calculated by expressing the uncertainties in peak and valley doses as a percentage and summing them in quadrature according to equation (3) below. The PVDR uncertainty is dominated by that of the valley dose:

$$\delta_{\mathrm{PVDR}} = \sqrt{(\delta_{\mathrm{peak}})^2 + (\delta_{\mathrm{valley}})^2}. \tag{3}$$

Closer inspection of the percentage depth dose curve for the peak doses (as measured with the HD-810 film) showed a distinct build-up effect. The dose was not maximal on the surface, but rather at a depth of 1 mm in solid water, the thinnest slab. This is the dose 'build-up' effect; dose depositing secondary electrons are set in motion when an x-ray photon beam bombards a medium (Johns and Cunningham 1983, Khan 2003). This build-up effect explains the large differences between the PVDR recorded on the surface and the PVDR recorded at a depth of 1 mm.

The Monte Carlo simulated depth dose curve also reproduces this build-up effect. The measured and simulated depth dose curves are shown superimposed in figure 5(a). The experimental film data were normalized to the maximum value at 1 mm depth. The Monte

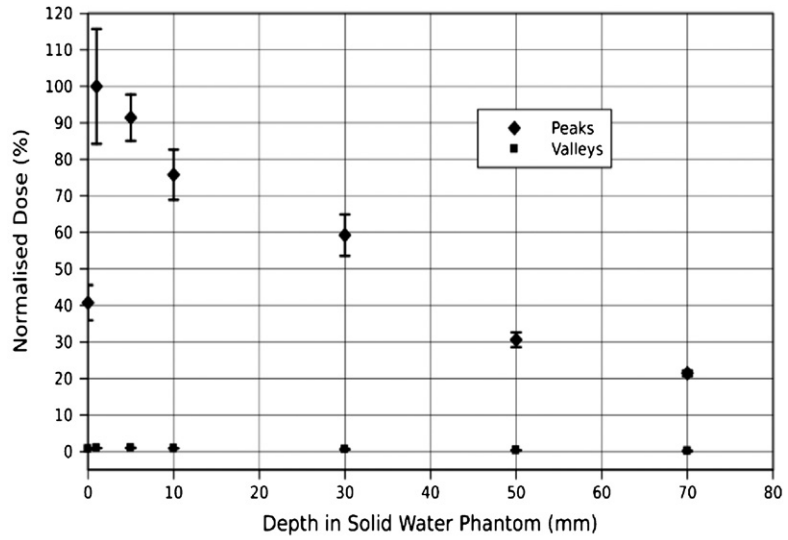

(a)

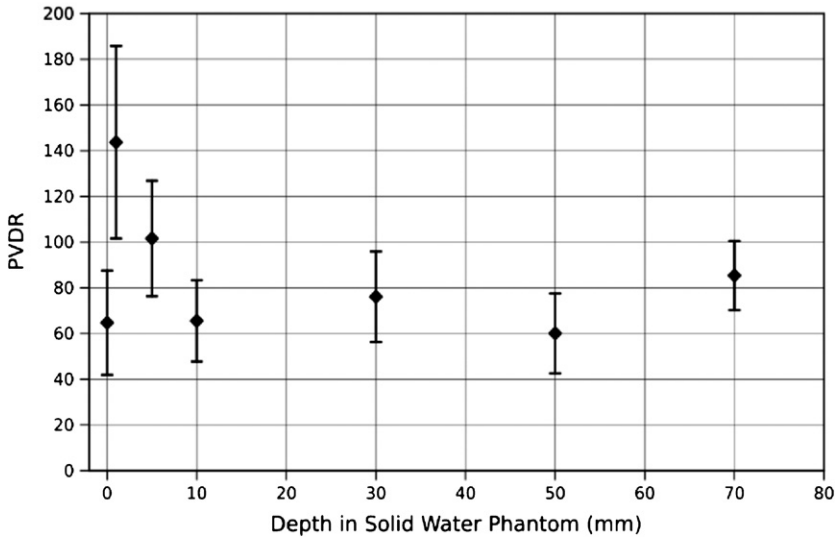

(b)

Figure 4. (a) Measured peak and valley doses at various depths in a water phantom, normalized to the peak dose at 1 mm depth. The uncertainties (error bars) represent two times the standard error of the mean across the left, centre and right sides of the film. Plot (b) shows the change in the peak-to-valley dose ratio (PVDR) with depth. The data points were obtained by dividing the mean peak dose by the mean valley dose. The uncertainties (error bars) represent the uncertainty in peak dose plus the uncertainty in valley dose summed in quadrature.

Carlo simulated depth dose curve was performed using a 100 μm step size and was normalized to the peak dose. The simulation was performed in liquid water. At a depth of 100 μm, the simulated depth dose curve was already 95% of its maximum dose. Figure 5(b) shows a Monte Carlo depth dose simulation using 1 μm step sizes. This plot shows that the dose builds up very rapidly, approaching its maximum value after only 20 μm. There are fluctuations in the

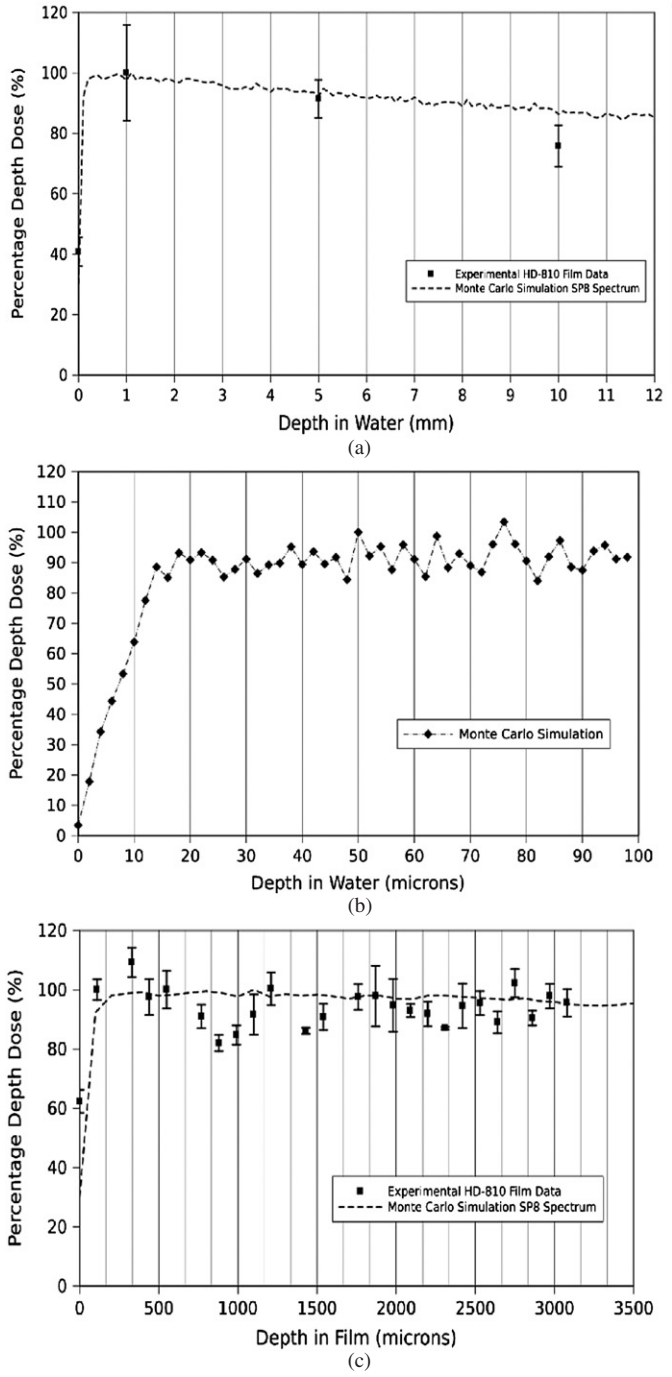

Figure 5. Percentage depth dose measurements compared against Monte Carlo simulations: (a) coarse measurements every 5 mm in solid water, (b) Monte Carlo depth dose simulations using a fine 1 μm step and (c) fine measurements every 110 μm in a stack of HD-810 films.

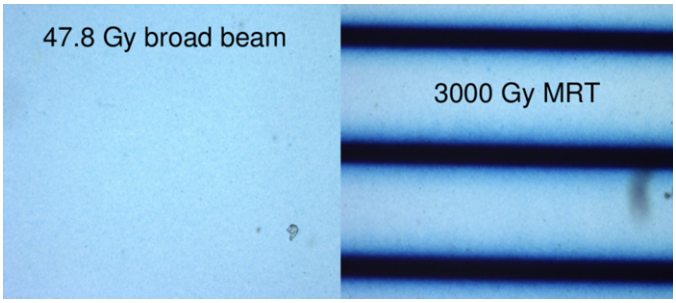

Figure 6. A visual comparison of the HD-810 film exposed to 47.8 Gy of broad beam radiation (left-hand side) and the HD-810 film exposed to MRT with an in-beam peak dose of 3000 Gy (right-hand side). The change in optical density (proportional to dose) elicited in the valley region of the MRT-irradiated film is comparable to the change in optical density in the broad beam-irradiated film.

(This figure is in colour only in the electronic version)

simulated data which make it difficult to quote a precise value of the depth of maximum dose other than to say that the dose is not maximal on the surface but builds up rapidly after a depth of some tens of μm. At the depth of 10 mm, the agreement between experiment and simulation is not as strong as at the other depths in figure 5(a). The experimental uncertainty in the film data is the most likely explanation for the difference.

3.2. Experiment 2—investigation of a dose build-up effect

Figure 5(c) shows the percentage depth dose curve in the 30-film stack of HD-810 films. These films were irradiated at the level of the free-air ionization chamber, situated approximately 400 mm downstream of the collimator. The combined thickness of the sandwich was 3.3 mm (or 3300 μm) since each film was approximately 110 μm thick. At all four irradiation positions, the relative surface dose (first film in the sandwich) was significantly less than the relative dose recorded from the second film, approximately 110 μm deep in the sandwich. The GEANT4 Monte Carlo simulated depth dose from figure 4(a) is included in figure 5(c) for comparison. The film sandwich experiment confirmed that the dose was not maximal on the surface.

There was quite a degree of experimental uncertainty (expressed as two times the standard error of the mean) in the film data presented in figure 5(c). In addition, the experimental curve was arbitrarily normalized to the second film at a depth of 110 μm. The Monte Carlo simulation of depth dose is the same curve from (a) albeit at a shallower depth, and the simulation was carried out in liquid water and not film material.

3.3. Experiment 3—accurate measurement of valley doses

Figure 6 shows a colour comparison on the HD-810 film between a broad beam entrance dose of 47.8 Gy and the valley region of the HD-810 film, irradiated with a peak, MRT dose of 3000 Gy. The optical density in the valley region was qualitatively comparable to that of the broad beam. The dose in the valley region of the MRT-irradiated film was found to be 56 $\pm$ 4 Gy, after scanning with the microdensitometer and converting to dose using the equation of fit. An extrapolation was required from the equation of fit as the maximum broad beam dose delivered was 47.8 Gy. The 'colour change', i.e. optical density (dose) in the valley region

Table 1. Half value layer (HVL) measurements of x-ray beam transmitted through the microbeam collimator (A), with the collimator removed (B) and with the ion chamber close to the collimator (C). The predicted HVLs are also shown.

HVL	A (mm Cu)	B (mm Cu)	C (mm Cu)	Predicted (mm Cu)
1	0.198	0.200	0.198	0.198
2	0.243	0.240	0.245	0.246
3	0.270	0.283	0.290	0.290

of the MRT-irradiated film, was greater than that in the broad beam film. The peak-to-valley dose ratio from this experiment was 55 ± 9%. This value is comparable to the lower end of PVDRs obtained in experiment 1 (figure 4(b)). The uncertainty in PVDR was lower in this experiment than in experiment 1, most likely a result of a stronger signal-to-noise ratio from the HD-810 film scans using the 'colour change' method.

3.4. Beam quality measurements

The beam quality, as measured by successive half value layers, of both the beam transmitted by the microbeam collimator and the broad beam was very similar and in good agreement with the predictions from the SPECTRA program. The HVL measurements and predictions are summarized in table 1.

We calculated the photon flux rate to be 1.96×10^{12} and 2.44×10^{12} ph s^{-1} mm^{-2} with and without the microbeam collimator. The 10 mm of kapton attenuates the flux rate by approximately 20%. The air kerma rate, as measured by the free-air ion chamber, for the microbeam and broad beam conditions was approximately 85 Gy s^{-1} and 105 Gy s^{-1}, respectively.

4. Discussion

Our results demonstrate that it is possible to use radiochromic films of different sensitivities to record the peak-to-valley dose ratio for synchrotron MRT and to track PVDR changes at various depths in a water phantom. The peak-to-valley dose ratio obtained for films placed flush against the collimator was almost 400. Combining the solid water phantom (experiment 1) and 'colour change' (experiment 3) data, a peak-to-valley dose ratio between 145 and 55 was recorded, depending on the depth in the phantom.

It has also been demonstrated, both experimentally and by computer simulation, that the dose is not maximal on the surface but builds up rapidly with depth after distances of some tens of μm. Other authors have shown a build-up effect via Monte Carlo simulation (Siegbahn *et al* 2006). Considering the dose builds up so rapidly with depth, over a distance of two or three cell diameters, it may not have a significant implication for MRT studies in biological tissue.

A distinct advantage to radiochromic film is its ease of use as a dosimeter. Other MRT dosimetry techniques have reported difficulties. For example, the alignment and stability concerns of MOSFET (metal oxide semiconductor field effect transistor) detectors (Brauer-Krisch *et al* 2003) do not apply to film. The combination of radiochromic film and microdensitometer provides sufficient spatial resolution for the measurements (section 2.4.1). We emphasize that the results obtained here are of real measurements and not simulated doses. It is important for MRT to have measurement-based dosimetry which can be used to benchmark computer simulations. The results presented here were for a fixed-geometry,

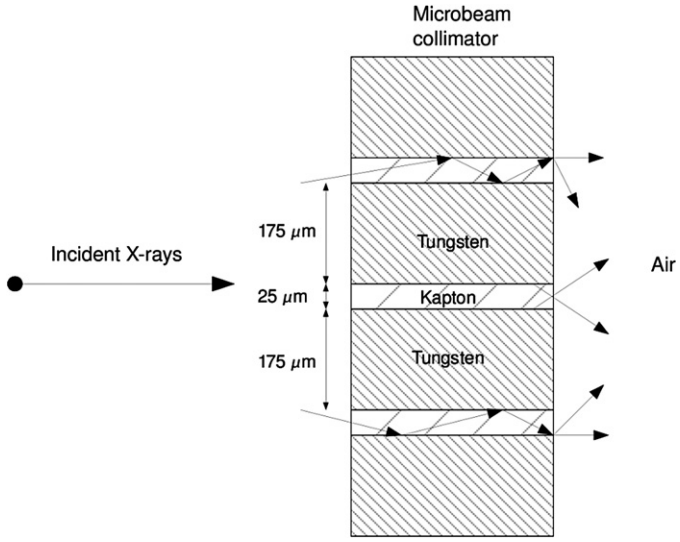

Figure 7. Schematic diagram of the tungsten/kapton collimator at SPring-8, illustrating the potential for the collimator to produce secondary radiation (e.g. scattered photons and tungsten characteristic radiation).

multi-slit collimator, but it should be possible to use the same technique on a variable width collimator, such as the collimators used at the National Synchrotron Light Source in the USA and at the ESRF in France.

The PVDR obtained for films placed flush against the collimator was significantly greater than the PVDRs in the solid water phantom (figure 4(b)). The sample stage for the phantom was approximately 1 m downstream of the collimator. The biggest difference between the collimator films and the phantom films was the dose in the valley region. The valley dose was observed to increase from approximately 0.2% of the peak dose at the level of the collimator, to approximately 2% of the peak dose in the water phantom.

It is possible that there occurs angular, multiple scattering and reflection of the x-ray beam from the tungsten/kapton borders into the valley regions, immediately beyond the collimator. This is illustrated schematically in figure 7. Scattered photons and characteristic radiation from tungsten may be generated inside the collimator as the incident x-ray beam is collimated by 175 μm thick planes of high-Z tungsten, spatially separated by 25 μm thick sheets of low density plastic. Our HVL data (table 1) obtained in the presence of and in the absence of the microbeam collimator were very similar, indicating that the microbeam collimator is not in fact producing significant amounts of secondary radiation. The microbeams from a collimator are not perfectly precise; they possess 'tails' of valley dose, which may contribute dose to adjacent microbeams.

The interaction of the incident x-rays with the tungsten/kapton collimator and the propagation of the segmented microbeams through air, prior to reaching the target, require more detailed modelling and measurement. A more realistic simulation, for example, would be to model a 25 μm thick sheet of kapton, sandwiched between two tungsten plates, and also to model a 'detector' of variable thickness and distance from the collimator face. The detector material could be more accurately modelled as film using the relative elemental constituents rather than simply liquid water.

Table 2. The Monte Carlo simulated peak-to-valley dose ratios as reported by a selection of authors for a 25 μm wide beam with a 200 μm wide centre-to-centre separation.

Author	Code	PVDR	Depth (cm)
Slatkin *et al* (1992)	CPE	35	0–1
		15	7–8
Stepanek *et al* (2000)	PSI-GEANT	29 (centre of field)	0–1
		44 (field edge)	
De Felici *et al* (2005)	EGS4	29 (centre of field)	7–8
		33 (field edge)	
Brauer-Krisch *et al* (2005)	Penelope	53	0–1 in PMMA
Siegbahn *et al* (2006)	Penelope	29	0–1
		14	7–8

The 'colour change' experiment on the HD-810 film (figure 6) provides convincing evidence that the dose in the valley region is between 1 and 2% of the peak dose, as observed at the level of the sample stage. Most of the Monte Carlo simulated PVDRs (for microplanar beams) published in the literature are lower than those reported in this paper. We obtained a maximum PVDR of 144 $\pm$ 29% at 1 mm depth in water and a minimum PVDR of 60 $\pm$ 29% at 50 mm depth. The Monte Carlo papers of Siegbahn *et al*, De Felici *et al*, Stepanek *et al* and Slatkin *et al* report PVDRs closer to 30. That is, a valley dose which is approximately 3% of the peak dose. In general, the literature on Monte Carlo simulations of MRT is rather consistent; the different radiation transport codes produce PVDRs which agree with each other reasonably well.

Table 2 lists the PVDRs reported by a sample of authors in articles on MRT dosimetry, which used Monte Carlo simulations. In the tabulated references, the quoted PVDR was for 25 μm wide beams at 200 μm centre-to-centre separations.

The Monte Carlo simulations do not fully simulate the synchrotron x-ray source or downstream features such as slits. Perhaps the major shortcoming of the simulations is that they do not actually simulate a collimator. Multiple, planar microbeams have been simulated as individual microbeams, propagating through a phantom and then positioned at 200 μm intervals. As a consequence, multiple, angular scattering events occurring inside and immediately beyond the collimator (illustrated schematically in figure 7) have not been adequately modelled.

In one publication (Siegbahn *et al* 2006), the x-ray source is assumed to originate on the surface of the water phantom, neglecting the effect of scatter into the valley region within the collimator, immediately post-collimator and pre-water phantom. Slight manufacturing imperfections (on a μm scale) in a real collimator will also affect the PVDR but would be difficult to simulate.

There is a paucity of synchrotron MRT studies with the emphasis on experimentally obtained data, an exception being MOSFET dosimetry for planar microbeams as described by Brauer-Krisch *et al.* The authors reported a measured PVDR of approximately 60 using MOSFET dosimetry averaged across different depths in a PMMA phantom (Brauer-Krisch *et al* 2003). This value is closer to our experimentally derived PVDRs than the Monte Carlo simulation data.

In general, film is not used for absolute dosimetry purposes in radiotherapy but rather for relative dosimetry. An ionization chamber at different depths in water would be the preferred dosimeter, but ultimately an alternative dosimeter may be required. While ionization chamber

dosimetry can give an estimate of the dose in the peaks, there is no easy way to measure the dose in the valley region. From a radiobiological standpoint, being able to quantify the peak dose to within an accuracy of 3% may not be so critical when delivering hundreds of Gray of radiation, since it is already a lethal dose to the irradiated cells. Accurate measurement of the valley dose on the other hand is essential, as this may be the limiting biological factor in MRT (Laissue *et al* 1998, 2001, Dilmanian *et al* 2003, Zhong *et al* 2003, Siegbahn *et al* 2006).

Trying to simultaneously measure the peak and valley doses, to obtain the PVDR, has proven difficult, until now. The strength of our paper lies in a simple and straightforward way to measure the PVDR for synchrotron MRT. A distinct advantage to the technique described in this paper is that one can measure fine spatial variations in the dose distribution within a bulk material. The MOSFET technique as well as in-air ion chambers typically only measure entrance dose distributions at a point. Inside a material, a significant contribution from scattered x-rays comes from all directions. Film is probably the only way to measure this.

Acknowledgments

We thank the reviewers of this paper for helpful comments and suggestions which have been incorporated into the text. The authors thank the following individuals for their assistance with this study: Dr Marian Cholewa, Dr Toby Beveridge and Dr John Gillam, Monash Centre for Synchrotron Science, Monash University; Mr Steve Morton and Mr Peter Oliver, School of Physics, Monash University; Dr Duncan Butler, Australian Radiation Protection and Nuclear Safety Agency; Dr David Lewis, ISP, New Jersey, USA; and Mr Andrew Campbell, Royal Perth Hospital, Western Australia. The authors have received funding from the following agencies: Cancer Council Victoria Venture Grant to PAWR, RAL and IS, Australian Nuclear Science and Technology Organisation (ANSTO) travel grants to JCC and PAWR, Monash University postgraduate scholarship to JCC, National Health and Medical Research Council of Australia (fellowship grant number 143805) to PAWR.

References

Agostinelli S *et al* 2003 G4—a simulation toolkit *Nucl. Instrum. Methods Phys. Res.* **506** 250–303

Brauer-Krisch E, Bravin A, Lerch M, Rosenfeld A, Stepanek J, Di Michiel M and Laissue J A 2003 MOSFET dosimetry for microbeam radiation therapy at the European Synchrotron Radiation Facility *Med. Phys.* **30** 583–9

Brauer-Krisch E *et al* 2005 New irradiation geometry for microbeam radiation therapy *Phys. Med. Biol.* **50** 3103–11

Butson M J, Yu P K N, Cheung T and Metcalfe P 2003 Radiochromic film for medical radiation dosimetry *Mater. Sci. Eng.* R **41** 61–120

Company F Z and Allen B J 1998 Calculation of microplanar beam dose profiles in a tissue/lung/tissue phantom *Phys. Med. Biol.* **43** 2491–501

De Felici M, Felici R, Sanchez del Rio M, Ferrero C, Bacarian T and Dilmanian F A 2005 Dose distribution from x-ray microbeam arrays applied to radiation therapy: an EGS4 Monte Carlo study *Med. Phys.* **32** 2455–63

Dilmanian F A *et al* 2002 Response of rat intracranial 9L gliosarcoma to microbeam radiation therapy *Neuro Oncol.* **4** 26–38

Dilmanian F A, Morris G M, Zhong N, Bacarian T, Hainfeld J F, Kalef-Ezra J, Brewington L J, Tammam J and Rosen E M 2003 Murine EMT-6 carcinoma: high therapeutic efficacy of microbeam radiation therapy *Radiat. Res.* **159** 632–41

Greening J R 1985 *Fundamentals of Radiation Dosimetry* (London: Taylor and Francis)

ISP 2007 GafChromic EBT Product Brief. International Speciality Products (ISP) Technologies http://online1.ispcorp.com/_layouts/Gafchromic/index.html

ISP 2007b GafChromic EBT White Paper, Self developing film for radiotherapy dosimetry. International Speciality Products (ISP) Technologies http://online1.ispcorp.com/_layouts/Gafchromic/index.html

ISP 2008 *Technical Report* GafChromic HD-810 radiochromic dosimetry film and D-200 pre-formatted dosimeters for high energy photons; Configuration, specifications and performance data. International Specialty Products (ISP) Technologies http://online1.ispcorp.com/_layouts/Gafchromic/index.html

Johns H E and Cunningham J R 1983 *The Physics of Radiology* (Springfield, IL: Charles C Thomas)

Khan F M 2003 *The Physics of Radiation Therapy* (Baltimore, MD: Williams & Wilkins)

Laissue J A *et al* 1998 Neuropathology of ablation of rat gliosarcomas and contiguous brain tissues using a microplanar beam of synchrotron-wiggler-generated x rays *Int. J. Cancer* **78** 654–60

Laissue J A, Blattmann H, Di Michiel M, Slatkin D N, Lyubimova N and Guzman R 2001 The weaning piglet cerebellum: a surrogate for tolerance to MRT (microbeam radiation therapy) in paediatric neuro-oncology *Penetrating Radiation Systems and Applications III, Proc. SPIE* **4508** 65–73

McLaughlin W L, Puhl J M, Al-Sheikhly M, Christou C A, Miller A, Kovács A, Wojnarovits L and Lewis D F 1996 Novel radiochromic films for clinical dosimetry *Radiat. Prot. Dosim.* **66** 263–8

Miura M, Blattmann H, Brauer-Krisch E, Bravin A, Hanson A L, Nawrocky M M, Micca P L, Slatkin D N and Laissue J A 2006 Radiosurgical palliation of aggressive murine SCCVII squamous cell carcinomas using synchrotron-generated X-ray microbeams *Br. J. Radiol.* **79** 71–5

Muench P J, Meigooni A S, Nath R and McLaughlin W L 1991 Photon energy dependence of the sensitivity of radiochromic film and comparison with silver halide film and LiF TLDs used for brachytherapy dosimetry *Med. Phys.* **18** 769–75

Niroomand-Rad A *et al* 1998 Radiochromic film dosimetry: recommendations of AAPM Radiation Therapy Committee Task Group 55. American Association of Physicists in Medicine *Med. Phys.* **25** 2093–115

Ohno Y, Torikoshi M, Suzuki M, Umetani K, Imai Y, Uesugi K and Yagi N 2008 Dose distribution of a 125 keV mean energy microplanar x-ray beam for basic studies on microbeam radiotherapy *Med. Phys.* **35** 3252–8

Orion I, Rosenfeld A B, Dilmanian F A, Telang F, Ren B and Namito Y 2000 Monte Carlo simulation of dose distributions from a synchrotron-produced microplanar beam array using the EGS4 code system *Phys. Med. Biol.* **45** 2497–508

Rink A, Vitkin I A and Jaffray D A 2007 Energy dependence (75 kVp to 18 MV) of radiochromic films assessed using a real-time optical dosimeter *Med. Phys* **34** 458–63

Siegbahn E A, Stepanek J, Brauer-Krisch E and Bravin A 2006 Determination of dosimetrical quantities used in microbeam radiation therapy (MRT) with Monte Carlo simulations *Med. Phys.* **33** 3248–59

Slatkin D N, Spanne P, Dilmanian F A, Gebbers J O and Laissue J A 1995 Subacute neuropathological effects of microplanar beams of x-rays from a synchrotron wiggler *Proc. Natl Acad. Sci. USA* **92** 8783–7

Slatkin D N, Spanne P, Dilmanian F A and Sandborg M 1992 Microbeam radiation therapy *Med. Phys.* **19** 1395–400

Soares C G 2006 New developments in radiochromic film dosimetry *Radiat. Prot. Dosim.* **120** 100–6

SPring-8 2008 http://www.spring8.or.jp/wkg/BL28 B2/instrument/lang-en/INS-0000000374/instrument_summary_view?q=BEwH&f=

Stepanek J, Blattmann H, Laissue J A, Lyubimova N, Di Michiel M and Slatkin D N 2000 Physics study of microbeam radiation therapy with PSI-version of Monte Carlo code GEANT as a new computational tool *Med. Phys.* **27** 1664–75

Tinaka T and Kitamura H 2001 SPECTRA: a synchrotron radiation calculation code *J. Synch. Rad.* **8** 1221–8

Zhong N, Morris G M, Bacarian T, Rosen E M and Dilmanian F A 2003 Response of rat skin to high-dose unidirectional x-ray microbeams: a histological study *Radiat. Res.* **160** 133–42